Understanding and Controlling Magnetic Damping Behaviour in Synthetic Ferromagnetic Thin-Film Multilayers

AZZAWI, SINAN,ABDUL,RAZAQ,HAMMOODI

How to cite:

AZZAWI, SINAN,ABDUL,RAZAQ,HAMMOODI (2018) *Understanding and Controlling Magnetic Damping Behaviour in Synthetic Ferromagnetic Thin-Film Multilayers*, Durham theses, Durham University. Available at Durham E-Theses Online: http://etheses.dur.ac.uk/12687/

DURHAM UNIVERSITY

DOCTORAL THESIS

Understanding and Controlling Magnetic Damping Behaviour in Synthetic Ferromagnetic Thin-Film Multilayers

---

Author:
Sinan Abdul Razaq
Hammoodi AZZAWI

1^{st} *Supervisor:*
Prof.Del ATKINSON
2^{nd} *Supervisor:*
Dr.Aidan HINDMARCH

A thesis submitted in fulfillment of the requirements
for the degree of Doctor of Philosophy

in the

Department of Physics

June 13, 2018

Declaration of Authorship

I, Sinan Abdul Razaq Hammoodi AZZAWI, declare that this thesis titled, "Understanding and Controlling Magnetic Damping Behaviour in Synthetic Ferromagnetic Thin-Film Multilayers", the work presented in it are my own and has not been submitted at any University as examination for any other degree.

The sample investegated in chapter 6 and 9 were made by the author with the help of Dr. A.T. Hindmarch, the samples investigated in chapter 7 where made by Dr. R. M. Rowan-Robinson and irradiated by Dr. J. A. King. The samples measured in chapter 8 were made by Dr. J. Brandão with the author help where the lithography and the lift-off processes for the nano-wires were done by Dr. J. Brandão. XRR and XRD for all the samples presented in this thesis were made by the author. All of the samples deposition, fabrication and structural analysis were done in Durham University.

The magnetic measurements presented in chapter 6 and 7 were carried out in S.N. Bose National Centre for Basic Sciences by Dr. A. Ganguly. Dr. J. Brandão performed the MOKE measurements of the samples presented in chapter 8, while the FMR magnetic measurements presented in chapter 9 were carried out by the author and Professor D. Atkinson in the University of Porto and the Brazilian Center for Research in Physics respectively. The analysis of the measurements in chapter 9 was preformed by the author with the help of Professor G.N. Kakazei and Dr. S. Bunyaev to extract the results using labview software made by Dr. S. Bunyaev. also Professor G.N. Kakazei and Dr. S. Bunyaev help to run the experimental device.

Mr. C. Swindells made a Python based software code that was used to extract some of the FMR data, presented in chapter 9. The micromagnetic simulations presnted in chapter 8 were done by Dr. J. Brandão. The theoretical work in chapter 9 was preformed by Dr. A.Umerski at Open University on structure defined by the author and Prof. D. Atkinson. The final discussion and the conclusion of the work presented in this thesis is the author's work.

Signed:

Date:


ferromagnetic
surface
intrinsic
contribution
precessional
extrinsic
interface
resonance
magnetic
materials
FM/NM
Magnetic
DMI
dynamics
damping
two-magnon
Gilbert
magnetisation
Dzyaloshinskii-Moriya
spin
doping
parameter
thickness
spin-pumping
Ferromagnetic
thin-films
irradiation

Abstract

Magnetisation precessional dynamics have a great role in ferromagnetic thin-films and nanostructures, where the underlying mechanisms of intrinsic and extrinsic damping are crucial for spintronic and magnonic devices. This important role drives the research activity with a goal of acquiring a better understanding and the ability to tune magnetic damping properties as desired. Research has tackled these issues through many routes linked with the ferromagnetic material type or thickness, while others have tried different aspects by including other nonmagnetic or ferromagnetic elements as dopants or adjacent layers.

The effect of the additional nonmagnetic materials on the magnetic damping in ferromagnetic system is the focus in this thesis, where a range of implementations of the nonmagnetic material was studied. The role of nonmagnetic layer on damping is shown in this study as the evolution of damping as the thickness of this capping layer developed gradually from none to a partial and to a full covering layer. The effect of nonmagnetic elements was also shown when the changes of the interface takes place, the magnetic damping depends on the development of the interface and the reduction of the NM capping layer is also demonstrated. These routes helps to establish an understanding of damping and the underlying mechanisms.

Linking magnetic damping with other dynamic magnetisation phenomena gives an insight into the reversal behaviour mediated by domain walls in ferromagnetic systems. Studying jointly the contributions of damping and interfacial Dzyaloshinskii-Moriya Interaction gives a better insight into the factor effecting the magnetisation dynamics. As the understanding of the magnetic damping became clearer and the underlying mechanism and effects, linking between two-magnon scattering, spin-pumping and spin-mixing conductance with the crystal structure give more information. This understanding and theory initiated a study to test the theory with a new route to control magnetic damping through modifying the contributions to the total magnetic damping that come from the individual atomic layers that make up a ferromagnetic thin-film. This showed outstanding results consistent with theory and demonstrating very low damping in a new synthetic ferromagnet.

Acknowledgements

I am glad to to express my deepest appreciation to many people who have supported and contributed in different ways to my work and my progress. I gratefully acknowledge the scholarship provides to from the Republic of Iraq, The Higher Committee for Education Development in Iraq (HCED) and the Ministry of Oil in Iraq, for a financial supports of my PhD.

I would like to offer my deepest gratitude to my first supervisor Professor Del Atkinson for his friendship, supervision and guidance. I am thankful for your support and valuable time. I would like as well to express my gratitude to my second supervisor, Doctor Aidan T. Hindmarch for the invaluable discussion, support and his contribution to my PhD research. I am grateful for my both supervisors for their commitments to help me through the writing of my thesis.

I would like to thank the search group leaded by Prof. A. Barman at the S. N. Bose National Centre for Basics Science for the collaboration with our group. I gratefully acknowledge Prof. G. N. Kakazei and Dr. S. Bunyaev, from University of Porto for their time devoted to my work and their hospitality.

I offers my thanks for all those involved in ESRF-The European Synchrotron and ISIS-STFC Rutherford Appleton Laboratory, for their time devoted to creates friendly and collaboration climate. I am grateful for Dr. T. Hase, University of Warwick and Dr. A. Umerski, The Open University for their assistance and support.

I am thankful for my fellows in room 12 and 142; both the former and present occupants: S. Jaiswal, J. King, R.R. Robinson, M. Tokaç, S. Dempsey, O.O. Inyang, L. Stubbington, A. S. Bahaaldin, J. Brandão, J. Troughton, C. Swindells, B. Nicholson and A. Mora-Hernández. Thanks for the fun and the discussion and the help with my work and revising my thesis. Also I would like to thank my house mates and all the technicians in the mechanical shop for their friendly and nice conversations. My gratitude for my friends A. Q. Ibrahim, A. Obied for their support and kindness.

Finally I would thank all my family, each one of them have great belief in me and they have been always the source of my strength.

Contents

Declaration of Authorship **iii**

Abstract **vii**

Acknowledgements **ix**

Contents **xi**

List of Figures **xvii**

List of Tables **xxix**

List of Publication **xxxiii**

1 Introduction and Thesis Structure **1**

1.1 Background 1

1.2 Aims of the Thesis 3

1.2.1 Thesis Outline 4

2 The Physical Basis of Magnetic Properties in Thin-Films **9**

2.1 Introduction 9

2.2 Atomic Magnetic Moment Origin 10

2.2.1 Hund's Rules 11

2.2.2 Spin-Orbit Interaction (Coupling) 12

2.3 Exchange Interaction and Exchange Energy 13

2.4 Band Theory of Magnetism 15

2.5 Dzyaloshinskii-Moriya Interaction (DMI) 18

2.6 The Interaction of Crystal Field and The Magnetic Moment 20

2.7 Magnetocrystalline Anisotropy 21
  2.7.1 Crystal Structure Changing in FM/NM and FM-NM Thin-Films 24
2.8 Magnetostatic Shape Anisotropy 24
2.9 Magnetisation Precession and Magnetic Damping 26
2.10 Polarised Light Interaction with Ferromagnetic Materials 27

3 Methods of Investigation: Physical Basis and Practical Implementation 29
3.1 Introduction: Structural Analysis and Functional Magnetic Measurements 29
3.2 X-Ray Scattering 30
  3.2.1 X-Ray Reflectivity: Refraction and Reflection 31
  3.2.2 Reflection from a Thin-Film 33
    Effect of Thin-Film Thickness 35
    Effect of Thin-Film Interfaces 36
    Yoneda Wings and Determining Interface Nature 38
  3.2.3 X-Ray Diffraction 41
  3.2.4 X-Ray Reflectivity and Diffraction; System Setup and Data Collection. 42
    X-Ray Simulations and Fitting of Experimental Data 43
3.3 Quasi-Static Magnetisation Measurements 45
  3.3.1 Magneto-Optical Kerr Effect Geometries 45
  3.3.2 Longitudinal Magneto-Optical Kerr Effect 47
    Longitudinal MOKE Experimental Setup 48
  3.3.3 Superconducting Quantum Interference Device (SQUID) . . . 50
    Experimental Condition and Setup 50
    SQUID Results and Interpretation 52
3.4 Dynamic Magnetisation Measurements 53
  3.4.1 Time-Resolved Magneto-Optical Kerr Effect (TR-MOKE) . . . 53
    Experimental Condition and Setup 54
    TR-MOKE Data Representation and Interpretation 55

3.4.2 Ferromagnetic Resonance (FMR) 56
Experimental Condition and Setup 59
FMR Results Representation 61
3.5 Summary 62

4 Sample Growth and Modification; Background and Practical Implementation 65
4.1 Introduction 65
4.2 Before Deposition 66
4.3 Samples Shape Related to Measurements Practicality 67
4.4 Deposition Modes and Techniques 68
4.5 Thin-Film Growth Modes 70
4.5.1 The Deposition System and Thin-film Growth Conditions . . . 72
4.6 Ion-Beam Irradiation 76
4.6.1 Ion-Beam Implantation Process 77
4.6.2 Surface Sputtering Process 78
4.6.3 Interface Intermixing and Thin-Films Alloying Process 79
4.7 Ion-Beam Irradiation Effect on Alloying Bi-Layer Thin-Films 82
4.7.1 Ion-Beam Irradiation Effect on Magnetic Properties. 83
4.8 Summary 83

5 An Introduction and Theory for Magnetic Damping Phenomena in Ferromagnetic Thin-Films and Multilayer 85
5.1 Introduction to Magnetic Damping 85
5.2 Intrinsic Damping and Landau-Lifshitz-Gilbert 86
5.3 Extrinsic Damping and Bloch-Bloembergen Equation 89
5.4 Intrinsic and Extrinsic Damping 92
5.5 Damping Description and Calculation 95
5.6 Observations of Damping in Thin-Film Systems 97
5.6.1 Damping in Ferromagnetic Materials 98
5.7 Damping in Bi-Layer and Multilayer Thin-Films 98
5.7.1 The Effect of Ferromagnetic Film Thickness on Damping 99

5.7.2 The Effect of Non-Magnetic Layer Thickness on Damping . . . 103
5.8 Damping in Doped and Alloy Thin-Films 108
5.8.1 Systems with Low Doping 108
5.8.2 Systems With High Doping: Alloys 111
5.9 Limitations of the Recent Experimental Results and the Focus of this Thesis 112

6 Damping Evolution in FM/NM Thin-Films as a Function of NM Thickness 115
6.1 Introduction to Damping 115
6.1.1 Formalism for Analysing Damping 117
6.2 Experimental Details 117
6.3 Thin-Films, Thicknesses, Interface Width and Crystal Structure 118
6.4 TR-MOKE, Data Analysis and Magnetic Damping Thickness Dependence 120
6.5 Chapter Summary 131

7 Damping Modification Through Interface Intermixing in FM/NM Bi-Layer Microstructures 133
7.1 Introduction 133
7.2 Experimental Details and Fittings 135
7.3 Results and Discussion 139
7.4 Chapter Summary 144

8 Understanding the Role of Damping and DMI on Magnetisation Reversal in Nanowires 147
8.1 Introduction 147
8.2 Experimental and Micromagnetic Simulations Details 150
8.3 Results, Analysis and Discussion 154
8.4 Chapter Summary 163

9 Controlling Magnetic Damping in Synthetic Ferromagnetic Thin-Films Via Surface Layer Modification 165

9.1 Introduction . . . 165
9.2 Underlying Theory and Experimental Details . . . 167
9.3 Results and Discussion . . . 169
9.4 Chapter Summary . . . 179

10 Conclusions and Further Work **181**
10.1 Conclusions . . . 181
10.2 Further Work . . . 186

Bibliography **189**

List of Figures

2.1 Illustration of (a) the atomic magnetic moment configuration with (b) and (c) the spin up, spin down and the origin of the atomic magnetic moment and (d) the total magnetic momentum. 11

2.2 Electron distribution according to Hund's rules for Fe atom with increasing energy by fulling the higher levels with electrons. 12

2.3 Schematic of the Bethe-Slater curve, illustrating the importance of the ratio of interatomic separation, r, to the radius of the d band, r_{nd}, on the sign and magnitude of the exchange interaction and sketches to illustrate to spatial overlap of the electronic wave functions. The n here represent the number of the d shell in different metals which is either 3, 4 or 5. 14

2.4 A schematic view of broadening of electron energy levels when the inter-atomic distance decreases. (b) Density of levels in the 3d and 4s bands. 16

2.5 Schematic to show the electronic band structure and density level of states for (a) anti-ferromagnetic transition metals, (b) non-magnetic transition metals, (c) weak ferromagnetic transition metals and (d) shows 3d band splitting in spin-up and spin-down states in ferromagnet with exchange energy effect. 17

2.6 Schematic of interfacial DMI showing thin-film magnetisation orientation, where it raise when a FM material coupled with adjacent NM layer with strong SOC. 20

2.7 Magnetisation curve along different crystallographic axes for single crystal of (a) bcc Fe, (b) fcc Ni and (c) hcp Co where the easy, medium and the hard axis showing the preferential alignment due to magnetocrystalline anisotropy. 23

2.8 Schematic illustration of demagnetisation field shows a material magnetisation in thin-film along the X, Y and Z direction, where the shape governs the magnetic alignment. 25

2.9 Shows a different types of precession modes with the final decay into lattice vibration and the transformation of the energy between modes. 27

3.1 Schematic illustration of the x-ray scattering from medium, showing refraction and reflection with respect to the refractive index. 32

3.2 Schematic illustration of the x-ray scattering from simple thin-film with single layer over substrate with the calculation of the total reflection from incident x-ray beam. This beam will be divided into reflected, r_{nm}, and transmitted, t_{nm}, beams from the top or the bottom interface of the first layer. If the reflection or the transmission direction is toward thin-film surface then $n > m$, while if the direction toward the substrates then $n < m$, where n and m = 0,1 or 2 only. 35

3.3 Specular reflectivity for 7 nm and 20 nm $Ni_{81}Fe_{19}$ thin-films on an infinite SiO_2 substrate as function of the wavevector q_z. The blue line shows the general decay of the intensity where the critical wavevector of the order 10^{-2} 37

3.4 Shows the effect of the interface width on the intensity reflectivity and the dips of Kiessig fringes, where three thin-films used with 4 nm of $Ni_{81}Fe_{19}$ and capped with Pt from 0.2-1 nm. The roughness show a larger amplitude of Kiessig fringes when the Pt capping layer is less thickness regarding the non-continues capping layer. 38

3.5 Schematic figures showing (a) Topological roughness, (b) Chemical grading or intermixing. Also showing Graphical representation of total interface width σ_{tot}, the contribution of the topological σ_{r} and the intermixing σ_{i} with the changing of the electron density as a function of (c) interface width Z and (d) the diffuse scattering angle θ. 39

3.6 Schematic figures showing (a) ideal perfect sharp interface , (b) rough interface with topological roughness and the diffuse non-specular x-ray with Yoneda wings of rough interface, where the incident angle θ changing to the critical angle θ_{c} while the reflection angle is fixed at 2θ. 40

3.7 Schematic figure showing Bragg's law of diffraction, the condition of the constructive interface between the incident and the reflective x-ray beams. 41

3.8 MOKE geometry with different light incident where it shows (a) and (b) longitudinal setting with S- and P-polarized incident light respectively, where it shows Kerr rotation. 46

3.9 MOKE geometry with different light incident where it shows (a) and (b) Polar with Kerr rotation and transverse setting with Kerr amplitude respectively, where the incident light is P-polarized. 46

3.10 Schematic of the longitudinal magneto-optical Kerr effect magnetometry system with all the principle components showing the light path through the optical enhancement and focusing. 48

3.11 A schematic figure for the SQUID , showing the sample position and the main detecting coils with the voltage changing with the sample movement through the device. 51

3.12 Shows (a) typical raw data from SQUID measurements, where the diamagnetic effect and (b) the final shape of the hysteresis loop with the analysis of the saturation magnetisation. 52

3.13 Schematic of the longitudinal magneto-optical Kerr effect magnetometry system with all the principle components showing the light path through the optical enhancement and focusing producers. 55

3.14 (a) TR-MOKE typical data trace from a Co10/Pt0.6 nm sample showing Kerr rotation with the T_1 and T_2 time base and (b) is Kerr rotation as a function of T_2, after removing the general recovery of the magnetisation. 56
3.15 Schematic showing the VNA-FMR system,where the microwave radiation signal and the rf field h_{rf} directions with respect to the external field. The coplanar waveguide (CPW) placed in the centre of an electromagnet and the ferromagnetic magnetic film is placed on the CPW mounted in non-magnetic sample holder with goniometer between a set of magnetic coils. 60
3.16 Shows a typical data of FMR measurements, where the rf signal changing as a function of (a) the external field and (b) the frequency, also (c) showing the imaginary and the real component for extracting the frequency linewidth, finally (d) showing the Kittel formula fitting according the relation between the field and the frequency. 61

4.1 Shows tools for cutting and masking the Silicon wafer (a) and (b) are the wafer holder from both up and down side respectively, (c) is the shadow mask with different shapes (d) the chamfered technique and finally (e) all the produced sample shapes. 68
4.2 Shows a schematic illustration of (a) deposition technique where the sputtered atoms ejected from the material target (cathode) to the substrate (anode) and (b) the sputtering process with the magnetron field. 69
4.3 Schematic illustration of thin-film growth modes including (a) Volmer-Weber island growth, (b) Frank-Van der Merwe layer-by-layer growth and (c) Stranski-Krastanov layer plus- island growth. 71
4.4 Shows side view of Mantis Qprep500 sputtering system in the lab with the main parts indicated. 73
4.5 A schematic illustration of ion-beam irradiation of thin-film showing the main processes and other events such as backscatter ions, electrons and the emission of x-ray as a result. 76

4.6 Recession of surface and the capping layer decreasing due to the surface Au atoms sputtering as a function of ion-beam irradiation dose for bi-layer thin-films the dashed line are guide to the eye, adapted from [99]. 79

4.7 The effect of ion-beam irradiation dose on topological roughness and chemical intermixing for Ni_{81}Fe19 20 nm/Au 2.5 nm thin-film by XRR. The same effect extracted from TRIDYN simulation, which shows agreement with the XRR results, the XRR and the simulation results adapted from [99] and [109] respectively. 82

5.1 Illustration of damping process of the magnetisation according to Landau-Lifshitz-Gilbert LLG model, precession as the first term and the damping force as the second term, where the magnitude of the magnetisation is constant. 88

5.2 Illustrations of the Bloch-Bloembergen (B-B) gyromagnetic process equation in the first term, the Z-component of the magnetisation remains constant, but the effective magnetisation reduces according to the second term. 92

5.3 Illustrates the spin-pumping effect in typical FM/NM thin-films with the effective spin-mixing conductance $g_{\mathrm{eff}}^{\uparrow\downarrow}$ at the interface and spin diffusion length λ_{sf}. 93

5.4 The effective damping parameter for elemental ferromagnetic transition metal thin-films: Fe in the range 4-30 nm; Co with thicknesses between 10 and 20 nm, $Ni_{81}Fe_{19}$ with thickness 3.5-20 nm and films of Ni $\geq$ 20 nm. The thicknesses indicated are in nanometres and the substrates and any additional underlayers and capping layers are also listed. 99

5.5 The effective damping parameter as a function of reciprocal FM layer thickness $1/d_{\mathrm{FM}}$ for (a) ordered and disordered NiFe thin-films. The figure shows linear and non-linear relations adapted from Ref. [179], (b) for amorphous CoFeB, showing the sensitivity of the damping to underlayer and capping layer materials, adapted from Ref. [187, 189],(c) NiFe with different underlayers/capping layers(d) Ni with different capping layers, adapted from Ref. [147, 173] respectively and (e) Co layer thickness for different combinations of NM underlayers and capping layers, from Refs [75, 151, 178]. 100

5.6 An examples of damping parameter contribution calculation from each mono-layer in bcc Fe, fcc Co and fcc Ni, of 18 ML thickness, adapted from [6]. 102

5.7 A summary of the effective damping parameter for NiFe thin-films combined with various NM layers. 104

5.8 Effective damping parameter as a function of Cu spacer layer thickness separating a FM layer (CoFe or YIG) from another NM layer (Ta or Pt) [195, 196], with large thickness range of capping layers. 105

5.9 Effective damping parameter as a function of NM layer thickness of either Pt or $SrRuO_3$ capping layers on different FM layers [195, 199, 202], with large thickness range of capping layers. 106

5.10 The effective damping parameter as a function of Pd capping layer thickness on CoFe ferromagnetic films with Ta/Pd underlayers [188, 196]. 106

5.11 Calculations of the damping contribution from each mono-layer of FM;Co and NM (a) Pt, where it shows the largest contribution to α from the mono-layers near to the interface and (b) Cu where it shows no contribution to the total damping, adapted from [6] 107

5.12 Damping parameter as a function of atomic concentration of (a) and (b) transition metals Ref. [217] and (c) rare-earth dopants. Results from two different studies: Solid symbols from Ref. [219] and open symbols from Ref. [220]. All figures show correlation between damping and the dopant concentration, however the trend in (b) shows more non-linear dependence at high concentrations. 109

5.13 Damping reduction as a function of focused ion-beam irradiation dose, the general trend shows linear reduction behaviour, adapted from Ref [222]. 110

5.14 The effective damping parameter as a function of the elementary compositions for binary alloys of Fe, Co and Ni from [119], $+$, $\triangledown$, $\triangle$, $\oplus$, $\ominus$ 112

6.1 Examples of x-ray reflectivity data and the best fitting simulations for (a) Co (10 nm)/Pt (d_{Pt}), (b) $\mathrm{Ni}_{81}\mathrm{Fe}_{19}$ (7 nm)/Pt (d_{Pt}), (c) Co (10 nm)/Au (d_{Au}) and (d) XRD structural analysis for Co and $\mathrm{NI}_{81}\mathrm{Fe}_{19}$ capped with Pt 119

6.2 Examples of the TR-MOKE data for (a) Co and $\mathrm{Ni}_{81}\mathrm{Fe}_{19}$ capped with 0.2 Pt and Au, (b) capped with 1 nm Pt and Au, and (c) illustrates the tin-film stack with the frequency. 121

6.3 α_{eff} as a function of d_{NM} for (a) Co/Pt and (b) $\mathrm{Ni}_{81}\mathrm{Fe}_{19}$/Pt. (b) frequency and saturation magnetisation as function of d_{NM} and $\sim$1.4 kOe of magnetic field strength, it shows similar trend in their variations. The shaded bar indicate the Pt thickness where the Pt became continuous. 123

6.4 Damping parameter α_{eff} as a function of precession frequency for 10 nm Co films capped with 0.6 nm and 2 nm Pt. The extrinsic damping decreases as $d_{\mathrm{NM}} = 2$ nm where it became a negligible value 124

6.5 Illustrates the interaction of (a) Pt and (b) Au with Co at the interface and development of the interface with increasing NM thickness. Also, (c) shows a comparison of the damping parameter, α_{eff}, as a function of Pt and Au thickness in relation to the interaction of these metals with Co, considering the bulk value from the literature [77], where regions I, II and III are labelled. 126

6.6 A comparison between (a) experimental and (b) theoretical (adapted from Ref. [6]) variations in damping data for Co/Pt and Co/Au as a function of d_{NM}. The star symbol is the literature value for pure cobalt. 130

7.1 Schematic illustration of a bilayer of a $\text{Ni}_{81}\text{Fe}_{19}$ 10 nm/Pt 3 nm circular structure with ion-beam irradiation. 136

7.2 Shows (a) Time-resolved Kerr images of the sample at three time delays. (b) A raw TR-MOKE data trace from a sample irradiated with ion dose d = 3.1 pC/μm^2, 1.9 × 10^{15} Ga$^+$/cm^2, as a function of the time delay [4]. 137

7.3 A comparison of TR-MOKE traces between (a) NiFe/Pt (dose = 0.3 pC/μm^2) and NiFe films. Symbols correspond to experimental data while the solid curves are fits to Eq. 7.1. (b) Power spectra of the NiFe/Pt sample at different bias field values H. (c) Frequency vs the bias magnetic field for the NiFe/Pt (d = 0.3 pC/μm^2) sample. Here the symbols represent experimental data points and the solid curve is a fit of the Kittel formula [4]. 138

7.4 Damping parameter is plotted as a function of dose. The shaded box represents the transition between regions I and II. 140

7.5 Variation of damping parameter as a function of irradiation dose in the lower dose regime for $\text{Ni}_{81}\text{Fe}_{19}$/Pt (filled circles) and $\text{Ni}_{81}\text{Fe}_{19}$/Cu (filled triangles). 141

7.6 Dependence of the damping on the precession frequency, controlled by the bias field, for three different doses, with their linear fits. 143

7.7 (a) FFT power spectra of the TR-MOKE data of ion irradiated NiFe/Pt samples at three different doses. (b) Variation of frequency f as a function of dose. Symbols are the experimental data and solid lines are linear fits. The shaded box represents the transition between two regions. (c) Magnetisation relaxation times τ_1 and τ_2 are plotted as a function of dose. Here the symbols are obtained from experimental data while the solid lines are only guides to the eye [4]. 144

8.1 SEM images of nanowires of bi-layers $Ni_{81}Fe_{19}$/Pt show different geometries produced by electron-beam lithography, to study DW propagation. Pinning the potential to the DW propagation is due to the triangle features placed on the nanowire edges. It shows that the pad and the tampered shape were used to inject and annihilate DWs, respectively. 151

8.2 Effective damping parameter obtained in $Ni_{81}Fe_{19}$/Pt thin-films. The damping increases rapidly between 0 and 0.6 nm Pt thickness, then above it goes down slowly. The dashed line illustrates the expected contribution to the damping from intrinsic processes. 153

8.3 Examples of axial magnetic hysteresis behaviour for nanowires (triangular modulated edges with 75 nm amplitude). (a) Measured hysteresis for $Ni_{81}Fe_{19}$ (10 nm) (continuous line) and $Ni_{81}Fe_{19}$ (10 nm)/Pt (0.6 m) nanowires (dots). The reversal field is observed to be higher for $Ni_{81}Fe_{19}$ (10 nm)/Pt (0.6 m) than the $Ni_{81}Fe_{19}$ (10 nm). (b) Simulated magnetic hysteresis for nanowires with a damping parameter of 0.01 (continuous line) and 0.04 (dots), showing that the increased damping provided by the Pt overlayer enlarges the reversal field for larger damping. 155

8.4 Reversal field as a function of Pt thickness. In (a), for different periodic edge-modulated nanowires with the general trend of the reversal field increasing as a function of d_{Pt}. In (b), the normalised reversal field shows that the reversal field independent of the nanowire geometry. Insert, scanning electron microscopy (SEM) images of nanowires show the different geometries used to study DW propagation in $\mathrm{Ni_{81}Fe_{19}}$ with a Pt overlayer. 156

8.5 Reversal field simulated as a function of (a) the intrinsic damping parameter , where it shows the reversal field goes up rapidly from 0 nm to 0.6. In (b), the reversal field shows that the behaviour as a function of IDMI has two different damping values of 0.01 and 0.04. Both the reversal fields as a function of IDMI show a smaller influence on the DW propagation, though for higher damping the IDMI makes a more important contribution to the reversal field strength. 158

8.6 DW velocity calculated in parallel-sided nanowires for various IDMI and damping values 0.01 (a) and 0.04 (b), which shows the different Walker breakdown ranges. For both the damping values the velocity undergoes a reduction beyond the Walker field threshold. The Walker field is higher for damping values 0.04 than 0.01. However, the IDMI affects both the Walker field (c) and DW velocity (d), which for IDMI beyond 0.3 (mJ/m^2) are decreased. 161

8.7 Calculated along of the magnetisation component as a function of DW position in the nucleation process with a 0.01 damping value. In (a), the M_x changes from 1 to -1 due to the magnetic moments head to head in transverse DW. M_y is always positive, which is typical for transverse domain walls. M_z, however, the dashed blue line, emerges for a DMI value of 1 mJ/m^2. In (b), M_z magnetisation components were calculated for different values of DMI, where M_z increases as the DMI becomes larger. The continuous line shows the absence of the magnetisation component without DMI. In (c), the snapshots show the the transitions from transverse domain wall up to down, mediated by core vortex nucleation. 162

9.1 X-ray reflectivity results for selected samples, where it shows (a) specular x-ray with the best fit and (b) specular diffuse scattered x-rays. . . 169
9.2 The FMR signal in (a) S_{12} is changing as a function of both frequency and field, also (b) shows the variation of the peak and the dip as with increasing field and frequency in 3D projection, where the colour legend stand for S_{12} signal. (c) damping fitting using field linewidth domain and (d) shows Kittel fitting for Co 5 nm/Cu 2 nm. 170
9.3 Damping extraction from FMR measurements of field and frequency linewidths, where (a) shows the same general trend of α_{eff} reduction with increasing Cr concentration for 0- 0.8 % Cr doping, (b) the extrinsic contribution to damping, which shows big contribution from the inhomogeneous component to α_{eff}. 171
9.4 Saturation magnetisation is plotted as a function of the Cr concentration, where it is calculated from (a) frequency and (b) field linewidths. It shows reduction in magnetisation with the increasing of doping. . . 172
9.5 Saturation magnetisation as a function of the Co surface layers doping concentration with Cr. The general trend of M_S shows some similar behaviour between all results. Noting that ○ is the literature value of the saturation magnetisation of bulk Co [314]. 173

9.6 Inhomogeneous broadening to the damping as a function of Cr concentration where it shows the homogeneities of the system. 174

9.7 Intrinsic damping parameter α_{eff} extracted from FMR measurements in frequency linewidth and field linewidths analysis. The data shows the general trend of the damping behaviour as a function of the Cr doping concentration and the difference in the results between the frequency and field linewidth measurements. 175

9.8 Intrinsic damping results extracted from FMR measurements in the field linewidth and the calculated Radiative, α_{rd}, and the spin-pumping, α_{sp}, where their contributions subtracted from the total damping. The final corrected net damping, α after the subtraction of both contribution shows very low values especially at 50 % Cr doping concentration and beyond. 176

9.9 Theoretical calculation for damping contribution form each individual layer, with a schematic illustration shows the Cr concentration increasing from (a) 10 %, (b) 20 %, (c) 30 % and (d) 40 %, where the effect on damping starts by decreasing the contribution to the total damping from the boundaries atomic layers. 177

9.10 Comparison between theoretical calculation and the final extracted experimental results. 178

List of Tables

3.1 Density ρ of different pure and alloyed material in kg/m^3 and $u/\text{Å}^3$ . . 44

4.1 Deposition conditions, showing the system parameters of the bi-layer thin-film fabrication from 10 nm Cobalt and 0.2 nm Platinum capping layer. 75

4.2 Deposition conditions, showing the system parameters of the bi-layer thin-film fabrication from 4 nm $Ni_{81}Fe_{19}$ and 2 nm Platinum capping layer. 75

4.3 Deposition conditions, showing the system parameters of the bi-layer thin-film fabrication from 5 nm [$Co_{60\%}$-$Cr_{40\%}$ 1.25/C 4.75/$Co_{60\%}$-$Cr_{40\%}$ 1.25] and 2 nm Copper capping layer. 75

6.1 Structural properties for selected Co/Au, Co/Pt and NiFe/Pt bi-layers samples extracted from XRR measurements: FM layer thickness, d_{FM}; NM layer thickness, d_{NM} and roughness at the FM/NM interface. . . . 119

List of Abbreviations

B-B	**B**loch-**B**loembergen
bcc	**B**ody-**c**entred **c**ubic
bct	**B**ody-**c**entred **t**etragonal
CPW	**C**o**p**lanar **w**aveguide
DMI	**D**zyaloshinskii-**M**oriya **i**nteraction
DOS	**D**ensity **o**f **s**tates
DW	**D**omain **w**all
fcc	**F**ace-**c**entred **c**ubic
FFT	**F**ast **F**ourier **t**ransform
FIB	**F**ocused **i**on-**b**eam
FM	**F**erro**m**agnetic
FMR	**F**erro**m**agnetic **r**esonance
FWHM	**F**ull-**w**idth-at-**h**alf-**m**aximum
hcp	**H**exagonal **c**lose-**p**acked
IDMI	**I**nterfacial **D**zyaloshinskii-**M**oriya **i**nteraction
LLG	**L**andau-**L**ifshitz-**G**ilbert
MO	**M**icroscope **o**bjective
MOKE	**M**agneto-**o**ptical **K**err **e**ffect
NM	**N**on**m**agnetic
OBD	**O**ptical **b**ridge **d**etector
QCM	**Qu**artz-**c**rystal **m**icrobalance
RKKY	**R**uderman-**K**ittel-**K**asuya-**Y**osida
SHA	**S**pin **H**all **a**ngle
SO	**S**pin-**o**rbit
SOC	**S**pin-**o**rbit **c**oupling
SOI	**S**pin-**o**rbit **i**nteraction
SQUID	**S**perconducting **q**uantum **i**nterference **d**evice
T-DW	**T**ransverse **d**omain **w**all
TR-MOKE	**T**ime-**r**esolved **m**agneto-**o**ptical **K**err **e**ffect
UHV	**U**ltra-**h**igh **v**acuum
V-DW	**V**ortex **d**omain **w**all
VW	**V**ortex **w**all
WF	**W**alker **f**ield
XRR	**X**-**r**ay **r**eflectivity
XRD	**X**-ray **d**iffraction

List of Publication

- "Tunable Magnetization Dynamics in Interfacially Modified $\mathrm{Ni_{81}Fe_{19}}$/Pt Bilayer Thin Film Microstructures"

  Arnab Ganguly[1], **Sinan Azzawi**[2], Susmita Saha[1], J. A. King[2], R. M. Rowan-Robinson[2], A. T. Hindmarch[2], Jaivardhan Sinha[1], Del Atkinson[2] & Anjan Barman[1], ***Sci. Rep.*** 5, 17596, Published: 01 December 2015.

- "Evolution of damping in ferromagnetic-nonmagnetic thin film bilayers as a function of nonmagnetic layer thickness"

  S. Azzawi,[1] A. Ganguly,[2] M. Tokac,[1] R. M. Rowan-Robinson,[1] J. Sinha,[2] A. T. Hindmarch,[1] A. Barman,[2,*] and D. Atkinson[1,†] ***Phys. Rev. B***, 93, 054402, Published: 1 February 2016.

- "Understanding the role of damping and Dzyaloshinskii-Moriya interaction on domain wall dynamic behaviour in platinum-ferromagnet nanowires"

  J. Brandão, **S. Azzawi**, A. T. Hindmarch & D. Atkinson, ***Sci. Rep.*** 7, 4569, Published online: 04 July 2017.

- "Magnetic Damping Phenomena in Ferromagnetic Thin-Films and Multilayers"

  S Azzawi, A T Hindmarch and D Atkinson, ***J. Phys. D: Appl. Phys.,*** Vol. 50, No. 47., Published: 25 October 2017.

Dedicated to my father's soul and to my mother

Chapter 1

Introduction and Thesis Structure

1.1 Background

Magnetic damping and ferromagnetic resonance are important fundamental phenomena in ferromagnetic materials and thin-film systems. The role of the magnetisation precession in magnetic data storage and sensors has been the focus of many studies in the field of spintronics and magnonics research, which arose from the need to control magnetic properties of thin-films and nano-structures. Achieving high magnetic damping in a ferromagnetic system is one of the desirable features in application technologies. Increasing the damping rate of the precessional magnetisation in data storage and memory devices lowers the time of magnetic precession, which is a key factor for speeding up the data writing and transformation process. On the other hand, decreasing magnetic damping in ferromagnetic material is in favour in cutting-edge technologies such as spin-transfer torque magnetic random access memory (STT-MRAM or STT-RAM) and magnonic devices, where low damping in such applications leads to reduce write-current and improves the spin wave propagation respectively [1, 2].

These issues were tackled by different studies, where this has been done through the investigation of magnetic damping and ferromagnetic resonance through experimental observations and theory calculation. The role of the underlying phenomena that give rise to the magnetic damping behaviour, such as spin-orbit interaction, exchange interaction and density of states were investigated in relation with magnetic damping. In the theoretical understanding, spin-orbit coupling is considered with the d orbital electron contribution to the energetic states at the Fermi energy level as the main contribution to the behaviour of any given FM system. These studies contributed to the general understanding of magnetic damping and the rise of several phenomena together offer a clear image of the magnetic spin precessional dynamics in ferromagnetic systems. These phenomena can be seen as fundamental intrinsic effects within the ferromagnetic material essence such as spin-pumping, spin-mixing conductance and spin-diffusion length or as extrinsic additional factors such as two-magnon scattering. All of these are related with the spin-orbit coupling of the material being investigated and its electronic and energetic behaviour, as a stand-alone element or in combination with other elements. The spin-wave and spin-current interaction, mobility and transformation are the focus point of many studies.

In experimental research, damping was investigated in a range of systems with different levels of complexity starting from the simple bulk system, where damping was investigated as a function of the ferromagnetic material type, thickness and crystal structure. Raising the level of complexity to more than one layer and shape including not only ferromagnets, but also non-magnetic materials, gave more understanding of damping and the underlying phenomena. In such studies understanding and modifying magnetic damping has been achieved through different methods, some of them linked with nano-shapes such as nano-wires [3] and structures [4]; others are linked with additional effects. These effects are linked to the addition of dopants or adjacent material layer [5]. This opens research for investigations regarding the dependence of damping enhancement on the non-magnetic layer material type, thickness, concentration and number of layers. Electron beam lithography is one of the research techniques used to control the shape of ferromagnetic systems, while sputtering and ion-beam irradiation are used to build nano-structures from the simple to complicated systems. The findings of theory and experimental contributes to the understanding and the application of magnetisation precession in devices. In spite of the big effort and the number of studies in the field of magnetic damping in terms of understanding and controlling damping for application, there is a need for further research.

The research in this thesis aims to contribute to the understanding of magnetic damping phenomenon through experimental research with the aid of theory, to understand the role of damping in general and the modifications that can be implemented for both increasing and decreasing it. The focus was to investigate damping variation as a function of interface change, the non-magnetic layer type and thickness, and varying the contribution of each mono-layer to the total damping by synthetically engineering it with a dopant. The results of this thesis give a better understanding on magnetic damping and show interesting results on some underlying phenomena, which, linked with damping, also links to other effects such as the Dzyaloshinskii-Moriya interaction.

1.2 Aims of the Thesis

The aim of this thesis is to provide insight into the understanding of magnetisation damping in thin-films and nano-structures. Techniques including sputter deposition, co-sputtering and ion-beam irradiation were used to structure layered thin-films and control the concentration of the materials. The study focuses on damping in Co and $Ni_{81}Fe_{19}$ as ferromagnetic materials and Pt, Au, Ag, Cr and Cu as non-magnetic materials. Bi-layer samples were produced as thin-films, micro-structured dots and nano-wires, with co-sputtering used to synthesise doped ferromagnetic films of layers within some of the thin-films.

Measurements have been carried out in terms of investigating the precessional magnetisation in the time domain by the time-resolved magneto-optical Kerr effect and wave excited ferromagnetic resonance. Furthermore, thin-film thickness, interface roughness and crystal structure were investigated using x-ray reflectivity and diffraction to link and aid the explanation of the magnetic behaviour with structural changes. A range of other measurements, such as using a superconducting quantum interference device and the magneto-optical Kerr effect magnetometry were done in order to investigate other magnetic properties.

A better understanding of magnetic damping and the underlying effect, a deeper insight into the relation between damping and other relative interfacial phenomena such as Dzyaloshinskii-Moriya interaction with the new concept of damping are presented. The results are important in relation to application in cutting-edge technologies in terms of optimising the speed of data writing and transformation.

1.2.1 Thesis Outline

This thesis starts with a general introduction to the magnetic damping role in research and application fields, the role of damping in modern technologies as required to improve their performance. The theory to understand these phenomena and enhance the microscopic view of the underlying mechanisms is followed by the experimental aspects investigating the origin and the modification of the magnetic precession and damping in different systems.

In Chapt. 2, the physical basis of magnetism and magnetic behaviour is presented as an introduction. Starting with the origin of magnetism at the atomic level, the magnetic moment is followed by a further description that leads to many phenomena and fundamentals which affect the magnetic behaviour in any given ferromagnetic system. Other effects or phenomena are included as a result of the magnetic moment or as effects that can shape the final magnetic behaviour of the material such as shape anisotropy. Damping in the simplest terms of energy dissipation is introduced with some of the effects that can be detected in ferromagnetic systems.

A detailed explanation is presented in Chapt. 3, which covers the theory and the underlying physics of the experimental implementation of each technique. This chapter is divided into three sections which represent different types of measurements. Firstly, the structural investigation, including x-ray reflectivity and diffraction, is presented as a part of the crystal structure and thin-film thickness and interface width investigation. Secondly is the quasi-static measurements that investigate the magnetic states without including time variations. These measurements represented by superconducting quantum interference device and magneto-optical Kerr effect magnetometry. The final part is the dynamic measurements which are more related with magnetisation precession in two main techniques the time-resolved magneto-optical Kerr effect and ferromagnetic resonance. The data analysis and experimental setup are discussed in detail to gain a better understanding regarding the measurement results.

In Chapt. 4 the background theory and the practical implementation of all the sample fabrication is explained. Starting from the stages before deposition, the cleaning and cutting in relation to the sample size and the experimental requirements are explained. This is followed by the background of the material deposition with a focus on the main deposition system and its main features and the growth conditions. Growth modes are explained in order to give insight and link the results with any structural changes that may take place through the deposition process. The main system used is explained with examples of some of the fabricated samples. In another section, ion-beam irradiation is presented with the theory and the experimental results from the literature showing the main effects that take place in the range of ion beam doses used here. The investigations of the ion irradiation are discussed as it brings structural effects and changing the thin-film layers intermixing and finally this impacts on the magnetic behaviour.

Since magnetic damping is the main focus of this thesis, it seems a better idea to dedicate a full chapter to review this phenomenon, which is Chapt. 5. This chapter is based on published review study of damping and used to produce an extended background on magnetic damping phenomenon in thin-films and nano-structures. It starts with the mechanisms that define the nature of damping and then extends the explanation further to cover many related effects, using the theory to develop an understanding of damping. In the second section experimental studies are reviewed, their findings are presented as linked results, with the dependence of damping on ferromagnetic and non-magnetic and the thickness and number of layers in more complicated systems. The damping variation is also shown as a function of dopant and doping concentration. Finally, the current status of the general understanding of magnetic damping is discussed. This chapter is limited to the topics related to the subject of this thesis.

The results of the work in this thesis starts in Chapt. 6. This chapter is one of the published works in which the evolution of magnetic damping is investigated as a function of Pt and Au capping layer thickness in bi-layer thin-films. The main techniques that are used to produce and investigate the samples are explained with examples of some of selected data. The work is presented as a comparison with a recent theoretical study by Barati *et al* [6]. In the chapter a background on the subject is presented and an analysis of the experimental results with an explanation of the different effects. The damping results in this chapter are supported by structural analysis and with the aid of the theory and other magnetic measurements.

In Chapt. 7 a study of the damping dependent on interface modification of bilayer micro-structures fabricated with electron beam lithography is reported. Pt was used as capping layer and the interface structure was changed by focused ion-beam irradiation induced intermixing. The chapter includes the related theory and a comparison with results from earlier studies. The magnetic damping behaviour is explained with the aid of a structural investigation of a similar system due to the same irradiation process. Time-resolved magneto-optical Kerr effect observations were used and explained along with the method of extracting the damping parameter.

The study of Chapt. 8 is based on the results of Chapt. 6. The influence of enhanced damping obtained from the experimental study was combined with the interfacial Dzyaloshinskii-Moriya interaction, taken from the literature and used in micromagnetic simulations on the magnetisation reversal of domain wall propagation in nano-wires. Switching nano-wires was also studied experimentally, the fabrication of the samples as nano-wires with different-sided shape features is explained with examples of the wires, microscopic images, where the electron beam lithography technique was used to produce the nano-wires. Experimental and simulation details about the measurements such as magneto-optical Kerr effect magnetometry and Mumax^3 code are explained. The results and the analysis are discussed with the contribution of damping enhancements and interfacial Dzyaloshinskii-Moriya interaction on the domain wall magnetisation reversal. The reversal field and Walker breakdown and domain wall velocity behaviour are also included. This was done for different ranges of damping and interfacial Dzyaloshinskii-Moriya interaction. Then in the final section, the conclusion and the summary show the findings of this study.

In Chapt. 9, a study is reported on a new route to damping control, through the synthetic engineering of specific mono-layers in ferromagnetic material via doping with non-magnetic material. The study was built upon the results from a theoretical study and previous well-known experimental observations in order to came up with a new proposition which can be executed in terms of thin-film fabrication and measured in terms of magnetic damping. The results are presented in this chapter of two main damping measurements in order to verify the results. Furthermore, theory calculations were carried out with calibration to compare the results, which show good agreement. Structural analysis and other quasi-static measurements are included in order to provide a full understanding of the findings of the study. In this chapter this is the final study, which represents a significant achievement, showing controlling of damping in synthetic ferromagnetic thin-films.

The final Chapter is the conclusion of the thesis, which summarises the main results in the experimental chapters with the interpretation and the most significant findings and their role in the research and the application field. This is followed by a discussion of the featured work as new ideas and measurements which can be considered as a step toward new futuristic studies in the research and technology field. The results of this thesis may have a remarkable influence on the cutting-edge technologies such as spintronic and magnonic devices.

Chapter 2

The Physical Basis of Magnetic Properties in Thin-Films

2.1 Introduction

The aim of this chapter is to give an insight of the underlying physical phenomena and the basic concepts in thin-film magnetism. We start by discussing the origin of atomic magnetic moments before considering the distribution of electrons in single and multiple atoms given by Hund's rules, that links with a material's magnetic properties. The next topic of consideration is the spin-orbit interaction (SOI) or spin-orbit coupling (SOC), regarded as an important physical concept for behaviour of ferromagnetic (FM) systems. The magnetic interactions in multiple atom systems can be explained by the band theory, which helps to explain the more complicated magnetic behaviour in crystal systems. The electronic ordering in a system, which is explained by this theory, gives rise to interactions such as exchange and crystal field interactions. These interactions can work together to give the final magnetic state of the material. This can be seen in Dzyaloshinskii-Moriya interaction and magnetocrystalline anisotropy that are based on the exchange and crystal field interactions.

As a main part of this thesis, ferromagnetic resonance and magnetic damping are explained here in terms of energy origin, transformation and dissipation mechanisms. These mechanisms give a general understanding on the energy transformation, dissipation and magnetisation precession in ferromagnetic (FM) materials. The underlying effects for these mechanisms are discussed more in depth in a later chapter. The final part of this chapter describes the interaction between a magnetised sample and polarised light, which provides a useful probe into the quasi static and dynamic magnetic properties of a system. The Faraday and Cotton-Mouton effects, which are linked to the basis of magneto-optical Kerr effect (MOKE) are explained. The magneto-optical Kerr effect is used dynamically to measure magnetic damping, which is called the time-resolved magneto-optical Kerr effect (TR-MOKE). Having these basics gives a starting point to show the focus of this thesis and to provide a suitable explanation to these effects and phenomena, so that in the following chapters they can aide the understanding of the work in this thesis.

2.2 Atomic Magnetic Moment Origin

In an atom, the atomic magnetic moment (μ) is related with the total angular momentum ($\mathbf{J}$) by the gyromagnetic ratio (γ) or the Landé g-factor (g_0) [7]. The total angular momentum is the sum of the spin (S) and orbital (L) angular momentum, Fig. 2.1 shows an image for spin and orbit momentum in simple schematic atom configuration where the total angular moment for both S and L is:

$$S = \sum m_s \tag{2.1}$$

and

$$L = \sum m_l \tag{2.2}$$

The interaction between the intrinsic spin moment (m_s) and the orbital moment (m_l) of each electronic level is the origin of the total angular momentum hence the atomic magnetic moment. Atoms with partially filled shells have a higher magnetic moment and for the metallic ferromagnets Co and Ni having the highest magnetic moment while Fe magnetic moment is less [8–10].

The atomic magnetic moment is the source of the magnetic properties and it is the key of many magnetic behaviours. The different magnetic properties of materials are related the electron distribution that are determined using Hund's rules, which are discussed more in detail in the following section [8, 9, 11].

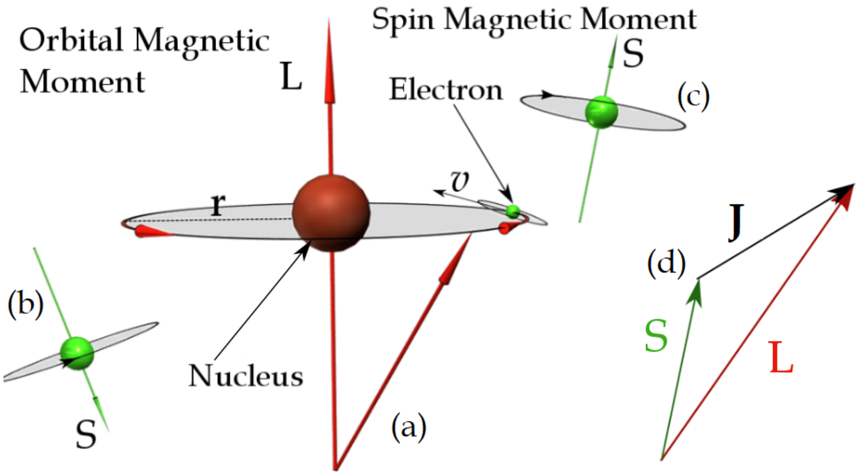

FIGURE 2.1: Illustration of (a) the atomic magnetic moment configuration with (b) and (c) the spin up, spin down and the origin of the atomic magnetic moment and (d) the total magnetic momentum.

2.2.1 Hund's Rules

The distribution of the electrons in an atom obey empirical rules known as Hund's rules that aim to explain the energy properties of the atoms and thus the physical and chemical interactions between them. The rules take into account the arrangement of the electrons due to their spin and all angular momentum and the spin-orbit interaction strength. The three Hund's rules give the arrangement for the electrons in the main and sub shells of an atom that achieve a minimum energy configuration. Taking into consideration Pauli's exclusion principle and the application of these three rules sequentially explains a lot of ferromagnetic properties, interactions and the different magnetic moment within materials, even when they have very similar numbers of electrons [9, 12].

The sequence of these rules are; firstly the total atomic spin S from Eq. 2.1 is maximised, which will reduces the spin-spin exchange energy. Secondly, the total orbital momentum L is maximised without violating the first rule. Finally if the shell is less than half full $J = |L - S|$, if the shell is more than half full then $J = |L + S|$ [9, 12]. The application of these rules can be seen in Fig. 2.2, which illustrates the arrangement of the electrons in an atom in the ground state.

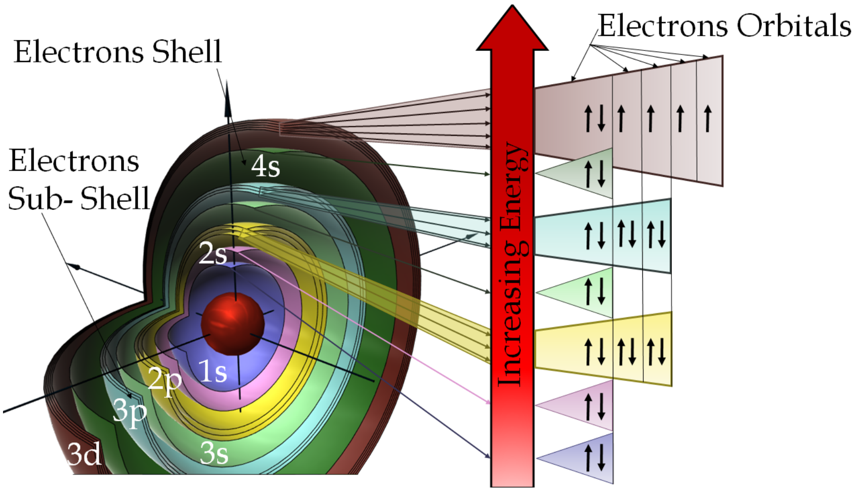

FIGURE 2.2: Electron distribution according to Hund's rules for Fe atom with increasing energy by fulling the higher levels with electrons.

2.2.2 Spin-Orbit Interaction (Coupling)

The Spin-orbit interaction (SOI), also known as the spin-orbit coupling , is an interaction associated with the magnetic moment of the spinning electron on its axis with associated orbital angular momentum. The SOI formula was first derived from the relativistic principle in term of the interaction energy, E_{rel}, between an electron in an atom with a positively charged nucleus [7]. The interaction energy between the magnetic moment of the electron spin moment and the magnetic flux density (B) which rise from the orbital motion can be written as:

$$E_{rel} = -\mu_e.B \tag{2.3}$$

The ratio of the spin electron magnetic moment (μ_e) in Bohr magneton units (μ_B) to the angular momentum is g_0 [7]. The final equation for the SOI can be written as:

$$E_{rel} = g_0 \mu_B \hbar \frac{Z_e}{8\pi\epsilon_0 mc^2 r^3} l.s \tag{2.4}$$

It can be seen from equation 2.4 that the interaction between the spin and the orbital momentum is dependent on the spin (s) and the orbital (l) quantum numbers. Fig. 2.1 shows the spin and orbital momentum and the total momentum that results from their interaction. The Landé g-factor, g_0, is linked to the gyromagnetic ratio ($\gamma = g_0|e|/2mc$) and both are related to **J** and μ. These two terms have been used interchangeably, but with different descriptions such as the "magnetomechanical g-factor" due to the dynamic relation [13–15] or the "spectroscopic g-factor" due to the separation of the energy eigenvalue under excitation [13, 16]. Both magnetomechanical and spectroscopic g-factor should have the same value when the total magnetic momentum is equal to the total spin momentum S only where L=0. This is happened when the orbital angular momentum is quenched by the crystal field as it is explained in Sec. 2.6.

2.3 Exchange Interaction and Exchange Energy

The exchange interaction is the combination of the Pauli exclusion principle, which explains the quantum mechanical interactions between neighbouring spins, and the Coulomb repulsion between charges [17]. Electrons obeying Pauli exclusion principle leads to the result that some electrons occupy the ground state energy while other electrons occupy higher energy states. With this occupation of a higher state of energy the system exchange energy will also increase.

Calculating the exchange energy (E_{ex}) of a magnetic system is the summation of the spin over all pairs of magnetic moments in the system. This energy is dependent on the exchange interaction, which is a very short range effect. Increasing the separation means that the interaction quickly becomes negligible. The exchange interaction is limited to nearest neighbouring moments, which implies that the summation is only over nearest neighbouring atoms. With adjacent spins S_{i} and S_{j} nearest neighbours, the exchange energy E_{ex} is given by:

$$E_{\text{ex}} = -2J_{\text{ex}}S_{\text{i}}.S_{\text{j}} \tag{2.5}$$

The term (J_{ex}) refer to the exchange interaction. The angle (ϕ) between the spins changes the energy, Eq. 2.5 thus can be expressed as

$$E_{\text{ex}} = -2J_{\text{ex}}\sum_{ij} s_{\text{i}}.s_{\text{j}} \cos\phi. \tag{2.6}$$

If J_{ex} is positive, E_{ex} is a minimum when the spins are parallel ($\cos\phi = 1$) and a maximum when they are anti-parallel ($\cos\phi = -1$). If J_{ex} is negative, the lowest energy state results from anti-parallel spins. A positive value of the exchange integral is necessary for ferromagnetism [18].

Fig. 2.3 shows that the value of the exchange interaction as a function of the interatomic distance between any two neighbouring atoms. This is the Bethe–Slater curve, it can be seen that the ratio r/r_{nd}, where r is the interatomic distance and r_{nd} the radius of its nd shell, is important for the spin alignment.

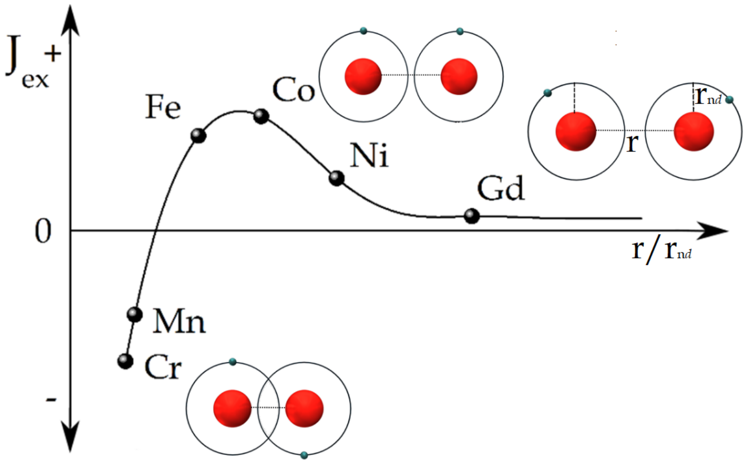

FIGURE 2.3: Schematic of the Bethe-Slater curve, illustrating the importance of the ratio of interatomic separation, r, to the radius of the d band, r_{nd}, on the sign and magnitude of the exchange interaction and sketches to illustrate to spatial overlap of the electronic wave functions. The n here represent the number of the d shell in different metals which is either 3, 4 or 5.

The exchange energy can be simplified by introducing some assumptions. The first assumption is related to the crystal field and it leads to the quenching of the orbital angular momentum, as described in Sec. 2.7.1. It states that the exchange for all the electrons in the material is the same. The second assumption is that the spins of the electrons in the same atom are not quenched, which mean that the exchange of these electrons is constant. This simplifies the exchange energy calculation. SOI along with the exchange interaction and the band theory of magnetism are working together to give this type of interaction, specially with heavy and transition FM metals. In transition FM materials, Exchange interaction take place when the asymmetry broken in FM material or/and by adding NM adjacent layer with strong SOC.

Both ways can lead to introduced new interactions based on the exchange interaction known as Dzyaloshinskii-Moriya Interaction [19, 20].

2.4 Band Theory of Magnetism

The band theory, or as it is also known the collective-electron [21] theory, is used widely to explain physical properties in metals, semiconductors and insulators. The principle of band theory is based on the electronic structure in these material in order to explain many of the physical properties which magnetism. This theory was first derived between 1933-1936 by E.C. Stoner and J.C. Slater [22–24] to explain many materials properties and behaviours beside magnetism, such as; cohesiveness, elasticity, thermal and electrical conductivity, which are out of the scope of this thesis. The origin of the non-integer effective Bohr magneton μ_{B} values of transition metals ferromagnets is one of the aims of the band theory. The effective number of Bohr magnetons (n_{eff}), is the equivalent moment per atom. This number differs according to the material and it can be found according to:

$$n_{\mathrm{eff}} = \frac{M_{\mathrm{S}}(0)}{n\mu_B} \tag{2.7}$$

Where ($M_{\mathrm{S}}(0)$) is the saturation magnetisation at T= 0 K, and (n) is the number of atoms per unit volume.

Before further explanation of n_{eff}, it is important to explain the electronic structure of free atoms. According to the Pauli exclusion principle, any two electrons in the atom can have the same energy level; “shell”, sub-level and finally the spin (spin-up ↑ or spin-down ↓). Noticing that some of energy levels can have more than two electrons such as $3p$ shell which mean they split in to more sub-levels in order to preserve Pauli exclusion principle. The application of Pauli exclusion principle is simple up to when the $3p$ shell is filled and reaching to heavier elements. Heavy transition metals have electrons that extend to $3d$ and $4s$ shells and because these two levels overlap with each other, this will increases the complexity of the application of this principle when forming a solid due to the extensive splitting and the overlapping of the sub-levels of the atoms.

Fig. 2.4 (a) shows the overlapping of $3d$ and $4s$ orbit levels and (b) the Fermi level for different materials according the their occupation states in each shells. The final distance between any approaching atoms will define the overlap in energy levels. This effect is more common with $3d$ and $4s$ because the lower energy levels such as $1s$ and $2s$ are nearer to the nucleus and thus the distance need to be reduced much more. For example in 1 mg of Iron 10^{19} energy levels will be created, which forming bands rather than separate atomic levels, as the solid state is formed. By creating that many sub energy levels, it is better to be describe a density of levels $N(E)$ as a band, which is continuous energy band of allowed levels. This term describes the density of states between two different energy levels, also it is considered as a function of the energy it self, which explains the term density of levels, $N(E)dE$, instead of number of levels. The separation of the energy between each level in the energy band is the reciprocal of the density of levels $1/N(E)$ [25].

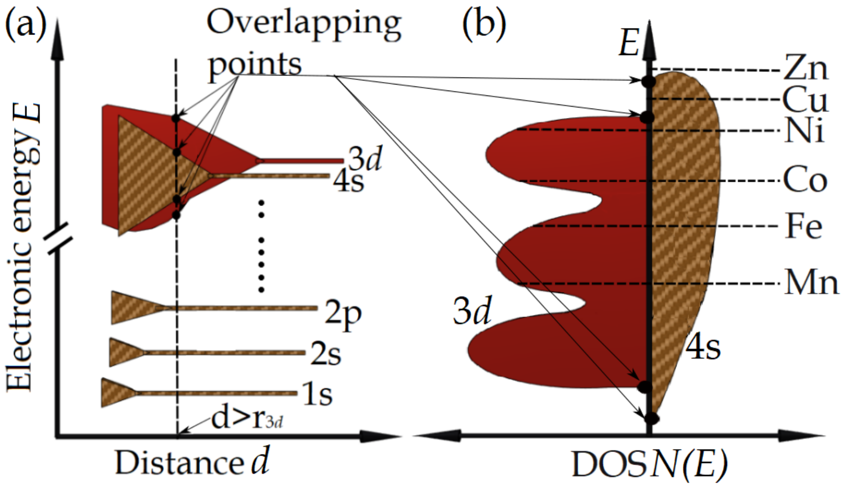

FIGURE 2.4: A schematic view of broadening of electron energy levels when the interatomic distance decreases. (b) Density of levels in the 3d and 4s bands.

The concept of $3d$ and $4s$ level overlapping is a key factor for defining the available states at the Fermi level. This may show contributions of both $3d$ and $4s$ electrons to the physical properties in general, but only the $3d$ levels are responsible for the magnetic features of FM transition metal [8]. Even though the $4s$ levels have broader spherical shape but, $3d$ level have the advantage to reaches nearer to Fermi energy level. This may explain the strong magnetic behaviour in FM elements which have higher number of electrons in their 3d shell [25].

Fig. 2.4 (b) also shows the different density of states for transition metals and the contribution of 3d and 4s shells in different non-magnetic (NM) and FM metals. The total number of electrons that occupy (3d+4s) will determined the Fermi level.

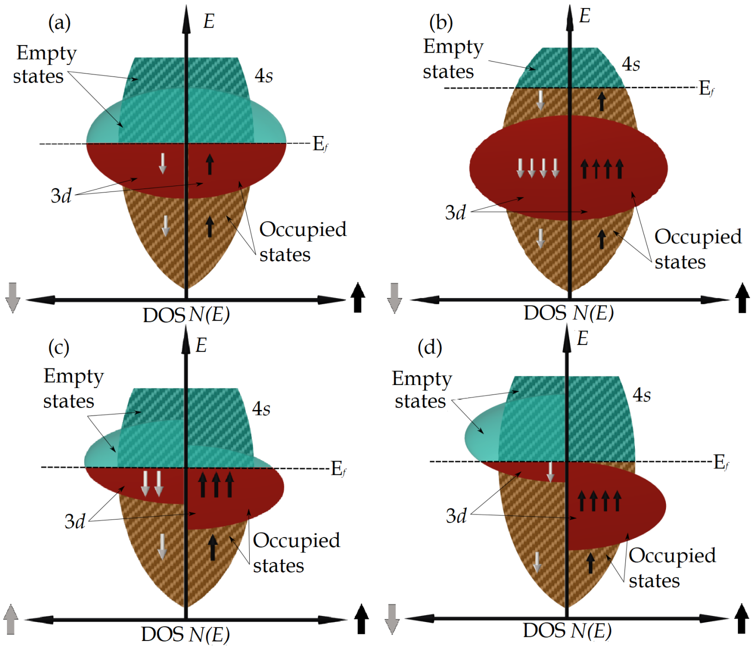

FIGURE 2.5: Schematic to show the electronic band structure and density level of states for (a) anti-ferromagnetic transition metals, (b) non-magnetic transition metals, (c) weak ferromagnetic transition metals and (d) shows 3d band splitting in spin-up and spin-down states in ferromagnet with exchange energy effect.

Going back to use the effective number of Bohr magnetons, n_{eff}, to explain the ferromagnetic properties in material, n_{eff} is dependent on the extent to which these levels are occupied and also depends on the total number of (3d+4s) electrons, in the atoms. Considering n is the number of (3d+4s) electrons per atom, which is 10 electrons in a single Ni atom, if (x) is the number of 4s electrons per atom then 3d electrons per atom is represented by (n-x). The relation between the number of unpaired spins per atom (n_{eff}) for Ni is given by:

$$n_{\text{eff}} = [10 - (n - x)]\mu_B \tag{2.8}$$

Due to the overlap between 3d and 4s bands, the valence electrons partially occupy each of these bands. When the electronic structure of Ni is considered, the exchange interaction displacement is very strong such that one 3d sub-band is completely filled with 5 spin-up electrons and (n-x-5) electrons have spin-down. Using the experimental value of n_{eff} =0.60 μ_{B} and the n value into Eq. 2.8 gives an x value of 0.6. This is proportional to number of 4s electrons below the Fermi level, which indicates that 9.4 electrons are in the 3d band, and 0.6 electrons in the 4s band. The calculation for a free atom is 8 electrons in 3d band and 2 electrons in 4s band. Doing the same for Fe, Co, the spin imbalance is found to be, 2.6 μ_{B} and 1.6 μ_{B}, respectively. This almost explains the ferromagnetic moment of Fe,Co and Ni.

For lighter transition metals, such as Mn, the weak exchange interaction is playing an important role, while the band energy is larger, hence ferromagnetism is not observed because these metals do not meet the Stoner criterion. The existence of ferromagnetism is governed by the Stoner criterion; I N(E_{F}) > 1 where (I) is the exchange parameter and (N(E_{F})) is density of states at the Fermi energy [23]. Fig. 2.5 illustrates Fermi energy level in different materials, also compares the density of electrons occupancy according to their magnetic tendency. The effect of the exchange biased of the applied field is also illustrated for FM materials.

Using the band theory further to explain the origin of Pauli paramagnetism is straightforward. As any systems, all levels up to the Fermi level are full and all higher levels completely empty. There is an absence of a net moment without an applied field, however, the external field will create a spin imbalance, which is the reason for of weak spin paramagnetism [25].

The effect on magnetic properties of combining a lighter materials such as Cr or heavy metals; Pt and Au as dopant or adjacent layers, with FM thin-film materials such as Co and $\text{Ni}_{81}\text{Fe}_{19}$, is discussed in the Chapt. 6, 7, 8 and 9. The use of such NM elements with FM transition metals gives the ability to control the magnetic properties.

2.5 Dzyaloshinskii-Moriya Interaction (DMI)

Dzyaloshinskii-Moriya interactions (DMI) are considered as one of the important mechanisms, fundamental in systems where strong SOC and exchange interaction occur. This kind of interaction can take place directly when the range between the magnetic spins is very short. It is always linked to the exchange of the ferromagnetic and anti-ferromagnetic interaction. The combination of DMI and magnetic field can work together to effect magnetic structure, for example to create very stable micro-magnetic textures know as skyrmions [26].

DMI creates a chirality between neighbouring atoms at an interface which has strong Spin-Orbit Coupling. SOC is essential to canting the magnetisation in the system [27–29]. The DMI interaction can be described by the equation [19, 28–31]:

$$H_{\mathrm{DM}} = -D_{12}(S_{\mathrm{i}} \times S_{\mathrm{j}}) \tag{2.9}$$

Where D_{ij} is the Dzyaloshinskii-Moriya vector, S_{i} and S_{j} are adjacent atomic spins in the interface layer. Similar spin textures also can be result from the long ranged magnetic dipolar interaction which is based on the magneto-static interaction of two layers of thin-films with the existence of bias applied field [19]. The SOI plays an important role between the ions of NM adjacent layer and the interaction with the FM atoms [32].

Interfacial DMI occurs, when a ferromagnet is coupled with non-magnetic heavy metals. This has been found in Pt/Co multilayers [20, 33]. In such systems, the addition of the heavy metal, such as Pt, is crucial to obtain DMI, as shown in Fig. 2.6. Systems where the preferential direction of the magnetisation is out-of-the-plane are well know to have Néel domain walls, which is one of the results due to the existence of the DMI in such systems. DMI induces a chirality to the domain wall that is dependent on the sign of D_{ij} [20, 34] and this also can be a vital important factor for creating skyrmions. Interfacial DMI my also affect other phenomena such as domain wall dynamics. This is discussed in more details in Chapt. 8.

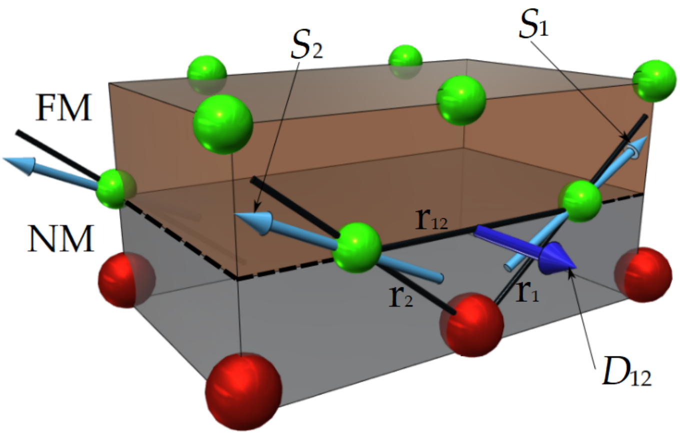

FIGURE 2.6: Schematic of interfacial DMI showing thin-film magnetisation orientation, where it raise when a FM material coupled with adjacent NM layer with strong SOC.

2.6 The Interaction of Crystal Field and The Magnetic Moment

The origin of the magnetic moment and the distribution of the elections in the bands shells give an insight to the magnetic behaviour of FM materials. These are not the only factors in any ordinary FM material, where the electrons in the d shell play an important role in the magnetic state of a ferromagnet [13]. Forming solid material will shape the energy level density, by creating a field known as crystal field, which strongly affects the $3d$ shell electrons. The expectation value of the orbital moment in a crystal averages to zero [13, 35], an effect known as orbital quenching. The forming of solid material will raise the d shell role, with the overlapping of these shells an imbalance with the spin states will take place, as it is explained in Sec. 2.4.

In ferromagnetic materials the electrons states are already unbalanced, unlike the NM materials, emphasising the importance of the d state and the quenching process. The quenching from the crystal field will pronounce the spin of the electrons but the spin changing will also bring the change again to the orbital moment through the SOI. Thus this leads to the change of the SOI energy and will change the total momentum. The crystal field and the changing of the SOI energy effectiveness, with regards to the quenching, is strong when the material has partially filled $3d$ shell and becomes stronger for the heavier transition $4d$ and $5d$ metals [12].

The orbital quenching, can be described as follows: when a crystal structure formed, with well known crystal structure the orbital moment is coupled to the crystal lattice, hence it is not stationary any more, where it is precess around the crystal field, however the term $J = L + S$ is remains unchanged. Thus the constant magnitude of the total moment means that the change will occurs to the spin magnetic moment, implying the interaction between L and S to maintain the total magnetic moment value. This can be seen latter in the experimental chapters, where some of the magnetic properties of the same material are altered substantially, while the total magnetic moment does not change with large magnitude.

2.7 Magnetocrystalline Anisotropy

FM material has a specific crystallographic orientation along which the magnetisation preferentially aligns, which is the result of the interaction of spin and orbital momentum with the crystal field. The atomic moments in a ferromagnet have an energetic preference for the magnetisation to be orientated along preferred crystallographic axes, the lowest energy orientation of magnetisation is known as the easy axis. Logically this will create another axis along which a large applied magnetic field is required to rotate the magnetisation i.e. the hard axis. The energy state of a ferromagnet depends on the alignment of the magnetisation along the specific crystallographic axis, known as magnetocrystalline anisotropy [25].

The magnetocrystalline anisotropy results from coupling the electron spins via their orbits to the lattice [36]. FM crystals can have easy, medium and hard axes, which are defined by the coupling between the spin and the orbital magnetic moment to the lattice. Material for example, have uniaxial anisotropy, or cubic anisotropy. The direction of the magnetisation is determined by the anisotropy, but the exchange interaction also plays a role in the alignment of the magnetic moments regardless of their direction.

This anisotropy can be seen in ferromagnets such as Co, Fe and Ni where the magnetisation curves with applied field along the easy and hard axes [37], for example, Fig. 2.7 show the easy , the medium and the hard axes , for body-centred cubic (bcc) iron; Fe, face-centred cubic (fcc) nickel; Ni and the hexagonal closed-packed (hcp) cobalt, note Co has no medium axis. It can be seen from Fig. 2.7 that Fe reaches the magnetisation saturation easier when the external field is applied on $\langle 100 \rangle$ axes, compared to the $\langle 111 \rangle$ directions. $\langle 100 \rangle$ directions in iron are the easy axes and the $\langle 111 \rangle$ directions corresponds to hard axes of magnetisation. Nickel, on the other hand saturates easily when the external magnetic field is applied on the $\langle 111 \rangle$ directions and the $\langle 100 \rangle$ directions represents the hard axes of magnetisation. For cubic crystals (such as iron and nickel), the magnetocrystalline anisotropy energy (E_{mc}) is expressed as:

$$E_{\text{mc}} = K_1(\alpha_1^2\alpha_2^2 + \alpha_3^2\alpha_3^2 + \alpha_1^2\alpha_1^2) + K_2(\alpha_1^2\alpha_2^2\alpha_3^2) \tag{2.10}$$

where, K_1 and K_2 are first and second order magnetocrystalline anisotropy constants for any given material and $\alpha_{1,2,3}$ are the direction cosines relative to the cube edges. It has been found that the values of K_1 and K_2, for Fe, are 4.8 $\times 10^4$ J/m^3 and -1.0 $\times 10^4$ J/m^3 respectively. The measured K_1 and K_2 are -4.5 $\times 10^3$ J/m^3 and -2.5 $\times 10^3$ J/m^3 respectively for Ni [37].

In hexagonal crystals the c-axis is the easy axis of magnetisation as shown in Fig. 2.7 (c). It is very difficult to rotate the magnetisation away from the c-axis. The magnetocrystalline anisotropy energy required to rotate the magnetic moments in hcp Co from the easy axis of magnetisation to the hard axis is higher than the one required in the case of Fe and Ni [25]. For uniaxial hcp Co crystals, the magnetocrystalline anisotropy energy is given by:

$$E_{\text{mc}} = K_1 \sin^2\theta + K_2 \sin^4\theta \tag{2.11}$$

Where K_1 = 4.5$\times 10^5$ J/m^3 and K_2 = 1.5$\times 10^5$ J/m^3 [25] are first and second order uniaxial anisotropy constants in the case of hcp Co, and θ is the angle between the easy axis and the magnetisation.

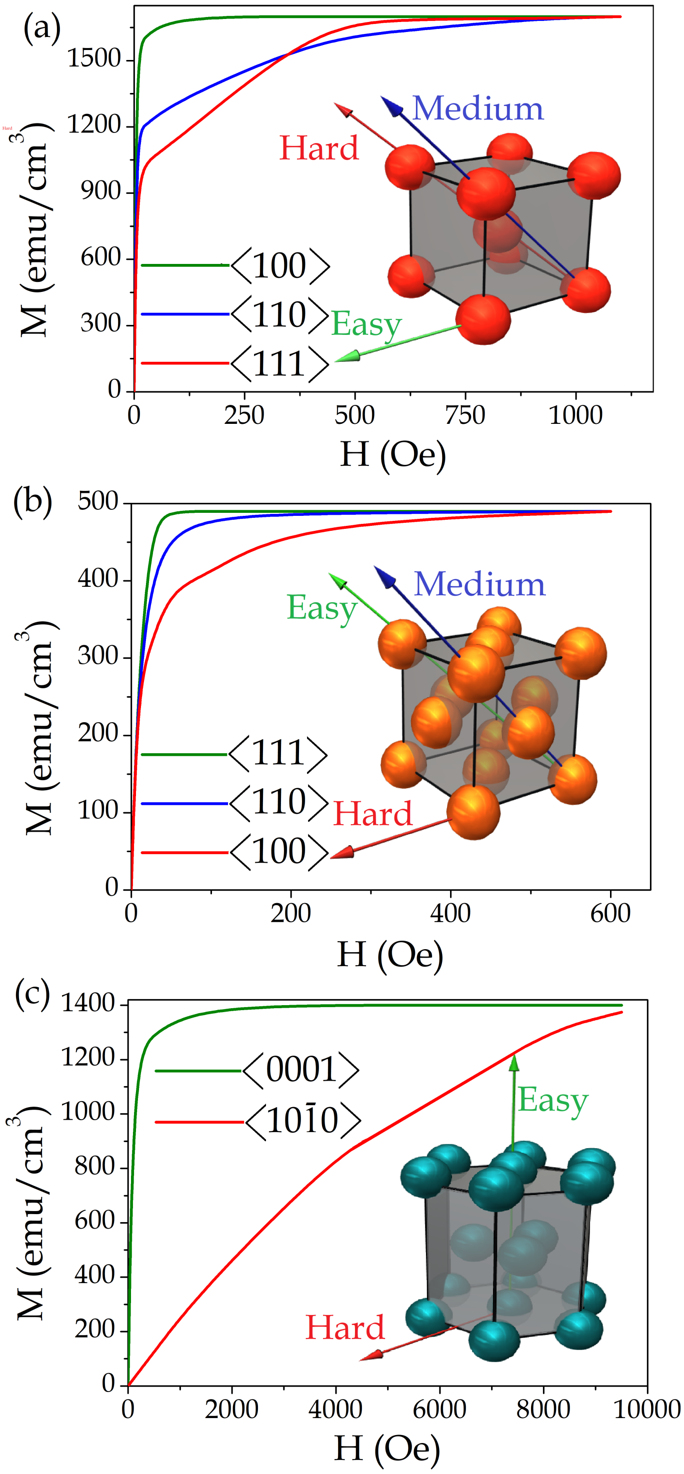

FIGURE 2.7: Magnetisation curve along different crystallographic axes for single crystal of (a) bcc Fe, (b) fcc Ni and (c) hcp Co where the easy, medium and the hard axis showing the preferential alignment due to magnetocrystalline anisotropy.

2.7.1 Crystal Structure Changing in FM/NM and FM-NM Thin-Films

The elemental ferromagnets Co, Fe and Ni have hcp, bcc and fcc crystal structure respectively see Fig. 2.7. Each crystal structure produces a different value for the total anisotropy. However, it is worth noting that some elements can have other crystal phase when they are combined with other elements or special conditions or thicknesses e.g. Co crystal structure changes to fcc when it is sputtered as very thin layer (sub 3nm) on fcc structure such as platinum (Pt) [38].

Thus, substrate type, doping, alloying or changing the thickness of the FM material can all change the crystal structure of the studied system. Changing thin-film thickness has a more general effect, and can work in two ways. First, for ultrathin-films on the order of a few Angstroms, the material can be forced to follow the underlayer crystal structure. Secondly, after a number of mono-layers this effect will be weakened, which allows the FM material to form its usual crystal structure.

2.8 Magnetostatic Shape Anisotropy

Shape or magnetostatic anisotropy also has an effect on the magnetisation on the sample in each direction. The importance of this effect can be seen when a sample which has non-spherical shape and can dominate when there is only very weak magnetocrystalline anisotropy. The free poles on different surfaces of a sample cause this effect by the stray fields which originate from these free poles. If the shape is non-uniform then magnetisation will be much easier along the longer axes. The longest axis can be considered as the magnetostatic easy axis of a sample. This difference can be computed by using the permanent magneto-static energy (E_{ms}). This energy is related to the the demagnetisation field H_{d} at zero applied field and to the magnetisation M, along a given geometrical axes:

$$E_{\mathrm{ms}} = \frac{1}{2} H_{\mathrm{d}} M \tag{2.12}$$

where $H_\mathrm{d} = N_\mathrm{d}M$, so it can be written as:

$$E_\mathrm{ms} = \frac{1}{2}N_\mathrm{d}M^2 \tag{2.13}$$

where N_d is the demagnetizing coefficient along a given axis, which is relates inversely with demagnetising field H_d, such that it is represents the reciprocal slope of H_d. As it can be seen in Fig. 2.8, in two dimensional thin-film structures, the axis perpendicular to the thin-film gives a high demagnetisation factor, $N_\perp \approx 1$, in comparison to the in-plane axis with $N_\parallel \approx 0$. The lower demagnetisation field for in-plane magnetisation has a lower magnetostatic energy and is therefore usually the ground state configuration.

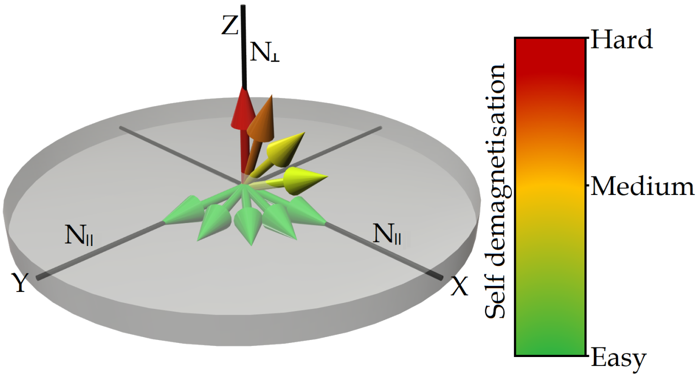

FIGURE 2.8: Schematic illustration of demagnetisation field shows a material magnetisation in thin-film along the X, Y and Z direction, where the shape governs the magnetic alignment.

Eq. 2.13 can be written as the difference between the demagnetizing coefficient for any giving axis ΔN:

$$E_\mathrm{ms} = \frac{1}{2}\Delta N M^2 \tag{2.14}$$

Experimentally ΔN correlates the ratio of the $\perp$ and the $\parallel$ axes; for example c/a for Co. Eq. 2.14 is the same as the magnetocrystalline anisotropy and also has angular dependence thus Eq. 2.11 can be same as below but with only K_1

$$E_\mathrm{ms} = K_\mathrm{s}\sin^2\theta \tag{2.15}$$

Where K_s is the shape anisotropy constant. $N \parallel$ to the long axis remains very small whilst for both of the orthogonal axes $N_\perp$ can be changed. Using the shape anisotropy effect with thin-film and nanowires gives control over the preferential alignment of the magnetisation. Using the shape to control magnetisation, and switching is developed in Chapt. 8.

2.9 Magnetisation Precession and Magnetic Damping

Damping is the mechanism which is used to define the magnetisation energy loss in ferromagnetic materials by transfer of precessional energy to microscopic thermal motion of the lattice [13, 39, 40].

The total energy in any given FM system is the summation of external field energy (E_{ex}), demagnetisation energy (E_{d}), exchange energy (E_{ex}) and anisotropy energy (E_{mc}) [39, 41–46]. The changing of the magnetic field magnitude or direction, leads to the dissipation of the energy through the system dissipation channels that represent damping [13].

The dissipation of energy is always related to the quantized spin waves; magnons and their interaction. These magnons may have the same or different wave number k, which transfer the energy from one state to another. In terms of magnons k here describes the precessional mode for the magnons in which k=0 when all moments ($\mathbf{m}$) precess with the same frequency in the same phase [12, 13, 40, 47, 48]. This is also known as the ”uniform relaxation mode”.

The annihilation of such magnons to create another with $k \neq 0$ will violate the momentum conservation, thus this ”non-uniform relaxation mode” can take place when the system perfection and ordering is broken by mechanical effects of foreign atoms [13, 47]. Different magnons dissipate the magnetic energy, all of them are based on the annihilation of the uniform mode magnon and creation of other non-uniform modes also known as ”two-magnon scattering”. In this frame work there are other possibilities for the magnons created to have the same wave number, k, and opposite wave vector, or they will have different k such as thermal [13, 47]. Fig. 2.9 shows different modes of energy dissipation with the final energy lost to the lattice.

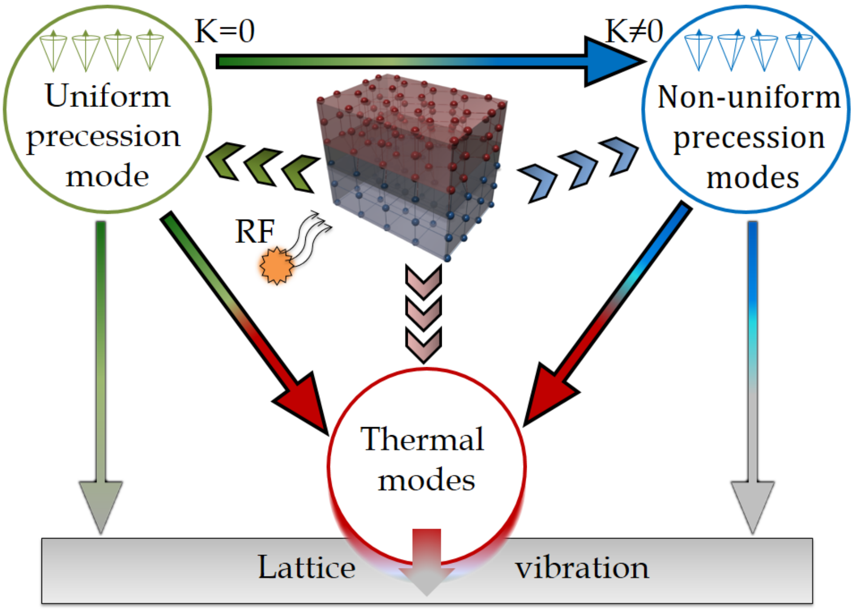

FIGURE 2.9: Shows a different types of precession modes with the final decay into lattice vibration and the transformation of the energy between modes.

The next relaxation processes to consider is one where energy can dissipate through magnon-phonon scattering. In ferromagnets, phonons and magnons can have the same energy and wave vector. Thus magnon-phonon scattering, which has several scattering probabilities, will lead to energy loss through the lattice vibration such as one-magnon one-phonon scattering and others.

2.10 Polarised Light Interaction with Ferromagnetic Materials

The interaction of light with a FM material either from surface reflection or by transmission, is an important phenomenon for magnetic research. This phenomenon gives an investigative tool to probe FM systems. The interaction of linearly polarised light, will change the transmitted/reflected properties of the light polarisation or intensity. The magneto-optical Kerr effect (MOKE) is based on the changing of polarisation state of reflected light from a FM. It is based on group of phenomena related to the optical magnetisation anisotropy at the surface of FM materials [49]. MOKE is a well-known phenomenon and provides the capability to determine the magnetisation in a quantitative way [50]. The effect of magnatisation on light was first discovered by Michael Faraday (1854), as a rotation in the polarisation axis of light when it pass through a piece of glass which was placed in a magnetic field. A similar effect was observed in 1877 by John Kerr [51] on reflection of the light from a polished metallic pole of an electromagnet. It has been found that the angle of rotation is a function of the magnetic field strength and thickness of the sample.

The underlying mechanisms of this effect is the interaction of electric field of light with Lorentz force inside the FM material as results to the effect of the magnetic induction. The incident light is interacting with a ferromagnet or a ferrimagnet, a large change in the light polarisation will be indicated [52], this is because such material are, even without applied external field, magnetically ordered. For other cases, such as when an external field is applied on the medium the same effect will take place. In general for both cases the magnetic effect will appear as changing in the optical anisotropy. The role of the applied magnetic field is to split the energy levels of the material which is know as the Zeeman effect [49]. There are three main geometries for magneto-optical Kerr effect: Polar, longitudinal and transverse. The difference between these geometries are related to the sample, the applied field and light propagation direction. Each geometry has a different effect on the reflective light polarisation status, however, all of them are related with the Faraday and Cotton-Mouton or Voigt effect [50, 51]. More details regarding the Kerr effect geometries used here are explained in depth in Chapt. 3

The effects and phenomena, which have been explained in this chapter, give insight regarding the physical basics in FM thin-film systems. In the follow chapters these phenomena aid the measurements and explanations as a discussion tool for the magnetic behaviour in the samples investigated.

Chapter 3

Methods of Investigation: Physical Basis and Practical Implementation

3.1 Introduction: Structural Analysis and Functional Magnetic Measurements

In this chapter, all the used experimental techniques in this study are explained in detail, where they cover the structural investigation and the functional magnetic measurements. The structural analysis is represented in this chapter by x-ray scattering, which offers two main methods that give insight regarding the sample thicknesses, interface width and the crystal structure. The functional magnetic measurements are represented by both quasi-static measurements and dynamic measurements. The first type of measurement is more related with the magnetisation state of the samples investigated and the dynamic measurements are related with the rapid changes of the magnetisation in time domain. Magneto-optical Kerr effect (MOKE) magnetometry and superconducting quantum interface device (SQUID) measurements represent the first type, while, time-resolved magneto-optical effect (TR-MOKE) magnetometry and ferromagnetic resonance (FMR) spectroscopy represent the second type. For each of theses techniques a background regarding the basic principles is first presented, followed by the experimental system setup and finally the data representation. This provides the fundamental physics that aids understanding of the results of the samples investigated in Chapt. 6, 7, 8 and 9.

3.2 X-Ray Scattering

Earlier, in Sec. 2.10, the interaction of coherent light waves with the magnetisation excitation was discussed in the scope of the material's magnetic properties investigation. The interaction of x-ray photons with a material can provide other information beyond the magnetic properties such as; the crystallography of the system investigated [53]. It is important to investigate the material structural and the crystalline characteristics, which give an understanding to the atomic arrangement and the inter-atomic spacing. Knowing these factors can aid the explanation of different magnetic behaviour. X-rays are extensively used in this work for their capability of determining material crystallography and thickness.

X-rays are electromagnetic waves and obey the scattering phenomena, by which the electron cloud of an atom will cause scattering of the x-ray waves as they excite the electrons to oscillate when they absorb the incident photons. The oscillation of the excited electrons then acts as a re-radiating source of photons with the same frequency as the incident x-ray waves. This energetic transition process is the elastic scattering process; non-resonant scattering. This is the classical description of scattering, which is the main process in x-ray reflectivity and x-ray diffraction. This simplifies the relation between the incident and the reflected x-ray beams as:

$$Q = k - k' \tag{3.1}$$

From Eq. 3.1, it can be seen that the difference between the initial and the final momenta is related to the difference of the wavevectors k and k' with the scattering vector, Q [53].

Elastic scattering, or Thomson scattering as it is known occur when the energy of the scattered beams are equal to the incident beam energy. In the case of matching between the incident photon energy and an atomic energy level transition, a resonant enhancement of the scattering occurs, due to excitation and spontaneous emission [54]. Thomson scattering assumes that the atoms are perfectly aligned in the system and the angle of the re-radiated photons are all in the same angle. It also neglects the re-scattered beams that occur along the beam travel which means that while the photons are travelling in the medium they may have interacted with different atom locations that will change the direction and the energy of the re-scattered photons. In situations with more complicated geometry and non-elastic scattering a dynamic theory is need in order to get a better approximation to the system characteristics. The main phenomena that are the focus of this study are the reflection and diffraction of x-rays to investigate the thin-film structural properties.

3.2.1 X-Ray Reflectivity: Refraction and Reflection

For a medium containing many atoms, many x-ray scattering and absorption events will take place. As waves, the incident x-ray photons will refract and reflect as they travel through media with different electron densities. In the case of refraction in thin-films, this can be due to different materials and when the x-rays propagate through the surface from the surrounding air. The incident x-rays will interact with the atoms of each layer. The atoms radiate spherical wavefronts that propagate out in all directions. This is the best explanation which can describe the atoms as a source of these waves. When the waves frequency, ω, of the incident x-ray photons corresponds with the electronic transitions resonance will occur. By this process the refractive index, n, increases with ω, so the excitation and the spontaneous emission will repeat rapidly. Above the resonance frequency n decreases a fewer electronic transitions take place. For x-rays the frequencies are very high and this will result in small n for x-rays propagating into a material with speed v and wavevector k. Thus, the refractive index of the material will be

$$n = \frac{c}{v} \tag{3.2}$$

The refractive index is related to the scattering property, the dispersion coefficient, δ, which relates to the wavevector of the incident beam k and the electron density of the material, ρ. A second factor is the absorption coefficient, β, that is responsible for the attenuation of the propagating photon beam. When the beam travels through the material it will suffer from attenuation in its intensity and amplitude. The refractive index equation can be written as:

$$n = 1 - \delta + i\beta \tag{3.3}$$

It is known that the value of δ and β are very small, which are in the order 10^{-6} and 10^{-8} respectively. Thus the value of n will be in the order of 10^{-5}. Fig. 3.1 shows the specular x-ray scattering geometry for a layer with refractive index as described. The combination of Eq. 3.3 and 3.2 implies that n is very small and thus v in the material is bigger than the speed of light, c, which cannot be true unless v is representing the phase velocity not the group velocity [53].

The total incident beam amplitude equals the sum of the refracted and the reflected amplitudes. The critical angle determines the occurrence of reflection and refraction. Snell's law can be used to find this critical angle, at which total external reflection occurs. This law relates the incidence and the refraction angles via the refractive indexes by:

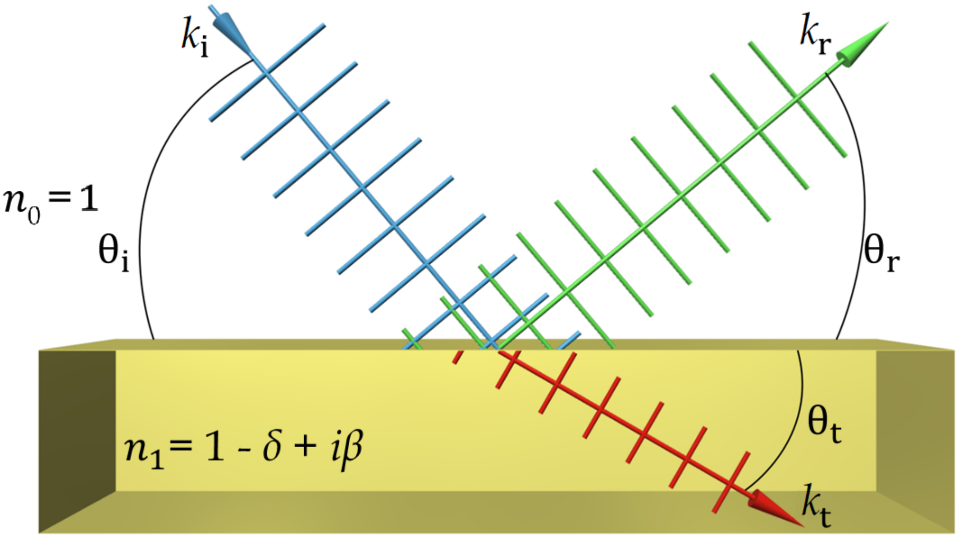

FIGURE 3.1: Schematic illustration of the x-ray scattering from medium, showing refraction and reflection with respect to the refractive index.

$$n_0 \cos\theta_i = n_1 \cos\theta_t \tag{3.4}$$

The condition that allows the total external reflection to take place is θ_t = 0 and θ_i is very small, thus Eq. 3.4 can be written as:

$$\theta_i = \theta_c = \sqrt{2(1 - n_1)} = \sqrt{2\delta} \tag{3.5}$$

The critical angle θ_c for the total reflection is very small, of the order of 10^{-2} radian, 10^{-1} degree or 10^{-2} Å^{-1} for the scattering vector. The refraction and the reflection are the main processes that occur when the x-ray beam propagates into a medium [53]. Complications can be added to the equation by increasing the number of material layers in the medium. The interfaces add another part that can impact the final result, as a lot of events can take place, such as multiple reflections from the upper and the lower interfaces within the medium. Changing the material will change the refractive index, also adding new material to the existing material will change the material electron density thus, its atomic arrangements. This can be done by intermixing of layers or co-sputtering of materials, as it is discussed in the following chapters, where the doping of a material will change the electron density. This change will affect the reflectivity profile that describes the structural properties.

3.2.2 Reflection from a Thin-Film

So far the simplest scenario of an x-ray propagating into a medium is explained by single refraction and reflection events. In the case of thin-films these processes can be repeated in each layer, where each layer has its own refractive index, n. The refractive index for the vacuum surrounding the thin-film is n_0 followed by the first layer of the thin-film with refractive index n_1 and the substrate with n_s, for one layer thin-film. Beyond the substrate layer there is no contribution to the sum intensity of the reflecting beams.

When the x-rays enter a thin-film at a finite incidence angle a series of reflections occur from both the top and bottom of each layer at the interfaces within the thin-film. Fig. 3.2 shows reflectivity from simple thin-film and the final resultant beam, which combines the reflected and transmitted beams. From the schematic figure, the total reflected x-ray intensity (r_{tot}) can be calculated, starting from the incident x-ray beam to the final reflected, r, and transmitted, t, beams:

$$r_{\text{tot}} = r_{10} + t_{01}t_{10}r_{12}p^2 \sum_{m=0}^{\infty} (r_{10}r_{12}p^2)^m \tag{3.6}$$

In this equation the film-layer density is considered homogeneous as this makes the calculation much simpler. Moreover, the reflectivity is related to the phase factor, p, and where there is a phase difference it can be determined by $p^2 = \exp^{(idq)}$. The thickness of the layer d and the wave number, q, are related to the wavevector, k_1, of the incident beam by the equation

$$q = 2k_1 \sin\theta_{\text{i}} \tag{3.7}$$

The calculation of the total reflectivity of the x-ray from thin-film can be done by using Snell's law. The latter is used to calculate the amplitude of both reflectivity and transmittivity. This equation leads to a relation between the reflected amplitude, α_R, the transmitted amplitude, α_T, and the incident amplitude, α_I

$$\alpha_T = \alpha_I + \alpha_R \tag{3.8}$$

From this equation, with small incidence and transmission angles θ_{i} and θ_{t}, r and t found as follow:

$$r \equiv \frac{\alpha_R}{\alpha_I} = \frac{\theta_{\text{i}} - \theta_{\text{t}}}{\theta_{\text{i}} + \theta_{\text{t}}}, \quad \text{and} \quad t \equiv \frac{\alpha_T}{\alpha_I} = \frac{2\theta_{\text{i}}}{\theta_{\text{i}} + \theta_{\text{t}}} \tag{3.9}$$

Using Fresnel's equations, the total reflectivity can be summed and then simplified, with the same assumptions of layer homogeneity and the phase difference between the reflections and the transmitted x-ray beams in each layer of a thin-film. Thus the total reflectivity amplitude r_{tot} can be written as below:

$$r_{\text{tot}} = \frac{r_{01} + r_{12}p^2}{1 + r_{01}r_{12}^2p^2} \tag{3.10}$$

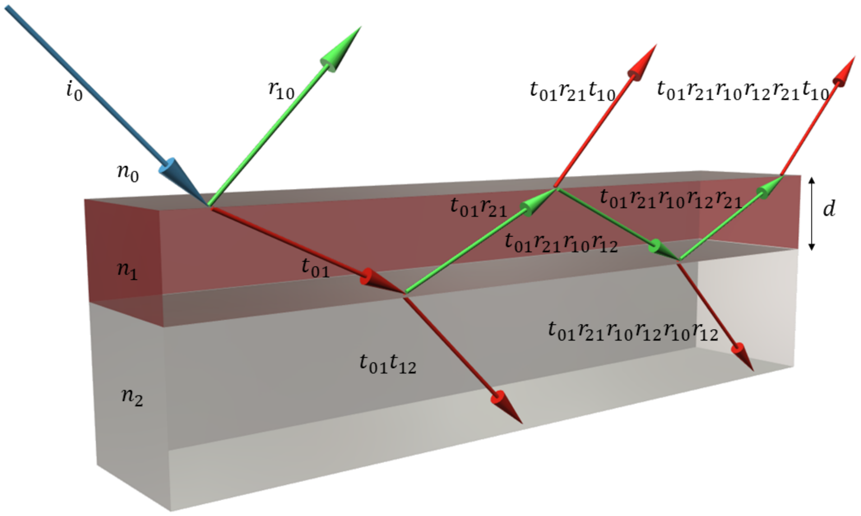

FIGURE 3.2: Schematic illustration of the x-ray scattering from simple thin-film with single layer over substrate with the calculation of the total reflection from incident x-ray beam. This beam will be divided into reflected, $\mathrm{r_{nm}}$, and transmitted, $\mathrm{t_{nm}}$, beams from the top or the bottom interface of the first layer. If the reflection or the transmission direction is toward thin-film surface then n > m, while if the direction toward the substrates then n < m, where n and m = 0,1 or 2 only.

Effect of Thin-Film Thickness

The intensity of x-rays reflected from a thin-film is due to many factors such as; numbers of layers, thickness and interfaces between layers. When the thin-film has more than one layer Eq. 3.10 will describe only the reflection intensity from the layer adjacent to the substrate. Considering N layers will add more to the equation as

$$r_{\mathrm{N-1,N}} = \frac{r_{\mathrm{N-1,N}} + r_{\mathrm{N},\infty} p_{\mathrm{N}}^2}{1 + r_{\mathrm{N-1,N}} r_{\mathrm{N},\infty} p_{\mathrm{N}}^2} \tag{3.11}$$

Parratt's recursion equation 3.11 [55] can be used to find the total reflected intensity of the x-ray waves from a thin-film system. As mentioned earlier, when the x-ray travels through a thin-film the x-ray intensity will be attenuated in relation to the thin-film thickness d. This attenuation of the intensity is by the factor of $e^{-\mu d}$, while the amplitude attenuation will be by the factor $e^{-\mu d/2}$. Increasing the incident angle beyond the critical angle will increase the distance travelled through the thin-film, thus, x-ray intensity will decrease rapidly in relation to the incident angle [53].

Beyond that, it has been found that the intensity also changes as a function of the phase factor between the reflected beams from the top and bottom interfaces.

This effect will leads to interference creating intensity oscillations known as Kiessig fringes. These fringes were found by Kiessig as experimental observations for the x-ray intensity due to reflection from thin-films. The fringes have a maximum and a minimum, the maximum or the peak of these fringes is a result of in-phase interference of the reflected x-ray waves from the top and the bottom of the layer interfaces. The dips or the minimum are due to out-of-phase interference [56]. In more detail, the peak should take place when the phase $p^2 = \exp(idq)$ and $q = 2k_1 \sin(\theta)$. This gives the condition at which high intensity specular reflection with respect to thin-film thickness d as follow:

$$d \sin(\theta) = m\lambda \tag{3.12}$$

Where m is an integer that refers to the fringe number of the peak. This equation can be used to find the relation between successive fringes and the thickness of the thin-film:

$$q_{\mathrm{m+1}} - q_{\mathrm{m}} = \frac{2}{d} \tag{3.13}$$

This can be seen in Fig. 3.3, which show XRR for two thin-films with different thicknesses, superimposed with the general trend decay regarding the thin-film thickness. The intensity of the reflected x-ray is plotted as a function of the scattering wavevector, q_z, as this is more useful than the angular variables θ.

Effect of Thin-Film Interfaces

The estimation of thickness explained earlier is done by calculating the summation of the reflectivity using Parratt's recursion method. The assumption of this method considers the interface between each layer in the thin-film as perfectly flat or smooth and that there is no intermixing at the interface. In this ideal case, the interface looks like a sharp line between adjacent layers. This not typically the real case for thin-films, at which the interface will have a certain amount of roughness. The interface width can be seen as topological roughness and/or chemical graded intermixing. The specular reflectivity is affected by the structure of the interface. Fig. 3.4 shows

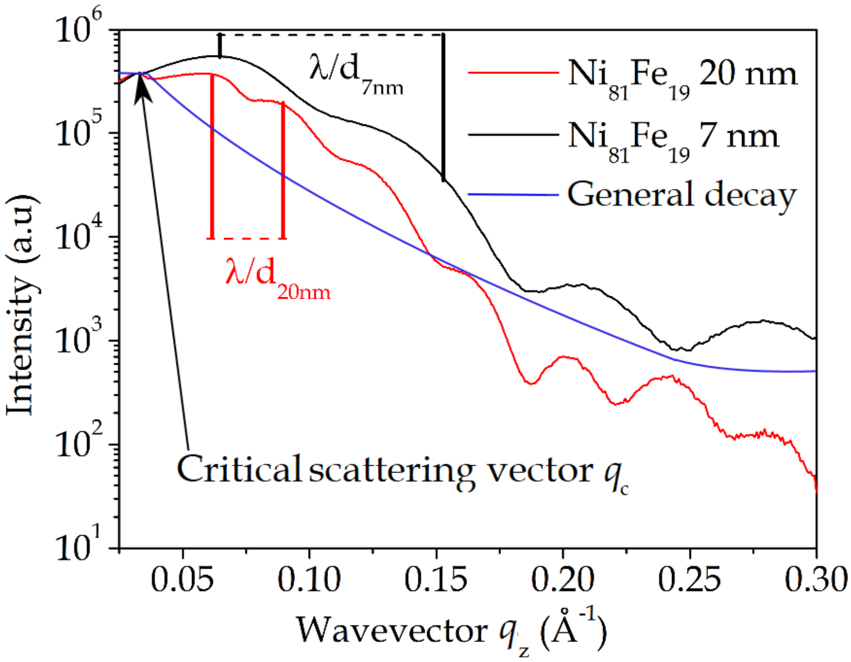

FIGURE 3.3: Specular reflectivity for 7 nm and 20 nm $Ni_{81}Fe_{19}$ thin-films on an infinite SiO_2 substrate as function of the wavevector q_z. The blue line shows the general decay of the intensity where the critical wavevector of the order 10^{-2}

x-ray reflectivity (XRR) for the same thin-film with changing the capping layer thickness within Å order, which modifies the surface roughness.

The depth of Kiessig fringe minimum are gradually reduced with the increasing of the capping of the thin-films. It can be seen in Fig. 3.5 two schematic images of thin-films where (a) represents the topological roughness and (b) the intermixing. The equation used for the ideal reflectivity of the flat interface (r_{smooth}) multiplied by the integral of the interface width (σ^2), regarding the changes of the electron density with the changes of the material distribution through the interface [53], which gives an equation after simplification as:

$$r_{\text{true}} = r_{\text{smooth}} \exp(-q^2\sigma^2) \tag{3.14}$$

where (r_{true}) is the true calculated specular intensity including the interface roughness effect. This equation gives the interface width, which is composed of both topological roughness, σ_{r}, and intermixing, σ_{i}, contributions, which can be calculated [57]

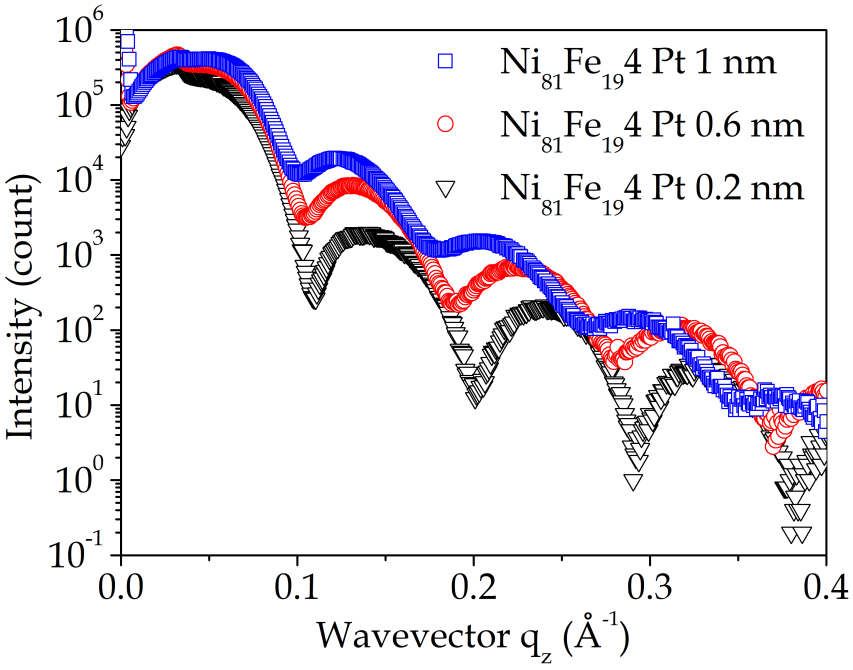

FIGURE 3.4: Shows the effect of the interface width on the intensity reflectivity and the dips of Kiessig fringes, where three thin-films used with 4 nm of $Ni_{81}Fe_{19}$ and capped with Pt from 0.2-1 nm. The roughness show a larger amplitude of Kiessig fringes when the Pt capping layer is less thickness regarding the non-continues capping layer.

as

$$\sigma_{\mathrm{tot}} = \sqrt{\sigma_{\mathrm{r}}^2 + \sigma_{\mathrm{i}}^2} \tag{3.15}$$

It is hard to calculate any of σ_{r} and σ_{i} effects separately along the z axis. But, using non-specular x-ray reflectivity the diffuse scattered x-rays in the in-plane can give more insight regarding the interface structure. This is shown in the Fig. 3.5, where the change of both types of interface as a function of (c) width Z and (d) diffuse angle (θ).

Yoneda Wings and Determining Interface Nature

Diffuse scattered x-rays have a vital role in detecting the in-plane component of the scattering vector. This gives the capability of non-specular x-rays to detect structural variations. If there is an intermixed interface the reduction in the specular reflectivity is due to the changing electron density over its constituent layer. This is regarding the out-of-phase destructive scattering of each x-ray reflected beam from different levels through the interface. Electron density variations cannot be detected in-plane

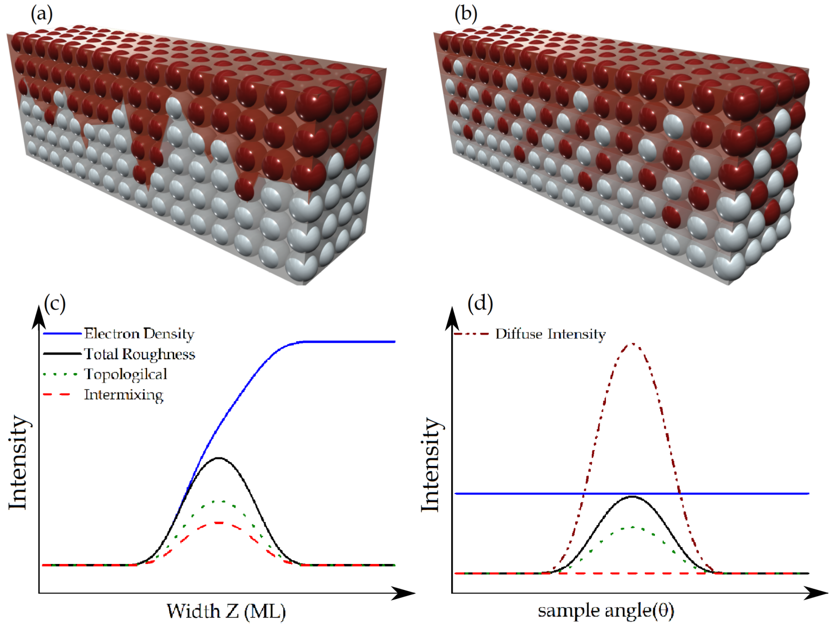

FIGURE 3.5: Schematic figures showing (a) Topological roughness, (b) Chemical grading or intermixing. Also showing Graphical representation of total interface width σ_{tot}, the contribution of the topological σ_{r} and the intermixing σ_{i} with the changing of the electron density as a function of (c) interface width Z and (d) the diffuse scattering angle θ.

because, the x-ray scattering beam will averaged over the density along the total incident area.

Fig. 3.5 show two types of interface width (a) and (b) and the changing of the electron density as function of the (c) interface width and (d) detector angle. For topologically rough interfaces, the electron density variation in-plane can be found. This can be done by small angle scans of the diffuse scatter, with a central specular angle at the first dip of Kiessig fringes. This range will extend from the critical angle to the central angle, where the specular condition is met, while the detector of the x-ray reflected beams is set at the specular reflection angle 2θ. By the resultant shape the effect of the in-plane topological roughness variation can be indicated due to the reduction of the intensity. A sample with an ideal sharp interface would be expected to give the highest intensity at the angle of specular reflection, with a dramatic reduction away from $\theta = 2\theta/2$. The difference from this ideal situation in a real sample is shown in Fig. 3.6. The two cases have a sharp reflection at the specular condition, superimposed on a broad diffuse scattered background. The diffuse scatter in the real case also shows features called Yoneda wings where diffuse scatter

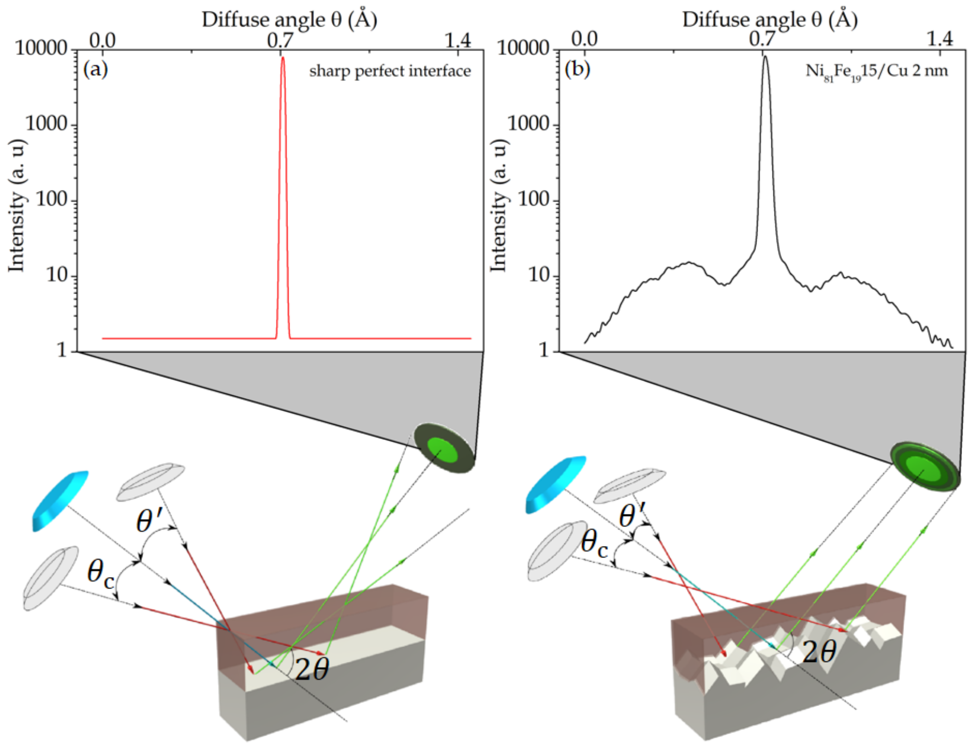

FIGURE 3.6: Schematic figures showing (a) ideal perfect sharp interface , (b) rough interface with topological roughness and the diffuse non-specular x-ray with Yoneda wings of rough interface, where the incident angle θ changing to the critical angle θ_{c} while the reflection angle is fixed at 2θ.

is enhanced at the critical incidence and exit angles due to electric field at the surface [58].

It can be seen that even though the roughness and intermixing affect the specular reflectivity in the same way, the diffuse scatter is sensitive to the nature of the interface structure. Identifying the interface structure is possible by combining the specular and the non-specular models, however the analysis will need an intensive calculation which can be only executed by super computers. Finally there are another way, based on the correlation between the diffuse, I_{d}, and specular, I_{s}, x-ray intensity. The relation is that the scattered intensities are related to a first approximation by the equation [57]:

$$\frac{I_{\mathrm{d}}}{I_{\mathrm{s}}} = \exp(q_{\mathrm{z}}^2 \sigma_{\mathrm{t}}^2) - 1 \tag{3.16}$$

The equation links exponential of the topological roughness, σ_{t}, with the relative diffuse and the specular intensities. The wavevector q_{z} is assumed to be large in order to measure all of the diffuse scatter and is related to the wavelength, λ, and the reflection angle, 2θ, as defined by Eq. 3.7. Finding q_z and calculating the transverse diffuse curve and the specular reflected component make it easer then to find the topological roughness. Eq 3.15 can then be used to calculate the chemical grading or the intermixing of the interface.

3.2.3 X-Ray Diffraction

For information regarding the material crystal structure, x-ray diffraction is an important method. X-ray diffraction produces high intensity x-ray peak when interference of scattered x-rays take place coherently from the electrons of periodically arranged groups of atoms. As mentioned earlier an incident wave interacting with an atom in a crystal lattice will act as an x-ray spherical wave source, when the x-ray wavelength corresponds to the electron transition wavelength. This has been described mathematically by Bragg [59]. It is explained in Chapt. 2 that each material has a certain crystal arrangement, where the crystal arrangement repeats parallel planes of ions separated by the inter-planar distance, d. Fig. 3.7 shows the Bragg condition for the constructive interference of x-ray beams scattering from atoms separated by d with the relation between the incident and reflection angles and the path difference [60].

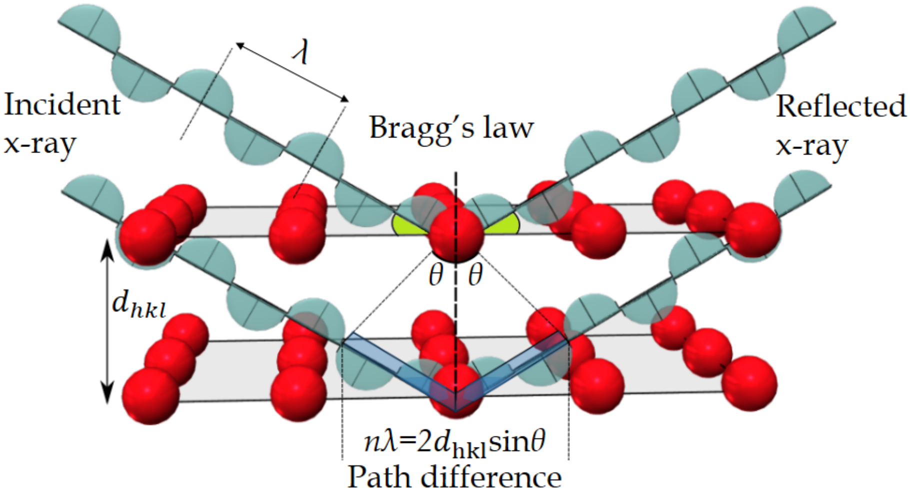

FIGURE 3.7: Schematic figure showing Bragg's law of diffraction, the condition of the constructive interface between the incident and the reflective x-ray beams.

When the x-rays diffract from different planes in the lattice, constructive interference occurs for a path difference

$$n\lambda = 2d_{\text{hkl}} \sin\theta \tag{3.17}$$

where λ is the wavelength of the incident x-ray, n is a positive integer, d_{hkl} is the inter-planar spacing and θ is the angle between the incident x-ray and the relevant lattice planes. hkl are the Miller indices, which are related to the reciprocal lattice parameters [53]. In cubic materials they are related with the inter-planar spacing giving by

$$d_{\text{hkl}} = \frac{a_0}{\sqrt{h^2 + k^2 + l^2}} \tag{3.18}$$

In order to satisfy Bragg's law, where the scattered x-rays interfere constructively, the difference between the path lengths of the two waves should be equal to $n\lambda$. The diffraction pattern refers to peaks which can be obtained by measuring the intensity of scattered x-rays as a function of the incident and the detector angle. Thus each peak is related to certain planes where the atoms are arranged.

3.2.4 X-Ray Reflectivity and Diffraction; System Setup and Data Collection.

The XRR and XRD techniques used for the measurements of all the thin-films through out this work were done by using a Bede D1 x-ray reflectometer. The x-ray system generates Cu-K$_\alpha$ and Cu-K$_\beta$ x-rays with a 40 kV voltage to accelerate electrons from a filament a Cu target. Through this process the electrons will lose some of their kinetic energy, thus they will radiate two distinctive photons, with the characteristic of Cu-K$_\alpha$ and Cu-K$_\beta$, as emissions, along with Bremsstrahlung background to conserve the energy law. This process will generate heat so the Cu target is cooled by water. By passing the x-ray beam through a primary source slits it will contain the only two distinctive emissions from the Cu k shell α and β.

In order to produce high quality monochromated x-ray beam, a channel cut Si crystal was used. By the application of Bragg's law only the reflection of the diffracted x-ray beams from the (111) plane in the Si crystal will be selected. Beyond the monochromator a fine filtered beam will be produced, but with broadening, by passing through the second slit the width of the beam will adjusted according to the slit aperture in use. The final x-ray beam is directed to the sample mounted on a stage, which has three angular and three cartesian coordinate degrees of freedom. The cartesian coordinates X, Y, and Z can be changed to make sure that the sample is in the right place for the incidence x-rays. The angle θ is used in the relation $q_{\mathrm{z}} = (4\pi/\lambda)\sin\theta$, where varying the incidence angle θ will change the specular reflected angle 2θ. The two other angles ϕ and χ are related with diffraction, where changing these angles will change the XRD intensity by changing the orientation of the sample thus the incident lattice planes [57].

As explained before, regarding the interface structure and the inhomogeneities of a given material, the reflected x-ray beam will have some diffuse scatter. A detector slit is aligned to the reflection angle 2θ to reduces the width of the detected x-ray beam and allows only the specular beam. Measuring XRR, the incidence angle, θ, and the reflected angle, 2θ, are changed over a small grazing range of angle. The intensity variation of the specular reflection as a function the angle range changing will give the final XRR. However, there is some non-specular diffuse background. This can be eliminated by executing another scan; an off-specular scan that is subtracted from the raw specular XRR to obtain the true-specular reflectivity. The final shape is a general decay superimposed with Kiessig fringes with a range of complexity regarding structural properties, number of layers, interface nature and the thickness of the film. Using suitable codes best fitting simulation can be calculated to interpret the structure of thin-films and multilayers [61].

X-Ray Simulations and Fitting of Experimental Data

From simulating the x-ray reflectivity shape information regarding any sample structure, thickness and the nature of the layering interface can be obtained. GenX, a freely available [61] simulation code, was used for the modelling of reflectivity curves. This software uses Parratt's recursion formalism [55] in order to find the best fit to the specular and non-specular x-ray reflectivity. There is a wide range of data that can be simulated using a set of parameters including each layer thicknesses, densities and each interface width. All the samples investigated are stacks with a wide range of thickness of ferromagnets including; Co and $Ni_{81}Fe_{19}$, capped with a wide range of nonmagnets; Pt, Au, Cr, Ag and Cu with different thicknesses. All of these stacks are deposited on Si/SiO_2 substrate. The density of each used element in formula units per $Å^3$ should be input in the simulation model. This unit can be transformed from kg/m^3 unit,

$$\rho[u/\text{Å}^3] = \frac{\rho[kg/m^3]}{1.66054 \times 10^3} \tag{3.19}$$

By estimating the initial thickness(es) for the layer(s) in the thin-film the simulation can be started by inserting these parameters into the model. The roughness of some known material, such as Si/SiO_2 which is about 3-6 Å from the literature [62], can be inserted to the model also as a primary figure. The simulation can reach to accurate results with an error of 10^{-2} order or even better. As mentioned in Sec. 3.2.1, the electron density of a given material is the key to its refractive index. Thus it is most useful to distinguish between layers in a thin-film by their densities. The density of the alloyed materials, which contained different concentration of more than one pure element, can also be obtained with the same equation when the ratio of the compositions are considered. This can be seen in Table 3.1 where it shows some examples for calculated densities for pure and alloyed materials used in spintronic thin-films. The resultant specular reflectivity is put into the GenX modelling code

TABLE 3.1: Density ρ of different pure and alloyed material in kg/m^3 and $u/Å^3$

Material	Density ρ in kg/m^3	Density ρ in $u/Å^3$
Co	8.9	0.090
Ni	6.7	0.068
Fe	7.874	0.084
$Ni_{81}Fe_{19}$	8.711	0.045
Pt	21.09	0.065
Au	19.3	0.059
Si	2.33	0.049
SiO_2	2.533	0.025

with the initial figures regarding each layer. The initial values need to be sufficiently close to the best fit values to allow the model to get the best fit from the input shape. the next step is to execute the code computationally with the suitable logical adjustments in order to get the best fit. Only the parameters such as the layer thickness and interfacial roughness are allowed to vary. The best fit can more accurately represent the experimental data by adding more parameters and such as more layers. Although this can be done it is time consuming and computationally extensive and adds complexity to the interpretation.

3.3 Quasi-Static Magnetisation Measurements

In this section measurement regarding the static magnetisation of the investigated samples is described. In these types of measurement there is no investigation to the magnetic behaviour changing as a function of time, where the final magnetic status is the final result. In this type of measurements magnetic behaviour can change sufficiently slowly with time, where the system can be taken to be in equilibrium at all times. Such measurements are Magneto-optical Kerr effect (MOKE) and Superconducting quantum interference device (SQUID) magnetometers.

3.3.1 Magneto-Optical Kerr Effect Geometries

There are three geometries which can be used to detect magneto-optical Kerr effect, longitudinal, polar and transverse. The difference in Kerr effect, regarding these geometries, is due to the orientation of magnetisation vector with respect to the sample surface and direction of the interacting light; plane of incidence of light [63]. The longitudinal geometry is that the vector of M is parallel to both the sample surface and the plane of incidence, as shown in Fig. 3.8.

In the polar geometry the vector of magnetisation, M, of the applied field is perpendicular to the sample surface and parallel to the plane of incidence as it shows in Fig. 3.9 (a). Similar effect with the longitudinal geometry, can be seen in the polar geometry with one difference that the maximum effect can be indicated when the incidence is normal to the sample surface. The transverse MOKE geometry is when M

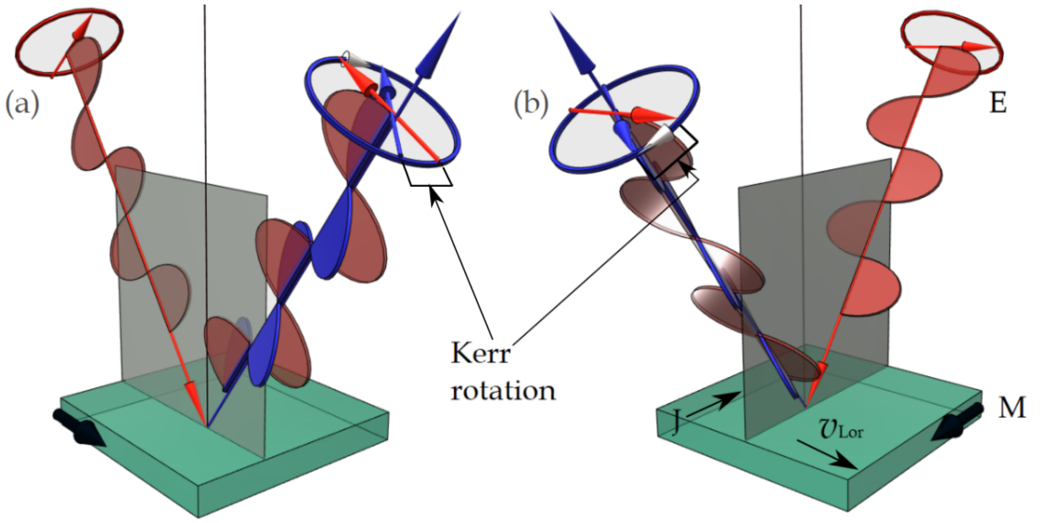

FIGURE 3.8: MOKE geometry with different light incident where it shows (a) and (b) longitudinal setting with S- and P-polarized incident light respectively, where it shows Kerr rotation.

vector is in the plane of the sample, but perpendicular to the plane of the incidence of light as it is shown in Fig. 3.9 (b). The only allowed light beam polarization, in order to detect this effect is P-polarization. This is due to the cross product, which is either zero or point along the vector propagation direction. Thus the reflected beam remains linearly polarized and the magnetisation changes sign from +M to -M.

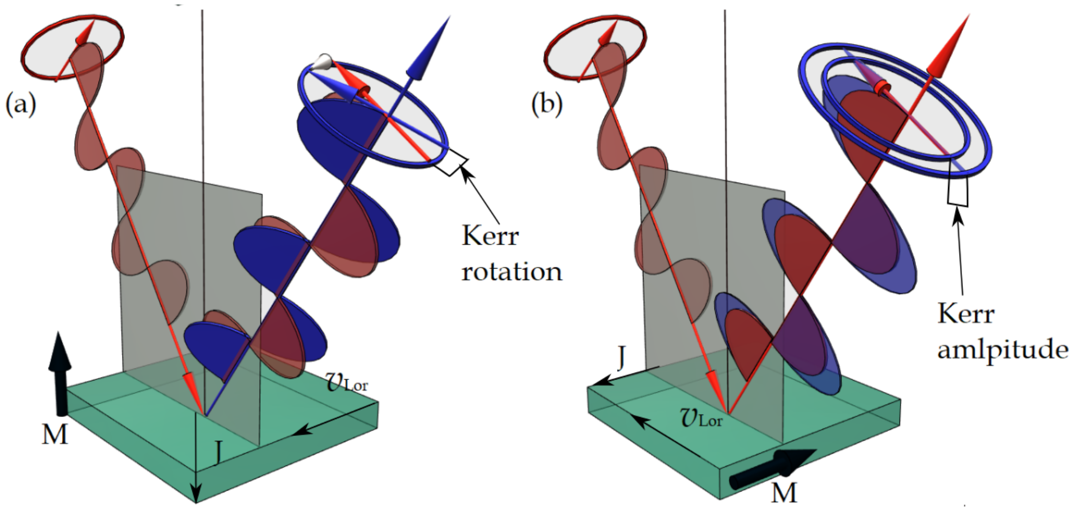

FIGURE 3.9: MOKE geometry with different light incident where it shows (a) and (b) Polar with Kerr rotation and transverse setting with Kerr amplitude respectively, where the incident light is P-polarized.

3.3.2 Longitudinal Magneto-Optical Kerr Effect

Here we discuss in more depth the polarisation change specific to longitudinal MOKE. This effect is related to the interaction of the incident light with the orbital motion of the electrons in the material and the Zeeman splitting effect. The equation which describes the magneto-optic interaction of the material with the incident light relates the polarization P with the dielectric displacement (D), through the electric field [64], by:

$$P = \chi E, \text{and } D = \epsilon E \tag{3.20}$$

Using the Fresnel reflection matrix R will leads to the longitudinal complex Kerr angle for the S-polarized light by:

$$\Theta^{\mathrm{s}}_{\mathrm{K,long}} = \left(\frac{r_{\mathrm{ps}}}{r_{\mathrm{ss}}}\right)_{\mathrm{long}} = \frac{\cos\theta_0}{\cos(\theta_1 - \theta_2)} . \frac{\sin^2\theta_1}{\sin\theta_2} . \Gamma \tag{3.21}$$

and and P-polarized light by:

$$\Theta^{\mathrm{p}}_{\mathrm{K,long}} = \left(\frac{r_{\mathrm{sp}}}{r_{\mathrm{pp}}}\right)_{\mathrm{long}} = \frac{\cos\theta_0}{\cos(\theta_1 + \theta_2)} . \frac{\sin^2\theta_1}{\sin\theta_2} . \Gamma \tag{3.22}$$

Where θ_0, θ_1 and θ_2 are the incident angle of the beam from the air to medium, the refracted angle of the beam in side the medium and the refracted angle of the beam when it transmits to the air again respectively. $\Theta^{\mathrm{s,p}}_{\mathrm{K,long}}$ are the Kerr rotation angle for s- and p-polarized light in the longitudinal geometry. Γ is a factor that depends on the medium thickness d [65], where:

$$\Gamma = \frac{4\pi n_0 n_1^2 Q d}{\lambda(n_2^2 - n_0^2)} \tag{3.23}$$

The quantum mechanical explanation of this effect is due to the optical transition of electrons from the initial state to the final state which should be in the FM materials in the same range of the incident beam wavevector [66]. This allows the transition between the states where the difference in the absorption will give rise to the Kerr effect. The focus of this work is on the longitudinal MOKE geometry, with in-plane magnetisation. The measurements shows changes in the magnetisation behaviour regarding the type NM material added as an adjacent layer, doping, interface and synthetic mono-layers, and domain wall switching in nanowires of these materials.

Longitudinal MOKE Experimental Setup

Longitudinal MOKE is the technique that is used to investigates all the samples in this work. Co and $Ni_{81}Fe_{19}$ based thin-films with range of NM material type (Pt, Au, Cr, Ag, Cu) as capping and synthetic dopant show different magnetic behaviour. In the longitudinal MOKE geometry a diode laser is used as source of light where the wavelength is 658 nm. The laser beam passes through a beam expander. The light polarization was set using a Glan-Taylor polarising prism (with an extinction ratio $< 10^{-5}$) before focusing it to a typical spot size of 5 μm with focusing lens on the sample. Fig 3.10 present a schematic illustration of the MOKE magnetometer system geometry.

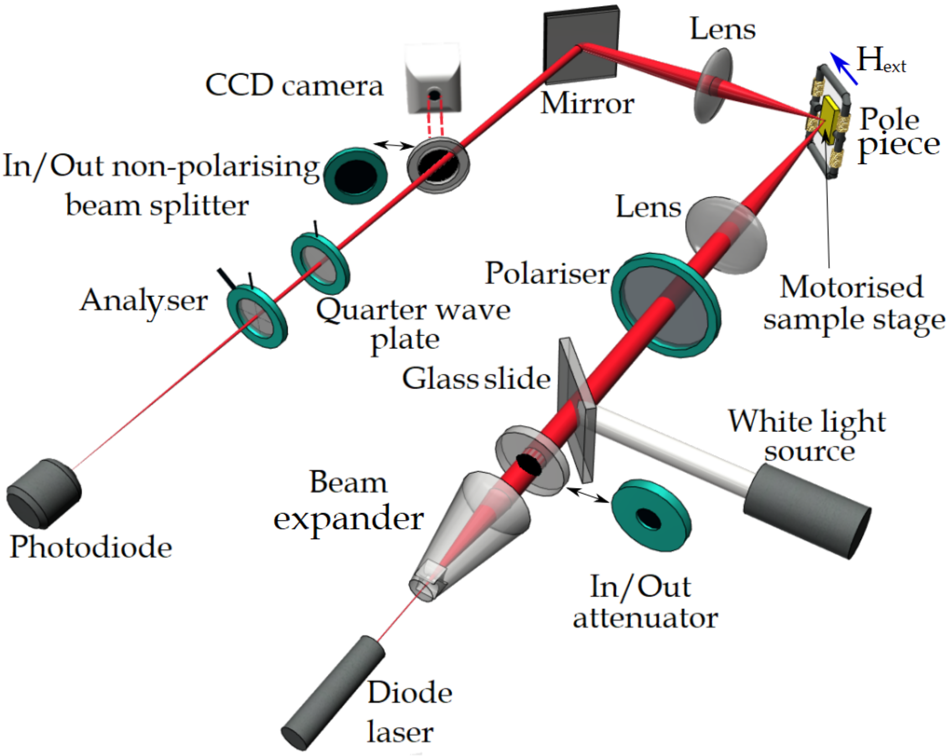

FIGURE 3.10: Schematic of the longitudinal magneto-optical Kerr effect magnetometry system with all the principle components showing the light path through the optical enhancement and focusing.

The sample is mounted on a motorized stage for X,Y and θ movement, so the magnetic measurement can be repeated at different positions on the sample and at different angles. Magnetic fields were typically swept at 23 Hz with an adjustable amplitude up to 400 Oe. The magnetic fields were generated in-plane of the sample by a small electromagnet powered by Kepco BOP 20-5M dipolar amplifier, driven by a function generator. The figure shows the optical path with the optical components plus the necessary components. An attenuator is placed between the expander and the polarizing prism to reduce the laser intensity, when focusing the laser spot, and locating the laser spot on the sample using the camera. The final polarized focused laser is projected onto the sample as an ellipse spot. The relative positions and direction of the incident plane, the sample and applied magnetic field give the longitudinal Kerr geometry.

The position of the objective lens was adjusted until the focused spot had a sufficiently high central intensity without significant higher order modes being present. Incident laser was linearly polarised and by the reflection from a magnetic sample it emerged elliptically polarised. A mirror is placed to direct the reflected beam toward the detector. The beam passes through a quarter-wave retardation plate, in order to restore polarisation linearity of the reflected beam, and the final step before detection is a Glan-Taylor polarizing analyser where it can be optimized to achieve the best extinction of the laser signal.

Extinction is achieved by rotating both the quarter-wave plate and analyser relatively. Then for measurements, the analyser is rotated by an appropriate angle away from extinction. This allows detection of the polarisation changes with positive and negative variations of magnetisation. A silicon photo-diode is used to detect light intensity. A CCD camera is used with an in/out mirror with a source of white light, to reflect the beam toward the camera and monitor the laser spot focusing and location on the sample surface. The longitudinal Kerr rotation leads to change of light intensity detected at the diode. The field and diode measurements use a digital oscilloscope, which is controlled and automated by computer in order to synchronized the full process. The data is saved as text file with information showing the changing of the Kerr voltage as a function of magnetic field.

3.3.3 Superconducting Quantum Interference Device (SQUID)

Some of magnetic measurements have been explained in this chapter where these measurement techniques can give some information about the FM measured materials. The information can show the magnetisation but, either relative to the saturation magnetisation such as MOKE or the magnetisation is calculated in an indirect way like FMR or TR-MOKE. The saturation magnetisation measurement is an important factor, where it can be implemented in the fitting of the measurements mentioned above, regarding the accuracy of the results. SQUID (Superconducting quantum interference device) magnetometer measurements were carried out using the Quantum Design Magnetic property Measurement System (MPMS) XL-7. The high sensitivity is the factor which made SQUID measurement technique ideal for monitoring very small changes in magnetic flux in a thin-films. The magnetometer is capable of measuring magnetic properties of samples as a function of temperature (1.9 K-400 K) and magnetic field up to (7×10^4 Oe) however, all SQUID measurements in this thesis were made at room temperature. The SQUID technique is an application of the Josephson junction [67–69]. The final magnetic flux will be converted to an electrical voltage, by coupling the superconducting ring to external circuits which can convert the changing in the current to measured voltage. Thus, an indication of the longitudinal magnetic moment will lead to extracting the saturation magnetisation [67, 70].

Experimental Condition and Setup

The experimental equipment for the magnetic measurements consists of a load-lock chamber and a main chamber, both of which can be evacuated. The magnetic sample is mounted on a sample holder with a long rod, the sample size is about 5×5 mm. To maintain the stability of the sample, two short pieces of drinking straws are used to get the sample to stick in the right position when the sample holder moves. The load-lock chamber is pumped-out before moving the sample into main chamber, because the device is working in vacuum in order to control the temperature. After reaching the required pressure, the sample travels to the main chamber, which contain the two superconducting detection coils. The magnetic flux of the sample induces an electric current and this current interacts with the detection coils. The latter current will be converted into a voltage, and this voltage varies in relation with the changing position of the magnetic sample with respect to the detection coils. The final result is a measurement of the magnetic moment as a function of the external applied field [71]. Fig 3.11 shows the main movement of the sample through the coils with four turns shown in the detection coil. Two of them are in the centre of the system and counter-wound ones at the top and the bottom. The top and bottom turns a second-derivative flux gradiometer used to cancel any noise due to fluctuations in the magnet. Such noise can be due to the sample holder which is usually the largest source of background signal, the plastic straw is weakly diamagnetic. Using the software with the SQUID system gives the central point for the sample starting position. The full measurement can then be automatically programmed to execute high resolution magnetisation measurement with applied magnetic field.

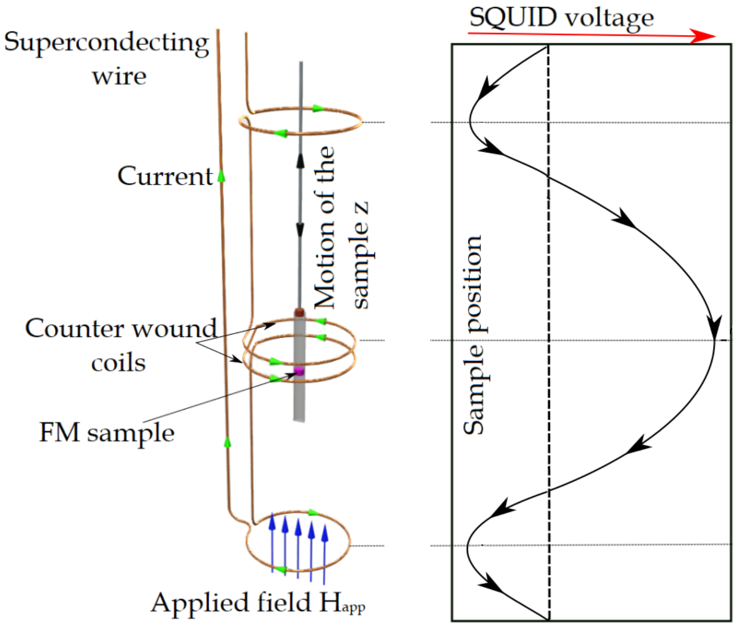

FIGURE 3.11: A schematic figure for the SQUID , showing the sample position and the main detecting coils with the voltage changing with the sample movement through the device.

SQUID Results and Interpretation

Magnetic hysteresis loops are the typical data extracted from the SQUID magnetometry in this work, where the maximum applied field was $\pm 1 \times 10^4$ Oe. Fig. 3.12 (a) shows an example of the raw acquired data for a Co film sample, The saturation magnetisation is easily saturated below $\pm 4 \times 10^3$ Oe magnetic field, the raw data have a diamagnetic contribution which may come from the silicon substrate, as shown in the figure (a). This diamagnetic effect can be eliminated by subtracting the diamagnetic slope from the general hysteresis trend. This measurement is sample-volume dependent, which required that the sample area is measurable. Calculation of the sample volume was done by using the image processing program; imageJ to calculate the surface area of the sample [72]. The thickness was obtained by the deposition time and sputtering rate or from XRR measurements. The maximum and the minimum values of the hysteresis loop, are used to obtained the saturation magnetisation. Adding these values and dividing their average on the sample volume will give the final magnetisation of the magnetic material as it is shown by the same figure (b).

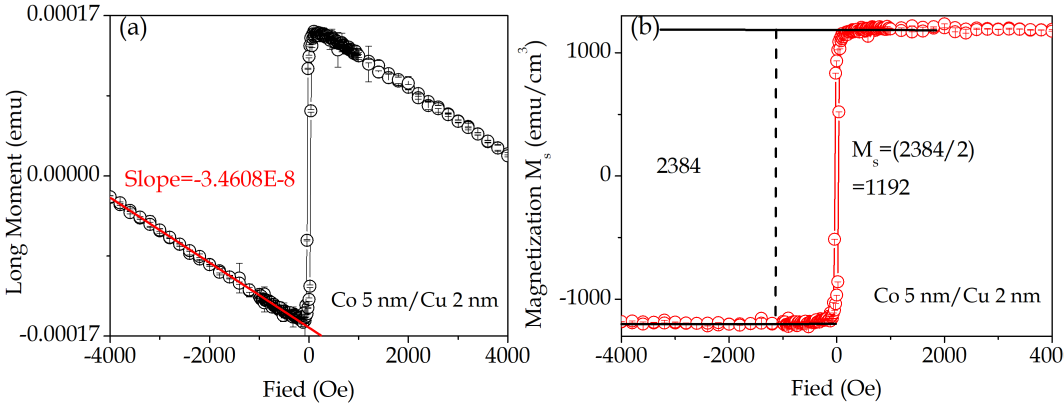

FIGURE 3.12: Shows (a) typical raw data from SQUID measurements, where the diamagnetic effect and (b) the final shape of the hysteresis loop with the analysis of the saturation magnetisation.

3.4 Dynamic Magnetisation Measurements

In this section magnetisation dynamics are the main concern, where two techniques were used for studying magnetisation dynamics. This type of measurement is more concerned by indication the spin, magnetisation direction variation as a function of time evolution, which indicates the precession rate of the magnetisation in the system investigated. The first technique is time-resolved magneto-optical Kerr effect, TR-MOKE, the second methodology is ferromagnetic resonance, FMR.

3.4.1 Time-Resolved Magneto-Optical Kerr Effect (TR-MOKE)

Timed-resolved magneto-optical Kerr effect (TR-MOKE) magnetometry uses a magnetic pulsed field to excite the sample and measure the dynamic magnetisation precessional in the time domain. As any other technique, TR-MOKE has it own down sides where its signal is exactly proportional to the magnetisation directly. This is because there three MOKE geometries, thus only longitudinal and polar geometries contributed and only if the polarization is s-polarized [73]. The spin and the general decay, of the the Kerr voltage with the time domain, is linked by the relation of Eq. 3.24. As spin relaxation time, T, can be determined by fitting the detected polar Kerr rotation, using the measured time-dependent field, $H(t)$. By using the equation below, noting that T depends on the field varying as function of time [74]:

$$M(t) = \chi \frac{e^{-t/T}}{T} \int_0^1 H(t') e^{t'/T} dt' \tag{3.24}$$

In a similar way a single frequency damped oscillatory behavior was obtained from any measuring samples and the time domain data were fitted with a damped sine curve as it is shown below:

$$M(t) = M(0) e^{-t/T} \sin(2\pi f t - \phi) \tag{3.25}$$

TR-MOKE and FMR are different methods of measurement regarding the time and the frequency domain. However, techniques are giving a good agreement in the damping value for measuring a ‘uniform’ layers of Ni. and the same was for the damping of Pt/Co/Pt thin-films as function of Co thickness, measured by TR-MOKE and x-band cavity FMR [75]. Furthermore, it can be seen in the results presented in this thesis Chapt. 6 and 9 that FMR and TR-MOKE can give similar results when the total damping is composed from both mechanisms intrinsic and extrinsic, where TR-MOKE measurements were made at the S.N. Bose Institute for Basic Sciences, Kolkata, as two publications have been made using this technique [4, 5].

Experimental Condition and Setup

Optical time-resolved Kerr effect measurement is based on a two-colour collinear pump–probe technique. This allows measurement of the picosecond magnetisation precessional dynamics in a ferromagnet. A linearly polarized high intensity pulsed laser (400 nm, pulse width 100 fs) is used as the excitation for the magnetisation in the thin-film [76]. This will cause a demagnetisation in the system with ultrafast order. Furthermore, a creation of an internal anisotropy field pulse in the system will alter the magnetisation toward the orientation of the field. Thus a dynamical precession will result to return to the equilibrium state. The micromagnetic precession is detected by using another MOKE laser pulse, weaker that the first one, of 800nm wavelength and polarized linearly. The key factor in this measurement is the time delay to the probe with respect to the pumped beam, which allows the magnetisation dynamics to be detected by the polar magneto-optical Kerr effect.

Fig. 3.13 shows the experimental setup with main parts and equipment regarding the laser generating, time delay and the final Kerr rotation measurement. It is shown that the laser beam is first split then modulated using a chopper with 2kHz allowing a phase-sensitive detection controlled by a lock-in amplifier. At the other end the probe laser beam is reflected and through time counter to control a delay stage in ordered to accurately synchronizes the pump and probe beams. The probe beam is focused through lenses, and passes through a polarizer before both beams are combined into a microscope objective (MO) and focused to less than 1 μm diameter spot.

For the reflected journey, the pump and probe beams a 50:50 beam splitter is used

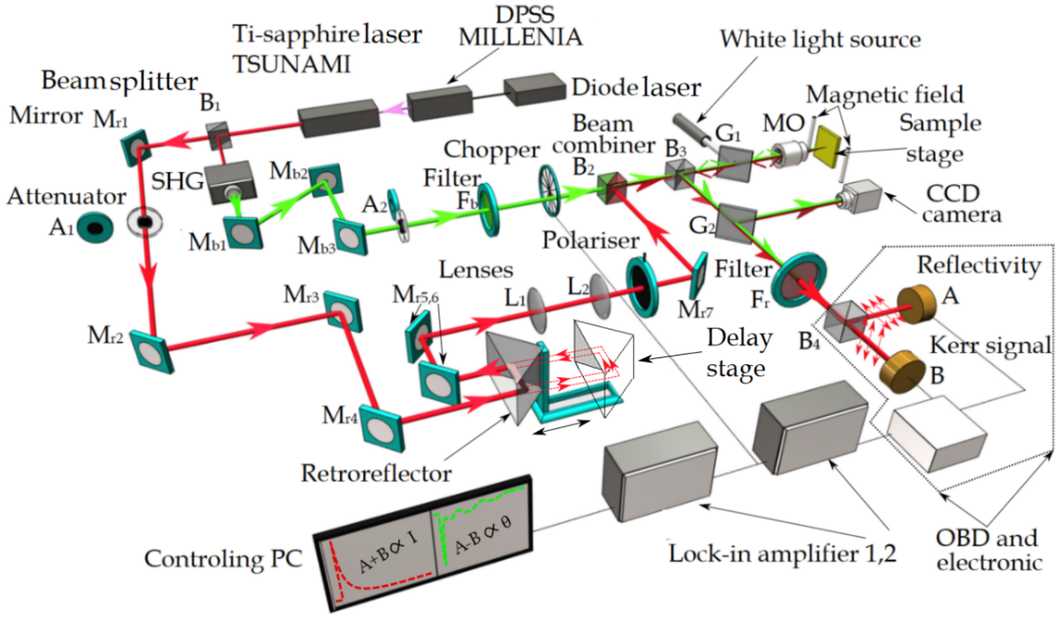

FIGURE 3.13: Schematic of the longitudinal magneto-optical Kerr effect magnetometry system with all the principle components showing the light path through the optical enhancement and focusing producers.

to collect them before they are sent toward the detector. A CCD camera for monitoring with a source of white light is supported to illuminate the sample for better viewing. Because the measurement interests is in the changing of the polarization of the probe beam, a filter is used to eliminate the pump beam from entering into the detector. An optical bridge detector (OBD) is used in order to achieve better spatial resolution and sensitivity [77, 78]. The OBD splits the final beam in two orthogonal component, each one goes to a separate photodiode. These two photodiodes with signals each have different proportional relation to the Kerr rotation [63]. The final result shows as electronic signal at the output of the optical bridge detector. The OBD is used to measure both Kerr rotation and Kerr ellipticity, where this is very useful with some of the FM materials where they have a much larger ellipticity than Kerr rotation. The ellipticity in such cases can be converted into rotation by introducing a $\lambda/4$ plate before the analyser.

TR-MOKE Data Representation and Interpretation

The results of the TR-MOKE shows the Kerr rotation as a function of the time as shown for example in Fig. 3.14 for a Co 10/Pt 0.6 nm sample. The figure shows two time precession regions, T_1 which is representing ultrafast demagnetisation and T_2 a slower precessional relaxation. The first takes place in 500 fs as a result of the pulsed laser excitation, the Kerr signal recovers quickly (fast relaxation) due to the electronic thermal bath equilibrating with the lattice. While the second is a slower relaxation with time which is due to the dissipation of the energy to the surroundings. Similar data in the same figure was obtained for all the samples studied here and the decay of the precession of the magnetisation was analysed, to obtain the dimensionless damping parameter α. Repeating the measurement for the same sample with different frequencies as a function of magnetic field was used in order to determined the saturation magnetisation using Kittel formula equation. In TR-MOKE there is no separation between the intrinsic and extrinsic damping parameter however, the contribution of both can be indicated by knowing the dependence of α on the measurement frequency.

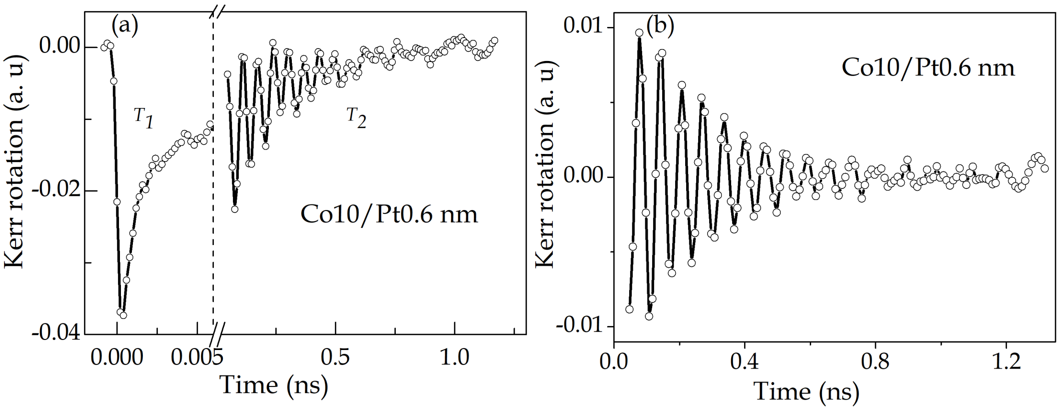

FIGURE 3.14: (a) TR-MOKE typical data trace from a Co10/Pt0.6 nm sample showing Kerr rotation with the T_1 and T_2 time base and (b) is Kerr rotation as a function of T_2, after removing the general recovery of the magnetisation.

3.4.2 Ferromagnetic Resonance (FMR)

Ferromagnetic resonance (FMR) spectroscopy is the other technique used to investigate magnetic damping in this work. It is a direct and very powerful technique to investigate the magnetisation dynamics in ferromagnetic thin-film using a range of frequencies [79]. The Kittel formula describes the ferromagnetic resonance in the frequency and field domains. The first experimentally study was done by Griffiths [80] in 1946. While the theoretical explanation was provided after two years by Kittel [81]. FMR can give the characterization of a magnetic materials with respect to its effective magnetisation and precessional damping. The Kittel equation relates field and frequency variation as

$$f = \frac{\gamma}{2\pi}\sqrt{H_{\text{eff}}(H_{\text{eff}} + 4\pi M_{\text{eff}})}\ (cgs) \tag{3.26}$$

This equation can be used for the fitting the frequency and field linewidth. H_{eff} is the effective field, which can vary according to the material and H_{eff} in isotropic FM materials is equal to H the applied field, while for non isotropic materials it includes contribution of anisotropy field. M_{eff} is the effective magnetisation which relates the perpendicular anisotropy magnetising field with the saturation magnetisation as follow:

$$M_{\text{eff}} = M_{\text{s}} - \frac{H_{\text{an}}}{4\pi}\ (cgs) \tag{3.27}$$

Beyond this, extracting of the dimensionless damping parameter α comes from the measurement frequency in the field domain, where the field linewidth (ΔH) can be extracted from the FMR measurements directly. The resolution in the field is much higher than in frequency. The ΔH is often used to extract α from the fitting of ΔH as a function of frequency by

$$\Delta H = \Delta H_0 + \frac{4\pi f}{\gamma}\alpha \tag{3.28}$$

Where ΔH_0 is the frequency independent extrinsic contribution which can be calculated separately and excluded from the total damping parameter value. However, this can be done also when the measurement is in the frequency domain [82]; the frequency linewidth (Δf) is the main and frequency f has much higher resolution than the field H. There are two ways to obtain α the first one which relies on the equation

$$\Delta f = \frac{\gamma}{2\pi}\alpha(2H + 4\pi M_{\text{eff}}) \tag{3.29}$$

This equation gives what is known as the damping line; for continuous values of α, the value is the average when the changing of α values as a function of the field is more or less negligible. The other way to obtain α is by using Eq. 3.28, after calculating the field linewidth ΔH from the giving frequency linewidth as

$$\Delta H = \frac{1}{\gamma\sqrt{1 + (\frac{\gamma M_{\text{eff}}}{f})^2}}\Delta f \tag{3.30}$$

However this equation can only be used in certain cases, where the contribution of the extrinsic linewidth approaches to zero [83]. Both approaches are used here. The measurement was implemented with Vector network analyser (VNA). The main usage of VNA is to investigate high frequency (GHz) circuits. The magnetisation dynamics in thin-films have a range of microwave frequencies. In Chapt. 9 a comparison between the precision of the two measurements in time domain due to the field and frequency linewidth, are presented.

It is known that there an inductive coupling between the sample and the waveguide, which leads to an additional radiative damping (α_{rd}) when using the FMR technique. This term contributes to the total measured damping, however it can be a very small addition which may have value of order 10^{-4}. This α_{rd} effect is due to the inductive interaction between the precessing magnetisation in the sample and the co-planar waveguide in the FMR system. Furthermore, the term is in relation with the measured perpendicular standing spin waves (PSSWs) profile, which explains the propagation of the microwaves from the co-planar waveguide to the sample and the modes related with such propagation. This effect may be very small, however in some FM systems with very low damping this can be crucial to lower the damping value further, and also it can help invoke any additional damping contributions in order to explain the data. For the calculation of α_{rd} it can be obtain by the equation [84–87]

$$\alpha_{\text{rd}} = \frac{\gamma\mu_0^2 M_{\text{S}} d_{\text{s}} l_{\text{s}}}{16 Z_0 W_{\text{CPW}}} \tag{3.31}$$

where Z_0 is the waveguide impedance, W_{CPW} is the coplanar waveguide width, which is = 450000 nm in our measurements, d_{s} and l_{s} are the thickness and the length of the sample. α_{rd} can also be found experimentally by putting $\sim 100\ \mu$m glass spacer between the waveguide and sample to decrease the radiative contribution, or it can be found through using Eq. 3.31. This was used in Chapt. 9 to find the net damping from FMR measurements.

Experimental Condition and Setup

FMR measurements were done in IN-IFIMUP, University of Porto, Porto, Portugal and Brazilian Centre for Research in Physics (CBPF) , Rio de Janeiro, Brazil. However in CBPF, they used RF generator and diode/lockin detection instead of VNA. The first FMR measurements were as a function of frequency linewidth, while the second one as a function of field linewidth. Both devices have a similar basis and the same measuring tools in general. FMR in general is based on measuring the total current and voltage however, at higher frequencies this is very difficult. So instead of that, S-parameters, are used in a two-port measurement configuration, which consist (S_{12},S_{21}) as transmitted and (S_{11},S_{22}) as reflected signals. As can be seen in the Fig. 3.15 the first subscript number refers to the port number which is used to produces the outgoing wave, while the second subscript number refers to the port used as the receiver.

These S parameters are related through the scattering matrix via the ratio of the reflected voltage wave to the incident voltage wave amplitude through the following equation:

$$S_{\mathrm{ij}} = V_i / V_j \tag{3.32}$$

This relation shows the relative voltage of the reflected wave i to the incident wave j. The measurement is carried out by changing the frequency at a fixed applied magnetic field or the other way around. The complex transmission parameter S_{12} is recorded as a function of the frequency or field changing. The signal indicated and registered at the maximum resonance, where the sample absorbs the maximum of the microwave signal, and changes the phase of the transmitted microwave signal. This is the resonance position of the FMR frequency field linewidth, the measurement here used an Anritsu (37247D), the VNA sweeps the excitation frequency of

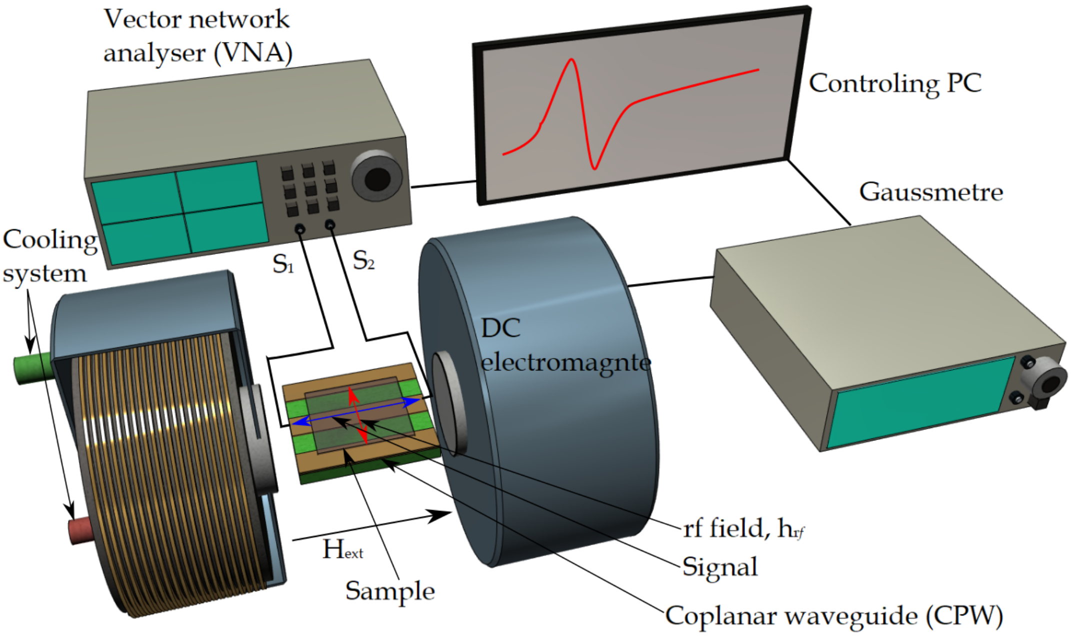

FIGURE 3.15: Schematic showing the VNA-FMR system,where the microwave radiation signal and the rf field h_{rf} directions with respect to the external field. The coplanar waveguide (CPW) placed in the centre of an electromagnet and the ferromagnetic magnetic film is placed on the CPW mounted in non-magnetic sample holder with goniometer between a set of magnetic coils.

the outgoing signal through a specified range from 45 MHz to 18 GHz. The signal is passed through a coplanar waveguide (CPW) on to which the sample is placed . This excites the precession of the magnetisation and changes the microwave signal propagating through the CPW.

Furthermore CPW has a central strip conductor of 3 cm length and 450 μm width surrounded by co-planar ground planes in each side. The gap between the central line and the ground planes is 300 μm. The connection to the CPW is done by using phase stable non-magnetic coaxial cables and microwave probes. The sample mounted on the CPW with the magnetic material facing down. the CPW is placed in the centre of an electromagnet which provide a static magnetic field from an electromagnet. The magnetic field was monitored by a Hall probe placed between the pole pieces, at the sample position. As it can be seen from Fig. 3.4.2 the static magnetic field is perpendicular to the microwave magnetic field.

FMR Results Representation

As explained earlier, that FMR linewidth measurements can be done as a function of frequency or field. Typical FMR data shows the S_{12} parameter changing as a function of the external field or the frequency. Fig 3.16 show examples for 5 nm Co capped with 2 nm Cu, where the signal varies with (a) the external field and (b) the frequency . Also in the same figure the real and imaginary components which both can be used to extract the linewidth value are shown in (c). The linewidth is either peak to peak in the imaginary component or the half width for the peak of the real component, where it is found using a Lorentzian fit. For the Kittel formula the resonant frequency is plotted against the field and by fitting the data the result is the Kittel non-linear fitting as it is shown in the same figure (d). Information are extracted from this fitting such as the saturation magnetisation M_s and the anisotropy field H_an.

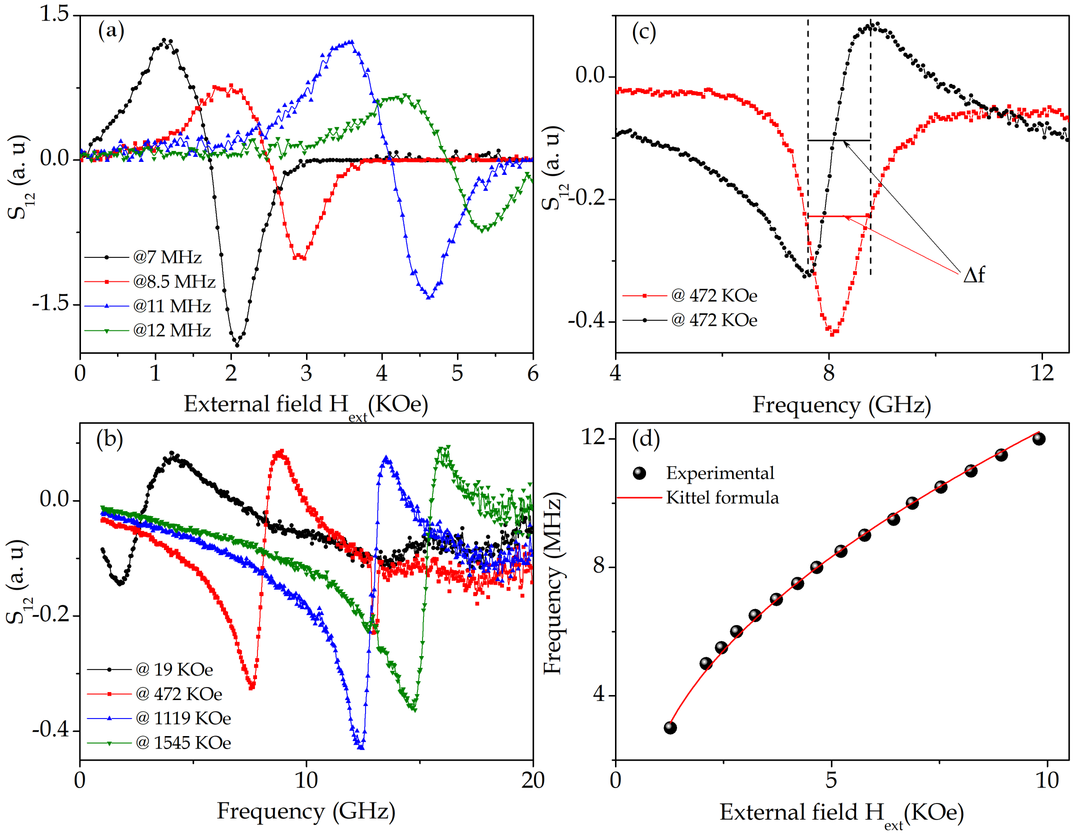

FIGURE 3.16: Shows a typical data of FMR measurements, where the rf signal changing as a function of (a) the external field and (b) the frequency, also (c) showing the imaginary and the real component for extracting the frequency linewidth, finally (d) showing the Kittel formula fitting according the relation between the field and the frequency.

The linewidth can provide more information, where calculating damping from Δf or ΔH as a function of frequency is the main. This can be done by fitting either equation 3.28 or 3.29, the analysis can be done by the available analytical softwares, where a lot of parameters vary in order to get the best fit such as the gyromagnetic ratio, the anisotropy and the effective field. The calibration procedure and measurement process are fully automated. The final result is the damping parameter value (α_{eff}) for a range of samples with different FM and NM material component as it is discussed in Chapt. 9. The result show an outstanding change of the magnetic damping and a better understanding to modify the material magnetic properties.

3.5 Summary

In this chapter the techniques regarding the crystal structure and thin-film studies are presented. The most important techniques with their theories are discussed from the simplest picture to the more complex. The use of reflectivity and refraction laws of optics are explained in order to understand the x-ray interaction with the material. Using x-ray reflectivity is an important technique regarding thin-film thickness with the electron density of each layer and the interface determining the behaviour. The XRD technique was used to obtained the crystal structure in each layer.

The next step is the techniques used to measure the magnetic properties, which are divided into static and dynamic magnetisation measurements. MOKE and SQUID are the static measurements, where the importance of these techniques is in the determining magnetisation properties. MOKE and SQUID are showing the relative or the direct magnetic moment for a FM material as a function of different measurement parameters. The vital role of these techniques is to give the final descriptive magnetisation of the material in general. The other division is the dynamic measurements, measuring magnetisation precession in time domain by TR-MOKE or in frequency and field domain by FMR which are the techniques that used in this thesis. The methods are described, along with the setup and the data analysis.

For all techniques there is an important point where they can show direct critical changing in the magnetic behavior of the investigated samples such as damping and saturation magnetisation. Or they can support the result or give more explanation regarding the critical changing as in XRR, XRD and also SQUID and MOKE. The results which have been extracted by using these techniques are shown in Chapters 6, 7, 8 and 9 where all the results show good agreement and give new understanding with the supportive explanations from the other techniques.

Chapter 4

Sample Growth and Modification; Background and Practical Implementation

4.1 Introduction

In this chapter, an explanation of the details regarding the fabrication of magnetic samples is presented. The thin-film production is presented starting with the steps before the actual deposition. This includes cutting and cleaning the substrates for FM and NM materials deposition, with shapes depending on the measurement practicality. Deposition techniques are presented in general and UHV deposition techniques are explained as the only methods used to fabricate all the magnetic samples. The operating conditions of the deposition system used is covered in order to show thin-films quality and thickness accuracy of the sample investigated. This demonstrates the sub-nanometre deposition capability for the samples investigated in Chapters 6 and 8 and the precision controlling of concentration from two co-sputtered materials as in Chapt. 9. The growth and the formation of the material layers on a substrate is discussed to give insight regarding the nature of thin-film layers and interfaces. Ion-beam irradiation is explained as one of the techniques that was used to modify the samples investigated in Chapt. 7. This is explained with respect to the main three processes; ion implantation, sputtering of material from the sample surface and with main focus on the intermixing at the interfaces in bilayered thin-films. The effect of theses main processes is discussed in relation to the modifications of the magnetic properties of the sample investigated. This facilitates understanding of the changing nature in the samples and links it with the changing of the magnetic behaviour.

4.2 Before Deposition

In order to made good samples, cutting and cleaning of high quality flat substrates is the first step, which is based on a silicon wafers. The process is used to prepared single crystal silicon wafers with 6 inches diameter, as substrates for all the samples in this thesis. These wafers are topped with ≈100 nm of SiO_2. The role of this layer is to prevent electrical conductivity as the electromagnetic measurements are carried out. Any contribution from the substrate is reduced to a minimum to avoid any confusion in the results. Going back to the wafer, a diamond cutter was used to produce chips and strips. Labelling on the back of the chips/strips was done using the same diamond cutter for the record. The dimensions of these shapes differ and are linked with the measurements, for which the samples were made. In the next section a full description regarding the samples dimensions and shape with respect to the intended measurement, is explained. After cutting the wafer in to chips/strips, the cleaning process, where the chips/strips were soaked in acetone. The beaker was placed in an ultrasonic bath for about 120 second to make sure the cleanliness of the chips/strips. To remove the acetone from the chips/strips, the same procedure was repeated but, with isopropan-2-ol (IPA) instead, where beaker was also placed in the bath for the same time. To remove the isopropan-2-ol, a N_2 gas gun was used to remove the remaining IPA before it evaporates. Cleaning and cutting processes are carried out in fume hood under lab working conditions with lab gloves on.

4.3 Samples Shape Related to Measurements Practicality

For matters of measurement practicality, different measurements are explained in Chapt. 3. Each of them can give the optimal result when the experimental conditions are considered precisely. One of these conditions is the shape of the sample, where it plays a key role in term of result accuracy. Some of these measurements share the same sample shape, where it may be either a square chip or a rectangle strip or approximate dot. Another shape related issue is magnetic shape anisotropy effect even when it is very small. For example x-rays sample surface needs to be a wide clean, on the other hand for MOKE and TR-MOKE a relatively small clean surface is sufficient. however TR-MOKE is more related with sample shape, which means that all the samples should be the same shape and size. So it is very good practice to control the shape of the samples for those reasons. Further reasons such as; sample mounting, fitting size with the measurement stage and insuring enough FM material exists to give sufficiently indicative results.

In order to cover this issue, a lot of samples were produced in the work of this thesis, all based on a square chip or rectangle strip but, with different area size. It can be seen in Fig. 4.1 some of the tools which have been designed and made to serve this purpose. In figure (a) and (b) a designed tool for holding the silicon wafer with milled grooves to help cutting stripes of silicon with the same dimensions, where the strips will be diced according to the desired strip/square size. In order to produce a semi or circular shape, or sample with a rounded edge a shadow mask was also made for this reason. Figure (c) shows the designed shadow mask with holes to allow the flux of atoms to be deposited only on the exposed silicon areas. The upper edges of the holes are chamfered where it shows in (d) the effect of this technique on the shape precision. The variety of shapes of the samples are shown in the same figure (e) with dimensions in mm. All the cut, cleaned and labeled samples are ready for deposition, where they attached one the back of the mask before they go in the deposition system.

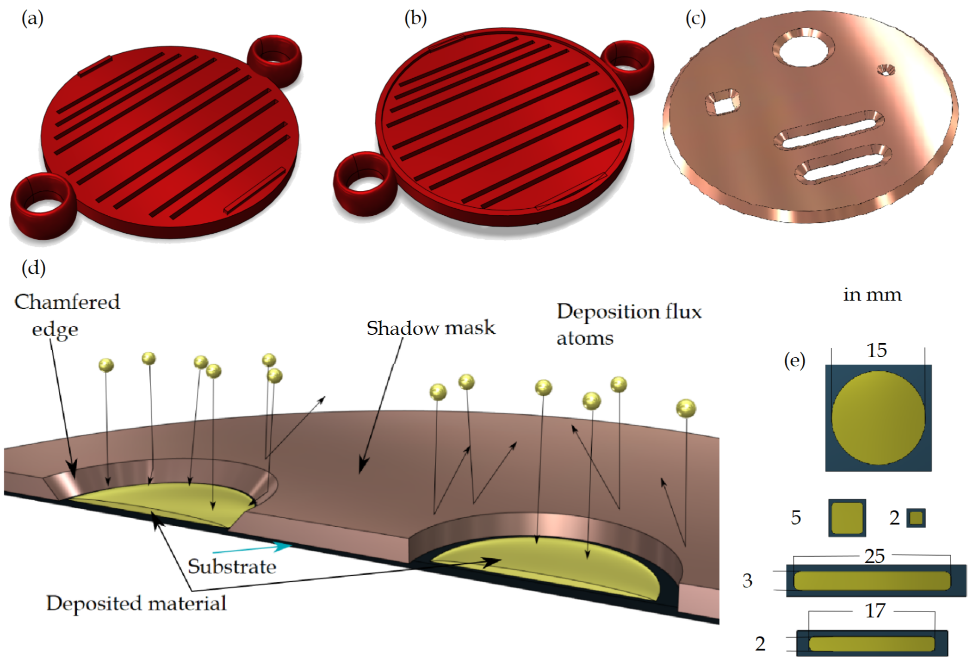

FIGURE 4.1: Shows tools for cutting and masking the Silicon wafer (a) and (b) are the wafer holder from both up and down side respectively, (c) is the shadow mask with different shapes (d) the chamfered technique and finally (e) all the produced sample shapes.

4.4 Deposition Modes and Techniques

Thin-film deposition can be divided in to two different methods of growth, which can observed during the deposition of metallic thin-films. The first method is: vapor-phase deposition, this covers sputtering, thermal evaporation and molecular beam epitaxy. The second method is: liquid-based deposition, which also covers electro-chemical deposition and Langmuir-Blodgett films. Sputtering is the main technique, used to fabricates all thin-films in the work of this thesis. The physical basics of this technique is the use of highly energetic ions to bombard a target material to eject atoms from its surface and for these atoms to be deposited on the surface of a substrate. It is first discovered by W. R. Grove [88] in 1852 and became widely used after that in thin-film fabrication. This technique has a lot of advantages, where it allows the use of wide range of materials with the capability of multilayer, alloying and co-sputtering.

Fig 4.2 (a) shows a schematic illustration of sputtering magnetron, where the atoms from the target are sputtered by the argon gas plasma created by a bias DC-voltage where the target represent the cathode. The ejected atoms travel from the target and coat all surfaces including the substrate located above the target. The atoms start to land on the substrate surface and a thin-film layer starts to form by the bonding between the atoms themselves and the substrate material. The bombarding process raises the temperature of the targets thus, cooling system is required to prevent damaging the target by milling.

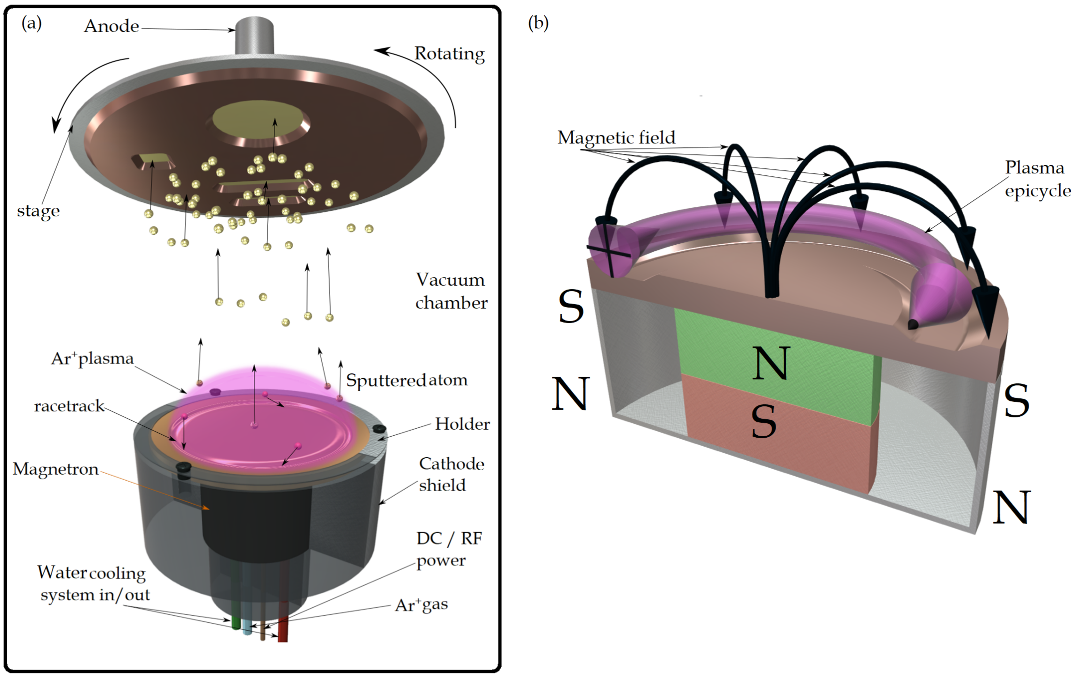

FIGURE 4.2: Shows a schematic illustration of (a) deposition technique where the sputtered atoms ejected from the material target (cathode) to the substrate (anode) and (b) the sputtering process with the magnetron field.

In the same Fig. 4.2 (b) the plasma phase is shown, where the target material mounted on a metal cathode with magnets in the core creates a magnetic field. The Ar gas ions interact with the magnetic field. The plasma phase is a mixing betweens ions and electrons, where the magnetic field will interact by the Lorentz force. Thus the electrons will be contained in a circular area near the target, restricted by the magnetic field to this track. Movement of the electrons in the circular track near the material surface will leads collisions. The Ar ions in the high density plasma will be accelerated to the target by the DC/RF power and by bombarding in to the target surface they will ejects the target's atoms. Due to the guided movement of the ions by the magnetic field, atoms will be lost from a certain area of the target material in the shape of circular track, which is called racetrack.

4.5 Thin-Film Growth Modes

The deposition of sputtered atoms is the initial step of forming any material layer on substrate. Repeating this step with time will increase the layer thickness in general and will leads to a thin-film. Forming layers of a thin-film takes place through three different ways, which are know as growth modes . All of these three modes are related to the bonding strength between the deposited atoms with each other atom-atom with respect to the bonding strength of these atoms with the substrate atom-substrate surface [89]. The first mode; Volmer-Weber growth mode, which is also known as island growth mode, is where the atom-atom bonding strength is much stronger than atom-substrate bonding strength. This mode starts with the atoms gathering with each other, forming islands in separated areas on the substrate, then these islands join with each other to form the thin-film layer. When the atom-substrate bonding strength is stronger than the atom-atom bonding strength the second mode of deposition dominates. This mode; Frank-Van der Merwe growth mode, is a layer-by-layer growth mode, where the deposited atoms will be arranged to form a full covering mono-layer over the substrate surface. The lattice matching between the substrate and the forming layer has a key role, which will increases the domination of layer-by-layer mode. The forming of these modes is illustrated in Fig. 4.3 with gradual increasing of thin-film layer thickness.

The third mode, as it shown in the same figure, is a mixing between the layer-by-layer and island growths, which is know as Stranski-Krastanov growth mode. It is start by the layer-by-layer growth mode until a full mono-layer covers the substrate, then island growth takes place to form the rest of the layer [90]. From the first and the second growing modes the atoms either form their own structural arrangement or follow the substrate structural arrangement, where this will lead to stress-free film. While the the third growth mode reduces the stress significantly, because the interface energy increases with the layer thickness, by changing the growth mode.

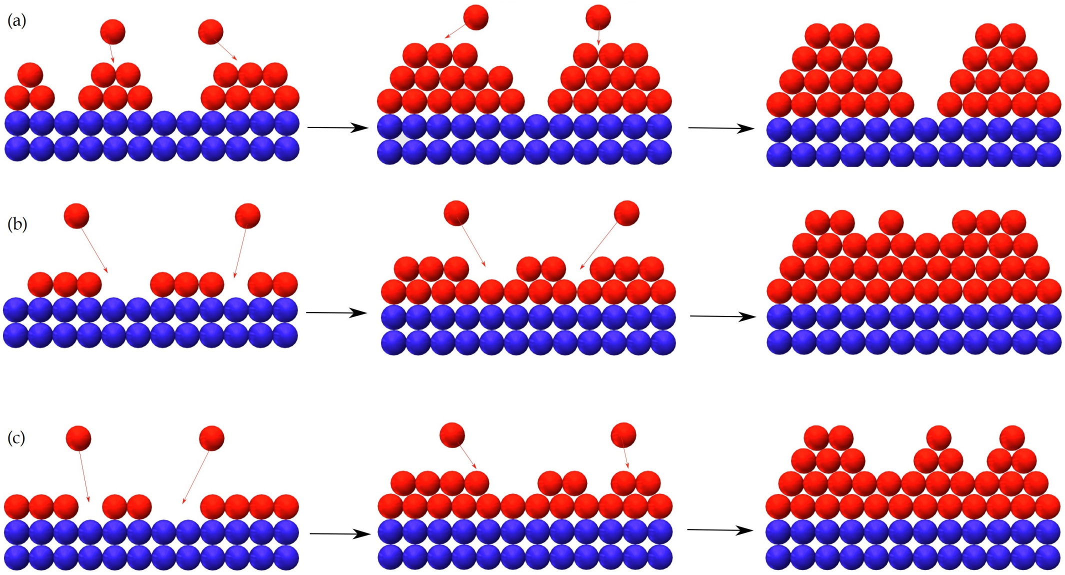

FIGURE 4.3: Schematic illustration of thin-film growth modes including (a) Volmer-Weber island growth, (b) Frank-Van der Merwe layer-by-layer growth and (c) Stranski-Krastanov layer plus- island growth.

This shows that the following deposited layers are strained to fit the substrate [91]. With these growth modes different surface structures are expected to be induced. Crystal structure changes can occur either in a layer or between two layers also as a function of increasing film thickness [92].

The structural changes are indicative of the presence of defects in thin-films. These defects can occur when two materials with different lattice parameters are adjacent with each other, when the thickness of the same material increases to the extent that the bonding strength of the deposited material is weakened. Thus the atom-atom bonding strength is more dominant in the formation of the material crystal arrangement. This has been explained in Sec. 2.6 where the pure material have a specific crystal arrangement preferentially. This arrangement leads the material's energetic status at the lowest ground state as explained in Sec. 2.7. However, it has been shown in Sec. 2.7.1 that the crystal structure can be changed by adding new material. By depositing thin-films with different thicknesses and with different capping layers a significant effect on their crystal structure and hence on their magnetic properties will be induced.

4.5.1 The Deposition System and Thin-film Growth Conditions

The system used to produced all the sample in this work is Mantis Qprep500 sputtering system [93]. This system provides an ultra high vacuum (UHV) base pressure for thin-film growth, with deposition capability of metals, by DC power source, and non-conducting materials, by RF power source. The vacuum system has two parts; load-lock and deposition main chamber, where both can reach to vacuum pressure $\approx 10^{-9}$ Torr or better. The load-lock chamber is connected to a rotary and relatively small but, sufficient, turbo molecular pump. It can hold 5 samples each time with a carousel. A gate valve is between the load-lock and the deposition chamber, in order to isolate the main chamber environment while new samples are loaded or taken out. Fig. 4.4 shows the Mantis Qprep500 sputtering system with main features indicated.

The main chamber is connected to two turbo pumps and one rotary pump to reach the right pressure within a reasonable time. It can hold 5 different material targets, each is supported with gas, cooling water lines and DC/RF power connections. The main chamber is supported with a gas analyser to monitor the chamber environment and to detect contamination. The substrate stage is located in the roof of the main chamber with a rotating capability for improving film uniformity [94]. A quartz crystal microbalance (QCM) is mounted and positionally engineered to determine the growth rate in (Å/Sec) unit. At working conditions the samples can be moved from the load-lock chamber to the main chamber by transfer arm to be mounted on the rotating substrate stage. Finally the system is connected to a controlling computer to synchronize the deposition time, where it opens and closes all the shutters to get an accurate deposition time by knowing the growth rate.

A wide range of thin-films have been fabricated including the ferromagnets; Co and $\mathrm{Ni_{81}Fe_{19}}$. The deposition conditions of the fabricated thin-films are controlled and monitored all the time. Keeping records is essential to track the history of thin-film fabrication and also to link any unusual results with fabrication conditions. These conditions either link to the main chamber environment such as pressure, temperature or argon gas flow, where they can change the general deposition process, or they linked to the voltage, current and DC/RF power of each target, which

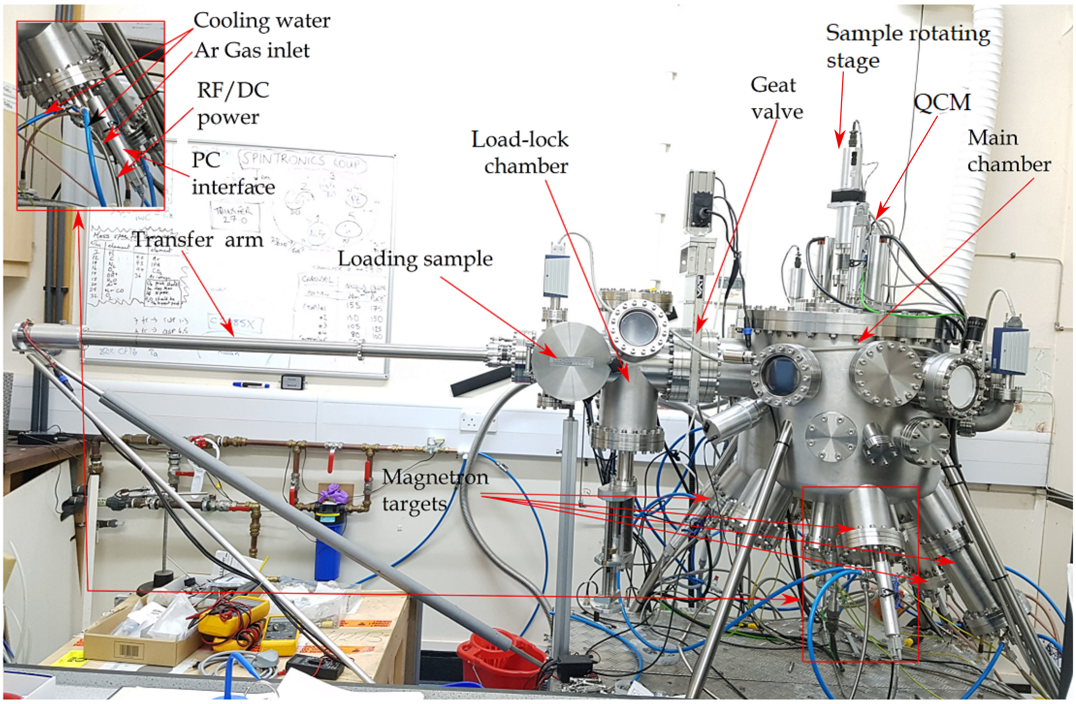

FIGURE 4.4: Shows side view of Mantis Qprep500 sputtering system in the lab with the main parts indicated.

affects the sputtering rate of the individual targets. For the environment conditions the typical parameters were 10^{-9} Torr order as the base pressure before starting the deposition, at room temperature and the gas flow of 18 sccm, standard cubic centimeters per minute, units. The pressure during the deposition process is of 10^{-3} Torr order. These parameters are stabilized during the deposition procedure. The current, voltage, power parameters are kept in range to stabilize the sputtering rate and thus fix the growth rate. The growth rate differs with the target material in use, linked to the DC or RF power.

All of the FM material targets need strong magnets to create a strong magnetic fields to overcome their flux guiding through the sputtering target. While with non-magnetic material targets a lower magnetic field will do. The current DC sputtering was in the range of 74-75 mA and the voltage was in the range 359-389 V with a power of 25-27 Watt. For the RF source the voltage was in the range of 145-209 V and the power was 50 Watt. This range of parameters covers all the samples fabricated in Chapt. 6, 7 and 8.

Changes in the voltage and current values as growing conditions have been made in purpose are in Chapt. 9. The samples which have been studied in Chapt. 6, 7 and 8, are bi-layer thin-films. The growing procedure was intend to deposits layers of FM material with a NM material capping layer. The samples investigated in Chapt. 6, related to the thickness of the capping layer. The NM capping layer thickness was controlled accurately with increasing thickness in the range of couples of Å. While the main concern of the samples investigated in Chapt. 7 was to maintained the same FM and NM layer thicknesses for all the samples. Then apply modifications afterwards using ion-beam irradiation in order to investigates the effect of these interfacial modifications on the magnetic properties of the thin-films. The same deposition procedures, which were used in Chapt. 6 were applied to the samples investigated in Chapt. 8 but, patterned in to nanowires using electron-beam lithography.

As mentioned, the voltage and current values were changed through the fabrication of the samples investigated in Chapt. 9. This was done in order to to control the growth rate, where it is essential for the co-sputtering process of two materials at the same time with correlated sputtering rates. By this correlation, the total sputtering rate of the two target materials will give the total required thickness yet with different material contribution. In these samples a precise deposition procedures was executed regarding the concentration of the two different materials forming boundary mono-layers in FM thin-films in Å thickness range. High level precise growth through low growth rate was established by changing the power feeding to each target. Examples of the deposition conditions can be seen in Table 4.1, 4.2 and 4.3, which shows the growth parameters of bi-layered samples of pure and alloyed FM layers capped with NM material.

All the film thicknesses have been verified by the QCM during the deposition and the accuracy of the QCM was calibrated by x-ray reflectivity measurement. The calibration of the QCM involves the execution of XRR on a fabricated sample with assumed thickness by using the growth rate of the QCM and knowing deposition time. The assumed thickness is compared with the extracted thickness from the XRR and by knowing the difference a correction factor is inserted in the QCM tooling parameter within the depositions controlling program.

TABLE 4.1: Deposition conditions, showing the system parameters of the bi-layer thin-film fabrication from 10 nm Cobalt and 0.2 nm Platinum capping layer.

File No: 50		sample Name: A12			User: Sinan		Date: 23/09/2014	
Sample structure (Å): Co 100/ Pt 2					Temperature= 22.8 °C			
Base pressure (Torr): 8.2×10^{-8}					Growth pressure (Torr): $1.1\times10^{-}3$			
Target and Cusp	Gas flow rate (sccm)	I (mA)	V (V)	Power (Watts)	Deposition rate used (Å/S)	Deposition rate measured (Å/S)	Deposition time (S)	Thickness (Å)
Co 2	17.9	74	369	29	0.2	0.2	500	100
Pt 4	17.9	RF	152	50	0.21	0.21	9.55	2

TABLE 4.2: Deposition conditions, showing the system parameters of the bi-layer thin-film fabrication from 4 nm $\mathrm{Ni_{81}Fe_{19}}$ and 2 nm Platinum capping layer.

File No: 43		sample Name: B5			User: Sinan		Date: 30/05/2015	
Sample structure (Å): $\mathrm{Ni_{81}Fe_{19}}$ 40/ Pt 20					Temperature= 23 °C			
Base pressure (Torr): 3.8×10^{-9}					Growth pressure (Torr): $1.2\times10^{-}3$			
Target and Cusp	Gas flow rate (sccm)	I (mA)	V (V)	Power (Watts)	Deposition rate used (Å/S)	Deposition rate measured (Å/S)	Deposition time (S)	Thickness (Å)
$\mathrm{Ni_{81}Fe_{19}}$ 3	17.9	74	383	29	0.24	0.24	166.6	40
Pt 4	17.9	RF	157	50	0.18	0.18	111	20

TABLE 4.3: Deposition conditions, showing the system parameters of the bi-layer thin-film fabrication from 5 nm [Co$_{60\%}$-Cr$_{40\%}$ 1.25/C 4.75/Co$_{60\%}$-Cr$_{40\%}$ 1.25] and 2 nm Copper capping layer.

File No: 423		sample Name: G73			User: Sinan		Date: 30/01/2017	
Sample structure (Å): Co-Cr 1.25/Co 47.5/Co-Cr 1.25/Cu 20					Temperature= 21.8 °C			
Base pressure (Torr): 7×10^{-8}					Growth pressure (Torr): $1\times10^{-}3$			
Target and Cusp	Gas flow rate (sccm)	I (mA)	V (V)	Power (Watts)	Deposition rate used (Å/S)	Deposition rate measured (Å/S)	Deposition time (S)	Thickness (Å)
Co 2		74	350	14	0.1	0.1		60% 0.753
	17.9						7.53	1.255
Cr 1		RF	129	40	0.067	0.067		40% 0.502
Co 2	17.9	74	378	28	0.2	0.2	237.5	47.5
Co 2		74	350	11	0.1	0.1		60% 0.753
	17.9						7.53	1.255
Cr 1		RF	129	40	0.067	0.067		40% 0.502
Cu 5	17.9	RF	126	50	0.16	0.16	125	20

4.6 Ion-Beam Irradiation

Ion-beam irradiation was carried out to introduce structural changes in some of the samples investigated. These samples are the focus of Chapt. 7, where the usage of ion-beam irradiation brought large change to the magnetic properties. Ion-beam irradiation in short is the irradiation of thin-films through their surface with a beam of ions, which will interact, scattered and intermix with the sample atoms. With using ion-beam irradiation, three main processes take place, which are ion implantation, sputtering and intermixing. The extent of these processes is related with the number of incident ions per unit area of the irradiated sample. The latter is known as the irradiation dose, which is expressed in this thesis in $\mathrm{Ga}^{+}/\mathrm{cm}^{2}$ and/or $\mathrm{pC}/\mu\mathrm{m}^{2}$ units. In Fig. 4.5 a schematic illustration of ion-beam irradiation, with the main three processes, shows the interactions of the ions with the surface, interface and beyond in a thin-film material.

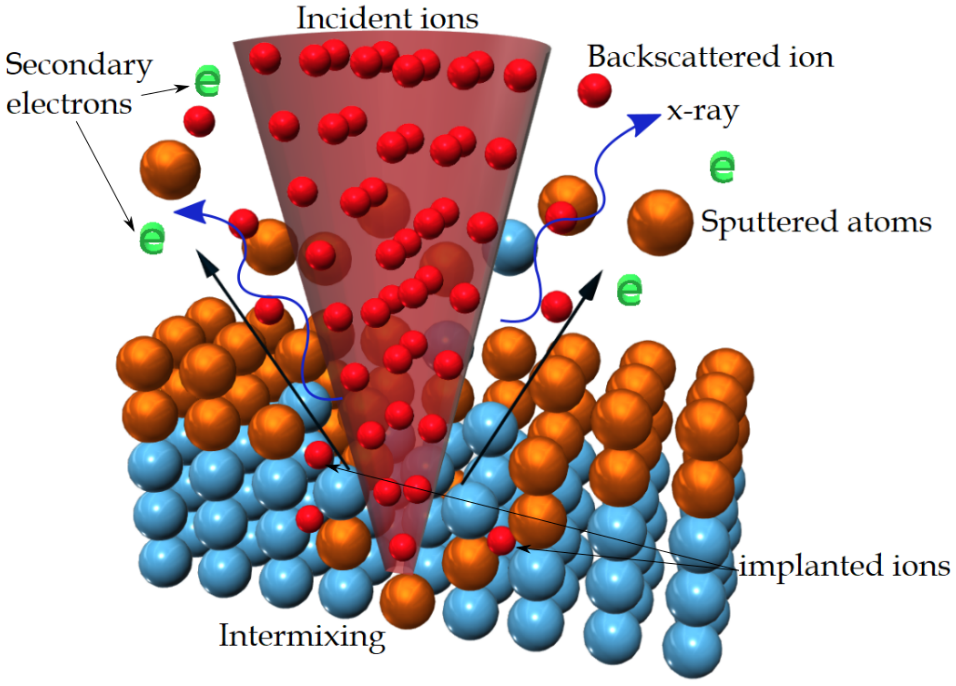

FIGURE 4.5: A schematic illustration of ion-beam irradiation of thin-film showing the main processes and other events such as backscatter ions, electrons and the emission of x-ray as a result.

4.6.1 Ion-Beam Implantation Process

Ion implantation as main process, has an impact on the irradiated sample, where this effect can be seen as structural changes. The change is due to the inclusion of the ions as a defects in the crystal lattice, by their physical existence, or it can be noticed as an intermixing of the implanted ions with the sample material atoms, through a chemical bonding. It is worth noting that the physical effect can leads to stress in the lattice due to the dislocation of the material's atoms or the insertion of the ion in new site in the crystallographic structure in the sample. The initial energy of the incident ion is the main factor.

After that, the incident ion will suffer from multiple scattering events while it propagates in to the sample, which depends on the ion energy. If its energy is less than the replacement threshold then the ion will rest within the sample but, if it is above the threshold energy, then it can backscattered to the vacuum. The concentration of the implanted ions in the sample can be calculated approximately with the Gaussian distribution with the equation below:

$$n(x) = n_0 \exp\left(\frac{(x - R_\mathrm{P})^2}{2\sigma_\mathrm{P}^2}\right) \tag{4.1}$$

Where x is the depth of the implanted ions and R_P its projected range, n_0 is the Gaussian peak concentration and σ_P is the standard deviation. The peak concentration n_0 can be calculated based on the ion dose per unit area, ϕ [95], which is described as:

$$n_0 = \frac{1}{\sqrt{2\pi}}\frac{\phi}{\sigma_\mathrm{P}} \tag{4.2}$$

Eq. 4.2 shows that increasing the irradiation dose leads to a linear increase in the concentration of implanted ions. This will lead to a sample material with high number of defects, or simply it can be considered as an alloy of the initial sample material and the implanted ions. Increasing the implanted Ga$^+$ ions leads to a significant phase shifting in the crystal structure however, the phase shifting occur at high concentration. For example a phase shifting occur in Fe material when Ga$^+$

fraction of around 15% [96]. The maximum doses which have been used in this investigation will produce much less Ga^+ concentration in the targeted material thus, such things are unlikely to happen.

4.6.2 Surface Sputtering Process

The second process which occur implicitly with the ion-beam irradiation is the sputtering of the targeted thin-film surface atoms. This is based on the energy exchange between the incident ions and the surface atoms, where the ions can transfer some of their energy to the atoms at the surface. If the surface atoms gain enough energy from the incident ions to over come their bonding then they can break their bonding with other atoms and escape the surface. The amount of ejected atoms; the sputtered atoms, is related with the amount of the incident ions and the sample surface binding energy. Thus, the amount of sputtered atoms per incident ions, which is also known as sputter yield, is linearly related with the ion energy to over come the surface binding energy and it is non-linearly related with the angle of the ion incidence.

The ion-irradiation incident angle for the samples investigated of this thesis was 90° and the energy of the incident beam was 30 keV. This indicates a possibility to sputter noticeable amount of the atoms from the surface of the samples investigated [97]. By using the stimulation program (TRIDYN) for ion-solid interactions for $Ni_{81}Fe_{19}$/Au irradiated with Ga^+ incident beam of energy 30 keV a prediction of the sample surface sputtering of atoms can be indicated. This can be seen in Fig. 4.6, where the recession of the sample surface, due to surface sputtering, and the reduction of the capping layer thickness are plotted as a function of the ion-beam irradiation dose [98–100].

The prediction of such irradiation shows that ≈1 nm of the surface is sputtered from $Ni_{81}Fe_{19}$ sampled capped with 5 and 3 nm of Au. This prediction is also verified by a study on $Ni_{80}Fe_{20}$ thin-films [101]. This effect was noticed in the investigation in Chapt. 7, a bi-layer of $Ni_{81}Fe_{19}$ 10 nm/ Pt 3 nm irradiated with Ga^+, where a Pt capping layer thickness reduction was indicated. More information regarding

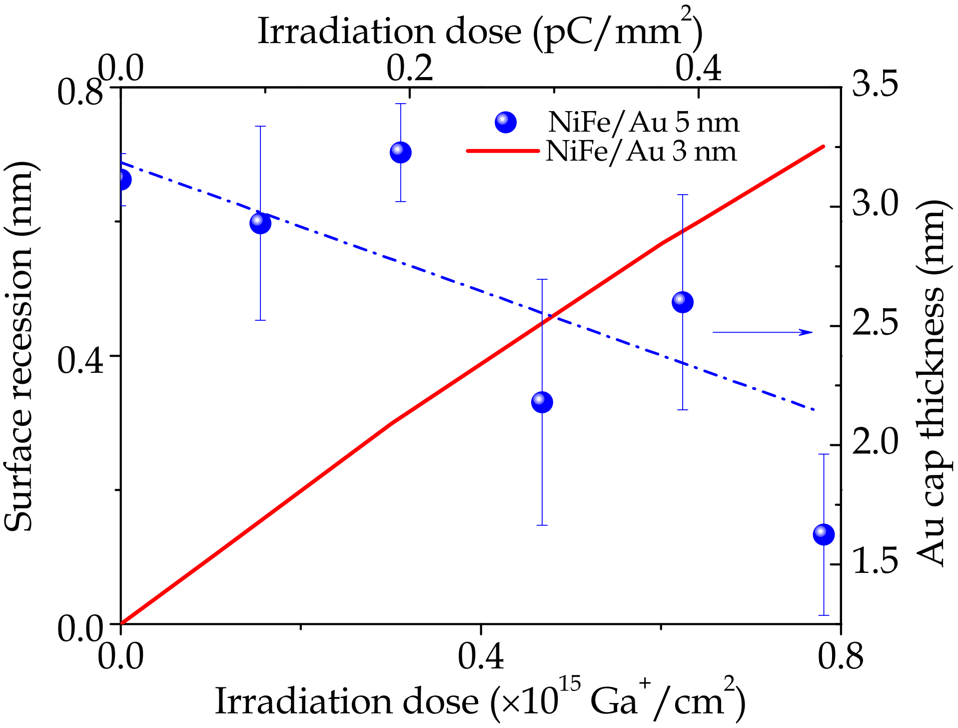

FIGURE 4.6: Recession of surface and the capping layer decreasing due to the surface Au atoms sputtering as a function of ion-beam irradiation dose for bi-layer thin-films the dashed line are guide to the eye, adapted from [99].

the TRIDYN simulation program can be seen in [102].

4.6.3 Interface Intermixing and Thin-Films Alloying Process

Beyond ion implantation and surface atoms sputtering, the arrangement of the atoms and the nature of the grain orientation inside the thin-film can lead to channelling effect. Due to this channelling effect the incident ions can lose their energy by travelling deep inside the sample. As a result of this, sputtered atoms and damage in the sample can be reduced significantly [103]. This also can extend the effect of the incident ions deeper into the sample and far from the surface. Hence, atoms located below the surface can interact with the travelling ions in to the sample. By this interaction these atoms can gain momentum from the ions, thus they will be relocated and intermixed within the sample. When the sample is bi-layered from two different materials this effect is more noticeable, due to the relocated atoms across the interface of the adjacent layers. This is the third main process of ion-beam irradiation, which is know as intermixing, its extent is a function of ion-beam irradiation dose.

Intermixing can be described by transferring some of the incident ion's energy to the targeted atom, by which the atom will gain energy will help to travel across the interface. The Ballistic model can describe this mixing, which is ion-beam irradiation dose based, head-on collision dependent and temperature independent. By using this model, it can be shown that targeted atoms can recoil deeply in to the material with ≈50 nm in forward-momentum model. However, this model is not that common and it fails to explain the isotropic intermixing broadening which take place by ion-beam irradiation [104–106]. This model can be used with some expanding for the collisions events, where additional collisions can be added between the atoms themselves. Due to these additional events, energy will be lost gradually without increasing the displacement distance. This model is know as cascade mixing, it is more diffusion-like mixing where the relocated atoms follow random paths moving across the interface. This model is more comprehensive in explaining the isotropic mixing and shows a gradient concentration of the relocated atoms as they are displaced farther beyond the interface [107].

The cascade mixing model uses a similar equation to thermally diffusion to describes the mixing as

$$Dt = \frac{n\alpha^2}{6} \tag{4.3}$$

where in the cascade mixing model equation jump distance, α, is replaced by the range distance, r, of the displaced atoms and the number of jumps, n, with number of the displacement per atom, dpa, thus, the diffusion cascade equation will be:

$$D_{\mathrm{c}}t = \frac{dpa(X)\langle r^2\rangle}{6} \tag{4.4}$$

The number of the displacements per atom dpa is related to the damage energy unit length, F_{D}, the atomic displacement energy, E_{d}, the ion-beam irradiation dose ϕ and the atomic density, N, by:

$$dpa = \frac{2F_{\mathrm{D}}\phi}{5e_{\mathrm{d}}N} \tag{4.5}$$

Substituting Eq. 4.5 in 4.4 will give the final cascade diffusion-like mixing as a function of ions beam irradiation as follow:

$$D_{\mathrm{c}}t = \frac{F_{\mathrm{D}}\langle r^2\rangle\phi}{15NE_{\mathrm{d}}} \tag{4.6}$$

There are other models [106, 108] which have been implemented in order to explain ion-beam intermixing process. All of them are give a similar results with the same mixing dependence upon the ion-beam irradiation dose ϕ and the damage energy F_{D}.

Experimentally the interface broadening effect can be seen in a thin-film sample by x-ray reflectivity measurements, where the interface width is changing due to the ion-beam irradiation. Fig. 4.7 shows XRR result for $Ni_{81}Fe_{19}$ 20 nm/Au 2.5 nm, where the interface width increases as a function of ion-beam irradiation dose.

Also it shows the contribution of both interface factors; topological and chemical to the total interface width. TRIDYN simulation shows a similar correlation, of the squared irradiation induced interface width, to the measure chemical intermixing by the XRR measurement. This gives an indication that increasing ion-beam irradiation will effect mainly intermixing, where the topological roughness almost has no change during the irradiation process.

The results shown in this section provide a structural basis for the explanation of the magnetic damping behaviour of the thin-film samples which have been investigated in Chapt. 7. These samples have been fabricated with the same FM material; $Ni_{81}Fe_{19}$ but, with 10 nm thickness and capped with 3 nm of Pt. The modification were done using ion-beam irradiation with a higher dose range. Noting that Pt and Au have a similarity thus, the same main three processes take place but with extended effect.

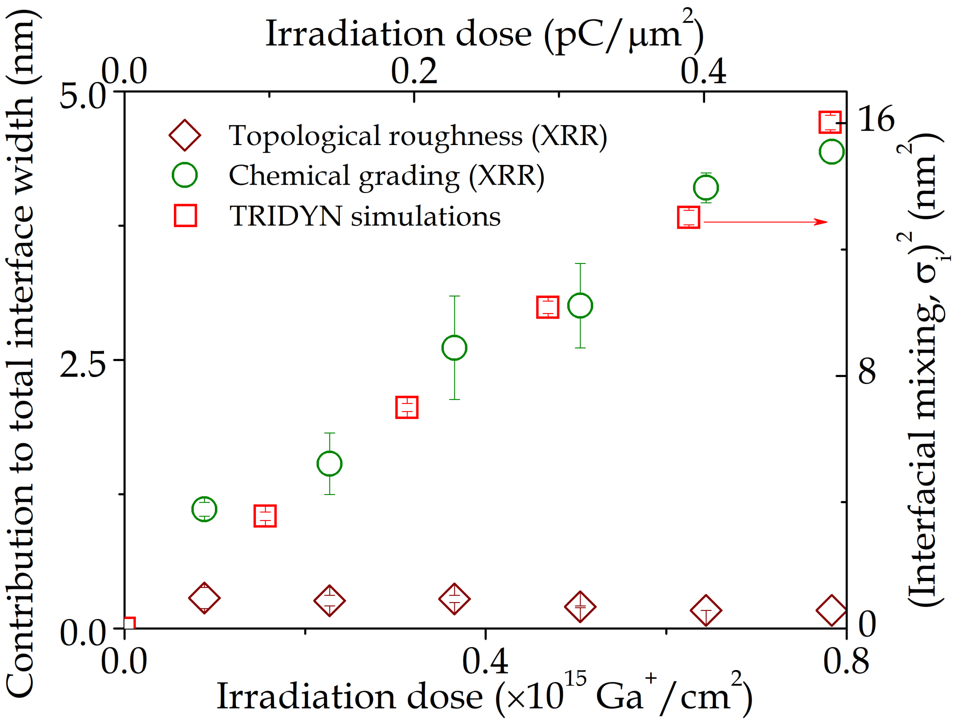

FIGURE 4.7: The effect of ion-beam irradiation dose on topological roughness and chemical intermixing for Ni_{81}Fe19 20 nm/Au 2.5 nm thin-film by XRR. The same effect extracted from TRIDYN simulation, which shows agreement with the XRR results, the XRR and the simulation results adapted from [99] and [109] respectively.

4.7 Ion-Beam Irradiation Effect on Alloying Bi-Layer Thin-Films

In the previous section, intermixing of the interface was discussed as a function of the ion-beam irradiation effect. The broadening of the interface is shown in term of experimental and simulation results as examples. However, the maximum dose which have been show previously is 0.8 Ga^+/cm^2, $\approx$ 0.5 $pC/\mu m^2$, which gives $\approx$ 5 nm of interface mixing. The thermodynamic effect used to explain the interface mixing ignores the material chemical properties. While this effect considers the preference of any two material A and B to form an AB alloy. In the thermodynamic case of preferential mixing, a graded alloy layer is expected to develop between the two layers, resulting in an enhancement to the interface width [110, 111]. In the case of Au capping layer on top of $Ni_{81}Fe_{19}$ a de-mixing effect is likely to be a competing with the mixing effect for Au mixed in $Ni_{81}Fe_{19}$ [112, 113]. For the samples investigated in this thesis the capping layer was Pt.

4.7.1 Ion-Beam Irradiation Effect on Magnetic Properties.

The effect of the main three processes of ion-beam irradiation was discussed and these processes affect the magnetic properties of the thin-films. Ion implantation is the least effective process, however the surface sputtering and the intermixing processes have a greater impact on the magnetic properties of the irradiated thin-films. They can change the magnetic properties of both FM and NM layers in thin-films. By surface sputtering and interface mixing, ion-beam irradiation led to the modification of the local environment and change the moment of the irradiated material. This effects will change the saturation magnetisation in general hence, will change other magnetic properties [114]. This effect can break through the changing of the grain size because, ion irradiation affects the grain growth of the irradiated material by the incident ion's energy. The energy exchange with the material will change the total magnetic moment of the arranged atoms in the material and thus, will changes the saturation magnetisation of the material [115].

4.8 Summary

The chapter discusses of the production procedures of the samples investigated in this thesis. This includes the preparation and the deposition of thin-films with effects regarding changing the deposition conditions. Next is the modification of the samples investigated using ion-beam irradiation and the effect of this process on the samples structural properties. Finally, the impact of structural effects on the magnetic properties is introduced as it required later.

Chapter 5

An Introduction and Theory for Magnetic Damping Phenomena in Ferromagnetic Thin-Films and Multilayer

5.1 Introduction to Magnetic Damping

Magnetisation precession and magnetic damping were discussed in Chapt. 2 with damping detailed using the dissipation of magnetic energy via uniform and non-uniform precession modes to the lattice. In this chapter a deeper explanation is presented regarding this topic, with a comprehensive description of the main mechanisms, both intrinsic and extrinsic that explain damping. This is done first by reviewing and summarising the literature with the aim of giving a clearer understanding of the damping mechanisms. The next section shows the recent experimental work and highlights the limitations of this work, which are addressed by the research in this thesis.

A variety of damping studies have been reviewed covering bulk, bi- and multi-layered, and doped thin-film systems. This chapter is a part of a review article paper published in the Institute of Physics publication, *Journal of Physics D: Applied Physics* (J. Phys. D. Appl. Phys.), [116].

5.2 Intrinsic Damping and Landau-Lifshitz-Gilbert

A key part of precessional damping in a ferromagnetic system is termed the intrinsic damping mechanism, which is related to the spin-orbit coupling. The coupling between the electrons spin- and the orbital-angular momenta links the precessing spin magnetic moment to the lattice as described in Chapt. 2. Without this type of coupling the $k = 0$ 'uniform mode' magnon would not be damped [47, 117–119]. This intrinsic mechanism is the simplest route to dissipate energy. The link between SOC and magnetic damping is explained theoretically by Kambersky using SOC and electron-hole recombination, which dissipates the energy to the lattice [40, 120–122]. This model focuses on the variation of the Fermi energy levels with two sources giving rise to the total damping. The first is the whole Fermi surface, which represents standard yet minimum contribution to the total damping. The second represents "special areas" which in total give a larger damping contribution [40, 120–122]. The model uses the Landau-Lifshitz-Gilbert equation to explain that these "special areas" or "hot regions" [43] result from the effect of SOC, which leads to degenerate band-crossing near the Fermi surface. These "hot regions" have k-space pairs of eigenstates with energies close to the Fermi level [6, 48].

A microscopic view of the electronic interactions was explained by Sparks [47]. This process involves the annihilation of uniform mode magnons and the creation of electron-hole pairs that scatter to the lattice leading to the energy loss, and thus magnetic damping [6, 39, 44, 48, 123]. This explains magnon-electron scattering through similar mechanisms, which suggest that damping is affected by electronic transitions into states close to the Fermi energy. The availability of such states determines the damping rate.

However, there are two suggested modes of electronic transition that can occur in bulk FM systems depending on the mode. The first is when magnon annihilation leads to electron-hole pair generation that occupy the same band (intraband). The intraband transition links damping with temperature inversely, which means that through this mode damping decreases with increasing temperature. The dependence of this mode on temperature mirrors metallic phenomena, hence it is termed 'conductivity-like'. The second mode also involves magnon annihilation leading to electron-hole pair generation, but in this case the pairs occupy different bands (interband). This also shows a temperature dependence, but has the opposite dependence so it is termed 'resistivity-like' [6, 40, 122, 124–127]. These modes shows that the damping is correlated with the density of states, showing the importance of the $3d$ band in ferromagnets, and that it strongly depends on the spin-orbit parameter for both the intraband and interband processes [6, 123, 127–129].

The dissipation of the energy via the the intrinsic mechanism is described through the magnetisation precession in the time domain by Landau & Lifshitz [130]. This was presented in a general equation:

$$\frac{\partial \mathbf{M}}{\partial t} = -\gamma \mathbf{M} \times \mathbf{H}_{\mathrm{eff}} - \frac{\lambda}{M^2} \mathbf{M} \times \mathbf{M} \times \mathbf{H}_{\mathrm{eff}} \tag{5.1}$$

where gyromagnetic ratio (γ) and the phenomenological relaxation parameter (λ), are the inverse time units and $\mathbf{H}_{\mathrm{eff}}$ is the effective magnetic field. Later, this equation was modified by Gilbert to produce the Landau-Lifshitz-Gilbert (LLG) equation

$$\frac{\partial \mathbf{M}}{\partial t} = -\gamma \mathbf{M} \times \mathbf{H}_{\mathrm{eff}} + \frac{\alpha}{M} \mathbf{M} \times \frac{\partial \mathbf{M}}{\partial t} \tag{5.2}$$

It can be seen that α the "dimensionless" Gilbert damping parameter, $\alpha = \lambda/\gamma M$, is a parameter which describes the damping of the system.

Eq. 5.2 suggests that there is an impact on γ from the magnetic precessional effect. This effect is small enough in many materials to be neglected. Thus both Eq. 5.1 and 5.2 were used to represent the precessional damping behaviour in any giving FM system. The usage of these equations is more related with their practical suitability, depending on the computation and modeling processes. For example, having $\partial \mathbf{M}/\partial t$ on one side in Eq. 5.1 makes the equation easy to solve [9, 13].

Explaining LLG equation further, the first term represents the magnetisation precession about $\mathbf{H}_{\mathrm{eff}}$ [131–134]

$$\frac{\partial \mathbf{M}}{\partial t} = -\gamma \mathbf{M} \times \mathbf{H}_{\mathrm{eff}} \tag{5.3}$$

The presence or absence of a negative sign in Eq. 5.3 is linked with the definition of the direction of the applied torque on **M**, which indicates the precession direction. This is done recently by considering $\gamma > 0$ to over come the sign issue. The second term of the LLG equation represents the 'viscous' damping force perpendicular on **M**, by which the magnetisation magnitude is constant, as shown in Fig. 5.1.

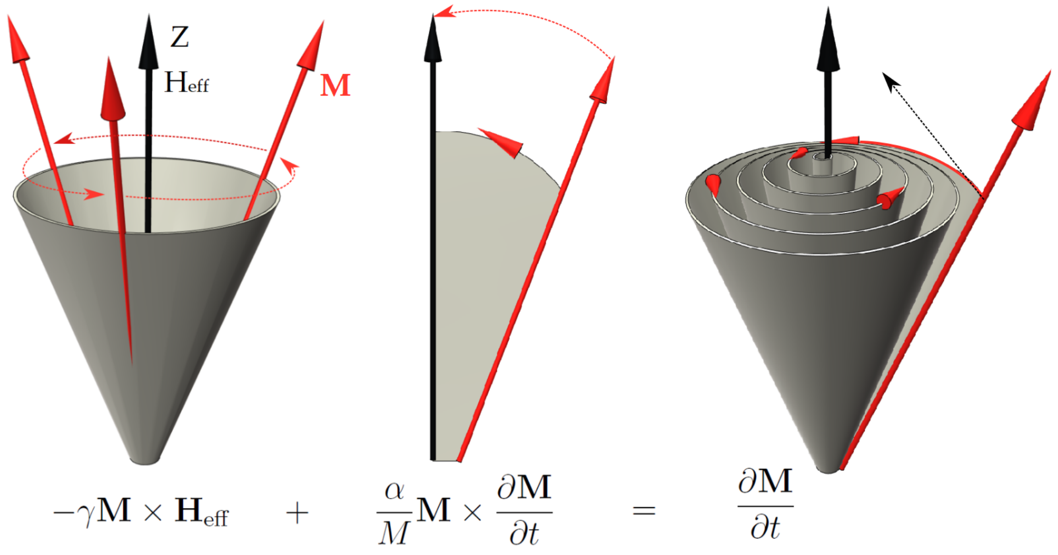

FIGURE 5.1: Illustration of damping process of the magnetisation according to Landau-Lifshitz-Gilbert LLG model, precession as the first term and the damping force as the second term, where the magnitude of the magnetisation is constant.

This term adds a perpendicular torque to the magnetisation that moves it towards the effective magnetic field by reducing the rotating diameter gradually.

$$\frac{\alpha}{M}\mathbf{M} \times \frac{\partial \mathbf{M}}{\partial t} \tag{5.4}$$

The value of α is the indication factor of how fast the magnetisation precession damped in any FM material [39].

The LLG equation provides a description of the macrospin but, in order to describe the effect of the dynamic precession on each individual moment **m**, the LLG equation can be expressed as:

$$\frac{\partial \mathbf{m}}{\partial t} = -\gamma \mathbf{m} \times \mathbf{H}_{\text{eff}} + \frac{\alpha}{m}\mathbf{m} \times \frac{\partial \mathbf{m}}{\partial t} \tag{5.5}$$

The first term shows the interactions between moments and $\mathbf{H}_{\text{eff}}$. Furthermore all moments $\mathbf{m}$ precess at the same frequency and are in phase; in what is termed the uniform precession mode. The second term shows that α affects individual moments $\mathbf{m}$ rather than on the macrospin $\mathbf{M}$.

The LLG equation for damped uniform precession is valid for bulk and pure FM materials however, for doped or capped FM materials and thin-film with non-magnetic (NM) elements some modifications are required for a further dissipation. These modifications should be able to describe the effects of other mechanisms which can exist with the NM materials present. It is worth mentioning that the damping enhancement, which results from doping and capping with NM material, is due the additional energy dissipation channels that lead to increasing damping. Some of these effects are associated with interface(s), and with spin-wave and spin-current propagation from FM into other layer(s) or with the modification of the energy levels which increases the energy dissipation to the lattice and hence damping[46, 135, 136].

However, beyond the intrinsic nature of these effects the addition of NM material can lead to extrinsic damping effects. By these effects the energy is transferred between uniform and non-uniform precessional modes beyond the simplest picture of intrinsic Gilbert damping of a single precessing macrospin.

5.3 Extrinsic Damping and Bloch-Bloembergen Equation

As the second main part of magnetic damping, extrinsic mechanisms represent the non-uniform modes magnons. It is linked with energy transformation from the uniform to non-uniform precessional modes and is often termed “two-magnon scattering”. Through this mechanism two counter propagating spin-waves are required with different spin wavenumber k. The “extrinsic” mechanisms is one of the terms which adds complications to the image of the energy dissipation through damping.

Extrinsic damping is associated with inhomogeneities, which are present within a ferromagnetic system. Microscopic crystalline variations in thin-films; such as point- [137] and line-defects [138] are considered as sources of extrinsic mechanism, local structural defects arising from impurities, non-uniformity of the sample surface, sample thickness variation and strain due to lattice mismatches, as well as local variations of the magnetic properties are all responsible for extrinsic mechanism. Systems with a low density of inhomogeneities have a uniform precession, but when the density of inhomogeneities within a ferromagnetic system is higher the precession can occur in a number of local resonant modes [6, 44, 46, 118, 138–140].

It has been mentioned that magnon-electron scattering can produce non-uniform magnons. This occurs when electrons scattered by non-spin-flip collisions (transitions between states having the same spin), cause a uniform mode magnon to be annihilated and a non-uniform magnon to be created. This can be seen when the exchange is anisotropic e.g. in the bulk of a single magnetic layer [13]. The broadening of the measured ferromagnetic resonance response is considered as an indication of damping involving these effects [42, 44, 46, 47, 118, 141].

In an a ideal system thin-film can be single domain, however many real systems are inhomogeneous with multiple magnetic domains, this will affect the energy loss. In these real systems the domain walls, which are separate the magnetic domains as a result, the interaction of the magnetisation precession in each domain with each other will excite the extrinsic two-magnon mechanism. Determining the enhancement of the damping though the extrinsic effect is hard to establish. This is because of the complex contribution of both intrinsic and extrinsic mechanisms. For example, the broadening of the resonance peak in ferromagnetic resonance (FMR) is the result of the uniform mode and the contribution of two-magnon scattering [42, 44, 47, 118, 142].

A theoretical description of the two-magnon scattering, with the attempt to quantify it in similar way to the LLG equation but taking in to account non-uniform modes was proposed by Bloembergen. His work was based on Bloch's dynamical proposal in his effort to explain nuclear magnetic resonance, leading to the Bloch-Blombergen (B-B) equation [13, 143, 144]. This equation describes the energy dissipation through two major relaxation channels to the final thermal bath of the lattice [44, 145].

$$\frac{\partial \mathbf{M}}{\partial t} = -\gamma(\mathbf{M} \times \mathbf{H}_{\text{eff}}) - \frac{M_x}{T_2}\hat{e}_x - \frac{M_y}{T_2}\hat{e}_y - \frac{M_z - M}{T_1}\hat{e}_z, \tag{5.6}$$

Here $\hat{e}_{x,y,z}$ are unit vectors in the x, y, and z directions, respectively, T_1 is the longitudinal (spin-lattice in NMR) relaxation time and T_2 the transverse (spin-spin) relaxation time. It can be seen that the B-B equation is not limited to the uniform mode but, it includes the non-uniform mode also. For comparison with Eq. 5.1 and 5.2 the B-B equation describes the transversal in-plane components of the magnetisation M_x and M_y. The difference between Eq. 5.6 and Eq. 5.1 and 5.2 in the damping term, is that the magnetisation projection along the the z-axis remains constant. It is suggested that the energy is dissipated via the x and y components of the magnetisation [44, 46, 47, 144]. This dynamic description is more reliable regarding the different modes, but the description lacks the individual moments as covered in LLG equation is a drawback.

It can be seen from Fig. 5.2, in comparison with Fig. 5.1, the difference between the two models of magnetic precession, where for B-B model the longitudinal process satisfies the condition of conservation of angular momentum, while the transverse component is lost. The description being limited to a certain type of magnon scattering in B-B equation is another issue, even when it is capable of explaining more than the LLG equation regarding non-uniform mode [13].

In spite of the complexity that is added by extrinsic mechanisms, magnetic damping motion has two main pathways; intrinsic and extrinsic. It can be seen that each mechanism can have its own measurable effects by which they impact the total damping. Some of these effects are changeable according to the host FM and the additional NM material, or affect both intrinsic and extrinsic mechanisms. For example, spin-pumping and d-d hybridization. These and others effects are covered in order to understand the current theoretical explanation of damping phenomena.

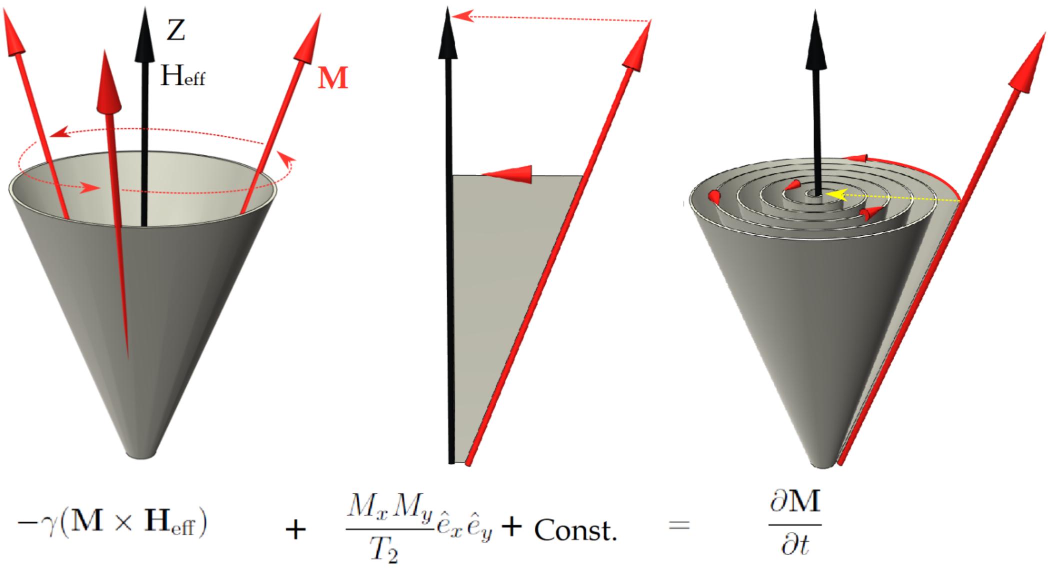

FIGURE 5.2: Illustrations of the Bloch-Bloembergen (B-B) gyromagnetic process equation in the first term, the Z-component of the magnetisation remains constant, but the effective magnetisation reduces according to the second term.

5.4 Intrinsic and Extrinsic Damping

One of the underlying effects, in magnetisation damping is the angular momentum dissipation in the form of a "spin-current" in thin-film multilayer systems. This effect takes place when the FM materials are coupled with adjacent NM material layers, most effectively with heavy metals. The mechanism by which this effect occurs is that a spin-current transmits from the ferromagnetic layer to the non-magnetic heavy metal layer through the interface, which is known as "spin-pumping". The transmitted energy carried by the spin-pumped current dissipates in to the NM layer by spin relaxation processes, due to the non-equilibrium spin population in this layer as it is shown in Fig. 5.3.

It may seem that spin-pumping is an additional effect, arising externally to the FM material, but the spin-orbit interaction is the reason that spin-pumping can be be considered as an underlying intrinsic effect [129, 134]. Another factor is that calculation of this effect can be done under the FMR conditions, where the density of the pumped spin (j_s) in DC form can be calculated [146] using

$$j_s = \frac{\omega}{2\pi} \int_0^{2\pi/\omega} \frac{\hbar}{4\pi} g_{\text{eff}}^{\uparrow\downarrow} \frac{1}{M^2} \mathbf{M} \times \frac{\partial \mathbf{M}}{\partial t} dt \tag{5.7}$$

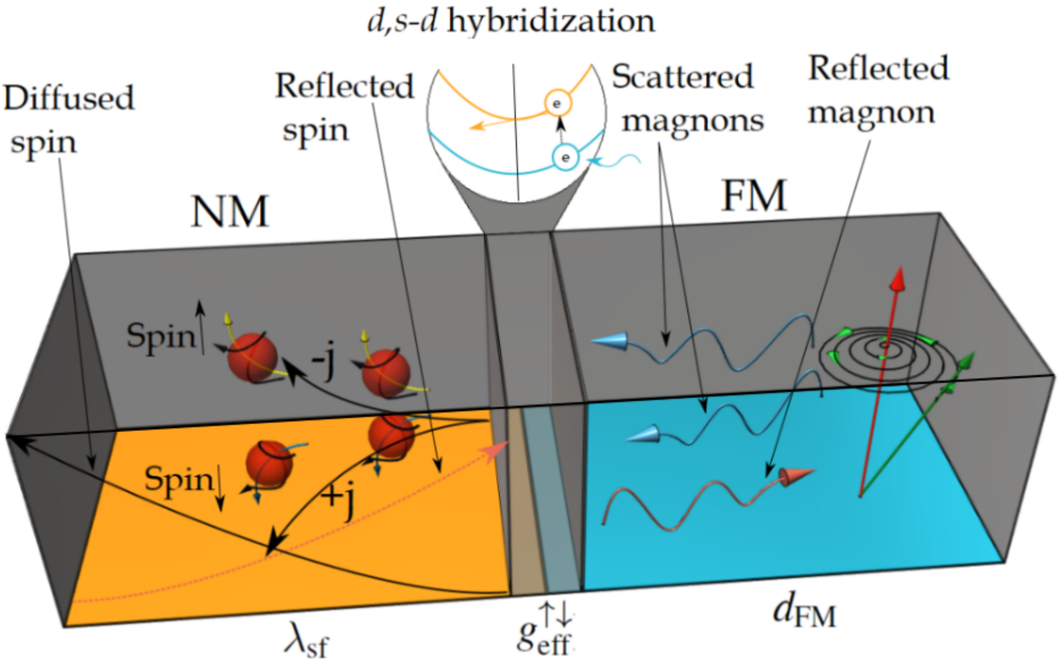

FIGURE 5.3: Illustrates the spin-pumping effect in typical FM/NM thin-films with the effective spin-mixing conductance $g_{\text{eff}}^{\uparrow\downarrow}$ at the interface and spin diffusion length λ_{sf}.

Where ω is the angular frequency of magnetisation precession and $g_{\text{eff}}^{\uparrow\downarrow}$ is the effective spin-mixing conductance at the interface, which is discussed next. It can be seen from the equation, the similarity of the spin-pumping contribution to the precessing magnetisation $M\frac{d\mathbf{M}}{dt}$ in the NM layer to the damping term of the LLG equation. The contribution of the spin-pumping can therefore be also calculated from the dimensionless Gilbert damping parameter α. This enhancement is inversely dependent on the ferromagnetic layer thickness (d_{FM}), which is explained due to the interfacial nature, which has a huge impact on this effect [147] as

$$\alpha = \alpha_0 + \frac{g\mu_{\text{B}}}{4\pi M d_{\text{FM}}} g_{\text{eff}}^{\uparrow\downarrow} \tag{5.8}$$

The term "effective interfacial spin-mixing conductance", $g_{\text{eff}}^{\uparrow\downarrow}$, is an integrated term with spin-pumping, which measures the effectiveness of the spin-current pumping. By this term the spin states at the interface of FM/NM layer is understood by the conductance at the interface itself. Also $g_{\text{eff}}^{\uparrow\downarrow}$ depends on the spin rotating along the magnetisation axis which is known as mixing conductance. Spin-mixing conductance is a description of variety of events as shown in the same figure. 5.3. These events take place at the FM/NM interfaces at the same time as the energy bands for electrons of FM and NM material interact, where the coupling of the electrons in the conduction band with the electrons of the exchange split d-band increases the spin-pumping [129]. The pumped spins diffuse in the NM layer or flow-back as unrelaxed spin-current into the FM layer [147–151].

The final state of the injected spin through the interface is shown in Fig. 5.3 with three possibilities; either have full decay, diffuse and relax in the NM layer or flow back as unrelaxed spin to the FM layer or have a mix between these states [6, 128, 129, 134, 145]. The term spin diffusion length (λ_{sf}) represents the length scale at which pumped spin-current diffuses in to the NM layer [152, 153]. This effect can be found experimentally through measurements of the spin resistance, which is a quantity showing the remaining spin-current after crossing the interface by using a spin-dependent Ohmic law. The damping contribution of the NM material to the bulk system can be calculated in terms of λ_{sf}

$$\frac{\alpha'_{\infty}}{\alpha'} \approx 1 + \left[\sqrt{\epsilon}\tanh\left(\mathrm{d}_{\mathrm{NM}}/\lambda_{\mathrm{sf}}\right)\right]^{-1} \tag{5.9}$$

where α'_{∞} is the Gilbert damping enhancement assuming infinite spin-flip rate in the normal metal, α' is the additional damping constant due to the interfacial coupling, ϵ is the spin-flip probability, d_{NM} is normal metal thickness [129]. The NM materials that have the shortest spin-diffusion length are ideal spin-sinks. The value of this length is related to the spin-orbit interaction and the spin-flip rate of the NM material [152, 153]. The damping enhancement depends on the NM material and the interface atomic intermixing between the FM and NM layers through the effective spin-mixing conductance $g^{\uparrow\downarrow}_{\text{eff}}$.

The next effect found at the interface of the FM/NM thin-film arises from doping of the FM material with NM elements that leads to d-d or s-d hybridization. Band theory and exchange interaction can provide an explanation for this effect, though the s-d or d-d exchange interactions, or by Ruderman-Kittel-Kasuya-Yosida (RKKY) interaction [154–156]. For more clarity regarding the s-d and d-d exchange explanation, this effect is the result of "magnetic spin exchange-coupling" of the $3d$ electrons in FM material [156] to the itinerant $4s$ or $3d$ electrons respectively. This kind of exchange is due to the electronic hybridization. It takes place at the FM/NM interface. This has been shown by theoretical calculations of the spin density perturbations due to the electron magnetic moment interaction [41, 155, 156]. This effect has a major impact on the spin-flip scattering across the FM/NM interface and hence the spin-mixing conductance and spin-pumping [155, 156]. The damping enhancement contribution due to d-d hybridization varies with the adjacent or doping NM material [6, 156]. However, in the case of doping there are also extrinsic channels for spin-wave relaxation. Damping enhancement, due to doping of a FM material with a NM transition metal or rare-earth is explained through the relaxation of a spin-wave by local changes to the exchange interaction [141, 157]. The d-d hybridization effect can be seen as the main source for the intrinsic mechanism however, it may also be a source for the extrinsic mechanism. This is explained in more depth in Chapt. 6.

It is important to get better knowledge of the underlying correlation of these effects in order to measure or control damping as it is established in Chapt. 9. It is also beneficial to understand the relation between the electron distribution and enhancement of damping in both mechanisms. The separation between these two mechanisms was the focus of many studies by calculating the damping enhancement value from each separately [6, 48, 86, 147] but, the complication of detecting each effect individually is one of the main issues which make the separation between intrinsic and extrinsic not a straightforward process. This is discussed in Chapt. 3.

5.5 Damping Description and Calculation

In general these are based on the direct magnetic dynamic precession and the spin dynamic motion respectively. The first method is represented by the Kittel formula [81]

$$f = \frac{\gamma}{2\pi}\sqrt{H_{\mathrm{eff}}^{\mathrm{Res}}(H_{\mathrm{eff}}^{\mathrm{Res}} + 4\pi M_{\mathrm{eff}})}. \tag{5.10}$$

were f is the resonance frequency, it is related to material parameters, $H_{\text{eff}}^{\text{Res}}$ is the effective field at which resonance occurs and M_{eff} is the effective magnetisation. The latter is related with many terms, including saturation magnetisation M_{s} and effective surface/interface anisotropy constant, K_{S}.

The principle way of measuring damping is by knowing the resonance field linewidth (ΔH), which is usually taken as the full-width-at-half-maximum (FWHM) of the magnetic field-swept absorption. This can be done by using an empirical relation [158] through field domain measurements of ferromagnetic resonance

$$\Delta H = \Delta H_0 + \frac{4\pi\alpha}{\gamma} f, \tag{5.11}$$

where ΔH_0 is termed the "inhomogeneous linewidth" and represents the extrinsic contributions to the damping of the precessing magnetisation. The intrinsic contribution to the linewidth is derived from the LLG equation in the limit of small α [159]. For a frequency-swept absorption measurement, the FWHM of absorption vs frequency may be separated in a similar fashion [82]. The equation of the frequency linewidth (Δf) can be written

$$\Delta f = \frac{\gamma}{2\pi} \alpha (2H + 4\pi M_{\text{eff}}) \tag{5.12}$$

It can be seen that in this equation the extrinsic damping is not well distinguished, which is responsible for the different value of the measured α. There is another way to find the linewidth for either H or f sweeps, by using the conversion equation. It has been suggested that this is valid only when the FM material has negligible inhomogeneous extrinsic damping contribution [83].

It is worth noting that the field derived linewidth is the derivative of the LLG equation (describing intrinsic damping only), as shown [44, 160, 161]:

$$\Delta H_{\text{LLG}}(\omega) = \frac{2}{\sqrt{3}} \frac{G}{\gamma^2 M} \frac{\omega}{\cos\beta}, \tag{5.13}$$

where β is the angle between the equilibrium magnetisation vector and the applied field. Comparing the field linewidth with the B-B equation shows different dependence . The linewidth ΔH_{BB} from the B-B equation (Eq. 5.6) gives the linewidth due to the transverse relaxation as [44, 162]:

$$\Delta H_{\mathrm{BB}}(\omega) = \frac{\partial H_{\mathrm{Res}}}{\partial \omega_0} \frac{1}{T_2}, \tag{5.14}$$

Where H_{Res} is the applied magnetic field at resonance, and $\partial H_{\mathrm{Res}}/\partial \omega_0$ may be obtained from a suitable version of the Kittel formula. Eq. 5.14 is more representative of the two-magnon scattering, while Eq. 5.13 is limited to the intrinsic mechanism.

The second method to find damping is by using a quantum mechanical equation of spin dynamic motion which is related to the LLG Eq. 5.3 [163]. The equation of motion for a single spin can be written as:

$$\frac{\partial}{\partial t} \langle \mathbf{S} \rangle = \frac{g\mu_B}{\hbar} (\mathbf{S} \times \mathbf{B}). \tag{5.15}$$

In the macrospin model the magnetisation **M** is supposed to be uniform throughout the sample. The relation between **S** and **M** can be written as

$$\mathbf{M} = \frac{g\mu_B}{\hbar} \langle \mathbf{S} \rangle \tag{5.16}$$

5.6 Observations of Damping in Thin-Film Systems

A lot of studies have focused on ferromagnetic resonance and damping of the transition metal ferromagnets such as Fe [119, 127, 164–172], Ni [119, 127, 173–175] and Co [5, 75, 119, 127, 151, 164, 170, 176–178]. These elements have been studied as alone, capped or doped with other materials. Adding another material can prevent surface oxidation in the FM material and change the damping value. All of these reasons depend on the magnetic and mechanical properties of the NM material such as density of state (DOS), electron status on the s and d shell and the material miscibility. In order to establish any of these goals, choosing the right material is required. In general Cu, Au, Si and maybe Ta are considered to have the minimum effect on damping of a FM material as capping layer. On the other hand other materials have an impact to different extents for both capping and doping. Studying damping in bulk systems shows that the main mechanism is intrinsic damping, even though the two-magnon scattering is there, but phonons have the largest effect in these systems [179]. In ultra thin-film system two-magnon scattering is more important however, the scattering range occurs within hundreds of nanometres. This is because of the inhomogeneities features within the ultra thin system will acting as sources for the spin-wave and magnetisation precession. But, these sources will be separated by a relativity large distance, hence two-magnon scattering may be detected as uniform spin precession. Thus, scattering mode considered in the uniform mode range with wavelength magnitude of magnon $k \approx 10^4$ cm^{-1} [44].

5.6.1 Damping in Ferromagnetic Materials

It has been found that damping in FM thin-film depends on two main factors the FM material type and the film thickness, d_{FM}. Regarding the first factor, studies show that Fe has the lowest damping value followed by Co, and Ni has the highest value. Alloying and doping with different concentrations are discussed in Sec. 5.8 but, $\mathrm{Ni_{81}Fe_{19}}$ which is known as Permalloy is a common ferromagnetic material particularly the alloy ratio 81:19 [5, 119, 180–182]. In this section, $\mathrm{Ni_{81}Fe_{19}}$ is discussed along with Co, Ni and Fe because there is no changing in alloying ratio. The damping dependence on film thickness, d_{FM}, was widely studied [119, 180–182] and shows the same thickness dependence. Fig. 5.4 summarizes the damping data for a range of elemental thin-films and $\mathrm{Ni_{81}Fe_{19}}$. It can be seen in Fig. 5.4 that damping value of $\mathrm{Ni_{81}Fe_{19}}$ is between the values for Ni and Fe. The figure shows a reasonable results for damping dependence on FM type, the high values of damping are linked with the magnetic anisotropy in such systems.

5.7 Damping in Bi-Layer and Multilayer Thin-Films

In bi-layered FM/NM, trilayered NM/FM/NM and other multilayers the damping can be affected by several factors such as the thickness of the FM, the associated NM layers, the interface properties and if there is a spacer layer between the FM and the

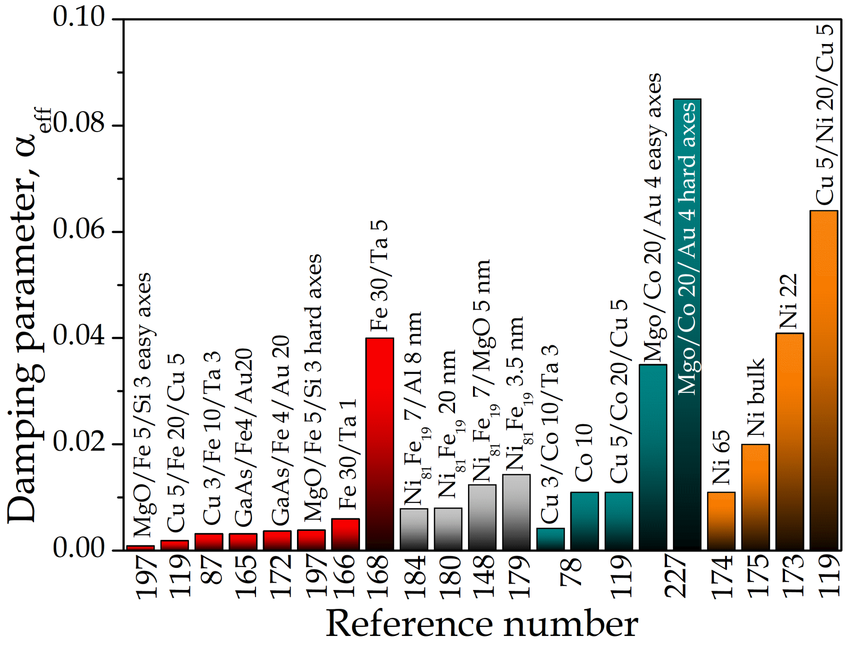

FIGURE 5.4: The effective damping parameter for elemental ferromagnetic transition metal thin-films: Fe in the range 4-30 nm; Co with thicknesses between 10 and 20 nm, $Ni_{81}Fe_{19}$ with thickness 3.5-20 nm and films of Ni $\geq$ 20 nm. The thicknesses indicated are in nanometres and the substrates and any additional underlayers and capping layers are also listed.

target NM layer in multilayered systems. The spacer layer here refers to a material with almost no effect on the damping that is used to provide separation between the FM and NM target layers which can have a significant effect on damping. The next section discusses the effect of the FM layer thickness dependence.

5.7.1 The Effect of Ferromagnetic Film Thickness on Damping

The variation of the damping parameter with thickness is more complicated for a ferromagnetic film because of surface and interface effects, which scale in proportion to the inverse of the film thickness. That is why it is often presented graphically as a function of the reciprocal thickness, $1/d_{\mathrm{FM}}$ where it shows a linear or non-linear trends. The general trend of the damping dependence on FM thickness is that the damping increases as the film thickness decreases. Where it is reported in the studies by different parameters such as: Gilbert damping constant, G, dimensionless parameter, α, and ΔH, which all have the same trend with the reciprocal thickness [75, 77, 151, 165, 170, 171, 173, 178, 179, 183–192]. Some of these studies show a linear damping reduction with the reciprocal of the FM layer thickness [75, 173, 178, 179, 183, 185–187, 191, 192], and others show a non-linear decrease [77, 100, 151, 172, 184, 188, 189]. The reason for these different behaviours is related in some studies to the magnetisation orientation, where this can be seen in two thin-films of the same FM material fabricated under different growth conditions [179], or due to the type of the NM material used as capping or under layers [75, 147, 151, 173, 178, 179, 187, 189]. These two damping dependencies are shown in Fig 5.5 (a), (b), (c), (d) and (e).

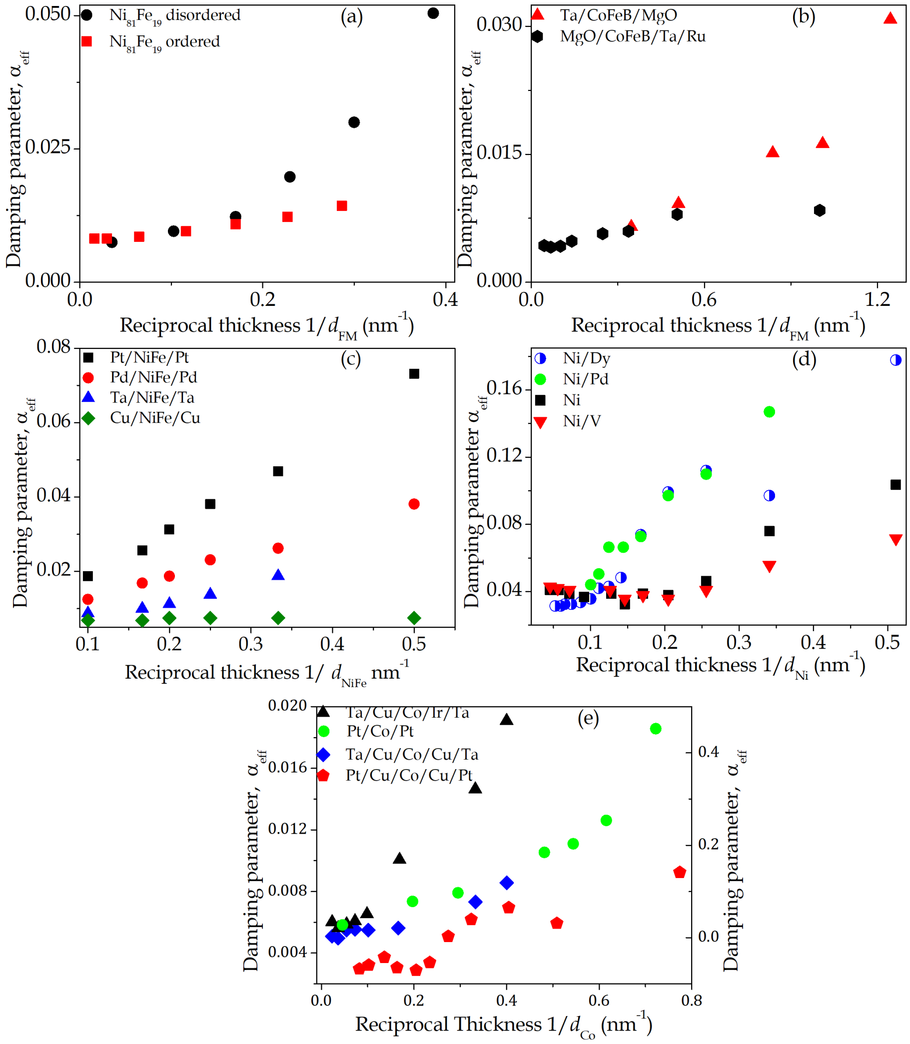

FIGURE 5.5: The effective damping parameter as a function of reciprocal FM layer thickness $1/d_{FM}$ for (a) ordered and disordered NiFe thin-films. The figure shows linear and non-linear relations adapted from Ref. [179], (b) for amorphous CoFeB, showing the sensitivity of the damping to underlayer and capping layer materials, adapted from Ref. [187, 189],(c) NiFe with different underlayers/capping layers(d) Ni with different capping layers, adapted from Ref. [147, 173] respectively and (e) Co layer thickness for different combinations of NM underlayers and capping layers, from Refs [75, 151, 178].

Studies have tried to link the damping enhancement with the magnetisation orientation in bi-layer thin-films through underlying effects. These studies show that spin-mixing conductance at the FM/NM interface is changing due to the changing of the magnetisation orientation. This has been linked to the crystal structure, where a study showed that the thinnest Co layers is formed with fcc crystal structure while thicker Co layers have the hcp structure [151].

With the non-linear damping dependence, it has been found that α increases rapidly with reciprocal thickness when the FM layer thickness is in the range of $d_{\mathrm{FM}} < 1$ nm. Both intrinsic and the extrinsic mechanisms explain this strong thickness dependence. In more depth, the intrinsic enhancement of the damping coming from the d-d hybridization effect in thin-films is strongly related to film thickness d_{FM} [75], while the significant changes of film structure and surface roughness in ultra-thin-films can increase the extrinsic two-magnon scattering [100].

The damping dependence on film thickness also shows an interface/surface effect. Another issue to add is that there is lack of information regarding how magnetic damping varies for each mono-layer that contributes to the total magnetic damping of the FM system. The contribution from each mono-layer is still not well understood or accessible experimentally, and there is a lack of information regarding this contribution. The interface/surface effect on damping will be discussed in the next section, where adding a NM material shows the impact of this factor on damping. A theoretical study by Barati *et al.* discussed the contribution effect by calculating α for each individual mono-layer in Co and Co/NM, (NM = Cu, Pd, Ag, Pt, and Au) thin-films, where the calculations have been done using a realistic nine-orbital tight-binding model including spin-orbit coupling. This calculation used spin orbit, SO, torque term with the Lorentz functions of the electron scattering rate, Γ, at Fermi energy ,ϵ_{F}. The final equation used to calculate α is written as:

$$\alpha = \frac{1}{N_{\mathrm{FM}}} \sum_{\mathrm{l}} \alpha_{\mathrm{l}} \tag{5.17}$$

where N_{FM} is the number of atomic layers in the FM parts of the thin-film, (α_{l}) is the individual contribution from each layer l. Fig. 5.6 shows the calculation of α_{l} for

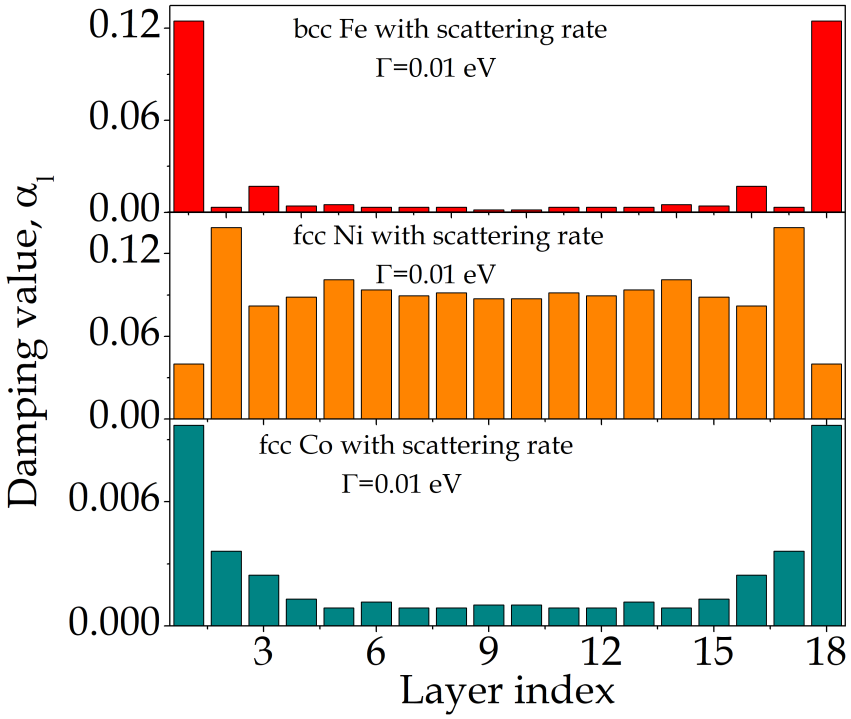

FIGURE 5.6: An examples of damping parameter contribution calculation from each mono-layer in bcc Fe, fcc Co and fcc Ni, of 18 ML thickness, adapted from [6].

bcc Fe, fcc Co and fcc Ni, where it shows the largest contribution to the damping is from the outer layers and damping decreases with moving to the material central layers [6, 193]. These two studies have good agreement regarding the contribution to the damping in the FM thin-film however there is no experimental results which can support this theory.

In terms of damping variation with each atomic layer inside FM films, these studies suggest that damping distribution inside specific FM layer is not homogeneous. It is related to the intraband transitions which seems to be take place in Co and Fe heavily in the outer atomic layers to the surface. Such transitions in Ni are more likely take place in the second and toward the centre of the layer. It has been argued that intraband transition are the results of considering SOI term in such materials. The suggestion, which have not been approached yet is that the variations that can occur on damping in total and damping in these atomic layers with large contribution, in case of outer layer modification. This will be seen and discussed in details in Chapt. 9.

5.7.2 The Effect of Non-Magnetic Layer Thickness on Damping

Adding NM layer(s), adjacent to a single FM layer thin-film, can change the damping. As discussed in Chapt 2 this can also subtly change the structure of the ferromagnetic layer. The general effect of adding NM as capping and/or under layer is the enhancement of damping via both intrinsic and extrinsic mechanisms [4, 5, 75, 100, 116, 151, 165, 169, 173, 177–179, 183–189, 194–196]. The various mechanisms responsible were discussed earlier in sections 5.2, 5.3 and 5.4.

Before discussing the relationship between damping and capping layer thickness, d_{NM}, it is important to explain the influence of the specific non-magnetic material on damping value. For the same FM material the specific NM material can be classified into three categories. Pt and Pd are considered as the most effective atomic species for damping enhancement. Cr and Ir have a smaller effect in comparison, while Au, Ag and Cu, have almost no effect on damping [4, 5, 100, 151, 165, 172, 177, 178, 183–186, 194, 195, 197]. Fig. 5.7 shows a good example of the damping value of FM (NiFe) with various NM capping layers. The difference in the enhancement can be seen in the figure, by adding a specific NM mentioned. The details can also be linked to interface intermixing, improving the spin-pumping effect and diffusing the spin with minimum reflectance to the FM layer.

Fabricating more complicated structures like NM layers as capping and under layers or repeating the FM/NM system to n times enhances the damping. The first case shows a doubling of the damping value in some studies [5, 198] or just a little enhancement in others [165] which is attributed to providing extra spin sinking for the pumped spin-waves in the system, while for the second case the damping increases with the increasing of n [77, 176] but, linking this to a specific effect is difficult. Also there are studies on various complicated thin-film structures such as $\mathrm{FM/NM_1/NM_2}$, $\mathrm{NM1_1/FM/NM_1/NM_2}$, $\mathrm{NM_2/NM_1/FM/NM_1}$ or $\mathrm{NM_2/NM_1/FM/NM_1/NM_2}$ [169, 177, 178, 194, 195]. These studies used Co, Fe, $\mathrm{Ni_{80}Fe_{20}}$, $\mathrm{Ni_{81}Fe_{19}}$, CoFe and YIG as FM layer, Cu, Cr, Pd, Ir and MgO as the first non-magnetic layer, $\mathrm{NM_1}$, and Ta or Pt as $\mathrm{NM_2}$. Many of these studies investigated the role of the spacer layer on damping enhancement by changing the spacer

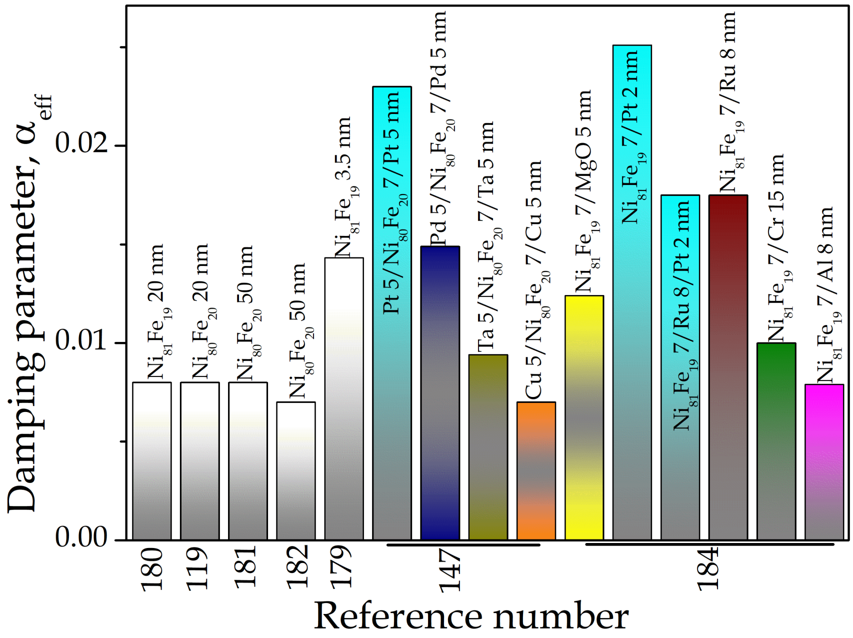

FIGURE 5.7: A summary of the effective damping parameter for NiFe thin-films combined with various NM layers.

layer thickness, where Cu was used as the spacer layer [169, 177, 184, 194–196]. In these studies the role of the spin diffusion length, λ_{sf}, was discussed beside spin-pumping, which determines the spin current reaching the second NM layer when d_{NM_1} is small. It was also shown that Cu has not much effect on the damping because with increasing the Cu thickness in general the damping decreases, which is not the case for other NM capping materials such as Pt or Pd, as it can be seen in Fig 5.8 as example. The status is that Cu prevents spin-current to reach to the second NM layer at thickness between 2-100 nm or even more [169, 177, 194–196]. This shows the importance of using a material with a large λ_{sf}, which has no significant effect on damping.

After discussing the effect of the NM material type on the damping, with the thickness dependence of damping of Cu only, we now move to the damping dependence on the thickness of NM materials and to focus on the most effective ones on damping such Pt and Pd, where these metals were used as capping or under layers or both. The general thickness dependence of damping for these two metals is that the damping increases rapidly with increasing d_{NM} then it usually reaches saturation at a certain thickness [5, 188, 195, 196, 199]. The main effect on damping

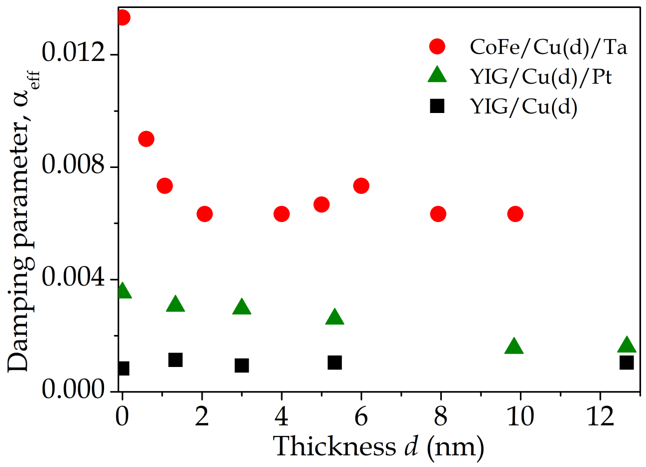

FIGURE 5.8: Effective damping parameter as a function of Cu spacer layer thickness separating a FM layer (CoFe or YIG) from another NM layer (Ta or Pt) [195, 196], with large thickness range of capping layers.

in these studies is associated with spin angular momentum pumped from the FM layer to the NM layer. These materials provide a good spin sink to absorb spin-current with minimum back reflection to the FM layer, since Pt and Pd have low spin diffusion lengths of less than 1 nm and 10 nm respectively [188, 196, 200, 201]. The main differences in these studies is the thickness at which damping approaches a plateau and the maximum damping value as can be seen in Fig 5.9. These studies used 30 nm of Finmet ($Fe_{66.5}Cu_1Nb_3Si_{13.5}B_9Al_7$), 19 nm of YIG and 10 nm of LSMO ($La_{2/3}Sr_{1/3}MnO_3$) as the FM material, with Pt and $SrRuO_3$ as NM capping layers respectively [195, 199, 202]. The saturation damping values were 8.6×10^{-3} at d_{Pt} ≥ 4 nm for the first study [199], $\sim (35.4 \pm 0.6) \times 10^{-4}$ at $d_{Pt} \geq 3$ nm for the second study [195] and 0.002 at $d_{SrRuO_3} \geq 5$ nm for the third study [202]. The range of the NM material used in these studies was 1-15 nm with relatively large steps of d_{NM} see Fig 5.9.

For the second element; Pd, a similar damping dependence on d_{NM} has been observed, even though the studies investigated more than one capping layer system. Studies of trilayer thin-film systems, using $Co_{90}Fe_{10}$ with Pd capping, and with different number of layers and other materials as an underlayer, showed the damping saturates when the NM_1 layer thicknesses is between 5-10 nm. The maximum damping value saturates at 0.020 to 0.023 [188, 196] as shown in Fig 5.10. This is in good agreement with the spin diffusion length of Pd [201], which would provide an

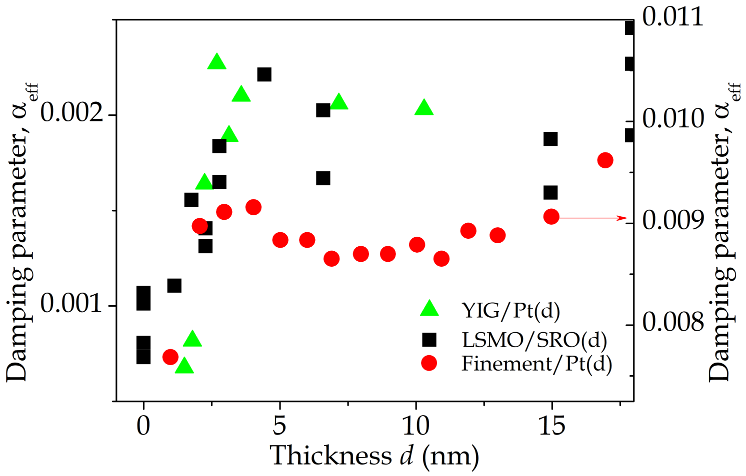

FIGURE 5.9: Effective damping parameter as a function of NM layer thickness of either Pt or $SrRuO_3$ capping layers on different FM layers [195, 199, 202], with large thickness range of capping layers.

explanation consistent with other work on capping layers.

There are other studies which investigated the role of the NM thickness on damping in other more complicated systems $[FM/NM]_n$, where n is the number of repetitions [203, 204], or they have investigated temperature dependence of damping in NiFe [205–210], ultrathin $Co_{40}Fe_{40}B_{20}$ [211, 212] or Co thin-films [213, 214]. However these studies are outside the focus of this thesis, but more information can be seen in the main source of this chapter [116].

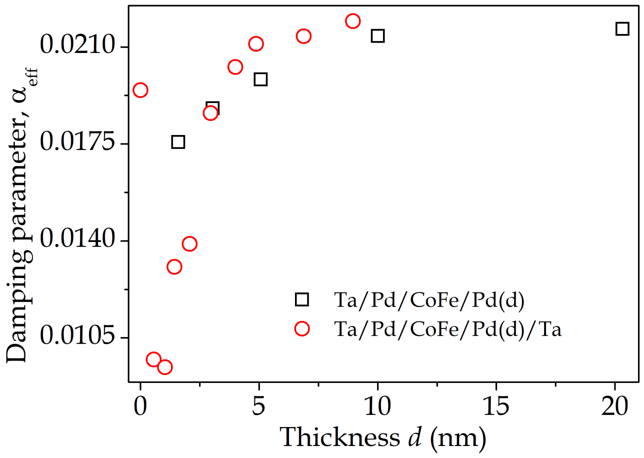

FIGURE 5.10: The effective damping parameter as a function of Pd capping layer thickness on CoFe ferromagnetic films with Ta/Pd underlayers [188, 196].

Summing up the results of the studies that investigated the damping dependence on d_{NM}, these studies have used a wide range of thicknesses of the NM materials and show the effects of the spin diffusion length and the spin-pumping. The effect of the interface/surface was produced in general the same thing for d-d hybridization effect. The theory that describes damping in bulk FM systems and the contribution from each mono-layer, provides a theoretical explanation regrading the effect of the NM material as an adjacent layer on damping with contributions from each individual NM mono-layer. The surface/interface effect is explained by this study by calculation α of the FM/NM system, with various NM material coupled with Co, showing that main contribution to damping at the FM/NM interface is intrinsic. It can be seen from Fig. 5.11 that the largest contribution to the total damping is from the first mono-layer in the adjacent NM material especially Pt, while there is no effect when the NM layer is Cu [6]. In all experimental studies the interface is already developed to a full intermixed layer which gives the final status of the underling mechanisms mentioned above.

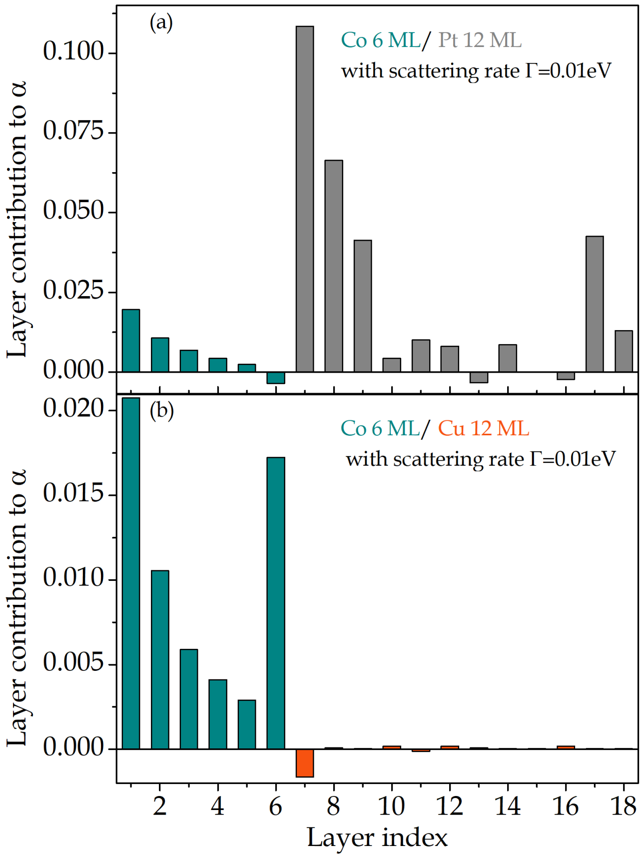

FIGURE 5.11: Calculations of the damping contribution from each mono-layer of FM;Co and NM (a) Pt, where it shows the largest contribution to α from the mono-layers near to the interface and (b) Cu where it shows no contribution to the total damping, adapted from [6]

5.8 Damping in Doped and Alloy Thin-Films

Doping in the literature is somewhat flexible terminology, because it is linked with the percentage of dopant at which changes in the magnetic and/or crystallographic properties of the host material occur. For example adding a new material to the host up to 7 % can change the structure of the system from body-centred cubic (bcc) to body-centred tetragonal (bct) [215], on the other hand this is not the case even when the concentration change is more than 10 %, although it has a huge impact on damping [216]. In this thesis doping is defined as the addition of an impurity element(s) into a host material in concentrations up to 10 % and the aim is to show the general trend on damping.

Doping any FM system can be executed by three techniques, co-deposition e.g. co-sputtering [181, 182, 217–220], ion beam implantation [180, 221], or by ion beam intermixing of bilayers [4, 222]. These are explained in Chapt. 4. Doping in general can change a lot of properties in a FM system, including the electronic behaviour such as resistivity [223] or the magnetic behaviour such as saturation magnetisation [166, 182, 197, 218, 220] and magnetic anisotropy [180, 182, 197, 217, 224, 225] of the system. The general impact of doping on damping is that damping increases with increasing the concentration of doping, both via intrinsic and extrinsic mechanisms [4, 119, 181, 215, 217, 218, 221, 222]. As discussed earlier doping changes the crystal structure and the Fermi energy level [4, 119, 166, 181, 217–220, 223, 224]. Extrinsic damping is the dominant mechanism in very low doping regime, however, in the high doping regime alloying is a better term, which gives new magnetic properties including intrinsic damping [4, 119, 223, 224, 226].

5.8.1 Systems with Low Doping

The most common case of doping is by co-deposition, which has been used in many studies to investigate the effect on damping. The general trend of damping enhancement is linearly with increasing doping concentration in the low doping regime. This effect is much pronounced when the dopant are heavy transition metals [167, 181, 182, 217–220, 227] as shown in Fig 5.12. The strongest effect is with Os doping, which has strong SOC as a 5-*d* metals. It can be seen from the same figure (b) that Cr doping has a different effect on damping when the concentration is below 8 %. This behaviour is not explained in the studies but, it seems to be a key factor for Cr which is used later in this thesis to control damping. Higher enhancement of damping with lower dopant concentration is observed when using rare-earth elements such as Dy, Tb, and Ho, however, Gd did not show the same effect [181, 182, 217–220]. Damping increases with rare-earth dopants can not be explained due to their atomic number or SOC [219] and other studies did not show consistency with the earlier results of Sm, Eu, Tb, Dy, and Ho dopant [220], see figure 5.12 (c).

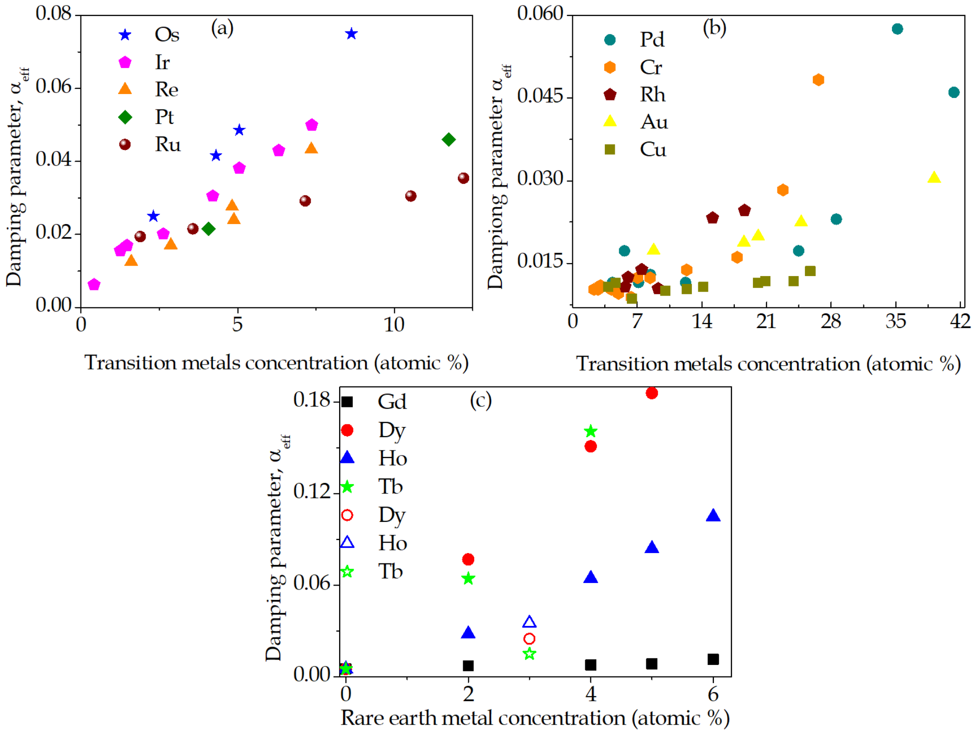

FIGURE 5.12: Damping parameter as a function of atomic concentration of (a) and (b) transition metals Ref. [217] and (c) rare-earth dopants. Results from two different studies: Solid symbols from Ref. [219] and open symbols from Ref. [220]. All figures show correlation between damping and the dopant concentration, however the trend in (b) shows more non-linear dependence at high concentrations.

For Ion-implantation of dopants the same damping enhancement trend is observed however, the trend is non-linear when the doping concentration is a few atomic percent. This has been explained by the inhomogeneities which result from lattice damage in $Ni_{81}Fe_{19}$ caused by the Cr ion-radiation [180]. On the other hand the opposite trend was observed, in a more complicated system with bi-layer of FM/antiferromagnet (AF)/FM ($Ni_{81}Fe_{19}/Ir_{23}Mn_{77}/Ni_{81}Fe_{19}$). In this system Cr ion-implantation decreases the exchange interaction at the interface [221].

The third doping method uses focused ion-beam (FIB) irradiation with 30 keV Ga^+-ions. This method is used with FM/NM bilayers thin-films, the effect of this method is interface widening, which leads to increasing damping via the extrinsic effect, where the dopants act to break the symmetry of the crystal system and creates a compositionally graded-alloy at the interface in a FM/NM bilayer system [166, 215, 221], which will create centres for two-magnon scattering. The Ga^+ implantation is very limited so its effect may be neglected. A recent study with this method investigated $Ni_{81}Fe_{19}$ capped with Au or Cr [222]. For Au the damping increased linearly with the FIB dose, which agrees with the suggested underlying mechanisms mentioned above, however, with Cr the inverse behaviour was observed. It can be seen in Fig 5.13 that the damping deceases with increasing FIB dose, where α value at 0 % dose is higher for the bulk $Ni_{81}Fe_{19}$. This was explained with the ion-beam effect on the capping layer where it is sputtered away by FIB milling which will reduce its thickness thus, the intrinsic mechanism [222]. This also agrees with the damping behaviour for the doping FM material with Cr in the previous section.

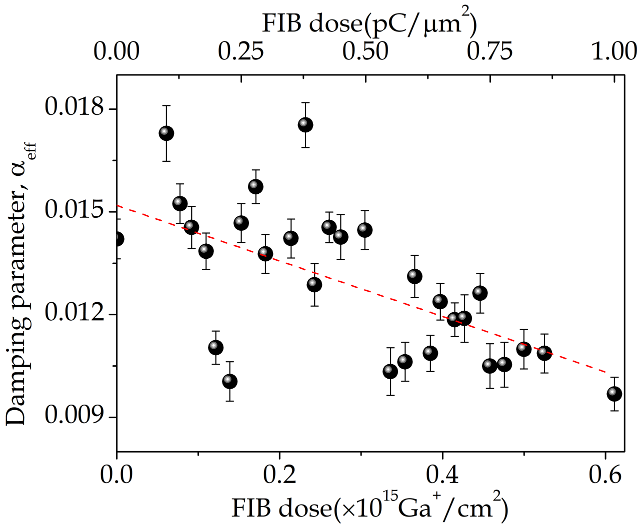

FIGURE 5.13: Damping reduction as a function of focused ion-beam irradiation dose, the general trend shows linear reduction behaviour, adapted from Ref [222].

5.8.2 Systems With High Doping: Alloys

It is more common to describe the combination of two FM materials as an alloy even when the atomic constituents range is few percentage [4, 166, 217, 219, 221, 222]. The combination of a NM metal with a ferromagnet is sometimes described as doping even when it is in the range of tens of atomic percent [181, 217–219]. As explained before dopants can act as defects and they will change the host material electronic structure and thus the material magnetic behaviour [167, 217, 223, 224, 228]. The most typical and clear indication that can be used to separate doping from alloying is the changing crystal phase of the resultant material [119, 166, 168, 180, 192, 197, 215, 216, 220, 227, 228].

As discussed in Sec. 5.6.1, $Ni_{81}Fe_{19}$ is one of iconic magnetic alloys and changing the atomic ratio will change the damping. For example, it has been found that changing the concentration of alloys of the three well know FM transition metals; Co, Fe and Ni has a great impact on the damping. It can be seen from Fig. 5.14 that the range of damping variation in CoFe alloys is small while the strongest effect on damping is in the alloys involving Ni; NiFe or NiCo. These effects are associated with the energy level modification regarding changes in the crystal phase with changes of the composition [119]. CoFe shows a crystal phase change effect on the damping where changing the Co concentration in the range 75-85 % impacts on the damping value as shown by two different studies, where the analysis shows that at 75 % Co the system will have a mixed bcc/fcc phase [87, 227]. Even though, both studies show agreement with Co concentration, the latter studies achieved a very low damping value, of order 10^{-4}, when the the composition of the alloy is $Co_{25}Fe_{75}$. The explanation to this low damping value is linked to the DOS, where this concentration leads to low DOS at Fermi level that minimises the contribution of intraband transition to the intrinsic damping [87]. Many other studies have investigated alloying or high doping on damping with many complicated systems such as: iron-, cobalt- rich Heusler alloys where the latter is very sensitive to the system composition [119, 216, 223, 224, 228]. However they are not the subject of this thesis.

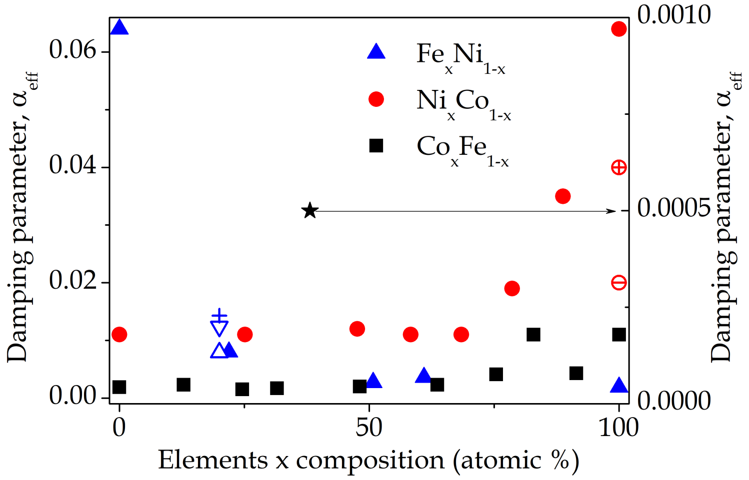

FIGURE 5.14: The effective damping parameter as a function of the elementary compositions for binary alloys of Fe, Co and Ni from [119], +, ▽, △, ⊕, ⊖ , ★ from [87, 173, 175, 179, 184] respectively and belong to the group colour.

5.9 Limitations of the Recent Experimental Results and the Focus of this Thesis

In this chapter magnetic precession and damping were introduced and linked to the most well-known mechanisms for damping, these mechanisms consider the underlying sources for damping. Many experimental studies have been reviewed with their results and analysis and with the support of the theoretical studies explained to gain a better understanding of the damping phenomena. However,there is lack of understanding of the source of damping in any systems the general idea is the SOC and its modification via spin-mixing, spin-pumping and spin diffusion length effects. However these effects are not well understood and the modification of these effect due to additional NM layers is still unclear. Also the correlation between d-d and s-d hybridization and the mentioned effects are not well understood. On the other hand, the intrinsic and the extrinsic mechanisms are thought to be separated from each other and they my come from different sources even when they share some underlying effects. Doping is mostly thought of as an extrinsic effect, where defects are created by the dopant in the host material, or as an intrinsic effect , by modifying the energy states at the Fermi energy level. Linking damping with other phenomena such as DMI is not well understood and the effect of both phenomena on domain wall motion is rarely investigated. All of these issues are the focus of the following chapters, showing new results regarding understanding damping at the interface in bi-layer thin-films, controlling damping by changing the interface nature, linking the effects of damping and DMI to gain a better understanding of the impact of these phenomena on domain wall motion and finally controlling damping in thin-films by synthetic modifications of band structure in surface mono-layers of Co to reduce the effective damping. These studies are presented in Chapt. 6, 7, 8 and 9 respectively. The work in these chapters is first, given insight to understand the development and the evolution of damping from the extrinsic to the intrinsic stage with clearer linkage and correlation between the main mechanisms and their underlying effects. Secondly, showing the same aspect with respect to the interface modification, thirdly, to show the impact of both mechanisms on DMI and the range at which DMI and damping have the strongest joint effect. Finally, the contribution to the damping is well investigated based on the theory and thus, damping is explained and controlled in macroscopic view with the capability to change its total value for well-known transition material; Co to ultra low value with an order of 10^{-4}.

Chapter 6

Damping Evolution in FM/NM Thin-Films as a Function of NM Thickness

6.1 Introduction to Damping

The precessional dynamics of magnetisation are important to both magnetic field and current driven applications such as; magnetic data storage. The magnetic precessional and damping govern the data writing speed and switching behaviour in magnonic-based device concept and spin-transfer torque magnetoresistive random-access memory (STT-MRAM) devices. Thus, understanding the role of damping in thin-film systems will add to the research and contribute to the knowledge on the magnetisation dynamics. The work in this chapter is published by the American Physical Society (APS), *Physical Review B* journal [5].

Damping and damping enhancement were explained in Chapt. 5 through the recent experimental studies on bulk FM material [4, 6, 44, 48, 217], bi- and multilayered thin-films [134, 147, 149, 165]. The origin of damped magnetisation precession was addressed in many studies in terms of theory and experiments [40, 44, 48, 151, 164, 195, 217, 229–232] with the aim of understand damping fundamentals. For the magnetic device applications Co and $Ni_{81}Fe_{19}$ are the focus magnetic research FM materials due to their attractive physical and magnetic properties. Combining these ferromagnets with a heavy NM material, as an adjacent capping layer, will change the total damping value. As mentioned elsewhere, intrinsic damping is a uniform mode magnon and extrinsic damping is associated with non-uniform modes, these two mechanisms are the result of spin-orbit interaction and energy dissipation. The first mechanism is linked with spin-mixing conductance, spin-pumping and spin-diffusion length, while the second mechanism is linked with roughness and defects in the system in general and at the interface region [6, 44, 48, 75, 77, 148, 151, 164, 176, 187, 195, 217, 231–234].

Intrinsic damping at the interface via spin-mixing conductance with the aid of the d-d hybridization effect facilitates the spin-pumping effect allowing the pumping of spin in the NM layer where it can dissipate [6, 48, 77, 147, 164]. The extrinsic mechanism provides additional channels for the energy dissipation due to defects and roughness via additional magnons associated with non-uniform precessional modes [6, 48, 187, 235]. The extrinsic damping is also linked with the interface in general, where roughness and intermixing can increase this mechanism and thus, the total damping [6, 44, 48, 77]. Linking these mechanisms and the effect of changing the density of states at the Fermi energy level is another factor that can explain the variation of magnetic damping at the interface region [6, 48, 77, 176, 231, 232]. The specific electronic behaviour has been explained for the materials involved in damping studied in a variety of systems with non-magnetic layers including Au, MgO, Cu and Ta on FM layers of Co, CoFeB and $Ni_{80}Fe_{20}$ [6, 48, 147, 187, 235]. In these studies d_{NM} was increased upto 15 nm with d_{NM} increasing steps of 1 nm, where the interface region was already structurally completed.

Thus, it is of great interest to study the evolution of magnetic damping in FM/NM bi-layers as the interface develops as a function of the NM layer thickness increasing through the sub-nanometre range. The role of both intrinsic and extrinsic mechanisms in the enhancement of damping is demonstrated by a comparison with recent theoretical predictions. These predictions were made in a theoretical study of FM/NM bi-layers by Barati *et al.* [6, 48], which reported the dependence of damping whilst increasing in mono-layers the thickness of the non-magnetic layer, assuming an ideal flat interface. It was predicted that for NM layers the damping depends on the specific material and the layer thickness. The largest impact was for the case of a Co/Pt bi-layer, where with the addition of Pt mono-layers the magnetic damping was found to increase significantly and non-linearly with NM thickness. Also, it was predicted in the same study that damping is not homogeneous throughout all the constituent mono-layers of the FM and NM materials. In order to investigate these predictions, a well-controlled thin-film deposition study was needed to establish precise NM layer thicknesses, the interface width and the FM crystal structure.

6.1.1 Formalism for Analysing Damping

The measured effective magnetic damping parameter, α_{eff}, can be written as the sum of the bulk, intrinsic and extrinsic contributions:

$$\alpha_{\text{eff}} = \alpha_0^{\text{int}} + \alpha_{\text{ext}} \tag{6.1}$$

where α_0^{int} and α_{ext} are the total intrinsic and extrinsic damping parameters of the system, respectively. Furthermore, α_0^{int} can be expressed such that:

$$\alpha_{\text{eff}} = \frac{G_0}{\gamma M_{\text{s}}} + \alpha_{\text{s}}/d_{\text{FM}} + \alpha_{\text{ext}} \tag{6.2}$$

where, G_0 is the bulk Gilbert damping parameter, γ is the gyromagnetic ratio, M_{s} is the saturation magnetisation, d_{FM} is the ferromagnetic layer thickness and α_{s} is the interface's contribution to the effective damping [6, 39, 48, 195].

The damping dependence on thickness may be explained by a mixture of spin-pumping, intermixing, and extrinsic two-magnon scattering effects. In this study, α_{eff} was measured as a function of the NM layer's thickness.

6.2 Experimental Details

A variety of Co and $Ni_{81}Fe_{19}$ based thin-films have been fabricated in this study, where bi-layer thin-films were deposited on a thermally oxidised silicon substrate with a 100 nm SiO_2 layer. This was done using UHV magnetron sputtering with a base pressure $\sim 10^{-8}$ Torr; more information about sample preparation and magnetron deposition can be seen in Chapt. 4. The FM layer was deposited directly on to the SiO_2 substrate and the complete structure for all the produced thin-films was $Si/SiO_2/FM/NM$. The FM layer had two selected thicknesses, 4 and 10 nm for Co and 4 and 7 nm for $Ni_{81}Fe_{19}$. The thicknesses were chosen to maximise the interaction between the films and the incident magneto-optical probe; however, the 10 nm for Co and 7 nm for $Ni_{81}Fe_{19}$ are the focus of this study. This is because the limitation of the damping sensing and the time available for extracting data from the measured samples. It may be considered that the FM material's surface in the thin-films may have oxidised completely or partially due to incomplete capping layers. Preventing this can be done by adding another capping layer, but this will increase the physical system's complexity, hence shift the results and may confuse the general trend. The study aimed to examine the sub-nanometre thickness effect of specific NM materials on the damping. So the nominal capping layer thicknesses was varied from 0.2 to 10 nm with extra care regarding the deposition parameters in order to achieve a 0.2 nm step difference to cover the capping layer range from 0-1 nm. After that, larger steps from 0.5-1 nm were made to complete the capping layer thickness range.

6.3 Thin-Films, Thicknesses, Interface Width and Crystal Structure

A structural analysis was carried out using a Bede-D1 diffractometer with a CuKα system for grazing incidence X-ray reflectivity (XRR) angle to study layer thicknesses and interfacial structures, and for X-ray diffraction (XRD) to analyse the crystal structure, more information can be found in Chapt. 3 and Ref. [57, 61, 236]. The true specular XRR data were obtained by subtraction of the measured forward diffuse scatter and was modelled with best fitting simulations generated using the GenX code [61]. Furthermore, XRD results were analysed to determine the out-of-plane lattice parameter. For thin-film thickness and interface roughness, Fig. 6.1 summarize the best simulated fit for samples of Co capped with Pt and Au, and $Ni_{81}Fe_{19}$ capped with Pt. The data represent the FM and the NM layers, thickness and roughness development at the interface. The data obtained from x-ray reflectivity are shown in Table 6.1, where the best fitting simulated thickness and roughness of the FM/NM bi-layers are presented. The data in the table provide crucial information, which gives an indication about the interface's nature between the FM and the NM layer.

TABLE 6.1: Structural properties for selected Co/Au, Co/Pt and NiFe/Pt bi-layers samples extracted from XRR measurements: FM layer thickness, d_{FM}; NM layer thickness, d_{NM} and roughness at the FM/NM interface.

Sample Structure	d_{FM} (nm)	d_{NM} (nm)	Interface Width (nm)
Co (10 nm) / Au (4 nm)	9.44 ± 0.05	3.5 ± 0.04	0.61 ± 0.11
Co (10 nm) / Pt (2 nm)	9.56 ± 0.09	2.8 ± 0.05	0.66 ± 0.07
$Ni_{81}Fe_{19}$ (7 nm) / Pt (1 nm)	7.24 ± 0.11	0.94 ± 0.08	0.92 ± 0.05

Increasing the NM layers thickness will reduce the interface's roughness and will form a complete layer. The reduction in the topological roughness is clear in Fig. 6.1 (a), (b) and (c), where the Kiessig fringes became shallower as the NM layer's thickness increased; for more information see Chapt. 3.

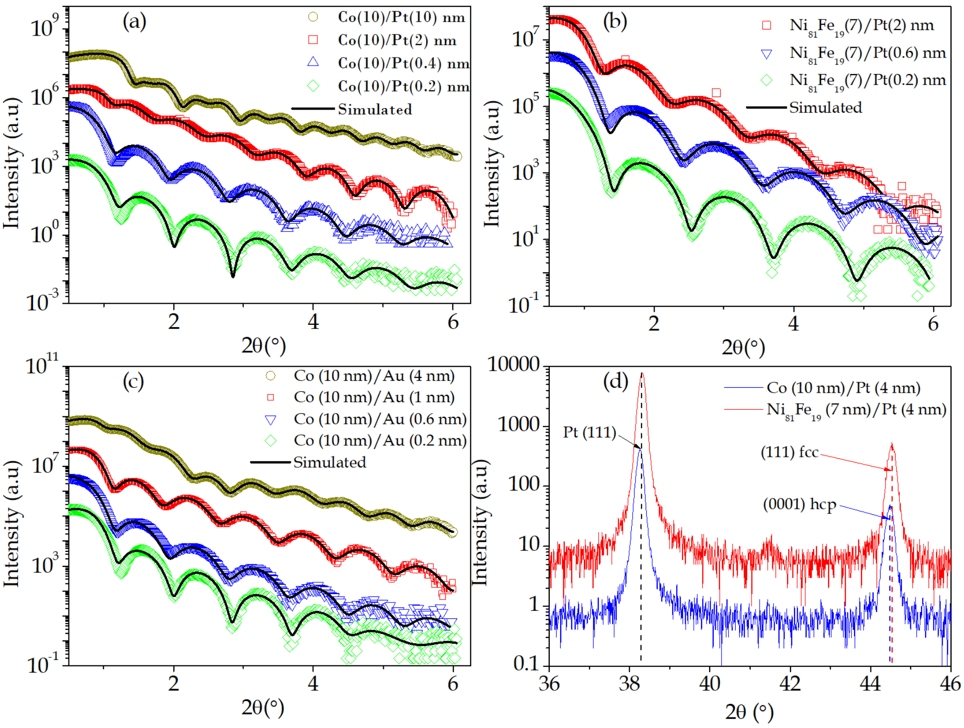

FIGURE 6.1: Examples of x-ray reflectivity data and the best fitting simulations for (a) Co (10 nm)/Pt (d_{Pt}), (b) $Ni_{81}Fe_{19}$ (7 nm)/Pt (d_{Pt}), (c) Co (10 nm)/Au (d_{Au}) and (d) XRD structural analysis for Co and $NI_{81}Fe_{19}$ capped with Pt

The most representative data for the FM/NM interfacial region relates to when the NM metal forms a complete layer over the FM layer. These data give the total interface width that includes topological roughness and intermixing. The interface width is important as it provides an indication of the thickness at which the NM capping layer changes from island-like coverage to continuous coverage of the FM layer. The XRR structural analysis shows that the interface width was in the range of 0.6 to 0.7 nm, which indicates that both Pt and Au form a continuous layer on Co at a thickness greater than $\sim$ 0.7 nm. However, the data for $Ni_{81}Fe_{19}$ shows that the NM capping layer becomes continuous at thicknesses above $\sim$ 0.9 nm due to the larger interface width. The differences in the interface widths between Co and $Ni_{81}Fe_{18}$ may come from their different crystal structures. The XRD analysis and literature show that $Ni_{81}Fe_{19}$ has a fcc crystal structure while Co's is hcp [6, 48, 151, 235]. As it can be seen in the same figure (d), the XRD pattern for Co 10 /Pt 4 nm and $Ni_{81}Fe_{19}$ 7/Pt 4 nm is where the first diffraction peak is for fcc Pt and the second represents the hcp Co (0001) and fcc $Ni_{81}Fe_{19}$ (111) [151, 237]. As it is known that Au and Pt are both fcc, for Au and Pt capping on Co, the interfacial roughness is very similar; however, details of the local atomic arrangement are likely to be different. This is because Co and Pt are miscible with each other while Co and Au are immiscible [238]. The deposition growth models in Chapt. 4 explain the formation of the localised islands-growth mode of the NM material; these islands will expand and develop into a continuous capping layer as the NM thickness increases.

6.4 TR-MOKE, Data Analysis and Magnetic Damping Thickness Dependence

Dynamic magnetisation behaviour was studied *ex-situ* using time-resolved magneto-optical Kerr effect (TR-MOKE) magnetometry, using an all optical pump probe technique at the S.N. Bose Centre for Basic Sciences, Kolkata, India, by A. Ganguly. More details about the TR-MOKE system can be found in Chapt. 3 and Ref. [239–242]. Raw data obtained by using this technique and use to give the first indication of the dimensionless effective damping parameter α_{eff}. The results shows a strong dependence of α_{eff} on d_{Pt} for Co and $Ni_{81}Fe_{19}$, while not much dependence on d_{Au} was observed. Fig 6.2 presents examples of the TR-MOKE raw data for Co and $Ni_{81}Fe_{19}$

with Pt and Au capping layers, which show different Kerr rotation oscillating values and damping for the Pt capping layer while there is almost no change for the Au capping layer.

The figure shows the final fit after removing the ultrafast demagnetisation and subtraction of the background signal. This was done by fitting with a bi-exponential function, as it is explained in Chapt. 3. The background signal was the result of the sample's initial recovery of magnetisation, after which there were two stages, which describe the pumps induced demagnetisation. The first one took about 1 ps for relaxation and the second about 20 ps. The latter is associated with dissipation of energy between the lattice and surroundings, which decreases with the addition of the capping layer. It can be seen from the figure that the magnetisation precession for the FM-NM bi-layers with certain NM capping thicknesses are damped faster. The best fit curves indicate single-mode damped precession behaviour, which represents the Landau-Lifshitz-Gilbert with the spin rotation relation, by which α_{eff} was obtained.

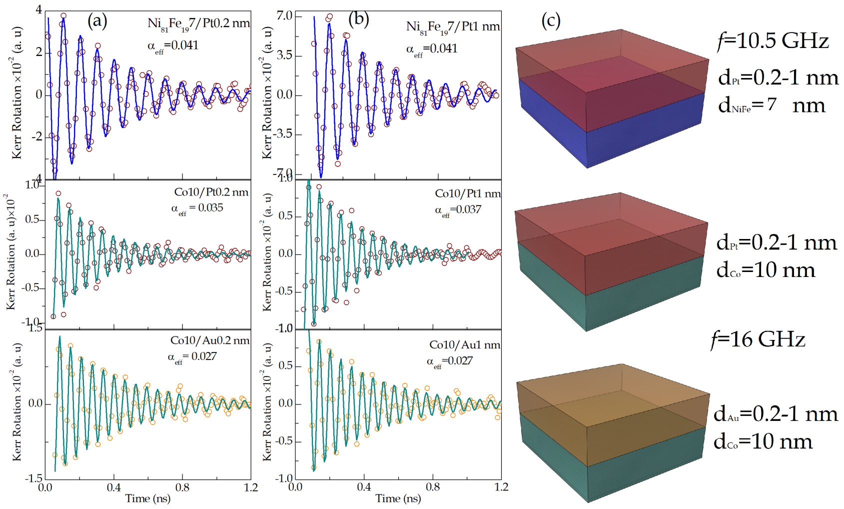

FIGURE 6.2: Examples of the TR-MOKE data for (a) Co and $Ni_{81}Fe_{19}$ capped with 0.2 Pt and Au, (b) capped with 1 nm Pt and Au, and (c) illustrates the tin-film stack with the frequency.

The final extracted α_{eff} as a function of d_{NM} is presented in Fig. 6.3 (a) and (c), where NM = Pt and Au. It can be seen that there is a significant increase in the effective damping parameter with the increase of Pt thickness for both Co and $Ni_{81}Fe_{19}$. Then α_{eff} reaches a broad peak when Pt's thickness is 0.7-0.8 nm for Co and 0.6 for

$Ni_{81}Fe_{19}$. For the Au capping layer on Co, however, the effective damping parameter is almost constant as the Au's thickness increases. It can be seen that the effective damping parameter value for a pure 10 nm Co thin-film is 0.029 higher than the reported value in the literature for hcp bulk Co: 0.011. This difference may be attributed to the surface oxidisation of the uncapped Co and $Ni_{81}Fe_{19}$ films, which may enhance α_{eff} in comparison with the α of the bulk Co. The oxidation effect is justified by the interface width in Table. 6.1 from the XRR measurements analysis. For $Ni_{81}Fe_{19}$, the increase in damping with d_{Pt} up to 0.6 nm is explainable, but, the damping data are limited to the Pt capping layer thickness, up to 1 nm. The behaviour of α_{eff} as a function of d_{NM} can be seen as three regions: an initial rapid increase with the Pt capping layer increasing up to 0.4-0.6 nm (region I), followed by a peak and stabilisation for Pt thickness 0.6-0.8 nm (region II), after that falling back to a lower α_{eff} value and remaining almost constant at Pt thickness > 0.8 (region III). Even though, α_{eff} fell in region III its value is still higher than the initial value. This is discussed in more detail later.

Going back to the same figure (b), the precessional frequency, f, and the saturation magnetisation, M_{S}, for Co/Pt thin-films, are plotted as a function of d_{Pt}. It can be seen that f and M_{S} show a similar dependence on Pt thickness. The highest values at which d_{Pt} increases are in the range of 0.6-0.8 nm. Furthermore, the M_{S} value obtained for bulk Co is lower than the reported value in the literature however, with Pt thickness increasing to 0.6 nm the M_{S} reaches a comparable value with the literature.

An indication of the damping nature and the dominant mechanism can be obtained, using TR-MOKE, as explained in Chapt. 3. This can be done by executing further TR-MOKE measurements in different applied bias magnetic fields, which will change the precessional frequency. The observed α_{eff} can be used to indicates the nature of the damping mechanism, where changes in the damping value are a sign of extrinsic non-uniform modes existing, which can impact the α_{eff} value. Increasing the applied field will suppress these modes however, calculating the contribution value of the extrinsic mechanism is not easy task.

Fig. 6.4 illustrates this process, where it shows α_{eff} as a function of f for two

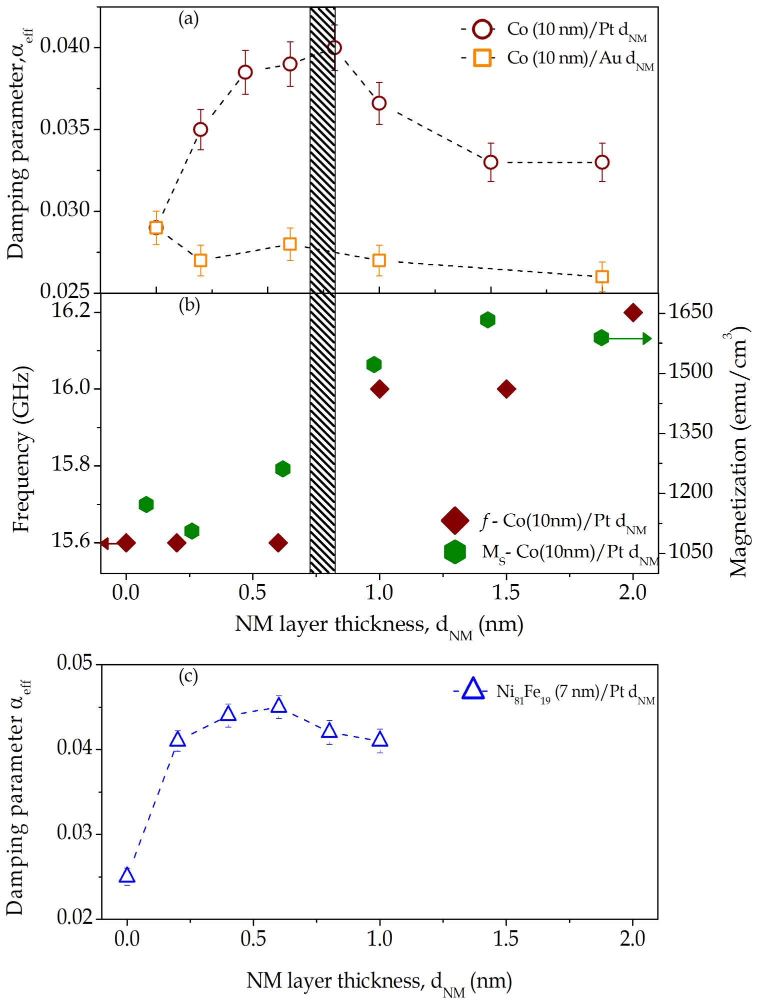

FIGURE 6.3: α_{eff} as a function of d_{NM} for (a) Co/Pt and (b) $Ni_{81}Fe_{19}$/Pt. (b) frequency and saturation magnetisation as function of d_{NM} and ~1.4 kOe of magnetic field strength, it shows similar trend in their variations. The shaded bar indicate the Pt thickness where the Pt became continuous.

selected Co thin-films capped with a discontinuous 0.6 nm and continuous 2 nm Pt capping layers respectively. It can be seen that for the 0.6 nm Pt capping layer, the variation in f shows suppression of the non-uniform modes, thus the effective damping parameter decreases linearly, while there is almost no impact of f on α_{eff} in the case of the 2 nm Pt capping layer. It has been shown that for 10 nm $Ni_{81}Fe_{19}$ capped with 3 nm Pt, where Pt forms a continuous layer, that the damping is also constant as a function of the precessional frequency. This result was found in the study of Chapt. 7.

The dependence of the effective damping parameter presented in Fig. 6.3 (a) and

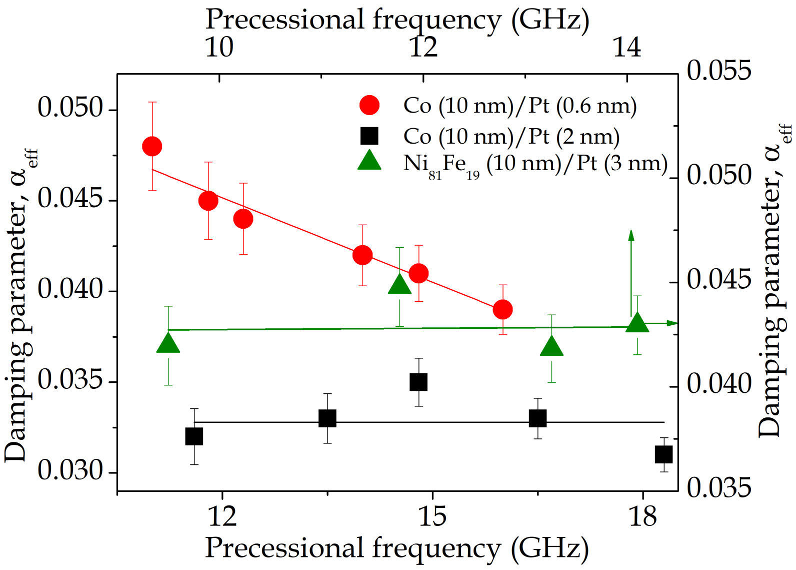

FIGURE 6.4: Damping parameter α_{eff} as a function of precession frequency for 10 nm Co films capped with 0.6 nm and 2 nm Pt. The extrinsic damping decreases as $d_{\mathrm{NM}} = 2$ nm where it became a negligible value .

(c) shows the complex behaviour as a function of d_{NM} that is linked with three distinct regions. This behaviour can be understood through the underlying contribution of the intrinsic and extrinsic mechanisms, explained in Chapt. 4, which occur at the FM/NM interface. The impact of such effects, d-d hybridization, spin-pumping and two-magnon scattering, are important factors for the enhancement of the damping in any given FM/NM thin-film [4, 6, 48, 77, 176, 195, 222, 231, 243]. The results shown in this chapter represent new experimental data that can be linked with recent theoretical studies [6, 48]. It is suggested in this study that damping increases as a function of increasing d_{NM} up to a certain value before it decreases again to a constant value when further increasing d_{NM}. However, in the theoretical study, damping was calculated for fcc Co, while in this chapter Co was largely hcp. A direct comparison between the results is still valid because the crystal structure of the Pt and Au capping layers are the same, which is fcc [244].

In order to understand the damping behaviour, the intrinsic and extrinsic nature of α_{eff} should be explained for each thickness region. The intrinsic contribution in region I can be attributed to two main underlying effects: d-d hybridization and spin-pumping. These two effects can be considered when the capping layer is Pt. The first effect will change the electronic structure at the FM/NM interface, while the second effect facilitates the dissipation of the angular momentum from the FM layer to the NM layer via the pumped-spin current, where both effects have an intrinsic nature. Considering the spin-pumping effect, this should be limited to the d_{Pt} range at which spin-pumping can be effective. This range is when Pt thickness is comparable with the spin-diffusion length, λ_{sd} [177, 184, 194, 195, 198]. Thus, d-d hybridization can be considered as the main intrinsic contribution to the enhancement of the damping in region I. It is worth noting that the d-d hybridization effect depends on the availability of electrons, which in this case is $5d$ for Pt, in the NM material and the opportunity for hybridization with the $3d$ electrons in the FM material, especially at the interface. This is one of the key factors which shows good agreement between this study and previous studies and also with the theoretical study by Barati *et al.* [6, 44, 48, 75, 77, 148, 151, 164, 176, 187, 195, 217, 231, 232, 234].

For the extrinsic contribution to the damping, two-magnon scattering is the main direct effect. The two-magnon scattering effect exists in the systems where local variations, topological roughness, defects and impurities exist, with the focus at the FM/NM interface. It is suggested that all the mentioned features may occur in region I, as the Pt capping layer in this region is discontinuous. This will create variations in the local electronic properties at the interface due to the Pt distribution variation. Hence, the interface will have areas with different intrinsic damping, which will cause local variation of damping precession. Thus, this will give rise to the two-magnon scattering, by which an interaction between different localised precessional modes occurs. This is supported by the dependence of damping on f in Fig. 6.4, where the damping increasing as the frequency decreases, which is a clear indication of the extrinsic effect's existence, especially when the Pt capping layer is not complete. It can be seen that both mechanisms contributed to α_{eff} in region I, but from the available damping and crystal structural data with the aid of the theory, it seems to be that the extrinsic mechanism's contribution is more pronounced in this region. Fig. 6.5 (c) shows the damping behaviour in region I with the damping value of bulk Co from the literature [77].

For region II, where the effective damping parameter reaches a broad peak, it is suggested that both mechanisms contribute to the damping. However, the contribution may be different from the contribution in region I. This is because in this region, Pt's thickness is in the range where a continuous capping layer is almost formed. So it is logical to assume that even if the extrinsic damping not decreases the intrinsic damping definitely increases. This is because the spin-pumping and the spin-diffusion length effects are more effective. However, this cannot be considered as the only explanation where the structural data shows that a complete Pt capping layer thickness is established beyond this region (see Fig. 6.5 (c)).

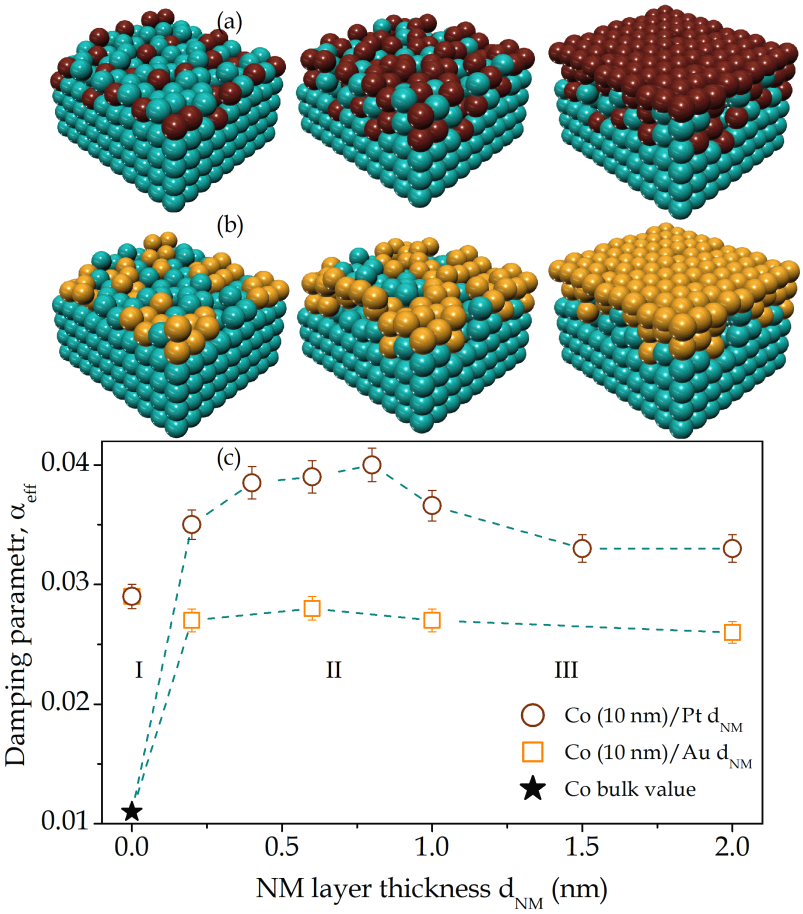

FIGURE 6.5: Illustrates the interaction of (a) Pt and (b) Au with Co at the interface and development of the interface with increasing NM thickness. Also, (c) shows a comparison of the damping parameter, α_{eff}, as a function of Pt and Au thickness in relation to the interaction of these metals with Co, considering the bulk value from the literature [77], where regions I, II and III are labelled.

The characteristics of region III are that damping falls from the maximum value and stabilises slowly to an intermediate value as a function of d_{Pt}. The main indication which can show the dominant damping mechanism is the dependence of the damping on the applied field. This is shown in Fig 6.4 for Co capped with 2 nm of Pt, where the independence of the damping on precessional frequency (bias field), demonstrates that the predominant mechanism of damping is intrinsic in this region. This also indicates that the reduction of the damping value in this region relates to the extrinsic mechanism, where its contribution vanishes at high d_{Pt}. It can be seen in Fig. 6.5 (c) that the final value of the effective damping parameter is higher than the initial value for the uncapped Co. This is because even when the extrinsic damping contribution at high Pt thickness vanishes, the intrinsic damping evolves and increases at this thickness. The behaviour in region III shows some variations in comparison with the theory, where in the theory, periodic oscillations are combined with the falling and the stabilisation of the damping. These oscillations are attributed to the formation of quantum well states [6, 48], which were not observed in the experimental results. The reason for this is that even though the range of d_{Pt} is small, the interfacial roughness will disrupt such oscillations.

In order to explain the extrinsic mechanism in Co/Pt thin-films, when the Pt capping layer is discontinuous, it is suggested that two-magnon scattering is a result of the local variation of the d-d hybridization of the Co and Pt at the interface. The miscibility of the NM material changes the electronic local structure by the hybridization via the interaction of Pt with Co. This produces Co-Pt clusters or islands at the surface [235], while for Au this leads to the formation of Au islands on Co in the low thickness regime [238]. This is illustrated in Fig. 6.5 (a) and (b); the different interactions between Pt and Co and Au and Co are a key factor for the damping's dependence on the thickness of these materials. For thin d_{Pt}, where the capping layer is incomplete, the formation of clusters or islands at the surface acts to break the translational symmetry. This will change the intrinsic damping at the FM/NM interface to high and low damping value regions, linked with the Co-Pt distribution. In this range of d_{Pt}, the Co-Pt islands are about one mono-layer, which is also the suggested reason for higher damping. This has been reported by a study on SOC in Pt, where it showed that 2D Pt has higher SOC than 3D as clusters and thus damping [245]. As the Co surface magnetic inhomogeneities increase due to the Pt effect at this low thickness, the extrinsic mechanism contributes more to the damping. However, when d_{Pt} is enough to form a continuous layer, the magnetic distribution at the interface is more uniform, thus the extrinsic mechanism vanishes or becomes unnoticeable [6, 48, 195, 217, 234].

The damping behaviour in Co/Au thin-films in comparison with Co/Pt can be attributed to two main reasons. Firstly, Pt has greater miscibility, which is considered as additional factor that can impact damping mechanisms at the interface, thus increasing α_{eff}. The interface nature analysis for both thin-films may supports this [238], which shows a lower intermixing for Au with Co than Pt .This may leads to a lower two-magnon scattering effect at the interface in the case of Co/Au. Secondly, the density of crossing electrons at the Fermi level from the d band state for Au is low compared with Pt [246]. This means Au makes a weak contribution to the intrinsic damping when coupled with Co, as shown in Fig 6.5. Even though $Ni_{81}Fe_{19}$/Pt and Co/Pt have the same general damping trends it can be seen that damping in $Ni_{81}Fe_{19}$/Pt is higher at lower d_{Pt}, as it is shown in Fig. 6.3 (a) and (c). As $Ni_{81}Fe_{19}$/Pt has a fcc and Co has a hcp crystal structure, this may change the interfacial interaction between those two materials with Pt, thus it may be attributed to higher spin-mixing conductance across the interface when the coupled materials have the same structure like in the case of fcc $Ni_{81}Fe_{19}$ with fcc Pt [164, 247]. Fig. 6.1 (d) shows the structural differences for Co (10 nm)/Pt (4 nm) and $Ni_{81}Fe_{19}$ (7 nm)/Pt (4 nm) thin-films, where the peaks for both are almost in the same position, they also shows the same peak for fcc Pt [151, 237]. The XRR result also shows that the interface width for $Ni_{81}Fe_{19}$ is larger than Co, which supports the higher interfacial mixing.

The spin-mixing conductance was estimated for both Co/Pt and $Ni_{81}Fe_{19}$/Pt using the damping data in this study. It is worth mentioning that the calculation was applied for thin-films where Pt thickness was more than 1 nm. This is because in this range, intrinsic damping is the dominant mechanism and there is minimum extrinsic contribution to damping , which is essential for the validity of the spin-mixing conductance value. The equation that can be used to show the dependence of spin-mixing conductance on damping changing is:

$$\Delta\alpha = \alpha_{\text{eff}} - \alpha_0 = \frac{g\mu_{\text{B}}}{4\pi M_{\text{eff}} d_{\text{FM}}} g_{\uparrow\downarrow}^{\text{eff}} \tag{6.3}$$

where g is the Landé g-factor, μ_{B} is the Bohr magneton, M_{eff} is the effective saturation magnetisation and $g_{\uparrow\downarrow}^{\text{eff}}$ is the effective spin-mixing conductance. This was done using the damping bulk value reported in the literature for hcp Co 0.011 [77] and fcc $\text{Ni}_{81}\text{Fe}_{19}$ 0.010 [55]. The saturation magnetisation is taken from the experimental results and used to obtain the spin-mixing value for the damping value at the mentioned d_{Pt} for these two thin-films. The results of spin-mixing conductance were $38\ \text{nm}^{-2}$ and $125\ \text{nm}^{-2}$ for Co/Pt and $\text{Ni}_{81}\text{Fe}_{19}$/Pt respectively, which are comparable with the recent experimentally observed value [148]. The higher value in spin-mixing conductance for $\text{Ni}_{81}\text{Fe}_{19}$/Pt also suggests that interface mixing between Co and $\text{Ni}_{81}\text{Fe}_{19}$ with Pt is different, which may be related to the crystal structures of hcp Co and fcc $\text{Ni}_{81}\text{Fe}_{19}$. This is supported by recent work on Co/Ir, where the Co structure at the interface was either hcp or fcc [151].

In Fig. 6.3 (b), the precessional frequency and saturation magnetisation as a function of d_{Pt} show similar trends, where M_{S} increases as the Pt capping layer increases. The increase in the net moment may be linked with proximity induced magnetisation (PIM) from Co to Pt [195]. However, the effect of PIM on damping is still unclear and debatable [148]. Furthermore, it can be seen from the figure that the initial M_{S} is lower than that reported in the literature. This may be attributed to oxidation of the uncapped Co surface. This supports the significant changes in the magnetisation when d_{Pt} becomes 0.6 nm, which means that the Pt forms a layer on the Co surface preventing oxidation. This cannot be the case when the magnetisation reaches a large value for d_{Pt} = 2 nm. By reviewing the crystal structure and the saturation value, it can be explained that when Co/Pt thin-films form a hcp crystal structure, M_{S} can reach this value. This is also supported by XRD analysis of this work and recently published study [151].

The results are in good agreement with the theoretical analysis of damping behaviour in Co/Pt and Co/Au as a function of Pt and Au thickness layers by Barati *et al.* [6, 48]. This is illustrated in Fig. 6.6 (a) and (b), which compares the results. The additional increase in damping in region I, as explained, is attributed to the extrinsic mechanism which was not calculated in the theoretical study. The peak position in region II shows the same thickness range at which damping reaches its maximum peak. In region III, the damping decreases to an intermediate damping value and levels out with further increases of d_{NM}. The oscillations in (b) cannot be observed in (a) because the roughness of the samples; however, the agreement between this work and the theoretical study is very good. Finally, this work also agrees with the calculations of the damping contribution from each mono-layer in the NM layer for both Pt and Au where, it shows that the contribution to damping can be attributed to the interface nearest the mono-layers in FM/NM thin-films.

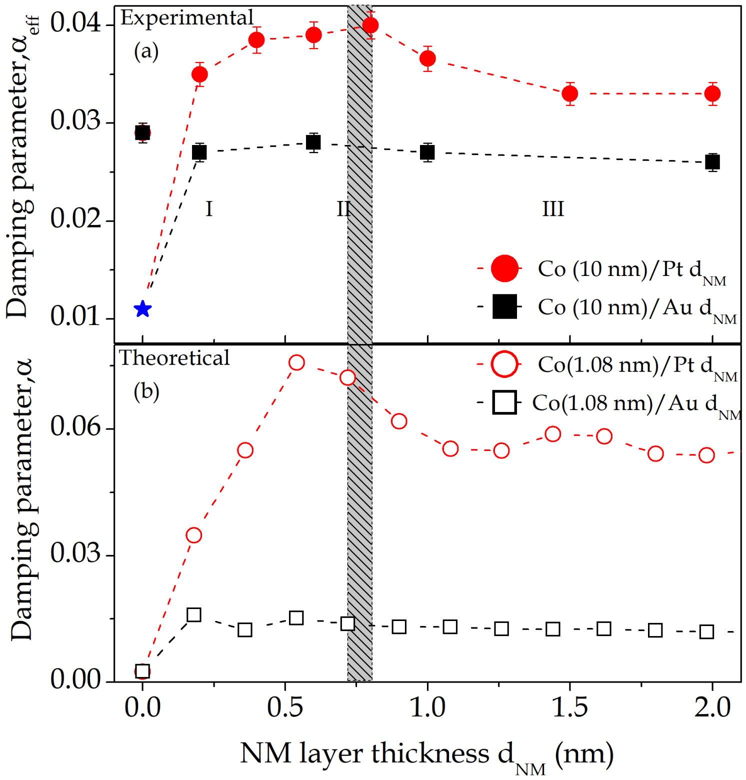

FIGURE 6.6: A comparison between (a) experimental and (b) theoretical (adapted from Ref. [6]) variations in damping data for Co/Pt and Co/Au as a function of d_{NM}. The star symbol is the literature value for pure cobalt.

6.5 Chapter Summary

In this chapter, a study was done with the aim to investigate precessional damping in a variety of FM/NM thin-films: Co/Pt, Co/Au and $Ni_{81}Fe_{19}$/Pt. The study focused on the dependence of damping enhancement on the NM = (Pt and Au) thickness within the sub-nanometre regime. The results show that damping in Co and $Ni_{81}Fe_{19}$ show an increase as a function of d_{Pt}, followed by a peak before it falls back, then stabilising to a low constant value that is higher than the bulk damping values for both Co and $Ni_{81}Fe_{19}$. While for d_{Au} almost no precessional damping dependence was observed. Crystal structure investigation techniques were used to help explain the damping evolution such as XRR and XRD, which aid the explanation. Intrinsic and extrinsic damping mechanisms are related to the damping enhancement. The extrinsic mechanism was related with the d-d hybridization effect at the Co/Pt interface when Pt coverage was partial in sub-nanometre range. This gives rise to two-magnon scattering at the interface due to these inhomogeneities, while these inhomogeneities are lost at d_{Pt} higher than one nanometre. The intrinsic mechanism is more dominant at high ranges of Pt thickness. A comparison between the damping behaviour of Co/Pt and $Ni_{81}Fe_{19}$/Pt was carried out through the calculation of the spin-mixing conductance, which showed that the latter is higher for $Ni_{81}Fe_{19}$/Pt. Furthermore, this is also supported by the structural analysis, where it showed different crystal structure type for both thin-films at the interface. Finally, the results of this study give a deeper understanding of the mechanisms of the complex damping interactions as the thickness of the NM layer increases and due to the development of the interface. Also, it shows the most effective mono-layer of the NM capping in terms of contribution to the effective damping parameter.

Chapter 7

Damping Modification Through Interface Intermixing in FM/NM Bi-Layer Microstructures

7.1 Introduction

The interface modification effect, via focused ion-beam irradiation (FIB), on magnetic damping and magnetisation properties of bi-layer $Ni_{81}Fe_{19}/Pt$ thin-films was studied in this chapter. The magnetic properties of FM materials are an important factor in magnetic data storage and sensor applications and drives research in spintronics and magnonics technology concept [248–250]. Optimising magnetic damping in FM materials is generally important for applications, where low magnetic damping enhances spin-transfer torque random-access memory and magnonic devices, while high damping is preferred in data storage devices due to the data bit rate process improving. Low damping leads to a reduction in the write-current and facilitates spin-wave propagation, and high damping will reduce the precessional dynamics, thus enhancing the suppression of the precession of the magnetisation vector. Lithographic patterning has been recently used to control spin-wave [2] propagation in magnonic crystals [251–254] and also used to control domain wall properties through modifications of the shape and anisotropy in FM thin-films by forming nano-wire structures [255, 256]. Fabricating such structures is a complicated process which may increase the chance of creating defects and inhomogeneities at the nano-scale. In order to control the impact of defects and inhomogeneities on magnetic behaviour, extra care should be taken.

Circular dots of 30 μm diameter bi-layer thin-films were investigated using an all-optical time-resolved magneto-optical Kerr magnetometry. Magnetic damping in the time domain and the spatial coherence of the magnetisation dynamics precession were analysed using the Landau–Lifshitz–Gilbert equation. The dimensionless damping parameter α_{eff} and resonant frequency f were extracted as a function of irradiation dose in the range of 0-3.3 (pC/μm^2) or 0-2.06 $\times$ 10^{15} (Ga$^+$/cm^2), where it indicates the interfacial mixing widening and sample alloying. The effective damping variation was interpreted with both variations of the intrinsic and extrinsic mechanisms at the interface. The results represent a better understanding and a level of control regarding tuning damping for enhanced magnetic device performance. This work is published in Nature publication, *Scientific Reports* journal [4].

In this chapter, a step towards understanding the interfacial structure's effect on damping is done through studying engineering of the interface of the bi-layer $Ni_{81}Fe_{19}$ 10 /Pt 3 nm with FIB irradiation with a low Ga$^+$ dose. As discussed in Chapt. 5, the ballistic cascade is the main effect for interface intermixing with a low level of ion implantation up to $\sim$ 1 % and relatively low sputtering of the thin-film surface. Damping as a function of the Ga$^+$ irradiation dose is compared in this chapter with a study that used Cr and Au as the capping layers on $Ni_{81}Fe_{19}$ with a low ion dose. The damping behaviour in this study was explained through the reduction of the intrinsic mechanism by the reduction of the capping layer's thickness in the case of Cr, while for Au the main reason for damping enhancement was extrinsic due to the increase in the inhomogeneities in the system [222]. A time-resolved magneto-optical Kerr effect (TR-MOKE) microscope was used to obtained damping, precession frequency and spatial coherence of the dynamic for the investigated samples. This was done in the S.N. Bose Institute for Basic Sciences, Kolkata, India by A. Ganguly.

Many magnetic phenomena have been revealed in bi-layer and multilayer systems such as spin-dependent scattering in giant magnetoresistance (GMR) multilayers [256], interface exchange coupling, interface hybridization, spin-injection [257, 258] and spin-pumping [259]. The interface properties are a key factor in all these phenomena, where the electronic structure and interaction behaviour are significantly affected by the modification of this layer. Thus, the modification of the interface gives the opportunity to investigate the interface's role in the magnetic behaviour. As discussed in Chapt. 4 and 6, the origin magnetic behaviour may linked with spin-orbit coupling and the electronic interaction in the s and d orbitals, which explains the intrinsic damping to some extent [179, 260]. The extrinsic mechanism is linked with defects and inhomogeneities which gives rise to the two-magnon scattering [261].

7.2 Experimental Details and Fittings

A set of 10 nm of $Ni_{81}Fe_{19}$ films capped with 3 nm of Pt were grown on a thermally oxidised silicon wafer, by the magnetron sputtering in a UHV deposition system with a base and growth pressure of $\sim 9 \times 10^{-8}$ and 1×10^{-3} respectively. Disks of 30 μm diameter, as illustrated in Fig. 7.1, were patterned using electron beam lithography. The irradiation was at normal incidence on the fabricated thin-films surface using an FEI Dual-beam FIB system with a circular ion beam focus area of 700 μm^2, this was done by J. A. King. The ion irradiation dose was gradually increased from 0 to 3.3 pC/μm^2; 0 to 2.06×10^{15} (Ga^+/cm^2). $Ni_{81}Fe_{19}$ was selected because of its relative low magnetic anisotropy. This will focus the study to the impact of Pt, as a protective and capping layer, and its role while the interface is widened, where Pt is known for its strong SOC [183] and proximity-induced magnetic moment, even though PIM is still not clear enough.

X-ray measurements of the as deposited thin-film show that both $Ni_{81}Fe_{19}$ and Pt have a fcc crystal structure with an interface width range of less that 1 nm, which shows both intermixing and topological roughness. A comparison with a study on $Ni_{81}Fe_{19}$/Au thin-films irradiated with lower Ga^+ showed that the Au capping layer became very thin and the film developed into a compositionally graded $Ni_{81}Fe_{19}$-Au alloy [98, 99], so it is logical that the extent of these two effects will be higher, the ion-beam irradiation is largely ballistic and Pt is similar to Au.

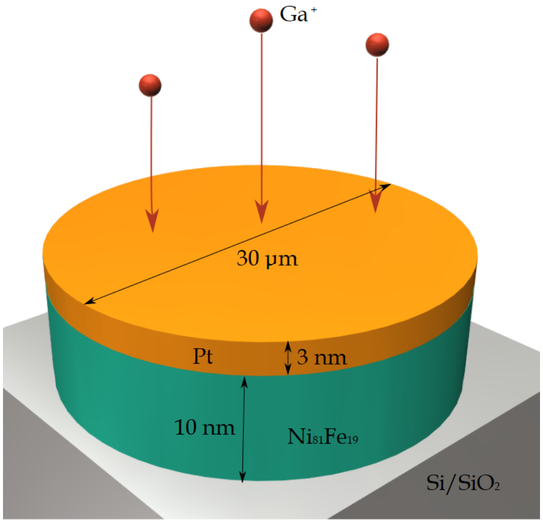

FIGURE 7.1: Schematic illustration of a bilayer of a $Ni_{81}Fe_{19}$ 10 nm/Pt 3 nm circular structure with ion-beam irradiation.

Time-resolved magnetisation dynamics were measured by using a TR-MOKE microscope. The samples were mounted on a stage where the external magnetic field was biased out-of-plane by an angle of 5°, where the magnetisation of the sample aligned with the H_{ext}. Laser source was used to pump and probe the magnetisation dynamics using the all-optical femtosecond method as a function of time delay with respect to the applied external field (for more information regarding the experimental setup see Chapt.3 and [241]). The stage was used to acquire a Kerr image of the sample under the probe spot at a specific X-Y-Z position and fixed time delay, where all the measurements were executed at room temperature.

An example is shown in Fig. 7.2 (b) of the evolution of the magnetisation of a part of a circular patterned disk, for a disk irradiated with 3.1 pc/μm^2 or 1.9×10^{15} Ga$^+$/cm^2 under a 0.8 kOe bias field. As can be seen in the figure, there are three regions with respect to the time delay (t). In region A, $t < 0$, the image shows no dynamics in the magnetisation, where in this region the demagnetisation laser pump pulse has not been applied yet. Region B shows the effect of the sample's recovery from demagnetisation, where it shows ultrafast magnetisation changing with quick relaxation as the magnetisation dynamics recover due to the fast energy dissipation via the thermal bath with the lattice [262]. Finally, in region C there is a slower relaxation, where a precession of the magnetisation with time is superimposed with the exponential recovery of the Kerr value to its initial value. This is illustrated by the red fit line in the same figure of the oscillation damped signal, where this is the description of the LLG equation.

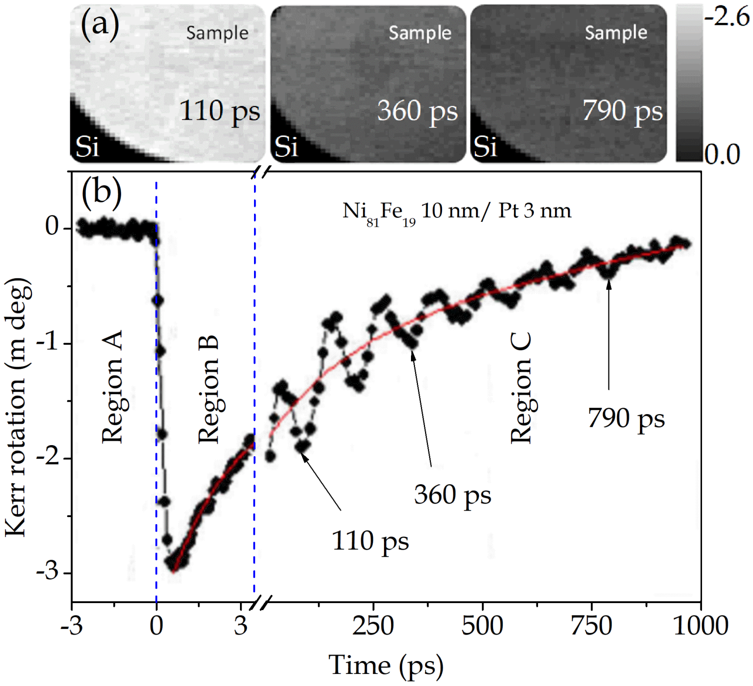

FIGURE 7.2: Shows (a) Time-resolved Kerr images of the sample at three time delays. (b) A raw TR-MOKE data trace from a sample irradiated with ion dose d = 3.1 pC/μm^2, 1.9×10^{15} Ga$^+$/cm^2, as a function of the time delay [4].

In the same figure (a), composite scanned Kerr images for the same sample at selected time delays are presented. The images are linked with (b), where the time is indicated by arrows. It is shown by the images the brightness scale that the Kerr rotation reduces within the time range of 100 ps to 360 ps and then to 790 ps. It can be seen that the image shows a spatially uniform magnetisation dynamics across the observed circular area and no multiple spin wave modes can be seen. This was seen for all the samples investigated in this work, which eliminates dephasing, two-magnon contributions to the damping. Furthermore, the sample size in comparison with the excitation and probe size, 1 μm^2, excludes the effect of the disk boundaries [249].

In order to extract the effective damping parameter, α, the background was extracted using

$$M(t) = M(0)e^{\frac{-t}{\tau}} \sin(2\pi f t - \phi) \tag{7.1}$$

where the relaxation time τ is related with α by the relation $\tau = \frac{1}{2\pi f}\alpha$, f is the precessional frequency and ϕ is the initial oscillation phase. By fitting this equation as shown in Fig. 7.2 (b), the damped precessional behaviour is isolated from the general exponential recovery of the Kerr signal. Examples of the isolated damped precession can be seen in Fig. 7.3 (a), where a comparison is shown between $Ni_{81}Fe_{19}$ and $Ni_{81}Fe_{19}$/Pt thin-films, under a 1.8 kOe external field and a Pt-capped thin-film irradiated with a 0.3 pC/μm^2 dose. It can be seen from the figure that the precessional damping from the bi-layer is faster than the uncapped $Ni_{81}Fe_{19}$ with α_{eff} of 0.15 and 0.042 respectively.

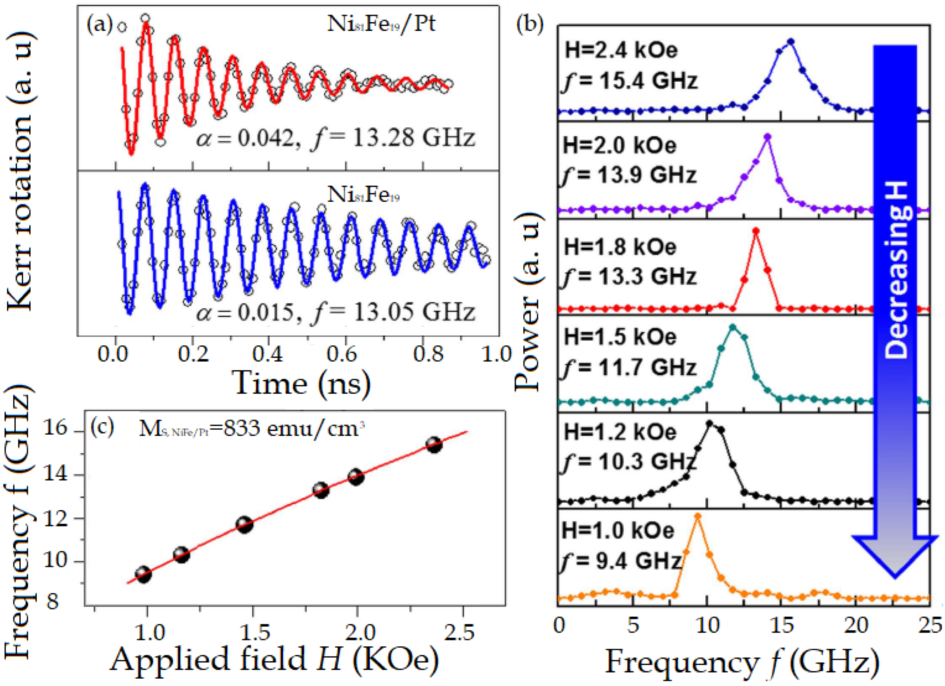

FIGURE 7.3: A comparison of TR-MOKE traces between (a) NiFe/Pt (dose = 0.3 pC/μm^2) and NiFe films. Symbols correspond to experimental data while the solid curves are fits to Eq. 7.1. (b) Power spectra of the NiFe/Pt sample at different bias field values H. (c) Frequency vs the bias magnetic field for the NiFe/Pt (d = 0.3 pC/μm^2) sample. Here the symbols represent experimental data points and the solid curve is a fit of the Kittel formula [4].

The damping value for the uncapped $Ni_{81}Fe_{19}$ is consistent with the bulk damping value reported in the literature, while the increase in the damping value for the bi-layer $Ni_{81}Fe_{19}$/Pt is by a factor of 3. This can be explained by the spin-pumping effect from the FM to the NM layer [262, 263]. It was found that the frequency for the uncapped thin-film was 13.05 GHz, while for the bi-layer thin-film was 13.28

GHz, this also indicates the increasing moment which is included at the interface by adding Pt as a layer adjacent to $Ni_{81}Fe_{19}$ due to Pt's PIM [183]. It can also be seen from Fig. 7.3 (b) the frequency reduction with the field reduction where it shows a monotonic relationship. As mentioned in Chapt. 3, this method can also be used to extract more than α_{eff}, where the saturation magnetisation and the gyromagnetic ratio can be extracted by using the Kittel formula. This can be seen Fig. 7.3 (c) , where the formula was fitted to precession from which the saturation magnetisation, M_S, was obtained as 833 emu/cm^3, with a fixed gyromagnetic ratio to 0.0176 GHz/Oe.

7.3 Results and Discussion

The overall magnetic damping dependence of $Ni_{81}Fe_{19}$ 10 nm/Pt 3 nm thin-films on the irradiation dose can be seen in Fig. 7.4, where the upper x-axis is the ion irradiation dose (d_{ir}) in Ga$^+$/cm^2 units and the lower axis is in pC/μm^2. The α_{eff} behaviour as a function of d_{ir} shows two distinct regions, I and II. In region I the effective damping increases monotonically with d_{ir} it reaches a peak value of 0.06 at the d_{ir} value of 2.0 pC/μm^2, 1.25×10^{15} Ga$^+$/cm^2, then it falls rapidly as d_{ir} increases further.

In order to understand the dependence of α_{eff} on d_{ir} in region I, the damping behaviour for $Ni_{81}Fe_{19}$/Pt was compared with $Ni_{81}Fe_{19}$ /Cu at the same dose range, as shown in Fig. 7.5. In spite of the offset shifting value of 0.019 between $Ni_{81}Fe_{19}$/Pt and $Ni_{81}Fe_{19}$/Cu, the damping values in both thin-films increases linearly as a function of d_{ir} at a rate of 0.015 pC/μm^2. The offset may be explained by the spin-pumping effect and the strong spin-orbit coupling of Pt, which makes it a good spin sink [134, 194, 264]. The α_{eff} value for the $Ni_{81}Fe_{19}$/Cu with irradiation dose = 0 is 0.015. The latter is comparable with the damping value of uncapped $Ni_{81}Fe_{19}$, where this suggests that Cu has insignificant impact on damping enhancement [194]. The same linear increase of damping is observed in both thin-films systems and cannot be justified by only SOC and spin-pumping effects. Furthermore, Ga$^+$ implantation is very low, within 1-2 %, which also fails to explain the linear dependence of damping on d_{ir} [99]. However, as it is known one of the effects of ion-beam irradiation

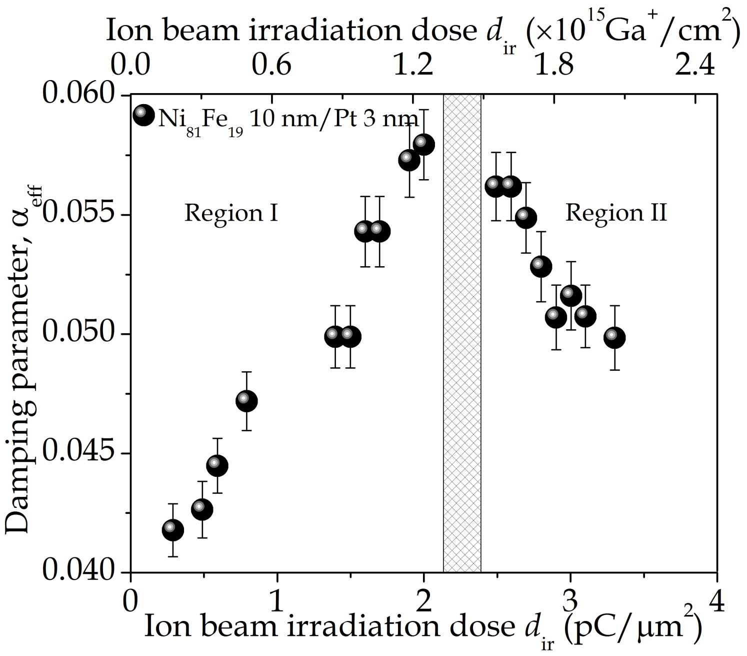

FIGURE 7.4: Damping parameter is plotted as a function of dose. The shaded box represents the transition between regions I and II.

is to produce an intermixing in the sample by the collision of the ions with the NM atoms, which forces them to move in the $Ni_{81}Fe_{19}$, this will cause structural changes and defects in the FM thin-film. These defects are known as a source for the extrinsic damping mechanism called two-magnon scattering, which can increase the effective damping [100]. With the increase of d_{ir}, the intermixing area increases, thus the defect density increases and the effective damping increases [98]. It was shown in an earlier study that the width of the intermixed region increases linearly with d_{ir} [222]. This suggests that the damping enhancement will also vary linearly as a function of d_{ir} through the two-magnon scattering effect, as this was also reported in a previous study on $Ni_{81}Fe_{19}$/Au [222]. As we know, increasing defects or disorder density at the FM/NM interface breaks the symmetry in this region [99, 235, 265]. This suggests that two-magnon scattering is the dominant mechanism for the d_{ir} dependence of damping on d_{ir} in region I. This also agrees with the results from several studies which focused on the interface of FM material coupled with Pt [99, 109, 217, 219, 235, 266, 267].

In Fig. 7.4, between regions I and II, damping was expected reached a maximum value from the observed trend of these regions. In region II, the dependence of α_{eff}

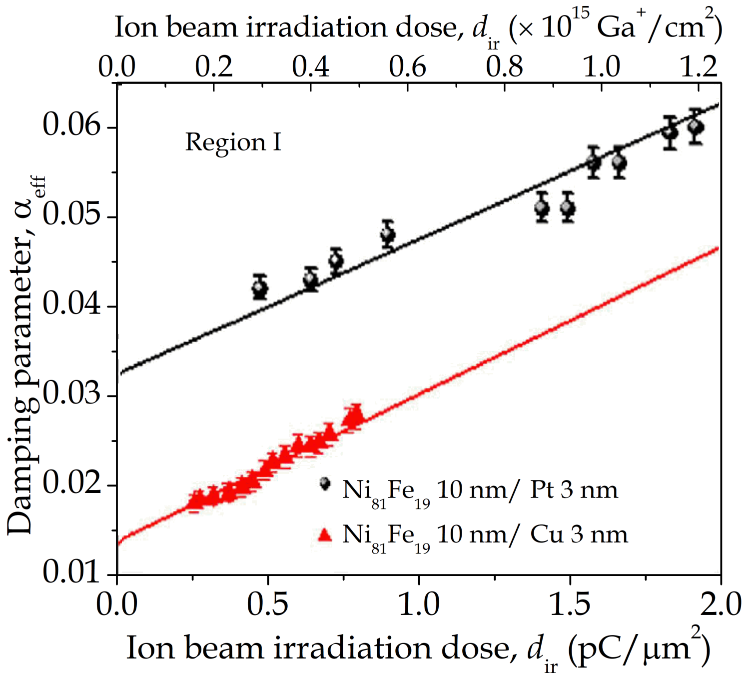

FIGURE 7.5: Variation of damping parameter as a function of irradiation dose in the lower dose regime for $Ni_{81}Fe_{19}$/Pt (filled circles) and $Ni_{81}Fe_{19}$/Cu (filled triangles).

on d_{ir} shows a different behaviour, where the damping decreases with further increases of d_{ir} beyond 2.4 pC/μm^2, as shown in Fig. 7.4. According to the structural analysis increasing d_{ir} beyond 2.4 pC/μm^2, 1.5 × 10^{15} Ga$^+$/cm^2 leads to the domination of the cascade ballistic intermixing. More insight regarding the development of the $Ni_{81}Fe_{19}$/Pt interface can be gained through the x-ray structural analyses from previous studies on $Ni_{81}Fe_{19}$/Au thin-films, which shows the effect of the focused ion-beam irradiation dose on the interface width [98, 99, 109, 268].

The similar atomic masses between Pt and Au allow such a comparison because momentum transfer is the main effect of the ballistic intermixing. It was demonstrated in these studies that the interface width for unirradiated $Ni_{81}Fe_{19}$/Au would be 1 nm also, as shown in Chapt. 5, and would increase with increases of d_{ir} linearly by increasing the intermixing between the FM and NM adjacent layers. Increasing intermixing creates a compositionally graded NiFe-Pt alloy layer between $Ni_{81}Fe_{19}$ and the Pt capping layer. The irradiation dose in the previous studies on $Ni_{81}Fe_{19}$/Au was limited to 1 pC/μm^2, which shows the same results regarding the intermixing of $\sim$ 4 nm, which also shows that about 1 nm of the NM capping layer is lost as a result of the sputtering effect of the ion-beam irradiation [98–100], see fig 4.6 and 4.7.

However, in this study d_{ir} extended beyond 2 pC/μm^2, which logically increased both intermixing and surface sputtering effects. On this basis it is suggested that the compositionally graded alloy width will extend through much of the $Ni_{81}Fe_{19}$ and also result in losing most of the Pt capping layer. This will form a NiFe-Pt thin-film, where the Pt concentration increases towards the thin-film surface. Thus, the reduction in the Pt capping layer's thickness will lead to reduced spin-pumping and spin-diffusion contribution in the intrinsic damping of the new NiFe-Pt alloy, which will lead to a fall in the effective damping parameter α_{eff}.

Fig. 7.6 shows the dependence of α_{eff} as a function of precessional frequency, f that is controlled by the bias field, for $Ni_{81}Fe_{19}$/Pt thin-films for three selected ion irradiation doses. It can be seen that for d_{ir} = 0.3 pC/μm^2, damping is independent of f, which shows intrinsic damping dominates α_{eff}. For the second and the third selected d_{ir}, 2 pC/μm^2 and 3.3 pC/μm^2, respectively, α_{eff} decreases with increases of frequency with nearly an identical trend. This shows that an extrinsic contribution is present in the effective damping. Increasing the applied field, H_{ext}, increases the precessional frequencies, which means that the magnetic dynamics are affected by H, thus extrinsic scattering is suppressed. The variation of damping on f for each dose suggests that the extrinsic mechanism is the reason for damping increasing, see Fig. 7.4, region I. Connecting this with the third dose indicates that the extrinsic mechanism's contribution to the effective damping reaches a saturation where the identical slope supports this view. As a result of α_{eff}'s variation in Fig. 7.4, region II may be related to the intrinsic damping contribution more than the extrinsic.

Fig. 7.7 (a) shows the fast Fourier transform ,FFT, power spectra of the frequency changing with the field for the three selected doses. It can be seen from the figure that the reduction of f is larger, between 0.3 and 2 pC/μm^2, while there is very little changes in f between 2 and 3.3 pC/μm^2. This variation is summarised in Fig. 7.7 (b) as the frequency is plotted as a function of d_{ir}, which shows two distinct regions, I and II. In the first region, f shows a linear decrease with increasing d_{ir}, until the dose reaches 2 pC/μm^2, then in region II, f does not show any changes as the ion-beam

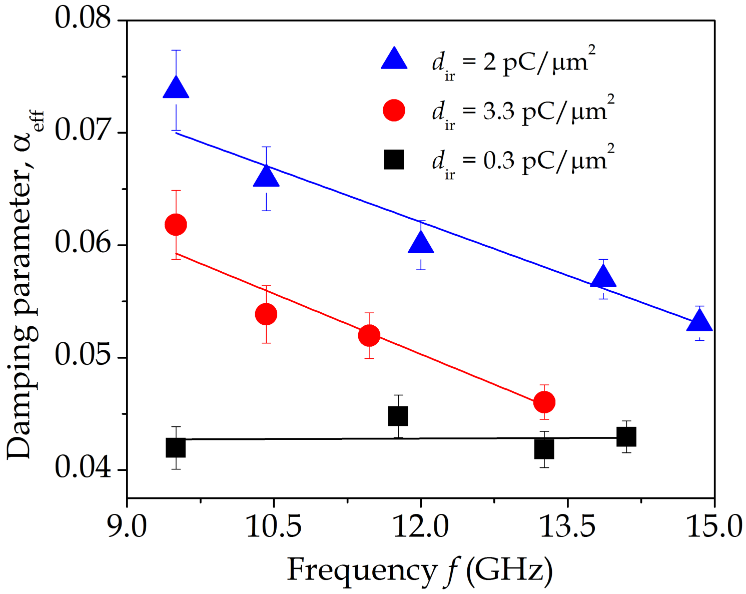

FIGURE 7.6: Dependence of the damping on the precession frequency, controlled by the bias field, for three different doses, with their linear fits.

irradiation dose increases further. As it has been reported in the literature, increasing the concentration of Pt in the Ni-Pt alloy will lead to a reduction in the magnetic moment of the alloy [261]. This may link the reduction of f with the reduction of the magnetic moment as the Pt concentration increases in Ni-Pt or Fe-Pt alloys in the $Ni_{81}Fe_{19}$ layer. Linking this with Fig. 7.4, increasing d_{ir} beyond 2 pC/μm^2 will not increase the number of Pt atoms in the $Ni_{81}Fe_{19}$ layer significantly but it rather increases the intermixing of the compositionally graded alloy, which agrees with the stability of f with increasing d_{ir} in region II.

Fig. 7.7 (c) shows another indication that can supports the explanation: the relaxation time (τ) as a function of d_{ir}. In this figure both fast, τ_1, and slow, τ_2, relaxation times are plotted, where the first relaxation time is linked with energy dissipation via electrons and spin wave to that lattice, while the second term is linked with the dissipation of the energy from the lattice to the surrounding. Both τ_1 and τ_2 are related with the specific heat of the lattice (S), which can represent an indication of the S state. It can be seen from the figure that both τ_1 and τ_2 show larger changes when $d_{ir} > 2$ pC/μm^2, which may provide evidence of the lattice changing by the formation of the $Ni_{81}Fe_{19}$-Pt alloy in region II.

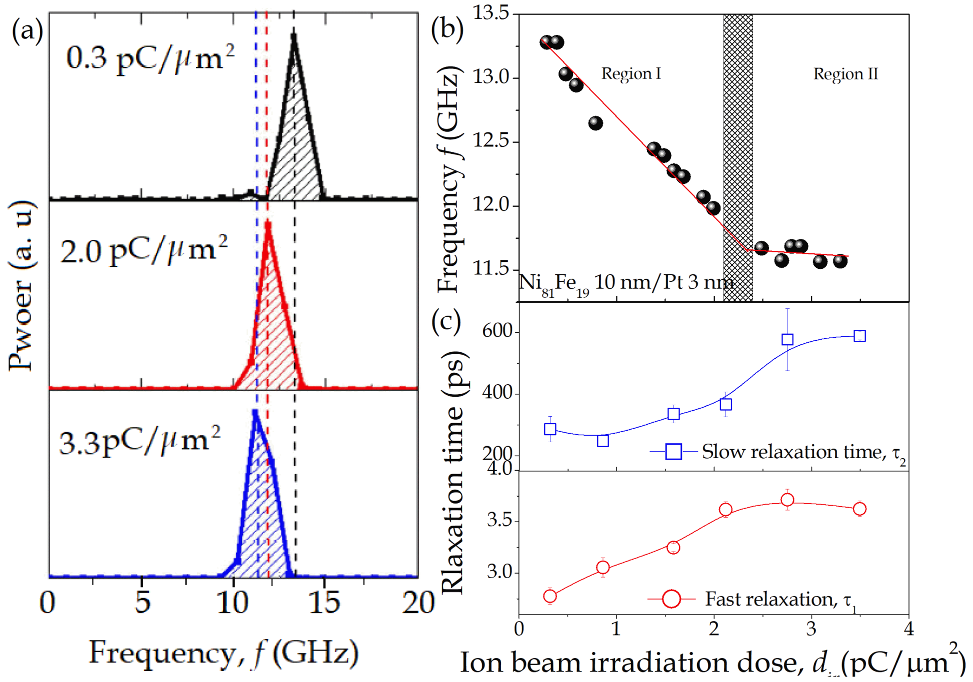

FIGURE 7.7: (a) FFT power spectra of the TR-MOKE data of ion irradiated NiFe/Pt samples at three different doses. (b) Variation of frequency f as a function of dose. Symbols are the experimental data and solid lines are linear fits. The shaded box represents the transition between two regions. (c) Magnetisation relaxation times τ_1 and τ_2 are plotted as a function of dose. Here the symbols are obtained from experimental data while the solid lines are only guides to the eye [4].

7.4 Chapter Summary

In this chapter the magnetisation precession was modified through the engineering of the interface of $Ni_{81}Fe_{19}$/Pt thin-films via Ga^+ ion irradiation. This was measured using TR-MOKE microscopy in order to study the variations of the ultrafast magnetisation dynamics and the slow and ultrafast relaxation times, the precession of frequency and the damping parameter as a function of the irradiation dose. It was found that the effective damping, precessional frequency and the relaxation times show two distinct regions of behaviour. In the first region, the low irradiation dose regime, the precession frequency falls and damping increases linearly as a function of the ion irradiation dose in the range 0-2.0 pC/μm^2. In the second region, ion irradiation dose > 2.4 pC/μm^2, the precession frequency shows almost no changes while damping falls slowly. The high magnetic damping for $Ni_{81}Fe_{19}$/Pt in comparison with the uncapped $Ni_{81}Fe_{19}$ is linked with the spin-pumping and spin-diffusion length effects which are provided by the Pt cap layer, as it is known as to be good spin sink. Furthermore, the increasing damping for low-dose irradiation shows an extrinsic nature associated with dislocated atoms and the creation of defects within the bi-layer thin-film, which brings about the two-magnon scattering mechanism. In the high dose irradiation regime, the intermixed interface will extend through the full thin-film, which will finally be transformed into a compositionally-graded alloy. Furthermore, sputtering of Pt capping layer thickness will lead to a reduction of the thickness below the spin-diffusion length, hence, a reduction of damping due to less contribution from SOC and the spin-diffusion length. This work gives insight into the magnetisation dynamics for understanding spintronic and magnonic applications.

Chapter 8

Understanding the Role of Damping and DMI on Magnetisation Reversal in Nanowires

8.1 Introduction

Domain wall propagation in nanowires has been the focus of interest of much research, where this magnetic process is key to applications such as magnetic logic, sensors and magnetic memory concepts [269–272]. In such applications, the writing is governed by the magnetisation reversal by the domain wall in nanowires. The impact of NM materials, especially Pt, as an adjacent layer to ferromagnetic layers is known very well and can play a role in the magnetisation behaviour in thin-films and nano-structures. The interfacial effect for example, which can emerge through the coupling between FM and Pt, is a modification of the magnetic spin orientation via the interfacial Dzyaloshinskii-Moriya interaction (IDMI). Another effect, which has been explained in Chapt. 6 and 7, is the enhancement of the magnetic damping via d-d hybridization and spin-pumping across the FM/Pt interface. Also, modification of the magnetisation switching is shown by the flow of current via the spin-Hall effect. It is important to understand the relationship between interfacial factors such as damping and IDMI with regards to the magnetisation reversal, investigated by domain wall (DW) motion. Here a system that has a weak IDMI and enhanced damping i.e. $Ni_{81}Fe_{19}/Pt$ was studied. The effect of damping was carried out with the aid of the findings from Chapt. 6 for the $Ni_{81}Fe_{19}/Pt$ system, while IDMI was taken from the literature and together they were combined in micromagnetic simulations of DW motion in planar nano-wires. The outcome of this work provides insight to understand and control DW behaviour in nanoscale devices by changing the magnetisation reversal via damping, as a function of Pt thickness, and IDMI relative impacts.

Heavy metals have been linked with such important phenomena when they are coupled with FM material as an adjacent layer, where the strong spin-orbit coupling has an important role in such behaviour. Enhancing the precessional magnetic damping and effecting magnetisation reversal via a spin-current resulting from the spin-Hall effect are all associated with the large SOC in heavy metals [4–6, 20, 273, 274]. The occurrence of such phenomena in thin-films may enhance spintronics-based device application performance. This raises the need to understand the contribution of each mechanism, any interactions with each other and their overall impact on the system.

The interfacial Dzyaloshinskii-Moriya interaction is an effect of anti-symmetric exchange at the interface of FM/NM thin-films [32, 34, 150, 275, 276]. This exchange will raise the IDMI, which varies in terms of strength due to the coupled materials, where it is reported that Co/Pt has a stronger IDMI than NiFe/Pt thin-films [277, 278]. However, the outcomes of these different studies show a range of IDMI values in such systems [277, 279–281] with magnitude near the direct ferromagnetic exchange interaction, but the impact of IDMI on the local magnetic orientation modification is noticeable. Thus, IDMI can affect the precessional magnetisation dynamics, which shows a vital role in such systems.

Damping phenomena are associated with the spin-orbit interaction, in NM heavy metals this enhances damping significantly in FM layers via spin-pumping from the FM layer to the NM layer providing an extra pathway to dissipate energy [4–6, 276]. In order to pump the spin angular momentum from the FM layer to the adjacent

NM layer, an interfacial hybridization via the electronic d orbitals facilitates the precessional spin-waves to be pumped into the NM layer from the FM layer [4–6, 129, 282]. These effects are typically associated with enhancing intrinsic damping, while the extrinsic enhancement of damping is a result of two-magnon scattering, which is linked with the density of inhomogeneities in the system at the interface. As shown in Chapt. 6, the magnetisation precession and magnetic damping are influenced by the Pt layer's thickness, which shows a rapid increase as the Pt thickness (d_{Pt}) increases, then reaches a plateau when d_{Pt} is over 1 nm [5, 6].

On the other hand, the spin-Hall effect has been studied in bi-layer thin-films [150, 283, 284], where it shows the influence of Pt material via the interface of Co/Pt based device structures. This influence emerges by the changing current in the Pt layer, which will create a spin-current in the Pt layer that can propagate into the adjacent FM layer across the interface, by which it can affect the domain wall motion in the system [150, 274]. It has been shown that the effectiveness of the spin-Hall process is influenced by the interface of the thin-film along with the spin-Hall angle (SHA) [150, 283, 284].

The interfacial effects in FM/NM thin-films, as a result of the addition of Pt, have been investigated on the magnetisation reversal of nanowires, where the systems have strong IDMI and out-of-the plane anisotropy, while a few studies investigated the same influence in in-plane systems [285, 286]. It is also known experimentally and through in-plane micromagnetic studies that the behaviour of the DW, which is driven by the field, is controlled by precessional processes that lead to Walker breakdown [287] and it has been shown that the latter can be controlled by periodic structuring of the nanowires [288, 289]. Gaining a better understanding of the impact of damping enhancement and IDMI on the domain wall dynamics gives new fundamental physics insight and it also links to potential technological applications.

The aim in this chapter is to gain an insight into the physical mechanisms, which impact the magnetisation processes in FM/Pt nanowire systems and separate their effects. In this study the spin-Hall effect was eliminated because no charge current was injected in to the nanowire structure, which means there was no spin-current due to the spin-Hall effect. The IDMI is known as an interfacial effect which arises at the interface between $Ni_{81}Fe_{19}$ and Pt; damping enhancement, on the other hand, varies as a function of d_{Pt}. Thus, measuring the magnetisation reversal as a function of d_{Pt} can give insight regarding the effect of both damping enhancement and IDMI on the magnetisation reversal process behaviour. This was done by combining the experimental results with micromagnetic simulations, where the effect on the domain wall dynamics can show the role of damping and IDMI as a function of the development of the $Ni_{81}Fe_{19}$/Pt interface. This work is published in Nature publication, *Scientific Reports 7* (Sci. Rep. 7) [3].

8.2 Experimental and Micromagnetic Simulations Details

A set of various nanowire geometries were fabricated using electron-beam lithography lift-off method by J. Brandão in Durham University, with a magnetron sputtering deposition system. The wire geometries were modulated from parallel-sided to fixed-angle periodic triangular features, where these features were selected for their impact on the DW propagation [289]. The focus here is on the Pt thickness' effect on the magnetisation reversal. The width of the parallel-side nanowire was 250 nm, see Fig. 8.1 (a). By adding triangle features, on both edges the width changes with magnitude of 30 and 75 nm, as shown in Fig. 8.1 (b) and (c) respectively. In order to inject an individual domain wall, a pad was fabricated at one end of each wire with 7 μm $\times$ 1 μm dimensions and a tapered end was patterned on the other end to prevent DWs nucleating. $Ni_{81}Fe_{19}$ (10 nm) was grown on Si/SiO_2 and capped with Pt with range of 0-3 nm d_{Pt}. The Pt thickness and the interfacial roughness were verified using x-ray reflectivity. The MOKE system was used to investigate the magnetisation reversal behaviour mediated by DW propagation in all nanowires [290]. The MOKE measurements were repeated and averaged over the wires' length of ~ 5 μm with longitudinal geometry; extra care was taken to improve the signal-to-noise ratio by averaging many hundreds of measured field cycles.

In order to aid the results and gain a better understanding, simulations were carried out using the Mumax^3 code [291], the DMI value and the range of the effective

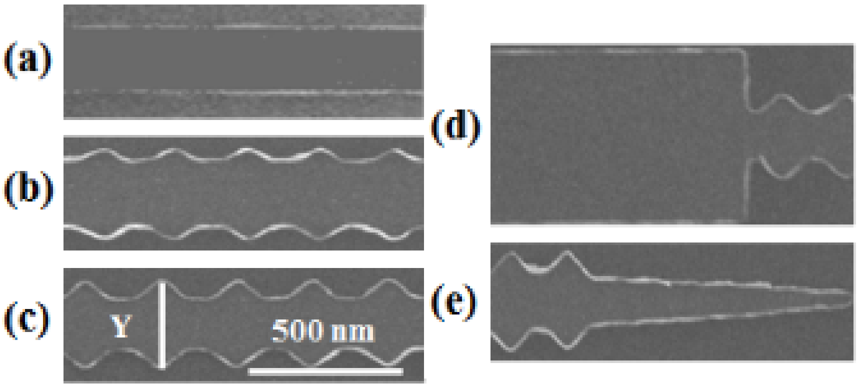

FIGURE 8.1: SEM images of nanowires of bi-layers $Ni_{81}Fe_{19}$/Pt show different geometries produced by electron-beam lithography, to study DW propagation. Pinning the potential to the DW propagation is due to the triangle features placed on the nanowire edges. It shows that the pad and the tampered shape were used to inject and annihilate DWs, respectively.

damping parameter (α_{eff}) were inserted in the simulations, which use the Landau-Lifshitz-Gilbert equation with a contribution from the effective DMI field (H_{DMI}) in the effective field $\mathbf{H}_{\text{eff}}$ as follows:

$$\frac{\partial \mathbf{m}}{\partial T} = -\mathbf{m} \times \mathbf{H}_{\text{eff}} + \alpha \mathbf{m} \times \frac{\partial \mathbf{m}}{\partial T}, \tag{8.1}$$

where T = $(\gamma M_s)^{-1}$, t is the time and the effective field can be written as follows:

$$\mathbf{H}_{\text{eff}} = H_{\text{ext}} + H_{\text{exc}} + H_{\text{ani}} + H_{\text{ms}} + H_{\text{DMI}} \tag{8.2}$$

Including the external field, exchange, magnetic anisotropy, magnetostatic fields and the DMI effective field, respectively in the energy of the system. In order to numerically study the field-driven domain wall behaviour these terms should all be considered in the general $\mathbf{H}_{\text{eff}}$.

In order to solve the LLG equation using Mumax^3 code, some magnetic parameters for $Ni_{81}Fe_{19}$ were required including the exchange stiffness constant A = 13×10^{-12} J/m, saturation magnetisation M_s = 860×10^3 A/m and zero magnetocrystalline anisotropy. The thickness, width and length of the simulated nanowires were 10 nm, 250 nm and 5 μm respectively for the parallel-sided structure. Periodic triangular edge features were implemented with amplitudes from 30 to 75 nm. The micromagnetic cell size was $5\times5\times10$ nm^3, which is reasonable with respect to the known exchange length for $Ni_{81}Fe_{19}$ [292] in the x-y plane, which can be found by

$$\text{exchange length} = \sqrt{A/K_{\mathrm{d}}}, \tag{8.3}$$

A is the exchange stiffness and K_{d} is the stray-field energy constant. Executing some simulations with a smaller cell size of 3 nm × 3 nm gave similar results. It was also found that transverse domain walls (T-DW) and vortex walls (VW) can be supported in these nanowires due to the small energetic difference [293]. However, T-DWs show higher energy and more consistency regarding its formation than in previous work [294, 295]. As a DW driver, the applied magnetic field was varied from 1 Oe to 200 Oe, while the reversal field for DW mediated magnetisation reversal was simulated over a range of α values between 0.01 and 0.1. The calculation was also done over a range of IDMI values starts from 0 up to 1 mJ/m^2 to gain better insights into DW propagation. The analysis of DW propagation dependence on both features shows no significant differences with respect to the DW chirality, which is to be expected by the symmetry of the nanowire system.

In Chapt. 6, the dependence of damping for $Ni_{81}Fe_{19}$/Pt thin-films as a function of d_{Pt} was discussed in detail. The extraction of α_{eff} was explained by fitting the magnetisation precession as it was damped, oscillating in the time domain as a single mode. The effective damping shows a rapid increase with d_{Pt} as it reaches its maximum value at a Pt thickness of 0.6 nm, then reduces again to an intermediate value and settles as shown in Fig 8.2. This was used as a guide for the experimental work and simulations here.

The dependence of damping on d_{Pt} in Fig 8.2 was explained in Chapt. 6 through the contribution of the intrinsic mechanism with the aid of the theory work [6] and the observation of the structural evolution at the FM/NM interface, which shows additional extrinsic contributions via the interface's roughness. For the $Ni_{81}Fe_{19}$/Pt interface, at $d_{\mathrm{Pt}} < 0.6$ nm, it was shown that the extrinsic mechanism emerges due to the incomplete layer formation of Pt, which will lead to the variation of the local magnetisation and damping. These variations initially change d-d hybridization

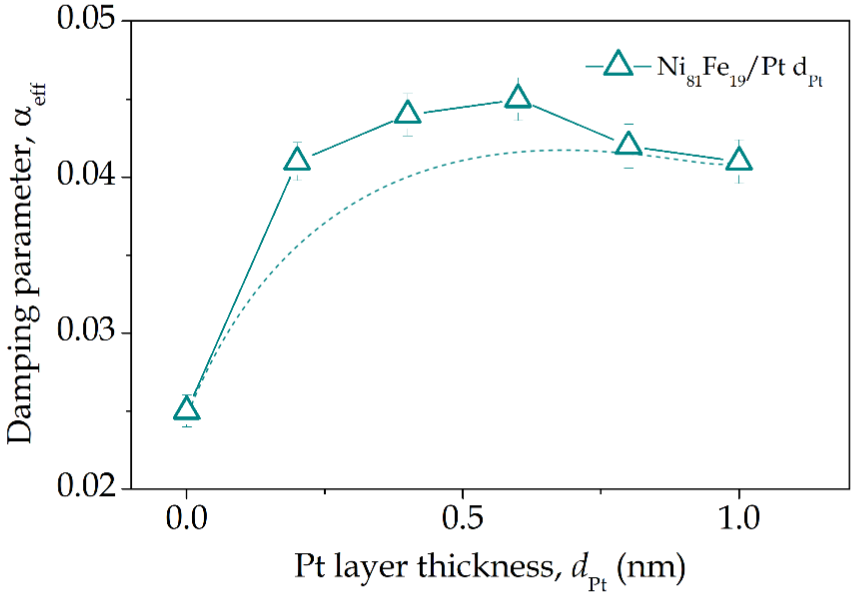

FIGURE 8.2: Effective damping parameter obtained in $Ni_{81}Fe_{19}$/Pt thin-films. The damping increases rapidly between 0 and 0.6 nm Pt thickness, then above it goes down slowly. The dashed line illustrates the expected contribution to the damping from intrinsic processes.

and spin-pumping locally at the interface, which is linked with the intrinsic mechanism; however, the variation will make two-magnon scattering arise due to the non-uniformity of the magnetisation [5]. Increasing d_{Pt} beyond 0.6 nm leads to a further enhancement for the effective damping via both mechanisms till it reaches its maximum and then levels out finally at $d_{\mathrm{Pt}} \sim 0.9$ nm. The intrinsic mechanism at this stage dominates the α_{eff} enhancement. Thus, it is logically expected that intrinsic damping will increase rapidly as d_{Pt} increases and stabilise at greater thicknesses, as shown by the dashed line in Fig. 8.2.

The enhancement of the damping behaviour as a function of d_{Pt} in studies of FM/Pt bi-layer thin-films shows a similar trend for a different range of Pt thicknesses. Such studies used different FM materials like $Ni_{81}Fe_{19}$, Co [5, 296], amorphous Finemet [199] and yttrium iron garnet (YIG) [195]. In these studies the mechanism for the damping enhancement trend may be the same, but the investigated samples show different features linked with growth conditions, material miscibilities and surface energy. This may explain the different d_{Pt} at which damping changes.

What is most important is that with Pt thickness variations, magnetisation precession and damping vary, thus this variation should be considered as an effective factor for the domain wall dynamics.

8.3 Results, Analysis and Discussion

In addition to the effect of the Pt layer thickness on the damping in $Ni_{81}Fe_{19}$/Pt thin-films, domain wall behaviour was investigated as a function of d_{Pt} in the same range in nanowires using longitudinal MOKE magnetometry to find the reversal field of DW mediated nanowire switching. As shown in Fig. 8.3 (a), the reversal field which is needed to propagate DW in $Ni_{81}Fe_{19}$/Pt 0.6 nm is higher than the one for the uncapped $Ni_{81}Fe_{19}$ wire.

This shows the role of Pt as a capping layer on the DW dynamics which increases the applied magnetic field needed for the magnetisation reversal process. As a comparison, in the same figure (b), micromagnetic simulations show hysteresis loops for the same nanowire geometries with damping parameter of 0.01 and 0.04 for uncapped and 0.6 nm Pt capped $Ni_{81}Fe_{19}$ respectively. The reversal field results in Fig. 8.3 (a) and (b) show good agreement between the experimental MOKE measurements and the micromagnetic simulations. A higher damping parameter increases the reversal field required to propagate the DW, which supports the suggestion that d_{Pt} affects the DW reversal process. This could be interpreted as the result of inhomogeneities, which increase initially due to the formation of Pt islands on the $Ni_{81}Fe_{19}$ surface that provide additional pinning or impede the DW motion. However, the reversal field trend continues to increase with increasing Pt thickness beyond 0.6 nm. The experimentally extracted values of the damping parameter as a function of d_{Pt} were in the range 0.025-0.045, while the simulations cover a wider range between 0.01 and 0.1.

The reversal field of DW propagation is plotted as a function of d_{Pt} in order to gain a full understanding of the general trend. It can be seen in Fig 8.4 (a) that in general the reversal field increases rapidly with increasing d_{Pt} from 0-0.8; beyond that the reversal field starts to slowly reach a maximum and stabilises. Another thing to

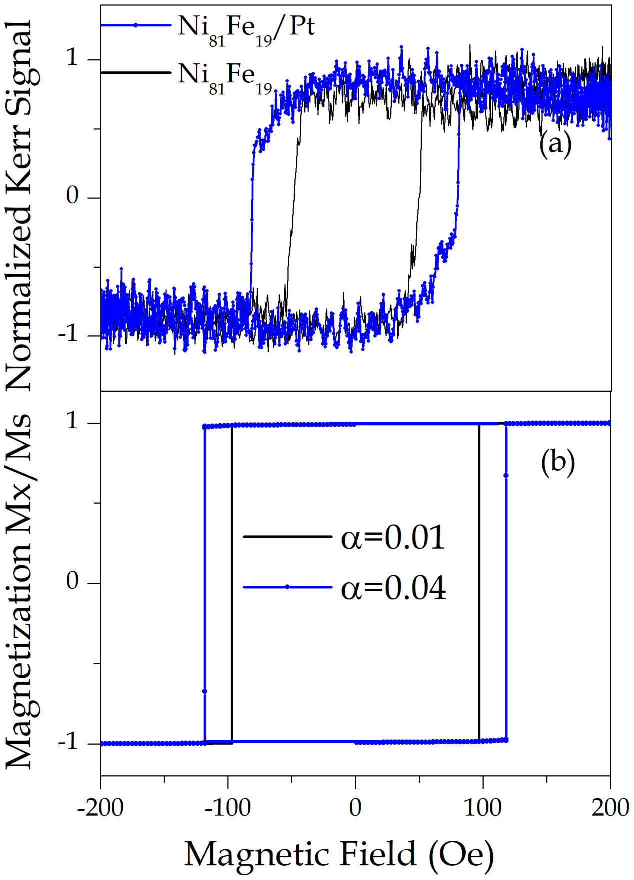

FIGURE 8.3: Examples of axial magnetic hysteresis behaviour for nanowires (triangular modulated edges with 75 nm amplitude). (a) Measured hysteresis for $Ni_{81}Fe_{19}$ (10 nm) (continuous line) and $Ni_{81}Fe_{19}$ (10 nm)/Pt (0.6 m) nanowires (dots). The reversal field is observed to be higher for $Ni_{81}Fe_{19}$ (10 nm)/Pt (0.6 m) than the $Ni_{81}Fe_{19}$ (10 nm). (b) Simulated magnetic hysteresis for nanowires with a damping parameter of 0.01 (continuous line) and 0.04 (dots), showing that the increased damping provided by the Pt overlayer enlarges the reversal field for larger damping.

note that the increasing magnitude of the reversal field increases for the nanowires with triangle features of 30 nm amplitude and increases more when feature amplitude is 75 nm. This shows the combined role of d_{Pt} and edge modulation on the DW dynamics.

To get a focused insight regarding the role of the Pt thickness effect, the normalised reversal field was plotted as a function of d_{Pt} for all three geometries as shown in Fig. 8.4 (b). It is clear that the general trend of the reversal field is independent of the geometry of the features, where the rapid increase followed by it slowly reaching a plateau occurred for all the nanowires investigated. This gives a further indication that the effect responsible for increasing the reversal field comes from the

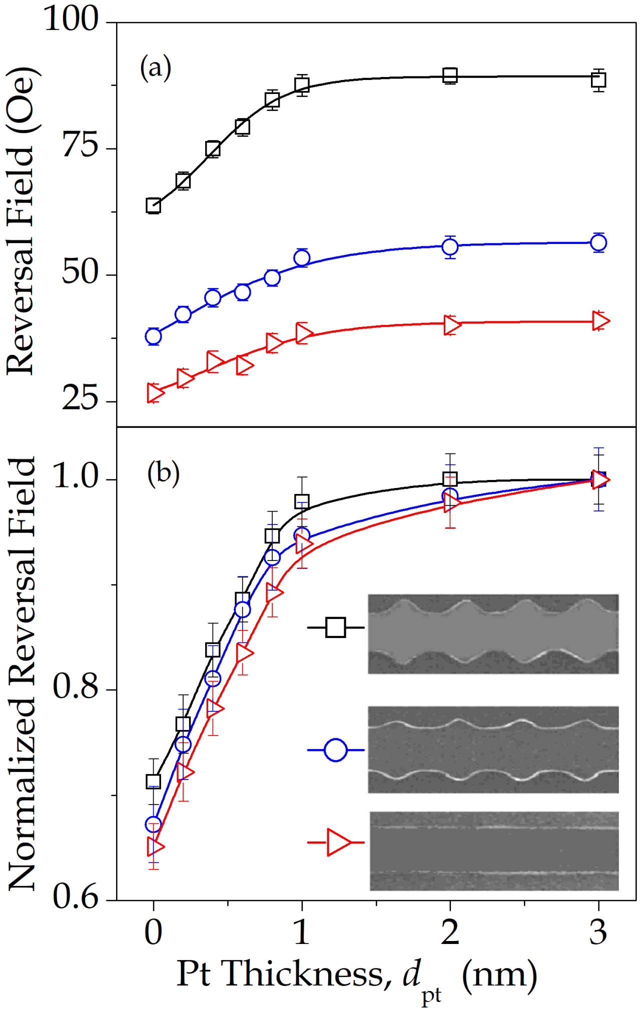

FIGURE 8.4: Reversal field as a function of Pt thickness. In (a), for different periodic edge-modulated nanowires with the general trend of the reversal field increasing as a function of d_{Pt}. In (b), the normalised reversal field shows that the reversal field independent of the nanowire geometry. Insert, scanning electron microscopy (SEM) images of nanowires show the different geometries used to study DW propagation in $Ni_{81}Fe_{19}$ with a Pt overlayer.

increase in Pt thickness up to 1 nm.

In order to explain the reversal field dependence on d_{Pt} with respect to damping mechanisms, there is a linear relation between intrinsic damping and the reversal field. As has been explained, damping enhances with increasing d_{Pt} via both intrinsic and extrinsic mechanisms, where the variation of the d-d hybridization and spin-pumping across the interface brings about both mechanisms. However, it has been shown by structural analysis that when d_{Pt} = 1 nm, a continuous coverage layer forms of Pt on $Ni_{81}Fe_{19}$ and more; the precessional frequency independence on d_{Pt} showing that intrinsic is the observed dominant mechanism. It is logical to suggest that the intrinsic mechanism increases with increasing d_{Pt} from 0.9-1 nm and then levels out for thicker Pt layers. Thus it is suggested that the DW reversal field is sensitive mainly to the intrinsic damping, rather than the extrinsic and increases linearly within this mechanism.

The micromagnetic simulations, which were done by J. Brandão, shows supportive results regarding the DW reversal dependence upon intrinsic damping, as shown in Fig. 8.5 (a). Furthermore, it has been argued that the indirect relaxation of precession will be inhibited at the length scale near to the domain wall width [297]. However, in the simulations the reversal field magnitude shows higher values than the experimental results, where this has been observed in the micromagnetic simulations for a cell size of 5×5 nm and also for 3×3 nm. The different values of the reversal field between the simulation calculations and experimental measurements may be attributed to the limitations of the physical modelling in calculating all of the various effects. For example, the simulations were executed at zero temperature, which is a known factor for increasing the reversal field; also, even though the parameters being inserted into the simulations were widely known for NiFe such as the exchange constant, the real NiFe investigated may have slightly different parameters. Finally, there are also differences regarding the simulated geometries and the real samples when edges roughness and shape accuracy in the real samples are limited, while in the simulations these factors are rendered with square cells.

The nearly linear relation between the reversal field and damping, which was shown by the micromagnetic simulations, suggests that increasing the intrinsic damping is able to explain the linear increase of the reversal field and plateau. The magnetisation precession also tends to reach an equilibrium faster when the damping is larger, which reduces the torque on the domain wall to less than that for low damping cases. This indicates that the magnetic field must be increased in larger damping cases in order to drive DW magnetisation reversal.

Besides damping there are other interfacial effects which may impact the DW dynamics, DMI affects the reversal behaviour and this was also implemented in the micromagnetic simulations. The range of IDMI values used were obtained from the

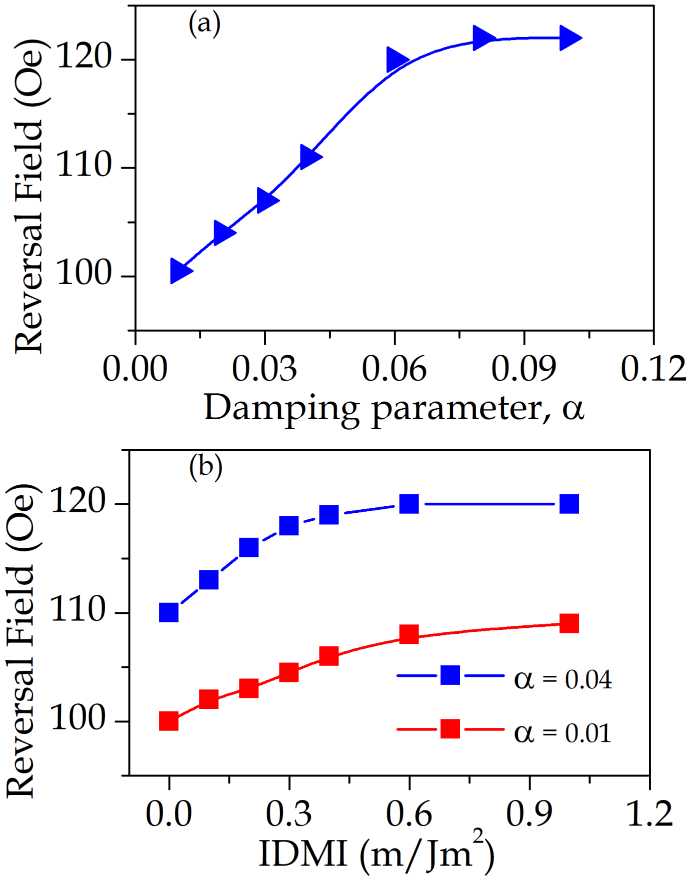

FIGURE 8.5: Reversal field simulated as a function of (a) the intrinsic damping parameter , where it shows the reversal field goes up rapidly from 0 nm to 0.6. In (b), the reversal field shows that the behaviour as a function of IDMI has two different damping values of 0.01 and 0.04. Both the reversal fields as a function of IDMI show a smaller influence on the DW propagation, though for higher damping the IDMI makes a more important contribution to the reversal field strength.

results of the experimental studies [298, 299], which showed that the IDMI strength has some dependence regarding the ferromagnetic and heavy metal layer's thickness. So, a range of IDMI values, from 0-1 mJ/m^2 were used in the simulations with damping values of 0.01 and 0.04.

The dependence of the reversal field on IDMI for two intrinsic damping values of 0.01 and 0.04, is plotted in Fig 8.5 (b). The figure shows a monotonic increase of the reversal field as a function of IDMI, where it can be seen that with a higher damping value of 0.04 there is a shift in the reversal field of about 8 % higher. Furthermore, increasing the IDMI in the range 0-1 mJ/m^2 increases the reversal field by $\sim$ 14 %, where this may be explained by the DW inertia due to the dual contribution of IDMI and damping at the interface [273, 300, 301]. The simulations of ferromagnetic nanowires by solving the Landau-Lifshitz-Gilbert equation gives an analytical result which considers the wire as one classical spin chain [301] by:

$$\Delta_0^{wall} = \sqrt{\frac{A}{k}}, \tag{8.4}$$

where A is the exchange coefficient, k is the anisotropy constant and Δ_0^{wall} is the domain wall width in the absence of DMI; and by inserting the DMI's influence, Eq. 8.4 becomes,

$$\Delta^{wall} = \sqrt{\frac{A}{2Ak - D^2}}, \tag{8.5}$$

It can be seen from Eq. 8.5 that Δ^{wall} is the domain wall width including DMI, which show the relation with the IDMI through the DMI constant (D). The D^2 indicates that Δ^{wall} does not depend on the IDMI sign, which means that increasing IDMI in any direction will lead to the domain wall width to enlarge. As a result, the magnetic field needed to propagate DW and produce magnetisation reversal must be larger than the case where there is no IDMI.

As a general result, this shows that damping has a major impact on increasing the DW propagation field as the damping increases with increasing d_{Pt}, but at high values of damping, the IDMI's role becomes significant, which increases the magnetisation reversal field, thus both effects will impact the DW dynamics significantly.

It is important to note that no modifications of the DW type or chirality were observed at zero magnetic field for the full range of IDMI and damping regarding the DW nucleation process in the simulations. Another thing to add is that there was no transformation from transverse DW to vortex DW for all the cases in the case of increasing the applied magnetic field. However, the DW mobility and the onset of Walker breakdown show different dependences on IDMI and damping.

Expanding the micromagnetic investigation regarding the impact of damping and IDMI on the DW velocity can provide further insight about the contribution of both effects on the magnetisation reversal mediation by the DW propagation in nanowires. This also provides more informative data in relation to applications based on DWs, as it helps in controlling the DW velocity and structure. The DW velocity from simulations is plotted in Fig. 8.6 (a) and (b) as a function of the magnetic field for different IDMI strength values, where (a) and (b) are for damping values of 0.01 and 0.04 respectively. The results show that the DW velocity increases with the magnetic field to certain point, at which the onset of Walker breakdown occurs. Above these magnetic field values, the velocity decreases significantly. Comparing the results of Fig. 8.6 (a) with (c), for precessional dynamics it was expected that for low damping the Walker breakdown would occur at lower field adjacent point, while increasing damping extends the magnetic field range, the green marked area, at which Walker breakdown occurs without changing the peak velocity. The behaviour also suggests that increasing damping increases the inertia of the DW, which slows the DW's motion in low fields. The impact of damping on the DW's velocity was explained in Ref. [302] and [303], as $W_F \propto \alpha$ as a derivative of Walker field from the LLG equation. Also, the domain wall mobility was predicted to depend on $\gamma.\Delta/\alpha$ (where Δ is the wall width), which gives support to the simulations.

As it is shown in Fig 8.6 (a) and (b), increasing IDMI in in-plane magnetised nanowires lowers the field at which Walker breakdown occurs, as is shown by the projection lines on the XY plane. From the same figure (c) and (d), it can also be seen that increasing IDMI will lead to a decrease in the Walker field (WF) and the peak DW velocity for both damping values 0.01 and 0.04. It can also be seen from Fig. 8.6 (c) and (d) that WF and peak DW velocity are constant for IDMI strengths that range from 0 up to 0.3 mJ/m^2. Beyond that both decrease, where a range above 0.3 mJ/m^2 is physically reasonable for a NiFe/Pt system. The highest change can be seen for WF behaviour as a function of IDMI, when the high damping value was implemented, while for Walker DW velocity the greatest change took place for the lower damping values as shown in (c) and (d) respectively. This gives a general indication that WF and velocity are modified due to the combined effects of damping and IDMI at the interface.

In order to explain this behaviour, the magnetisation components of the local reorientated spin-structure at the interface due to the impact of IDMI were extracted

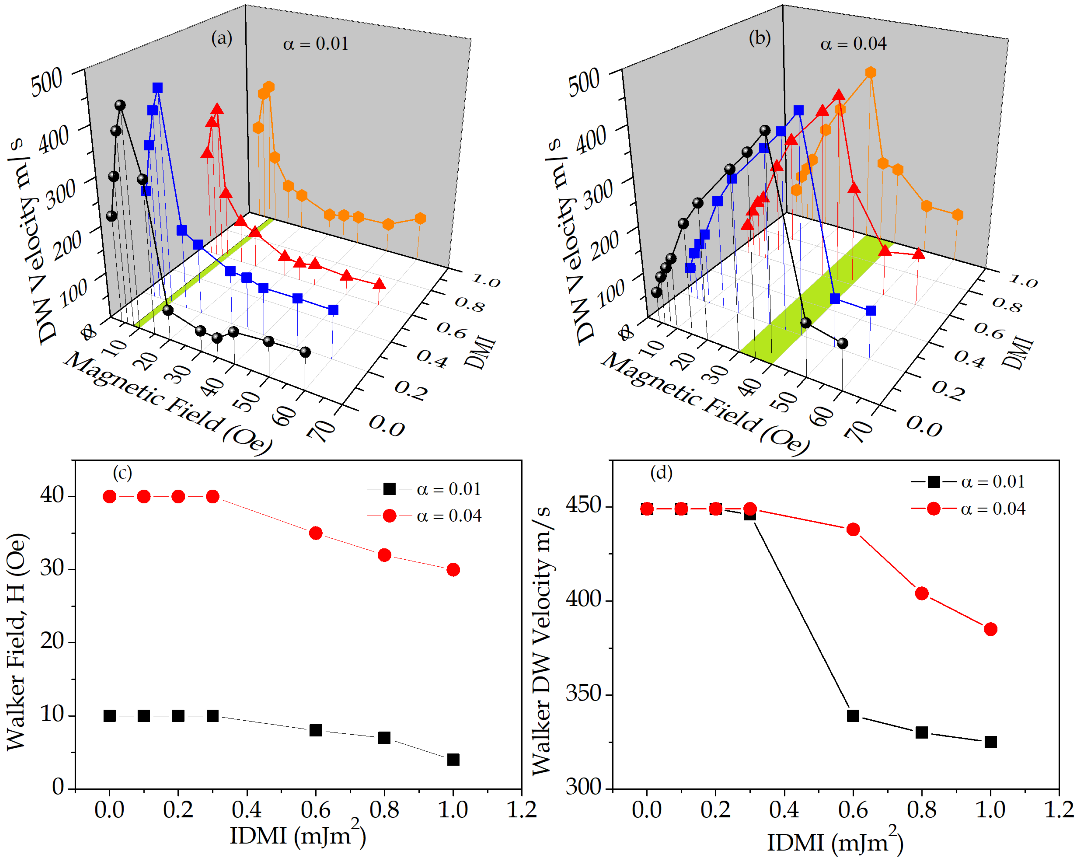

FIGURE 8.6: DW velocity calculated in parallel-sided nanowires for various IDMI and damping values 0.01 (a) and 0.04 (b), which shows the different Walker breakdown ranges. For both the damping values the velocity undergoes a reduction beyond the Walker field threshold. The Walker field is higher for damping values 0.04 than 0.01. However, the IDMI affects both the Walker field (c) and DW velocity (d), which for IDMI beyond 0.3 (mJ/m^2) are decreased.

from the micromagnetic simulations as a function of the DW's position in the nucleation process, as shown in Fig. 8.7 (a) and (b). From figure (a) it can be seen that the magnetisation components M$_x$, M$_y$ and M$_z$, are either transverse or perpendicular to the nanowire's axis. The M$_x$ value changes from positive to negative, which is typical for head to head DW separation, while M$_y$ is always positive because a transverse DW was shown with up polarisation in the simulations. M$_z$ is what gives an interesting result, showing changes in the values in the positive direction (see the dashed blue line). The behaviour along the Z-axis is shown in Fig 8.7 (b) in more detail as a function of DW position and for different IDMI strength values, 0, 0.6, 0.8 and 1 mJ/m^2, and for an α value of 0.01. It can be seen that for a high IDMI strength the magnetisation component along the Z-axis rose and became larger with higher

IDMI values. Without the IDMI's effects this behaviour cannot be observed.

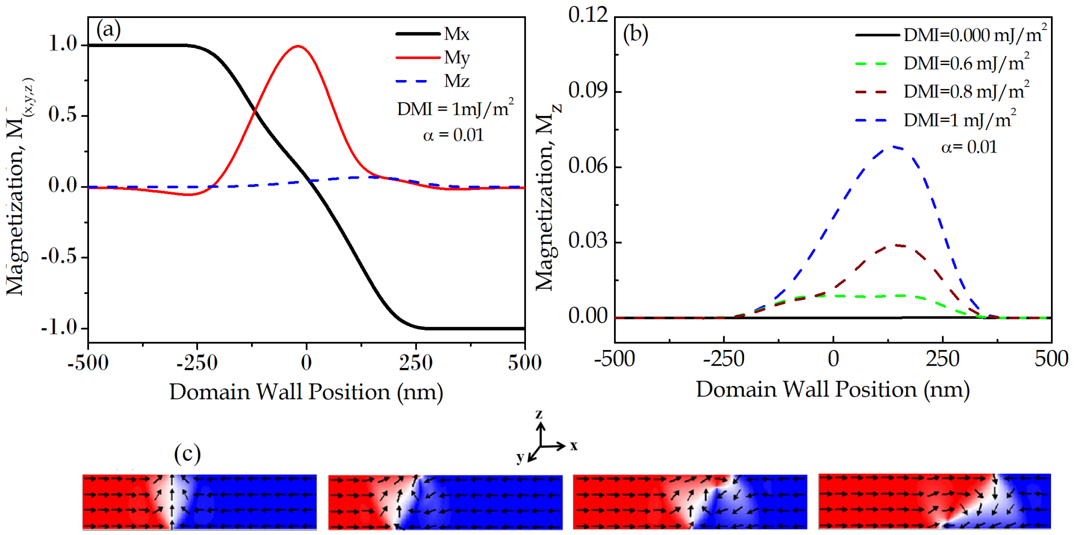

FIGURE 8.7: Calculated along of the magnetisation component as a function of DW position in the nucleation process with a 0.01 damping value. In (a), the M$_x$ changes from 1 to -1 due to the magnetic moments head to head in transverse DW. M$_y$ is always positive, which is typical for transverse domain walls. M$_z$, however, the dashed blue line, emerges for a DMI value of 1 mJ/m^2. In (b), M$_z$ magnetisation components were calculated for different values of DMI, where M$_z$ increases as the DMI becomes larger. The continuous line shows the absence of the magnetisation component without DMI. In (c), the snapshots show the the transitions from transverse domain wall up to down, mediated by core vortex nucleation.

Fig 8.7 (c) shows a snapshot of the magnetisation dynamics of the transition from T-DW to V-DW (vortex domain wall), which is explained by the energetic tendency of the magnetic components to vortex-core nucleation due to the out-of-plane nucleation [304]. This indicates that IDMI supports the magnetisation components for out-of-plane directions and by that it aids the DW vortex core. This means that nominally in-plane magnetisation wires required more control over the IDMI's strength to prevent DW velocity loss. A negative IDMI value in the simulations was also used to compare the results with a positive IDMI, where it shows that with negative IDMI values, the onset of the peak velocity is reduced when the IDMI value increases. Both negative and positive values show asymmetric behaviour, but the peak velocity is lower for a negative IDMI than for a positive value.

As a comparison with other studies, the findings in this study show a different impact for DMI on DW's velocity for in-plane nanowires, where as other studies investigate out-of-plane nanowires. It was shown in such studies that DWs changing from Bloch to Néel states with stability depending on the sign and the value of the DMI [305]. Furthermore, for the out-of-plane case, DW mobility is high and with increasing DMI stability increases and the Walker breakdown point occurs at a higher driven field [279]. Also, it was shown in out-of-plane magnetised wires that DW wall motion is robust, allowing for faster reversal of the magnetisation under strong DMI and with a constant DW angle [279, 306]. In these cases the DW can reach maximum velocity without precessional breakdown and also stabilise the DW angle, which allows the transition from a Néel to Bloch wall in the range of the magnetic field without rotation in DW. In the in-plane case this is not the same, where beyond the Walker field's threshold this field's transition from transverse to vortex domain wall is unavoidable. The simulations shows that the transition from T-DW to V-DW in larger magnetic fields is joined with the translation and rotation around the nanowire axis, which results in the slow motion of the DW velocity due to the back-and-forth motion as a result of the spin dynamics along the nanowire axis.

8.4 Chapter Summary

The study in this chapter was based on the experimental findings of Chapt. 6 on the the effect of the heavy metal on increasing damping in $Ni_{81}Fe_{19}$/Pt thin-films. This was done through experimental measurements and the micromagnetic analysis of the domain wall magnetisation behaviour for in-plane magnetised nanowires of $Ni_{81}Fe_{19}$ coupled with a Pt layer, which shows the effect of different phenomena taking place in the interface area. Investigating magnetisation reversal in parallel-sided and edge modulated $Ni_{81}Fe_{19}$/Pt nanowires as a function of Pt thickness increasing from 0-3 nm shows the impact of d_{Pt} on the magnetisation reversal behaviour. IDMI and damping were both investigated as influencing sources in order to gain a better understanding regarding the magnetisation reversal behaviour, where it showed that the reversal field increases with an increase in Pt thickness in the range of 0-1 nm, with rapid behaviour up to 0.8 nm then tending to a plateau when d_{Pt} is 3 nm.

Both a parallel-sided and edge modulated nanowire showed the same reversal behaviour, which suggests that this impact of the heavy metal is intrinsic regardless of the nanowire shape details.

More informative data regarding the damping and IDMI variation were extracted through micromagnetic analysis, as they give more insight into the damping and IDMI effects upon the magnetisation reversal. The results show that the propagation and the de-pinning of the domain wall depends on damping increasing more than IDMI; however, the latter has a significant role by increasing the magnetisation reversal at high damping. Further analysis shows that DW velocity and Walker field were varied in a significant way by both effects, where increasing the damping gave a higher magnetic field in which the peak velocity and Walker field occur, while the existence of IDMI will lead to a reduction in both the peak velocity and Walker field.

As a final result, coupling a heavy metal with high spin-orbit coupling with a ferromagnet changes the magnetisation behaviour of the ferromagnetic system by the effect of Dzyaloshinskii-Moriya interaction at the FM/NM interface and also due to the effect of damping increasing via hybridization and spin-pumping across the interface. The manipulation of damping and a weak IDMI may aid the control of the DW dynamics regarding the velocity and Walker field in order to improve the performance DW-based device.

Chapter 9

Controlling Magnetic Damping in Synthetic Ferromagnetic Thin-Films Via Surface Layer Modification

9.1 Introduction

In this chapter, a novel study has been carried out, on synthetic 5 nm Co thin-films, capped with 2 nm of Cu, where the upper and lower surfaces mono-layers of the FM material were modified via doping with Cr and Ag. The doping concentration was in the range of 0-80 % in the first couple of mono-layers on each side of the FM. This was compared with another set of samples with full FM layer doping in the range of 0-8 %. Magnetic damping measurements were carried out using ferromagnetic resonance (FMR) techniques in both the field and frequency domains. The dimensionless damping parameter α_{eff} was obtained for both methods. Magnetisation saturation was measured using an MPMS superconducting quantum interference device (SQUID). Structural investigations were carried out using x-ray reflectivity (XRR) to determined the film thickness and interface width. The experimental results were interpreted in relation to theoretical calculations undertaken by A. Umerski. This study shows significant new results regarding the understanding of damping, the control of damping and agreements between theory and experimental predictions providing a complementary novel route to lowering damping in FM material.

Low damping in general is key important to magnonic and spin transfer torque cutting edge technologies, by reducing the required writing-current and improving spin wave propagation, which represent an obstacle for many spintronic applications [1]. Understanding and improving magnetic damping has been the focus of research in both theory and experimental aspects [6, 87, 116, 120, 121]. However the damping contributions from individual mono-layers in FM systems has been reported in only a few theoretical studies [6, 193, 307]. These studies report that the largest contribution to the total damping is from the surface layers of FM films in case of Co and Fe and layers contributions decrease steadily toward the central layers For Ni, the largest contribution come from the second to the surface layers and the central layers.

Experimental studies have been focused on the dependence of damping on FM and NM material thickness on doping and alloying. Studies with doping and alloying show a reduction in damping with changing the concentration of the dopant element in NiFe [217, 222] and Fe [87, 227], where the dopant elements were Cr and Ag for NiFe and Co into Fe. Studies investigating Cr and Ag doping in $Ni_{80}Fe_{20}$ used co-sputtering to vary the concentration of the dopant material, the reduction in damping was small for the concentration range $\sim$ 0.06-0.07 for Cr and 0.1-0.11 for Ag. However, there is no explanation for the observed reduction at this range [217]. The reduction is more pronounced in a study investigated the effect of Cr intermixing in $Ni_{81}Fe_{19}$ on damping. That study used focused ion-beam irradiation to intermix a $Ni_{81}Fe_{19}$/Cr bi-layer thin-film and it is known that with increasing ion dose, intermixing between FM and NM layer increases. The explanation for the reduction in damping was attributed to the reduction of spin-pumping effects due to the sputtering of the atoms from Cr layer and reduces its thickness. However, through the full range of the ion dose, damping showed intrinsic nature and no observed extrinsic contribution due to the intermixing between Cr and $Ni_{81}Fe_{19}$ [222]. On the other hand, studies investigating Fe thin-films doped with Co showed significant reduction in damping [87, 119, 227], all these studies attributed the reduction in damping to the changing of density of states and showed a variation of the crystal structure with Co dopant concentration.

In experimental studies and most of the theoretical ones, the localized variation of magnetic damping cannot be separated or detected. In this study, we used a theoretical finding in Ref. [6] and used the results from an experimental studies on doping Cr and Ag in NiFe [217, 222] to produce a composite material by modifying both surface mono-layers of Co through doping with materials that show a reduction effect on damping in other experimental observations. This study shows new significant findings which supports the theoretical work on damping as it varies through a FM layer. The work here shows the capability to reduce the damping value to an order of 10^{-4} by targeting the surfaces of a Co film. This work opens a door to understand and control magnetic damping and build new materials that can be used to improve the technologies in spintronics, spin-orbitronics [248, 308, 309] and magnonics [249, 250].

Some other FM materials that have been reported to have ultra-low damping such as yttrium-iron-garnet (YIG) [310]. However, the use of YIG in spintronics, spin-orbitronics and complementary metal-oxide semiconductor (CMOS) is not easily applicable because it is an insulator. Some Heusler alloys are also predicted to have the same order of damping value, but the preparation process and high-temperature annealing are not suitable for spintronics and CMOS applications [311]. Thus, transitional metal ferromagnetic materials are considered for such applications due to their conductivity features and the capability to produced high quality systems with no high temperature required. The one feature which is thought to be hard to achieve so far is the ultra-low damping , where the role of electron-magnon scattering causes the high value of magnetic damping.

9.2 Underlying Theory and Experimental Details

Our original idea was developed from the theory work of Barati *et al* [6], based on a realistic nine-orbital tight-binding model that included spin-orbit coupling and electron-scattering rate (Γ), which describes the range of lifetimes electronic states. One of the findings of this study is the expression for the contribution to the damping from individual atomic layers in 18 mono-layers (ML) thick bcc Fe, fcc Co and fcc Ni with $\Gamma = 0.01$ eV [6]. The calculation of the contribution was based on the derivation of the Kamberský's expression for the Gilbert damping parameter from the effective magnetic field (H_{eff}) [274]. This equation used the Fermi-Dirac distribution function and the total spin magnetic moment, in units of the Bohr magneton, with the spin-orbit torque operator as a function of the Lorentz function of the electron-scattering rate. The damping parameter values in those studies are attributed to both intraband and interband processes, which arise from spin-orbit coupling, for more information see [6, 311, 312]. The different contributions to the damping is obvious between Ni on one hand and Fe and Co on the other, regarding the mono-layers contributions to damping, as explained in Chapt. 5.

We have used this theoretical work with suggestions based on the experimental results [217, 222], to test the concept of doping the atomic surface layers in Co with Cr or Ag to create a synthetic ferromagnetic layer with a lower damping parameter. A range of Co thin-films have been grown using a UHV magnetron sputtering system, the Co was capped with 2 nm of Cu to prevent surface oxidation. Cu was selected as capping layer as it show very low contribution to the damping enhancement in theoretical and experimental studies [6, 147, 195, 196].

Two sample sets with different doping were fabricated, the first one simply of Co that was uniformly doped with Cr or Ag with a concentration range from 0-8 %, while for the second set doping was limited within the first few atomic layers near to the upper and lower surfaces of the Co layer. Extra care was taken to optimize the accuracy of the co-sputtered deposition rate and to limit doping to the surface layers. Structural analysis was carried out to verify thickness, interface width and the doped atomic layers thickness. The main magnetic damping measurements were carried out in two different labs as frequency and field linewidth; in IN-IFIMUP, University of Porto, Porto, Portugal and by D. Atkinson in the Brazilian Center for Research in Physics (CBPF) , Rio de Janeiro, Brazil respectively. Finally a theoretical calculation on fcc Co doped with Cr in the first two atomic surface layers was done by A.Umerski who led the theoretical work in Ref. [6]. Due to the time and data limitation results, Ag doping will not be presented in this work.

9.3 Results and Discussion

Starting with structural analysis, Fig. 9.1 (a) shows XRR pattern with best fitting using GenX code, where the layer thicknesses and interface widths were extracted from the best fitting simulations code. The thickness of the Co layer was in the range 4.8 ± 0.1 nm, for the Co 5 nm/Cu 2 nm whiles Cu thickness was 2.9 ± 0.01 nm with the interface width between Co and Cu ∼ 0.8 ± 0.1 nm. For thin-films with Cr doping on the upper and lower surface of Co a similar ranges between 4.7-4.8 nm of Co and ∼ 3.5 nm of Cu was determined, the CoCr layers between SiO_2 and Co in the lower interface and Co with Cu in the upper interface with a range of 0.2-0.3 nm which seams to be targeting the right layer which will have the largest contribution to damping.

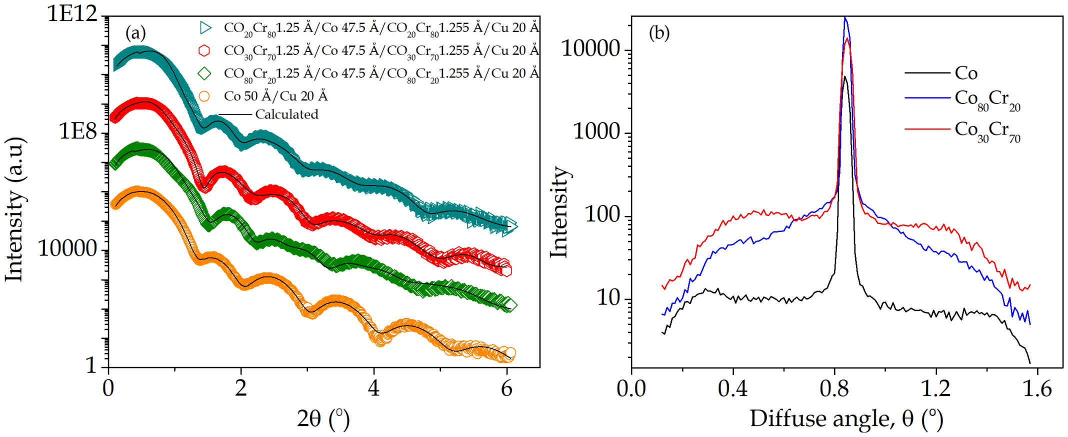

FIGURE 9.1: X-ray reflectivity results for selected samples, where it shows (a) specular x-ray with the best fit and (b) specular diffuse scattered x-rays.

Diffuse scattering x-ray measurements have been done to investigates the interface topological roughness. From the same figure 9.1 (b) it can be seen from the shape (Yoneda wings) that samples investigated shows a relatively smooth topological interface width. see Chapt. 3 for more information.

The field and frequency linewidths from FMR measurements were used to extract the dimensionless damping parameter α_{eff} and other parameters such as inhomogeneous line broadening (ΔH_0) and the saturation magnetisation (M_S). Fig. 9.2 (a) (b), shows selected samples raw data and FMR measurements with field and frequency variation for Co 5 nm/Cu 2 nm thin-film. For (a) and (b) the increasing of

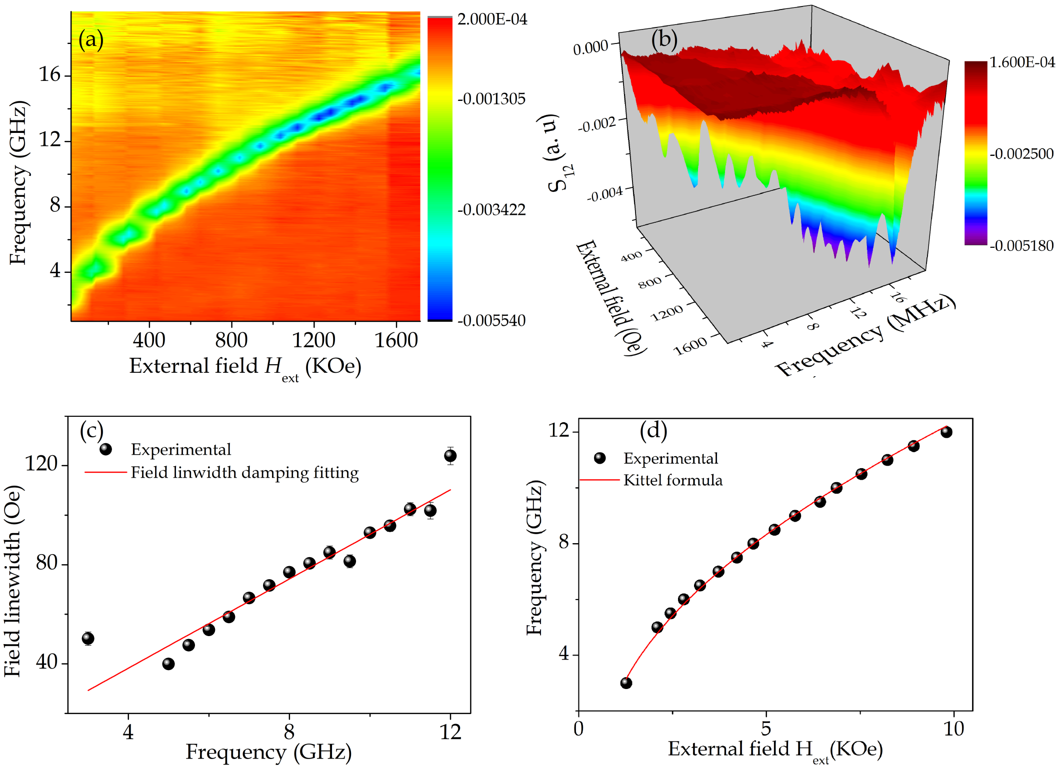

FIGURE 9.2: The FMR signal in (a) S_{12} is changing as a function of both frequency and field, also (b) shows the variation of the peak and the dip as with increasing field and frequency in 3D projection, where the colour legend stand for S_{12} signal. (c) damping fitting using field linewidth domain and (d) shows Kittel fitting for Co 5 nm/Cu 2 nm.

the resonant frequency can be seen as a function of the external magnetic field with the indication of the S_{12} signal variation.

The Kittel formula was fitted in order to extracts M_S using gyromagnetic ratio (γ) value of 2.96×10^{-6} GHz/Oe [14]. The same value was used to extracts α_{eff} by fitting the field linewidth damping equation derived from LLG equation. The fitting was done using python code program created by C. Swindells, and other program created by S. Bunyaev, used to separate the real and imaginary components. For measurements with frequency, a conversion between field and frequency was carried out in order to extracts α_{eff}, where the field linewidth in both measurements was used to find the value of α_{eff}. More information regarding Kittel formula and fitting damping equation can be seen in Chapt. 3.

In order to verify the experimental works on damping [217, 222], which showed a reduction in damping as a function of Cr concentration the first set of CoCr 5 nm/Cu 2 nm films were measured and damping parameter was extracted in field and frequency linewidth. The results show the same trend as for the previous work, as shown in Fig. 9.3 (a), with the exception that some points show high or low values of α_{eff}. However, from the figure it can be seen that the measurement in the field is more consistent with previous experimental results where the magnitude of α_{eff} value is within the range of 0.5. While for the frequency linewidth measurements the reduction was larger. This can be explained by a lack of accuracy with the conversion equation used to extracts the field linewidth from the frequency linewidth data [83]. The equations used to find the field linewidth, ΔH, from the frequency linewidth, Δf, and the other way around can be seen below:

$$\Delta f = \gamma\sqrt{1 + \left(\frac{\gamma M_{\text{eff}}}{f}\right)^2}\,\Delta H \tag{9.1}$$

and

$$\Delta H = \frac{1}{\gamma\sqrt{1 + \left(\frac{\gamma M_{\text{eff}}}{f}\right)^2}}\Delta f \tag{9.2}$$

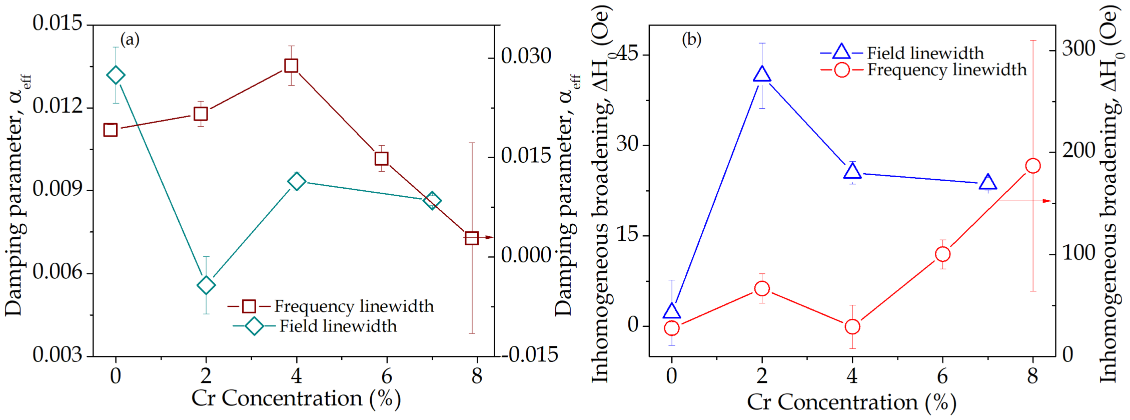

FIGURE 9.3: Damping extraction from FMR measurements of field and frequency linewidths, where (a) shows the same general trend of α_{eff} reduction with increasing Cr concentration for 0- 0.8 % Cr doping, (b) the extrinsic contribution to damping, which shows big contribution from the inhomogeneous component to α_{eff}.

The use of these equations to obtain the field linewidth from the frequency linewidth is linked with the condition that the inhomogeneous broadening contribution to the linewidth should be negligible [83]. This is also supported by the extrinsic damping components shown in Fig. 9.3 (b), which show that the extrinsic contribution starts at the same value for both measurements, but it increases rapidly with increasing Cr concentration according the filed linewidth directly, while for the frequency linewidth extrinsic contribution it can not be directly extracted since the damping in relation with frequency linewidth does not include the inhomogeneous line broadening contribution.

Other parameters have been extracted from fitting the Kittel formula. In Fig. 9.4 (a) and (b) M_S is plotted against Cr concentration which shows a reduction in M_S with increasing Cr concentration. The decreasing in M_S is in agreement with previous studies on Co doping with Cr [313–315]. However the results in Ref. [313]

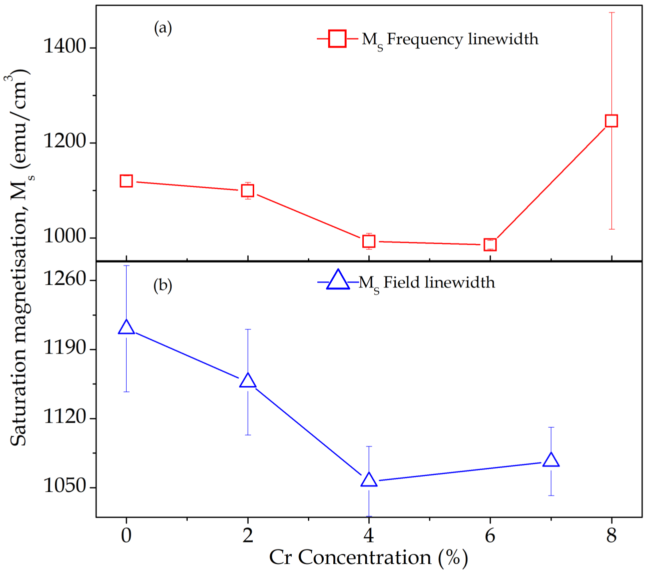

FIGURE 9.4: Saturation magnetisation is plotted as a function of the Cr concentration, where it is calculated from (a) frequency and (b) field linewidths. It shows reduction in magnetisation with the increasing of doping.

shows a smaller decreases of M_S with Cr doping. This may be attributed to the capping Co layer above and under the investigated thin-films in the previous study, which may reduces the Cr doping effect on M_S. This work shows a comparable magnitude of reduction M_S with the studies in Refs. [314, 315], where there is no FM capping layer. In Fig. 9.4 M_S start to level out after 4 % concentration for field linewidth and increases for frequency linewidth at 7 %, however the error bar in both measurements are large. Furthermore, there are no samples have been measured with higher doping. These results shows agreement with previous studies that investigated Co thin-films with Cr doping regarding damping [217, 222] and also with studies investigated other magnetic properties such as M_S [313–315].

Moving toward the main investigation where Co thin-films doped with Cr only in the outer layers. The films have the form $Co_{1-x}Cr_x$ 0.12/Co 4.8/$Co_{1-x}Cr_x$ 0.12/Cu 2 nm, where x= 0 to 0.8. The same measurements have been carried out for these samples, with SQUID measurement in order to compare the direct experimental M_S with the extracted from Kittel formula. M_S is plotted from the SQUID measurements and compared with values extracted from both set of FMR measurements, see Fig. 9.5.

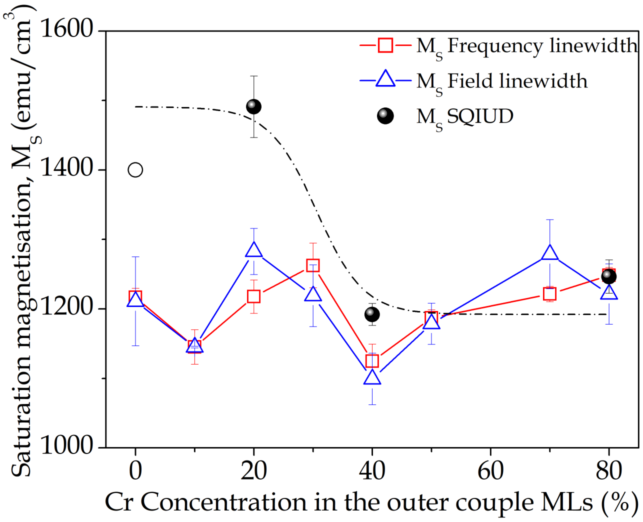

FIGURE 9.5: Saturation magnetisation as a function of the Co surface layers doping concentration with Cr. The general trend of M_S shows some similar behaviour between all results. Noting that ○ is the literature value of the saturation magnetisation of bulk Co [314].

The results of the SQUID show some similarity with the extracted results from FMR measurements. The figure in general shows a reduction in M_S with increasing Cr concentration, however after 40 % concentration of Cr, M_S shows almost constant behaviour, noting that the first point in SQUID results is taken from the literature [314]. The behaviour of M_S from SQUID measurement is similar to the previous study. In that study they used three layers of Co with thickness of 20, 66 and 20 nm respectively, while they doped only the middle layer with Cr. The reduction was attributed to the doping concentration of Cr in Co however, the constant behaviour witnessed is also justified in Ref. [313] by the layers of Co without doping where the M_S measured is averaged from the full samples. The magnetic moment in the boundaries layers is suppressed due to the Cr doping [314], while the middle Co layer has its own momentum which in total can produce the observed M_S value.

The extracted inhomogeneous broadening (ΔH_0) contribution to damping is shown in Fig. 9.6. It can be seen in this figure that ΔH_0 starts to rise with increasing of Cr concentration in both measurements. The extrinsic contribution then comes down almost to zero at 30 % Cr concentration, then it rises again at 40 %. However after that there is almost a settlement in the extrinsic contribution where it shows constant behaviour and near to zero contribution. This may shows that, with the exception to the point at 40 % Cr concentration, an homogeneous crystal structure system is formed and there are no changes in the system. This also agrees with the previous study which showed that at 30 % Cr concentration a hcp crystal structure is formed [313]. By linking the ΔH_0 behaviour of this study, it can be argued that our samples have the same hcp crystal structure at the same Cr concentration point except 40 %. XRD measurements were executed in this study to investigate crystal structure, however the measurements did not give any useful data to indicates the crystal structure of these thin structures. The largest effect which can be seen in Fig. 9.6 with low doping in just a few atomic layers can be attributed to the contributions of these atomic layers to the total damping.

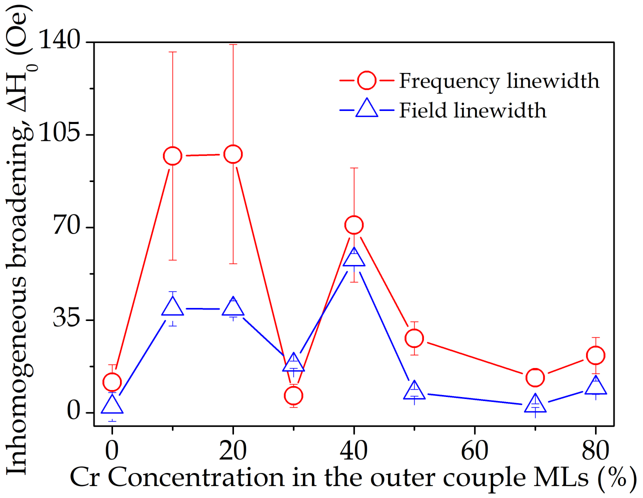

FIGURE 9.6: Inhomogeneous broadening to the damping as a function of Cr concentration where it shows the homogeneities of the system.

As the main concern of this study is the damping value, the intrinsic damping parameter was extracted from both the field and the frequency linewidth analysis of the FMR measurement. The damping parameter is plotted as a function of the Cr doping concentration in the boundaries of the Co layer. The results in Fig. 9.7 show good agreement in the overall trend as a function of doping between the frequency and field linewidths data, where it can be seen that damping in general starts from a high value and then declines rapidly with increasing Cr doping concentration between 30 to 50 %. After that point the damping shows almost constant behaviour.

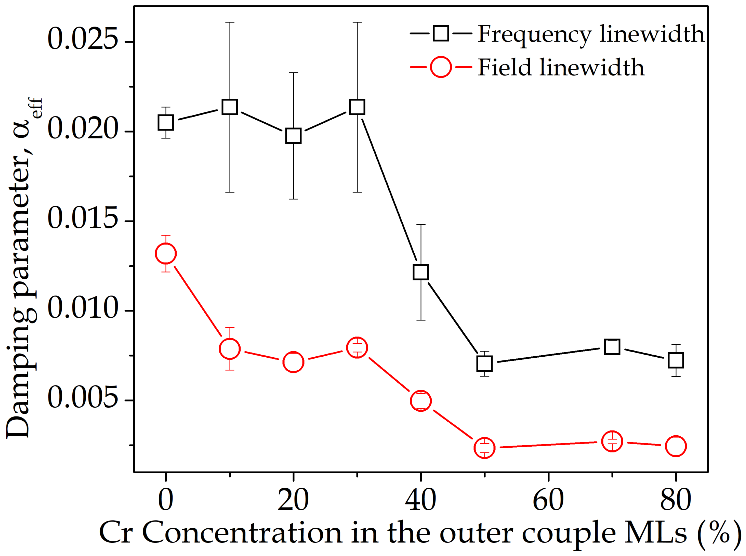

FIGURE 9.7: Intrinsic damping parameter α_{eff} extracted from FMR measurements in frequency linewidth and field linewidths analysis. The data shows the general trend of the damping behaviour as a function of the Cr doping concentration and the difference in the results between the frequency and field linewidth measurements.

The damping values extracted from the frequency linewidth are higher than the values of the field linewidth. This may be attributed to the issue with damping extracted from the frequency linewidth measurements, where the inhomogeneous broadening contribution to the damping is not distinguished and therefore adds to the damping value, noting that, this effect is weaker for higher doses where good hcp structure is expected. The damping value for pure Co, extracted from the frequency linewidth, in this study is comparable with the damping value for similar system studied in Chapt. 6. In that study, damping was measured using the TR-MOKE method, and the results are in good agreements. Furthermore, it is known that in TR-MOKE measurements, the total extracted damping value is the sum of both extrinsic and intrinsic contributions, by which, the damping extracted in this study in the frequency linewidth FMR is almost the same as the value extracted by TR-MOKE [5]. As it is known that the field linewidth is more accurate in terms of extracting the damping parameter, hence we will use the field linewidth results to discuss the main behaviour for the damping dependence on Cr doping concentration. The damping values show a significant drop in the range from 10 to 50 % Cr concentration doping, at 50 % Cr concentration and beyond the damping shows constant behaviour.

Before explaining the behaviour further corrections to the data have been calculated to obtain the true net damping parameter, α. The estimated radiative damping (α_{rd}) contribution, due to the inductive interaction between the precessing magnetisation in the sample and the co-planar waveguide in the FMR system, was subtracted, see Chapt. 3 for details of damping calculation. This effect can be extracted experimentally, but due to time limitation it is calculated for the time being. A second effect was also subtracted which comes from the contribution of the Cu capping layer to the damping, which is responsible for absorbing spin angular momentum pumped from the FM layer. This is the spin-pumping damping (α_{sp}) contribution which was calculated and subtracted from the term ($\alpha_{\mathrm{eff}} - \alpha_{\mathrm{rd}}$), see also Chapt. 5 and 6. Both α_{rd} and α_{sp} were very small, of order 10^{-4}, however for the lowest α_{eff} this can be significant. The measured and corrected results are shown in Fig. 9.8.

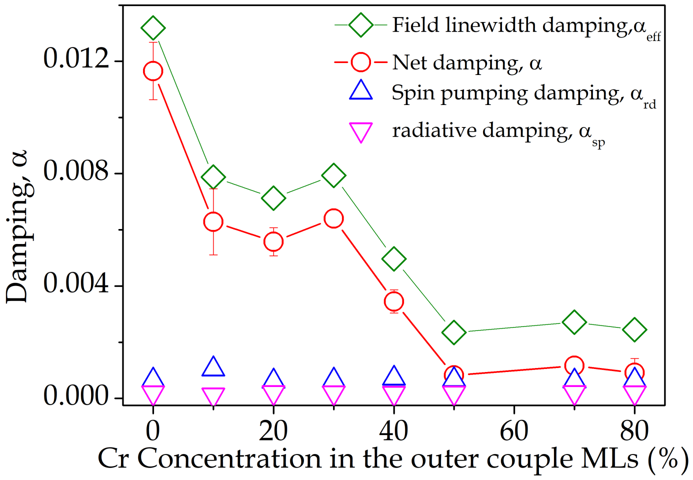

FIGURE 9.8: Intrinsic damping results extracted from FMR measurements in the field linewidth and the calculated Radiative, α_{rd}, and the spin-pumping, α_{sp}, where their contributions subtracted from the total damping. The final corrected net damping, α after the subtraction of both contribution shows very low values especially at 50 % Cr doping concentration and beyond.

It can be seen from the figure that a new final damping parameter, α, is obtained from the damping extracted from the field linewidth α_{eff}, which shows that α reaches very low values of order 10^{-4} with doping of the surface layers. The crystal structure changes with doping may be one of the explanations for the damping reduction as it was used to explain, ΔH_0, see Fig. 9.6 and $\mathrm{M_S}$, see Fig. 9.5. However this may not fully explains the low observed damping value.

In order to explain the behaviour that leads to this low damping value, a theoretical calculations were done by A. Umerski from the Open University over 12 mono-layers of Co layer with the same Cr doping from 10- 40 % in the surface mono-layers. Fig. 9.9 (a) (b) (c) and (d) presents the finding of the theoretical work, which shows the damping contribution from each individual layer for different Cr doping concentration.

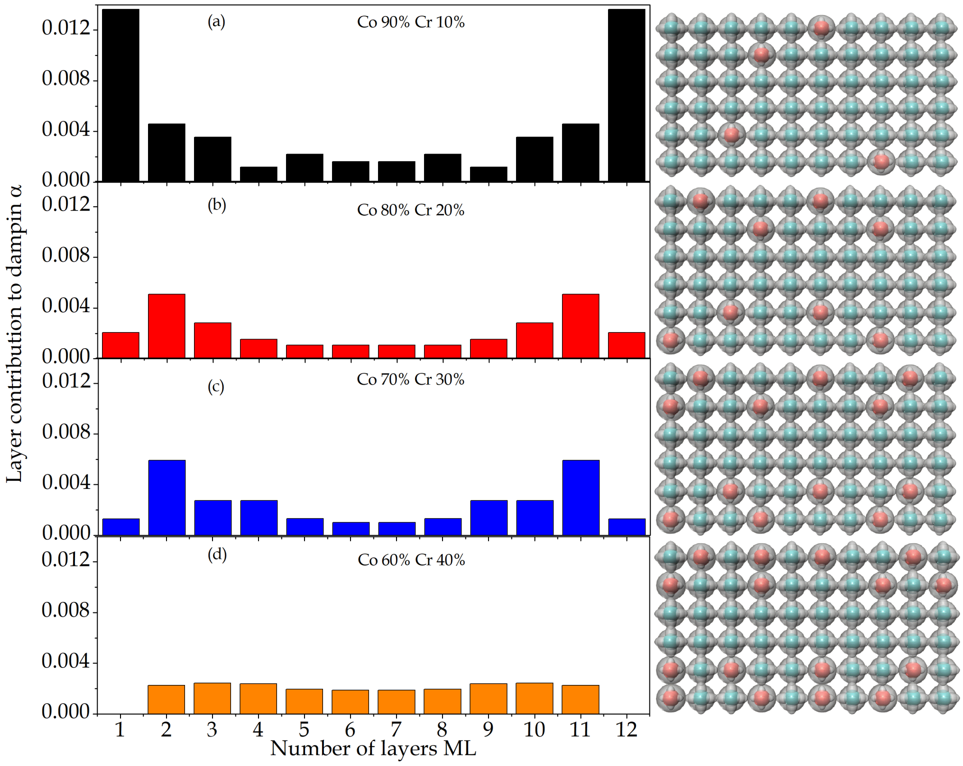

FIGURE 9.9: Theoretical calculation for damping contribution form each individual layer, with a schematic illustration shows the Cr concentration increasing from (a) 10 %, (b) 20 %, (c) 30 % and (d) 40 %, where the effect on damping starts by decreasing the contribution to the total damping from the boundaries atomic layers.

It can be seen that the doping affects the first couple atomic outer layers symmetrically. Higher Cr doping gradually reduces the contribution coming from the outer atomic layers, at the same time doping increases the contribution from the second outer layers at Cr concentration 30 %. Doping starts to impact the damping contribution value of the outer couple atomic layers at a Cr concentration of 40 %, at which a big drop in damping takes place. It is worth mentioning that the calculated in the theoretical work is was limited to 40 % Cr doping concentration. By calculating the total damping and using the same study to calculate the damping for pure Co the results from theory are compared with the experimental work as shown in Fig. 9.10.

In order to explain the behaviour of the intrinsic damping beyond the crystal phase changes, this theoretical work can aid the interpretation. Fig. 9.10 shows the comparison between the final net damping and the full damping calculated from the contribution of each individual layer. The value for the damping for pure Co is calculated from 18 mono-layers of Co in the same theoretical work [6]. It is worth mentioning that the real thin-films were much thicker than the Co thickness calculated in the theoretical work. However the initial points in Fig. 9.10 almost perfectly agree, which shows that the experimental results benefit from subtracting the spin-pumping and radiative damping effects.

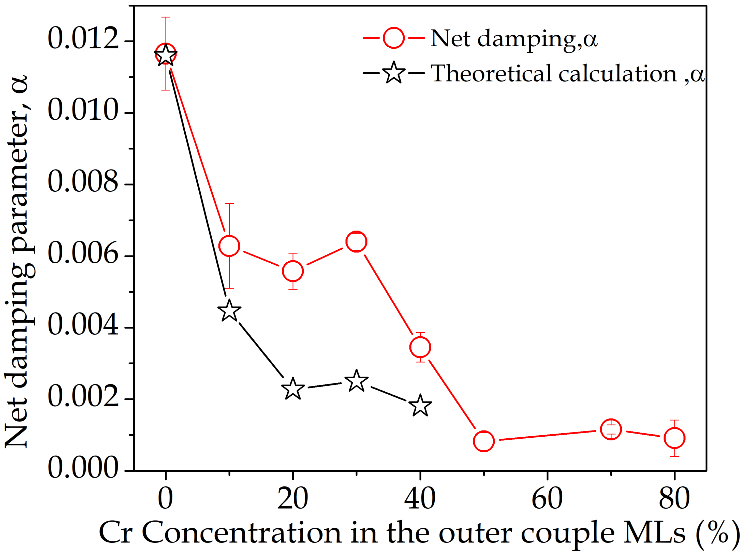

FIGURE 9.10: Comparison between theoretical calculation and the final extracted experimental results.

It is suggested that the rapid decreasing of damping from 0 up to 50 % is a mixed effect combining the crystal phase changes and the theoretical predicted energetic states of the system. However, the latter has more impact than the crystal changes as the changes in the crystal structure cannot leads to such low damping values. Furthermore, in Fig. 9.10 the calculations were executed on fcc Co, which as shown give almost perfect results for Pure cobalt. The theory behind the calculated damping used a nine-orbital tight-binding model including spin-orbit coupling, with the dependence on Fermi-Dirac distribution function. This shows that the damping is linked predominantly by states with energies close to the Fermi level. Furthermore, this effect is essential for the intraband transition which was explained previously [6]. It was also demonstrated by a previous study that structural phase transitions and ferromagnetic phase boundaries can be affected by variations of sample surface [316]. The electronic structure is re-engineered in the atomic boundaries by which the intraband transition events may reduced, which may lead to decreases in the scattering rate coming from these layers and finally lowering the states with energies close to the Fermi level ϵ_F. Thus damping as in the image of the dimensionless parameter will be reduced.

9.4 Chapter Summary

In this chapter novel work was done to create synthetic ferromagnetic systems by introducing new composite materials with new magnetic properties that may open the research field with a new method to reduce damping in FM material to value with order of 10^{-4}. In this study, results from a previous theoretical study were considered and developed experimentally and new theoretical calculations were undertaken to support this new idea. The samples were investigated in two laboratories for FMR measurements as a function of field and frequency linewidths. XRR measurements and SQUID magnetometry, were carried out to aid the results and gain a better understanding to the magnetic behaviour. The reduction in damping was significant and other magnetic properties varied, such as saturation magnetisation and the inhomogeneous damping of the system. Crystal structure insight from previous studies were considered to help explain the results. The existence of XRD result would help the research however, the results cannot be explained only by crystal structures effects. Theoretical work was carried out by the same group whom made the previous theoretical work, and shows some agreement with the experimental results. As a conclusion for this work, magnetic damping was controlled to a very low values by re-engineering the electronic structure of the outer layers of Co thin-film leading to reduction in the contribution to damping that comes from these atomic layers. This work can use as first step to investigates a lot of other materials to find their effect on damping, which may lead to further reductions in damping. Theoretical work also can be done on other pure and alloyed FM materials to find the atomic layers which largely contributes to damping, opening a new field, that can explore to reduce damping and feed into technology with new engineered materials.

Chapter 10

Conclusions and Further Work

10.1 Conclusions

In this thesis, the magnetic damping behaviour was investigated in ferromagnetic thin-film systems. In general the magnetic damping was studied and controlled in Co and $Ni_{81}Fe_{19}$ thin-films with a range of non-magnetic materials (NM = Pt, Au, Cr, Ag and Cu) as a capping layers or dopant. The studies in this thesis was focusing on the effect on damping behaviour through different approaches. This is done by firstly studying the additional capping layers and secondly the modification of the interface layer between the combined FM and NM layers. The third is studying the contribution of the damping variation with IDMI as interfacial localised magnetisation effects on the magnetic domain wall dynamics in terms of velocity and magnetisation reversal. Finally, new works demonstrates a novel method of controlling magnetic damping through the modification of the surface of a ferromagnetic layer. This was done using well-known fabrication techniques with well-established measurement methods. The results add new understanding of the magnetic damping behaviour with new findings in the research field.

The evolution of magnetic damping as a function of NM layer thickness in bilayer thin-films of a Co or $Ni_{81}Fe_{19}$ layer capped with Pt and Au shows a significant effect on damping for Pt on both FM materials, but not for Au. The dependence of damping on Pt thickness shows a rapid increase with increases in the Pt thickness in the range 0-0.6 nm for Co and 0-0.8 for $Ni_{81}Fe_{19}$. The investigation shows that this increase is due to the development of an interface between the FM material and Pt, where the local magnetisation is modified by the Pt atoms initially via forming islands of Pt-FM which have different magnetic properties. The variation of the magnetic properties at the interface between the FM layer and Pt is due to the incomplete coverage of the Pt layer on Co and $Ni_{81}Fe_{19}$ at the Pt thickness ranges mentioned above. By the creation of these islands, the intrinsic damping increases via the d-d hybridization effect. However, due to the inhomogeneities of the magnetic moment between the Pt-FM island and uncovered FM areas, two-magnon scattering emerges, thus damping in general seems to be extrinsically enhanced.

With increasing Pt thickness damping tends to a maximum and then falls to a plateau when the Pt thickness > 0.6 for Co and > 0.8 for $Ni_{81}Fe_{19}$. X-ray reflectivity shows that at these thicknesses Pt forms a continuous layer on Co and $Ni_{81}Fe_{19}$ respectively. This increases the uniformity of the interface and leads to increased intrinsic damping while the extrinsic effect is reduced, which explain the fall in damping from the peak. Comparing Co and $Ni_{81}Fe_{19}$ the latter shows higher damping values at lower Pt thicknesses. This is may be explained by the XRD investigation which shows that that Co has hcp structure while $Ni_{81}Fe_{19}$ has fcc, which may support the higher spin-mixing conductance for the case of $Ni_{81}Fe_{19}$ than for Co regarding their crystal structure with respect to Pt. The damping for the Au capping layer on Co did not show any enhancement, which may be attributed to the higher intermixing for Pt with Co and the higher density of states in comparison with Au. The damping behaviour shows good agreement with a recent theoretical study, with small differences arising from the uncalculated effects such as roughness in the real investigated in comparison with the theoretical study where the atoms arranged perfectly.

The variation of damping was investigated as a function of the modified interfacial region in $Ni_{81}Fe_{19}$/Pt thin-film microstructures. The interfacial modifications were done by focused ion beam irradiation in a low range of ion-beam doses. Magnetic damping shows a rapid increase as the dose increases up to a dose range 2–2.4 pC/μm^2. This increasing damping is due to a widening of the interface area between the $Ni_{81}Fe_{19}$ and Pt layer. The dependence of damping on frequency shows that the enhancement of damping has a contribution due to the extrinsic mechanism, via two-magnon scattering developed at the interface. The structural analysis shows that the interface changes as a function of the focused ion-beam irradiation dose in the previous cases with Au capping layer. The damping starts to fall and continues as the irradiation dose increases more than 2.4 $\mathrm{pC}/\mu\mathrm{m}^2$. In this region, however, intrinsic damping is responsible for damping decreasing. This is demonstrated by using the structural results of previous studies and the dependence of the frequency on irradiation dose. It shows that there are no contributions from the extrinsic mechanism to the total damping. Furthermore, new NiFe-Pt graded alloy is gradually formed with almost no Pt capping layer. This suggests that the reduction in damping is due to the reduction of the spin-pumping effect by the loss of the Pt capping layer by sputtering and intermixing due to irradiation. The variation of the precessional relaxation time as a function of irradiation dose also shows a change in the lattice configuration. These changes take place at irradiation doses in the same range as when the damping reaches the maximum value. The development of the interface in this microstructure and the change of the bi-layer thin-film into a compositionally-graded alloy with the loss of the Pt capping layer are the main events that explain the variation of magnetic damping.

Understanding the roles of damping and IDMI at the interface is the third conclusion. This work used the results of the damping enhancement in $\mathrm{Ni}_{81}\mathrm{Fe}_{19}/\mathrm{Pt}$ thin-films and was applied to differently shaped nano-wires. Also, this study shows the effect of the Dzyaloshinskii-Moriya interaction at the interface in micromagnetic simulations in order to understand the effect of both on the domain wall dynamics. The results show that the magnetisation reversal field for domain wall reversal increases linearly with the intrinsic damping and it appears to be independent of the extrinsic damping and is only secondarily dependent on the nano-wire shape. However, an independence of the reversal field on extrinsic effect is known at length-scales comparable with the domain wall width. Interfacial DMI shows large effect on the reversal field when the damping value is high. Damping and interfacial DMI shows a larger influence on the domain wall velocity and Walker field. Damping increasing shift domain wall velocity and Walker field maximum pekes to a higher magnetic field. The increasing of interfacial DMI however, reduces both to a lower magnetic field.

The results show differences between the micromagnetic simulations and experiment. This may be justified by the different parameters that were used in the simulations compared to the real values of the material investigated, such as the exchange stiffness constant, saturation magnetisation and temperature. Furthermore, there were differences in the details of modelling the geometry for the real wires and the simulation. In general, the strong spin-orbit coupling from Pt had an impact on the magnetisation behaviour in $Ni_{81}Fe_{19}$ through the variation of the interfacial damping and DMI. This study shows the possibilities to control domain wall propagation, mobility and stability by the modification of damping and IDMI.

Controlling damping through the modification of the surface atomic layer of Co is a new method, which implements the theoretical work of Barati *et al* [6], with the experimental results from well know previous studies [217, 222] to examine a new approach, by controlling the contribution to damping parameter expression from individual mono-layers in FM material . This has been done by modifying the surface atomic layers of each side in Co layer with Cr dopant. The latter shows a kind of reduction effect when it was used with very low concentration as dopant in FM material. Knowing from the theory that largest contribution to damping in Co, this concept was applied and measured. The first part of this study is to verify the results from the previous studies, by doping the full Co layer with Cr with range from 0 to 8 %, which shows good agreement regarding magnetic damping and saturation magnetisation. The results shows a reduction in damping and saturation magnetisation in the range of doping concentration upto 8 %. This reduction may attributed to the magnetic moment suppression due to the Cr dopant. This also shows good agreement with a similar studies on Cr doping effect on saturation magnetisation.

The second part is related with the doping of the surface atomic layers of the Co. In this part Saturation magnetisation shows a trend of reduction with Cr doping concentration between 0 to 40 % after that the trend almost constant. This behaviour may also attributed to the changing magnetic moment in these doped atomic layers, however the constant behaviour is may linked with the unchangeable magnetic moment in the rest of the undoped Co layer. The inhomogeneous broadening results shows similar trend to the saturation magnetisation, by reviewing previous work on doping and the effect on the crystal structure of the system investigated, this behaviour my be attributed to the crystal phase transition that occurs with increasing doping of Cr from 0 upto 30 %. After that it may argued that our samples formed a hcp structure where the inhomogeneous broadening shows constant behaviour and almost zero. Intrinsic damping show interesting results where damping parameter shows decreasing in value between 0 to 40 % Cr doping concentration. Beyond this concentration damping is very low and almost constant. The results was as a function of field and frequency linewidth, however the frequency linewidth's results show a higher value than the field linewidth. This was also my explained by the unseparated inhomogeneous broadening in the frequency linewidth measurements. Also the similar results with our previous study on similar system, where damping measured by TR-MOKE which is known that in this method the damping parameter is the sum of both extrinsic and intrinsic damping contribution.

By using the FMR field linewidth results, damping value was very low and by subtracting the radiative and spin-pumping damping contributions the results were significantly lower with an order of 10^{-4}, which represent a very low damping value in any given metal FM. The explanation was aid by theoretical calculations done by A. Umerski, where the results again show very good agreements. This behaviour of damping may attributed to the more than one effect. The first one is the crystal phase changing by Cr dopant concentration, which may have a lower impact than the second effect, which is the electronic distribution in the boundaries atomic layers in Co. Adding Cr in these atomic layer will firstly may suppress their magnetic momentum, secondly it may lower the intraband transition processes by decreasing the number of energy states close to the Fermi energy level, Thus it may decreases the contribution to the total damping from these atomic layers. Since, by theory, these layer are the most contributed to the total damping, the damping reduces significantly by doping these layer with Cr. This work can be considered as first step to try many other elements on Co or other pure or alloyed FM materials, which can be done with knowing the most affective regions by theory.

10.2 Further Work

The studies in this thesis have shown some contribution regarding understanding magnetic damping behaviour in ferromagnetic thin-films as a function of substantial variations. These variations involve non-magnetic materials in different locations in the ferromagnetic thin-films, including interface, capping layer and the border mono-layers of the ferromagnetic material. The studies lead to a new findings, but more investigations are required as the field of research continues to develop.

The study of the evolution of magnetic damping was focused on the damping dependence as a function of Pt thickness. The study shows that Co has a hcp crystal structure, which indicates the low value of damping compared with $Ni_{81}Fe_{19}$. A similar study can be carried out to show the effect when Co has fcc structure may lead to enhancement of the damping through the intrinsic mechanism. Trying other heavy metals, such as osmium will be good practice to find the limits of damping increasing, where osmium is reported as a very effective elements in increasing damping in the case of doping. This also may be true in the case of the capping layer.

For the study on the interfacial variation effect on damping in $Ni_{81}Fe_{19}/Pt$ microstructures, the focus was on the development of the interface layer and the reduction of the capping layer effects on damping. This study could be extended to include micromagnetic simulations in order to understand the role of IDMI while increasing the interface layer, which may provide more insights to the study. The study can include the effect of damping and the IDMI on the magnetisation dynamic and domain wall motion. Repeating the study for Ni and Fe only with the same Pt capping layer may show a comparison between the two cases and give insight regarding the effect of Pt on the damping of each thin-film. This may also show a comparison of the relative interaction of Pt with Ni and Fe.

The study focused on the effect of damping and interfacial DMI on the magnetisation reversal and domain wall motion, used the experimental results combined with micromagnetic simulations of $Ni_{81}Fe_{19}/Pt$ thin-films. IDMI can be found in thin-film materials known for their high spin-orbit coupling. This study could be extended by using a range of different ferromagnetic layers with Pt as a capping layer and the simulations can be compared with anisotropic magnetoresistance (AMR) measurements . DMI in the interface can show different behaviour with a very low applied magnetic field; this is because in the in-plane thin-films with IDMI, the localised magnetisation spin at the interface should have an out-of-plane combination, as it was shown by the snapshots of the simulation softwares; this can be simulated and compared with the experimental results for selected bi-layer thin-films with in-plane magnetisation and high expected IDMI strength values. This may help to gain better knowledge regarding IDMI in different ferromagnetic bi-layer thin-film systems.

As the final study in Chapt. 9 shows a significant and novel results by synthesising ferromagnetic material with changes on the bordering mono-layers, this study was a step toward controlling damping in Co by doping the outer mono-layers with Cr, where it shows a significant impact on damping due to this doping. This study opens the door to new research to investigate new materials using the same procedure by knowing the effect of the dopant material. The use of different materials is not yet explored and the theory behind damping reduction can be extended to any ferromagnetic material with different crystal structures. The study can be expanded to different levels with the effects on systems with out-of-plane magnetisation, nano-wires and other alloyed ferromagnetic materials. The results may allow further control in terms of magnetic damping, crystal structure and other magnetic properties.

Bibliography

1. Žuti ć, I., Fabian, J. & Das Sarma, S. Spintronics: Fundamentals and applications. *Rev. Mod. Phys.* **76,** 323–410 (2 Apr. 2004).
2. Stancil, D. D. & Prabhakar, A. *Spin waves* (Springer, 2009).
3. Brandão, J., Azzawi, S., Hindmarch, A. & Atkinson, D. Understanding the role of damping and Dzyaloshinskii-Moriya interaction on dynamic domain wall behaviour in platinum-ferromagnet nanowires. *Sci. Rep.* **7,** 4569 (2017).
4. Ganguly, A. *et al.* Tunable Magnetization Dynamics in Interfacially Modified $Ni_{81}Fe_{19}$/Pt Bilayer Thin Film Microstructures. *Sci. Rep.* **5,** 17596 (2015).
5. Azzawi, S. *et al.* Evolution of damping in ferromagnetic/nonmagnetic thin film bilayers as a function of nonmagnetic layer thickness. *Phys. Rev. B* **93,** 054402 (5 Feb. 2016).
6. Barati, E., Cinal, M., Edwards, D. M. & Umerski, A. Gilbert damping in magnetic layered systems. *Phys. Rev. B* **90,** 014420 (2014).
7. Bandyopadhyay, S. & Cahay, M. *Introduction to spintronics* (CRC press, 2015).
8. O'handley, R. C. *Modern magnetic materials: principles and applications* (Wiley, 2000).
9. Jiles, D. *Introduction to magnetism and magnetic materials* (CRC press, 2015).
10. Thomas, L. H. The motion of the spinning electron. *Nature* **117,** 514 (1926).
11. Björck, M. *A structural viewpoint of magnetism in Fe and Co based superlattices* PhD thesis (Acta Universitatis Upsaliensis, 2007).
12. Blundell, S. *Magnetism in Condensed Matter (Oxford master series in condensed matter physics)* (Oxford University Press, 2001).

13. Suhl, H. *Magnetism: Magnetic ions in insulators, their interactions, resonances, and optical properties* (Academic Press, 1963).
14. Kittel, C. On the Gyromagnetic Ratio and Spectroscopic Splitting Factor of Ferromagnetic Substances. *Phys. Rev.* **76,** 743–748 (6 1949).
15. Bozorth, R. M. *Ferromagnetism* (Van Nostrand, New York, 1951).
16. Shaw, J. M., Nembach, H. T., Silva, T. J. & Boone, C. T. Precise determination of the spectroscopic g-factor by use of broadband ferromagnetic resonance spectroscopy. *J. Appl. Phys.* **114** (2013).
17. Kläui, M. & Vaz, C. *Handbook of Magnetism and Advanced Magnetic Materials* 2007.
18. Morrish, A. H. *et al. The physical principles of magnetism* (Wiley Online Library, 1965).
19. Lin, Y., Grundy, P. & Giess, E. Bubble domains in magnetostatically coupled garnet films. *Appl. Phys. Lett.* **23,** 485–487 (1973).
20. Emori, S., Bauer, U., Ahn, S.-M., Martinez, E. & Beach, G. S. Current-driven dynamics of chiral ferromagnetic domain walls. *Nat. Mat.* **12,** 611–616 (2013).
21. Stoner, E. C. Collective Electron Ferromagnetism. *Proc.R. Soc. London. A, Math. and Phys. Sci.* **165,** 372–414. ISSN: 00804630 (1938).
22. Slater, J. C. The Ferromagnetism of Nickel. *Phys. Rev.* **49,** 537–545 (7 Apr. 1936).
23. Stoner, E. C. & Wohlfarth, E. A mechanism of magnetic hysteresis in heterogeneous alloys. *Philos. Trans. Royal Soc. A* **240,** 599–642 (1948).
24. Van Vleck, J. H. A Survey of the Theory of Ferromagnetism. *Rev. Mod. Phys.* **17,** 27–47 (1 Jan. 1945).
25. Cullity, B. & Graham, C. Introduction to Magnetic Materials. *Introduction to Magnetic Materials, Second Edition,* 241–273 (2009).
26. Rosch, A. Skyrmions: moving with the current. *Nat. Nanotechnol.* **8,** 160–161 (2013).

27. Fert, A., Cros, V. & Sampaio, J. Skyrmions on the track. *Nat. Nanotechnol.* **8,** 152–156 (2013).
28. Nagaosa, N. & Tokura, Y. Topological properties and dynamics of magnetic skyrmions. *Nat. Nanotechnol.* **8,** 899–911 (2013).
29. Yu, X. *et al.* Near room-temperature formation of a skyrmion crystal in thin-films of the helimagnet FeGe. *Nat. Mate.* **10,** 106–109 (2011).
30. Heinze, S. *et al.* Spontaneous atomic-scale magnetic skyrmion lattice in two dimensions. *Nat. Phys.* **7,** 713–718 (2011).
31. Okubo, T., Chung, S. & Kawamura, H. Multiple-q States and the Skyrmion Lattice of the Triangular-Lattice Heisenberg Antiferromagnet under Magnetic Fields. *Phys. Rev. Lett.* **108,** 017206 (1 Jan. 2012).
32. Moriya, T. Anisotropic Superexchange Interaction and Weak Ferromagnetism. *Phys. Rev.* **120,** 91–98 (1 Oct. 1960).
33. Hrabec, A. *et al.* Measuring and tailoring the Dzyaloshinskii-Moriya interaction in perpendicularly magnetized thin films. *Phys. Rev. B* **90,** 020402 (2 July 2014).
34. Thiaville, A., Rohart, S., Jué, É., Cros, V. & Fert, A. Dynamics of Dzyaloshinskii domain walls in ultrathin magnetic films. *E. P. L.* **100,** 57002 (2012).
35. Kittel, C. *Introduction to solid state physics seventh. JohnWiley and Dons* 1996.
36. Magnetoresistance of ferromagnetic metals and alloys at low temperatures. *Physica* **17,** 612–627. ISSN: 0031-8914 (1951).
37. Spaldin, N. A. *Magnetic materials: fundamentals and applications* (Cambridge University Press, 2010).
38. Cui, B. *et al.* Perpendicular magnetic anisotropy in CoFeB/X (X=MgO, Ta, W, Ti, and Pt) multilayers. *J. Alloys Compd.* **559,** 112–115. ISSN: 0925-8388 (2013).
39. Gilbert, T. L. A phenomenological theory of damping in ferromagnetic materials. *IEEE Trans. Magn.* **40,** 3443–3449 (2004).

40. Kamberský, V. On ferromagnetic resonance damping in metals. *Czech. J. Phys. B* **26,** 1366 (1976).

41. Berger, L. Effect of interfaces on Gilbert damping and ferromagnetic resonance linewidth in magnetic multilayers. *J. Appl. Phys.* **90,** 4632–4638 (2001).

42. Von Sovskii, S. V. *Ferromagnetic resonance: the phenomenon of resonant absorption of a high-frequency magnetic field in ferromagnetic substances* (Elsevier, 1966).

43. Korenman, V. & Prange, R. E. Anomalous damping of spin waves in magnetic metals. *Phys. Rev. B* **6,** 2769 (1972).

44. Lenz, K. *et al.* Two-magnon scattering and viscous Gilbert damping in ultrathin ferromagnets. *Phys. Rev. B* **73,** 144424 (2006).

45. Ho, J., Khanna, F. C. & Choi, B. C. Radiation-spin interaction, Gilbert damping, and spin torque. *Phys. Rev. Lett.* **92,** 097601 (2004).

46. Zakeri, K. *et al.* Spin dynamics in ferromagnets: Gilbert damping and two-magnon scattering. *Phys. Rev. B* **76,** 104416 (2007).

47. Sparks, M. *Ferromagnetic-relaxation theory* (McGraw-Hill, 1964).

48. Barati, E., Cinal, M., Edwards, D. M. & Umerski, A. *Calculation of Gilbert damping in ferromagnetic films* in *EPJ Web of Conferences* **40** (2013), 18003.

49. Zvezdin, A. & Kotov, V. *Modern Magnetooptics and Magnetooptical Materials Materials* (IOP Publishing Ltd., 1997).

50. Rave, W., Schäfer, R. & Hubert, A. Quantitative observation of magnetic domains with the magneto-optical Kerr effect. *J. Magn. Magn. Mater.* **65,** 7–14. ISSN: 0304-8853 (1987).

51. Kerr, J. XLIII. On rotation of the plane of polarization by reflection from the pole of a magnet. *Philos. Mag.* **3,** 321–343 (1877).

52. Kundt, A. XXXV. On the electromagnetic rotation of the plane of polarization of light by means of iron, cobalt, and nickel. *Philos. Mag.* **18,** 308–327 (1884).

53. Als-Nielsen, J. & McMorrow, D. *Elements of modern X-ray physics* (John Wiley & Sons, 2011).

54. Hecht, E. Optics. 2002. *Pearson Education, Inc.,* **360,** 366–367 (2002).
55. Parratt, L. G. Surface Studies of Solids by Total Reflection of X-Rays. *Phys. Rev.* **95,** 359–369 (2 July 1954).
56. Kiessig, H. Untersuchungen zur totalreflexion von röntgenstrahlen. *Annalen der Physik* **402,** 715–768 (1931).
57. Bowen, D. K. & Tanner, B. K. *X-ray metrology in semiconductor manufacturing* (CRC Press, 2006).
58. Kortright, J. Nonspecular x-ray scattering from multilayer structures. *J. Appl. Phys.* **70,** 3620–3625 (1991).
59. Bragg, W. L. The structure of some crystals as indicated by their diffraction of X-rays. *Proceedings of the Royal Society of London. Series A, Containing papers of a mathematical and physical character* **89,** 248–277 (1913).
60. Kittel, C. *Elementary solid state physics: a short course* (John Wiley & Sons, 1962).
61. Björck, M. & Andersson, G. GenX: an extensible X-ray reflectivity refinement program utilizing differential evolution. *J. Appl. Crystallogr.* **40,** 1174–1178 (2007).
62. Samitsu, Y. A study of silicon-wafer surface evaluation using atomic force microscopy. *Nanotechnology* **4,** 236 (1993).
63. Kasiraj, P., Shelby, R., Best, J. & Horne, D. Magnetic domain imaging with a scanning Kerr effect microscope. *IEEE Trans. Magn.* **22,** 837–839 (1986).
64. Qiu, Z. & Bader, S. D. Surface magneto-optic Kerr effect. *Rev. Sci. Instrum.* **71,** 1243–1255 (2000).
65. You, C.-Y. & Shin, S.-C. Generalized analytic formulae for magneto-optical Kerr effects. *J. Appl. Phys.* **84,** 541–546 (1998).
66. Bruno, P., Suzuki, Y. & Chappert, C. Magneto-optical Kerr effect in a paramagnetic overlayer on a ferromagnetic substrate: A spin-polarized quantum size effect. *Phys. Rev. B* **53,** 9214–9220 (14 Apr. 1996).
67. Josephson, B. D. The discovery of tunnelling supercurrents. *Rev. Mod. Phys.* **46,** 251–254 (2 Apr. 1974).

68. Deaver, B. S. & Fairbank, W. M. Experimental Evidence for Quantized Flux in Superconducting Cylinders. *Phys. Rev. Lett.* **7,** 43–46 (2 July 1961).

69. Clarke, J. Principles and applications of SQUIDs. *Proc. IEEE* **77,** 1208–1223 (1989).

70. Gallop, J. C. *SQUIDs, the Josephson effects and superconducting electronics* (CRC Press, 1991).

71. *MPMS-XL User's manual. Sandiego, CA, Quantom Design.* ().

72. Rueden, C. T. *et al.* ImageJ2: ImageJ for the next generation of scientific image data. *BMC Bioinformatics* **18,** 529. ISSN: 1471-2105 (Nov. 2017).

73. Hubert, A. & Schäfer, R. *Magnetic Domains: The Analysis of Magnetic Microstructures* (Springer Science & Business Media, 1998).

74. Freeman, M., Ruf, R. & Gambino, R. Picosecond pulsed magnetic fields for studies of ultrafast magnetic phenomena. *IEEE trans. magn.* **27,** 4840–4842 (1991).

75. Mizukami, S. *et al.* Gilbert damping in perpendicularly magnetized Pt/Co/Pt films investigated by all-optical pump-probe technique. *Appl. Phys. Lett.* **96,** 2502 (2010).

76. Barman, A. *et al.* Magneto-optical observation of picosecond dynamics of single nanomagnets. *Nano lett.* **6,** 2939–2944 (2006).

77. Pal, S., Rana, B., Hellwig, O., Thomson, T. & Barman, A. Tunable magnonic frequency and damping in [Co/Pd]8 multilayers with variable Co layer thickness. *Appl. Phys. Lett.* **98,** 082501 (2011).

78. Rana, B. *et al.* All-Optical Excitation and Detection of Picosecond Dynamics of Ordered Arrays of Nanomagnets with Varying Areal Density. *Appl. Phys. Express* **4,** 113003 (2011).

79. Farle, M. Ferromagnetic resonance of ultrathin metallic layers. *Rep. Prog. Phys.* **61,** 755 (1998).

80. Griffiths, J. H. E. Anomalous high-frequency resistance of ferromagnetic metals. *Nature* **158,** 670 (1946).

81. Kittel, C. On the Theory of Ferromagnetic Resonance Absorption. *Phys. Rev.* **73,** 155 (2 1948).
82. Kalarickal, S. S. *et al.* Ferromagnetic resonance linewidth in metallic thin films: Comparison of measurement methods. *J. Appl. Phys.* **99** (2006).
83. Wei, Y., Chin, S. L. & Svedlindh, P. On the frequency and field linewidth conversion of ferromagnetic resonance spectra. *J. Phys. D: Applied Physics* **48,** 335005 (2015).
84. Sanders, R. W., Paquette, D., Jaccarino, V. & Rezende, S. M. Radiation damping in magnetic resonance. II. Continuous-wave antiferromagnetic-resonance experiments. *Phys. Rev. B* **10,** 132–138 (1 July 1974).
85. Wende, G. Radiation damping in FMR measurements in a nonresonant rectangular waveguide. *physica status solidi (a)* **36,** 557–567.
86. Schoen, M. A. W., Shaw, J. M., Nembach, H. T., Weiler, M. & Silva, T. J. Radiative damping in waveguide-based ferromagnetic resonance measured via analysis of perpendicular standing spin waves in sputtered permalloy films. *Phys. Rev. B* **92,** 184417 (18 Nov. 2015).
87. Schoen, M. A. W. *et al.* Ultra-low magnetic damping of a metallic ferromagnet. *Nat. Phys.* **12,** 839 (2016).
88. Grove, W. R. *et al. On the electro-chemical polarity of gases* in *Abstracts of the Papers Communicated to the Royal Society of London* **6** (1854), 168–169.
89. Moorthy, S. B. K. *Thin Film Structures in Energy Applications* (Springer, 2015).
90. Ibach, H. *Physics of surfaces and interfaces* (Springer, 2006).
91. Venables, J. *Introduction to surface and thin film processes* (Cambridge University Press, 2000).
92. Guisbiers, G., Overschelde, O. V., Wautelet, M., Leclère, P. & Lazzaroni, R. Fractal dimension, growth mode and residual stress of metal thin films. *J. Phys. D: Applied Physics* **40,** 1077 (2007).
93. Mantis business webpage with general specifications of the Qprep500 sputtering system.

94. Chowdhury, N. & Bedanta, S. Controlling the anisotropy and domain structure with oblique deposition and substrate rotation. *AIP advances* **4,** 027104 (2014).
95. Nastasi, M., Mayer, J. & Hirvonen, J. K. *Ion-solid interactions: fundamentals and applications* (Cambridge University Press, 1996).
96. Ikeda, O., Kainuma, R., Ohnuma, I., Fukamichi, K. & Ishida, K. Phase equilibria and stability of ordered bcc phases in the Fe-rich portion of the Fe–Ga system. *Journal of Alloys and Compounds* **347,** 198–205 (2002).
97. Wei, Q., Li, K.-D., Lian, J. & Wang, L. Angular dependence of sputtering yield of amorphous and polycrystalline materials. *J. Phys. D: Applied Physics* **41,** 172002 (2008).
98. Burn, D., Hase, T. & Atkinson, D. Focused-ion-beam induced interfacial intermixing of magnetic bilayers for nanoscale control of magnetic properties. *J. Phys. Condens. Matter* **26,** 236002 (2014).
99. BURN, D. *et al. Domain wall behaviour in ferromagnetic nanowires with interfacial and geometrical structuring* PhD thesis (Durham University, 2013).
100. Rantschler, J. O. *et al.* Damping at normal metal/permalloy interfaces. *IEEE Trans. Magn.* **41,** 3523 (2005).
101. Kaminsky, W. *et al.* Patterning ferromagnetism in Ni 80 Fe 20 films via Ga+ ion Irradiation. *Appl. Phys. Lett.* **78,** 1589–1591 (2001).
102. Möller, W. & Eckstein, W. Tridyn—A TRIM simulation code including dynamic composition changes. *Nuclear Instruments and Methods in Physics Research Section B: Beam Interactions with Materials and Atoms* **2,** 814–818 (1984).
103. Robinson, M. T. & Oen, O. The channeling of energetic atoms in crystal lattices. *Appl. Phys. Lett.* **2,** 30–32 (1963).
104. Besenbacher, F., Bøttiger, J., Nielsen, S. & Whitlow, H. J. Short-and long-range ion-beam mixing in Cu: Al. *Appl. Phys. A* **29,** 141–145 (1982).

105. Banwell, T., Liu, B., Golecki, I. & Nicolet, M.-A. Chemical effects in ion mixing of transition metals on SiO2. *Nuclear Instruments and Methods in Physics Research* **209,** 125–129 (1983).

106. Sigmund, P. & Gras-Marti, A. in *Ion Beam Analysis* 389–394 (Elsevier, 1980).

107. Fick, A. On liquid diffusion. *J. Memb. Sci.* **100,** 33–38 (1995).

108. Sigmund, P. & Gras-Marti, A. Theoretical aspects of atomic mixing by ion beams. *Nucl. Instr. Meth. Res. A* **182-183,** 25–41. ISSN: 0029-554X (1981).

109. Arac, E., Burn, D. M., Eastwood, D. S., Hase, T. P. & Atkinson, D. Study of focused-ion-beam–induced structural and compositional modifications in nanoscale bilayer systems by combined grazing incidence X ray reflectivity and fluorescence. *J. Appl. Phys.* **111,** 044324 (2012).

110. Desimoni, J. & Traverse, A. Model for compound formation during ion-beam mixing. *Phys. Rev. B* **48,** 13266 (1993).

111. Kim, S.-J., Nicolet, M., Averback, R. & Peak, D. Low-temperature ion-beam mixing in metals. *Phys. Rev. B* **37,** 38 (1988).

112. Homma, M., Imakawa, M., Okada, M. & Tsutsumi, S. Au-Fe-Ni permanent magnet alloys. *IEEE trans. magn.* **21,** 1245–1249 (1985).

113. Traverse, A., Le Boité, M., Nevot, L., Pardo, B. & Corno, J. Initial stages of the ion beam mixing process. *Appl. phys. lett.* **51,** 1901–1903 (1987).

114. Fassbender, J. & McCord, J. Control of saturation magnetization, anisotropy, and damping due to Ni implantation in thin Ni 81 Fe 19 layers. *Appl. phys. lett.* **88,** 252501 (2006).

115. Park, C.-M. & Bain, J. Focused-ion-beam induced grain growth in magnetic materials for recording heads. *J. Appl. Phys.* **91,** 6830–6832 (2002).

116. Azzawi, S., Hindmarch, A. & Atkinson, D. Magnetic damping phenomena in ferromagnetic thin-films and multilayers. *J. Phys. D: Applied Physics* **50,** 473001 (2017).

117. Prange, R. E. & Korenman, V. Line width of ferromagnetic resonance in metals. *J. Magn. Reson.* **6,** 274–280 (1972).

118. McMichael, R. D. & Krivosik, P. Classical model of extrinsic ferromagnetic resonance linewidth in ultrathin films. *IEEE Trans. Magn.* **40,** 2 (2004).

119. Oogane, M. *et al.* Magnetic damping in ferromagnetic thin films. *Jap. J. Appl. Phys.* **45,** 3889 (2006).

120. Kamberský, V. On the Landau–Lifshitz relaxation in ferromagnetic metals. *Can. J. Phys.* **48,** 2906 (1970).

121. Kuneš, J. & Kamberský, V. First-principles investigation of the damping of fast magnetization precession in ferromagnetic $3d$ metals. *Phys. Rev. B* **65,** 212411 (2002).

122. Kamberský, V. Spin-orbital Gilbert damping in common magnetic metals. *Phys. Rev. B* **76,** 134416 (2007).

123. Mankovsky, S., Ködderitzsch, D., Woltersdorf, G. & Ebert, H. First-principles calculation of the Gilbert damping parameter via the linear response formalism with application to magnetic transition metals and alloys. *Phys. Rev. B* **87,** 014430 (2013).

124. Heinrich, B., Meredith, D. J. & Cochran, J. F. Wave number and temperature dependent Landau-Lifshitz damping in nickel. *J. Appl. Phys.* **50,** 7726 (1979).

125. Cochran, J. & Heinrich, B. Microwave transmission through ferromagnetic metals. *IEEE Trans. Magn.* **16,** 660 (1980).

126. Gilmore, K., Idzerda, Y. U. & Stiles, M. D. Identification of the dominant precession-damping mechanism in Fe, Co, and Ni by first-principles calculations. *Phys. Rev. Lett.* **99,** 027204 (2007).

127. Gilmore, K., Idzerda, Y. U. & Stiles, M. D. Spin-orbit precession damping in transition metal ferromagnets. *J. Appl. Phys.* **103,** 07D303 (2008).

128. Berger, L. Emission of spin waves by a magnetic multilayer traversed by a current. *Phys. Rev. B* **54,** 9353 (1996).

129. Tserkovnyak, Y., Brataas, A. & Bauer, G. E. W. Spin pumping and magnetization dynamics in metallic multilayers. *Phys. Rev. B* **66,** 224403 (22 2002).

130. Landau, L. D. & Lifshitz, E. M. Theory of the dispersion of magnetic permeability in ferromagnetic bodies. *Phys. Z. Sowietunion* **8,** 153 (1935).

131. Tserkovnyak, Y., Brataas, A., Bauer, G. E. W. & Halperin, B. I. Nonlocal magnetization dynamics in ferromagnetic heterostructures. *Rev. Mod. Phys.* **77,** 1375 (4 2005).

132. Heinrich, B. *et al.* Dynamic Exchange Coupling in Magnetic Bilayers. *Phys. Rev. Lett.* **90,** 187601 (18 2003).

133. Marcham, M. K. *et al.* Phase-resolved x-ray ferromagnetic resonance measurements of spin pumping in spin valve structures. *Phys. Rev. B* **87,** 180403 (18 2013).

134. Tserkovnyak, Y., Brataas, A. & Bauer, G. E. W. Enhanced Gilbert Damping in Thin Ferromagnetic Films. *Phys. Rev. Lett.* **88,** 117601 (11 2002).

135. Mikhailov, A. S. & Farzetdinova, R. M. Quantum-theory of relaxation of spin-waves by 2-level impurities. *Zhurnal Eksperimentalnoi I Teoreticheskoi Fiziki* **80,** 1524 (1981).

136. Van Vleck, J. H. & Orbach, R. Ferrimagnetic resonance of dilute rare-earth doped iron garnets. *Phys. Rev. Lett.* **11,** 65 (1963).

137. Safonov, V. L. & Bertram, H. N. Impurity relaxation mechanism for dynamic magnetization reversal in a single domain grain. *Phys. Rev. B* **61,** R14893 (2000).

138. McMichael, R. D. *et al.* Ferromagnetic resonance mode interactions in periodically perturbed films. *J. Appl. Phys.* **91,** 8647 (2002).

139. McMichael, R. D., Twisselmann, D. J. & Kunz, A. Localized ferromagnetic resonance in inhomogeneous thin films. *Phys. Rev. Lett.* **90,** 227601 (2003).

140. McMichael, R. D. & Kunz, A. Calculation of damping rates in thin inhomogeneous ferromagnetic films due to coupling to lattice vibrations. *J. Appl. Phys.* **91,** 8650 (2002).

141. Van Vleck, J. H. Ferrimagnetic Resonance of Rare-Earth-Doped Iron Garnets. *J. Appl. Phys.* **35,** 882 (1964).

142. Bonneau-Brault, A., Dubourg, S., Thiaville, A., Rioual, S. & Valente, D. Adjustable ferromagnetic resonance frequency in CoO/CoFeB system. *J. Appl. Phys.* **117,** 033902 (2015).

143. Bloch, F. Nuclear Induction. *Phys. Rev.* **70,** 460 (7-8 1946).

144. Bloembergen, N. On the Ferromagnetic Resonance in Nickel and Supermalloy. *Phys. Rev.* **78,** 572 (5 1950).

145. Kamberský, V. & Patton, C. E. Spin-wave relaxation and phenomenological damping in ferromagnetic resonance. *Phys. Rev. B* **11,** 2668 (1975).

146. Qiu, Z. *et al.* Spin mixing conductance at a well-controlled platinum/yttrium iron garnet interface. *Appl. Phys. Lett.* **103,** 092404 (2013).

147. Liu, Y., Yuan, Z., Wesselink, R. J. H., Starikov, A. A. & Kelly, P. J. Interface Enhancement of Gilbert Damping from First Principles. *Phys. Rev. Lett.* **113,** 207202 (20 Nov. 2014).

148. Rojas-Sánchez, J.-C. *et al.* Spin Pumping and Inverse Spin Hall Effect in Platinum: The Essential Role of Spin-Memory Loss at Metallic Interfaces. *Phys. Rev. Lett.* **112,** 106602 (10 Mar. 2014).

149. Chen, K. & Zhang, S. Spin Pumping in the Presence of Spin-Orbit Coupling. *Phys. Rev. Lett.* **114,** 126602 (12 2015).

150. Zhang, W., Han, W., Jiang, X., Yang, S.-H. & Parkin, S. S. P. Role of transparency of platinum-ferromagnet interfaces in determining the intrinsic magnitude of the spin Hall effect. *Nat. Phys.* **11,** 496. ISSN: 1745-2473 (2015).

151. Tokaç, M. *et al.* Interfacial Structure Dependent Spin Mixing Conductance in Cobalt Thin Films. *Phys. Rev. Lett.* **115,** 056601 (5 2015).

152. Kimura, T., Hamrle, J. & Otani, Y. Estimation of spin-diffusion length from the magnitude of spin-current absorption: Multiterminal ferromagnetic/nonferromagnetic hybrid structures. *Phys. Rev. B* **72,** 014461 (1 July 2005).

153. Jedema, F. J., Filip, A. & Van Wees, B. Electrical spin injection and accumulation at room temperature in an all-metal mesoscopic spin valve. *Nature* **410,** 345 (2001).

154. Šimánek, E. & Heinrich, B. Gilbert damping in magnetic multilayers. *Phys. Rev. B* **67,** 144418 (2003).

155. Šimánek, E. Gilbert damping in ferromagnetic films due to adjacent normal-metal layers. *Phys. Rev. B* **68,** 224403 (2003).

156. Berger, L. Gilbert damping and current-induced torques on a domain wall: A simple theory based on itinerant 3*d* electrons only. *Phys. Rev. B* **80,** 144427 (2009).

157. Hartmann-Boutron, F. Effect of Rare-Earth Impurities on the Ferrimagnetic Resonance and Nuclear Relaxation in Yttrium Iron Garnet. *J. Appl. Phys.* **35,** 889 (1964).

158. Rossing, T. D. Resonance Linewidth and Anisotropy Variation in Thin Films. *J. Appl. Phys.* **34,** 995 (1963).

159. Olsen, E. *Applied magnetism: a study in quantities* (N.V. Philips' Gloeilampenfabriken, Eindhoven, 1964).

160. Suhl, H. Ferromagnetic Resonance in Nickel Ferrite Between One and Two Kilomegacycles. *Phys. Rev.* **97,** 555 (2 1955).

161. Goryunov, Y. V. *et al.* Magnetic anisotropies of sputtered Fe films on MgO substrates. *Phys. Rev. B* **52,** 13450 (18 1995).

162. Hurben, M. J., Franklin, D. R. & Patton, C. E. Angle dependence of the ferromagnetic resonance linewidth in easy-axis and easy-plane single crystal hexagonal ferrite disks. *J. Appl. Phys.* **81,** 7458 (1997).

163. Hillebrands, B. & Ounadjela, K. *Spin dynamics in confined magnetic structures I* (Springer Science & Business Media, 2003).

164. Urban, R., Woltersdorf, G. & Heinrich, B. Gilbert damping in single and multilayer ultrathin films: Role of interfaces in nonlocal spin dynamics. *Phys. Rev. Lett.* **87,** 217204 (2001).

165. Woltersdorf, G., Buess, M., Heinrich, B. & Back, C. H. Time resolved magnetization dynamics of ultrathin Fe (001) films: Spin-pumping and two-magnon scattering. *Phys. Rev. Lett.* **95,** 037401 (2005).

166. Zhang, W. *et al.* Engineering Gilbert damping by dilute Gd doping in soft magnetic Fe thin films. *J. Appl. Phys.* **115,** 17A308 (2014).

167. Barsukov, I. *et al.* Magnetocrystalline anisotropy and Gilbert damping in iron-rich $\mathrm{Fe}_{1-x}\mathrm{Si}_x$ thin films. *Phys. Rev. B* **84,** 180405 (2011).

168. Sun, L. *et al.* Ferromagnetic resonance studies of Fe thin films with dilute heavy rare-earth impurities. *J. Appl. Phys.* **111,** 07A328 (2012).

169. Lubitz, P., Cheng, S. F. & Rachford, F. J. Increase of magnetic damping in thin polycrystalline Fe films induced by Cu/Fe overlayers. *J. Appl. Phys.* **93,** 8283 (2003).

170. Montoya, E., McKinnon, T., Zamani, A., Girt, E. & Heinrich, B. Broadband ferromagnetic resonance system and methods for ultrathin magnetic films. *J. Magn. Magn. Mater.* **356,** 12 (2014).

171. Kuanr, B. K., Kuanr, A. V., Camley, R. E. & Celinski, Z. Magnetization relaxation in sputtered thin Fe films: An FMR study. *IEEE Trans. Magn.* **42,** 2930 (2006).

172. Kardasz, B. & Heinrich, B. Ferromagnetic resonance studies of accumulation and diffusion of spin momentum density in Fe/Ag/Fe/GaAs (001) and Ag/Fe/GaAs (001) structures. *Phys. Rev. B* **81,** 094409 (2010).

173. Walowski, J. *et al.* Intrinsic and non-local Gilbert damping in polycrystalline nickel studied by Ti: sapphire laser fs spectroscopy. *J. Phys. D: Applied Physics* **41,** 164016 (2008).

174. Venkatesh, M., Ramakanth, S., Chaudhary, A. & Raju, K. Study of terahertz emission from nickel (Ni) films of different thicknesses using ultrafast laser pulses. *Opt. Mater. Express* **6,** 2342 (2016).

175. Sharma, M., Kuanr, B. K., Sharma, M. & Basu, A. Relation between static and dynamic magnetization effects and resonance behavior in Ni nanowire arrays. *IEEE Trans. Magn.* **50,** 1 (2014).

176. Barman, A. *et al.* Ultrafast magnetization dynamics in high perpendicular anisotropy $(\mathrm{Co/Pt})_n$ multilayers. *J. Appl. Phys.* **101,** 9D102 (2007).

177. Mizukami, S., Ando, Y. & Miyazaki, T. Magnetic relaxation of normal-metal (NM)/80NiFe/NM films. *J. Magn. Magn. Mater.* **239,** 42 (2002).

178. Beaujour, J.-M. L., Lee, J. H., Kent, A. D., Krycka, K. & Kao, C. C. Magnetization damping in ultrathin polycrystalline Co films: Evidence for nonlocal effects. *Phys. Rev. B* **74,** 214405 (2006).

179. Ingvarsson, S. *et al.* Role of electron scattering in the magnetization relaxation of thin $Ni_{81}Fe_{19}$ films. *Phys. Rev. B* **66,** 214416 (2002).

180. Fassbender, J. *et al.* Structural and magnetic modifications of Cr-implanted permalloy. *Phys. Rev. B* **73,** 184410 (2006).

181. Russek, S. E. *et al.* Magnetostriction and angular dependence of ferromagnetic resonance linewidth in Tb-doped Ni0.8Fe0.2 thin films. *J. Appl. Phys.* **91,** 8659 (2002).

182. Ingvarsson, S., Xiao, G., Parkin, S. S. P. & Koch, R. H. Tunable magnetization damping in transition metal ternary alloys. *Appl. Phys. Lett.* **85,** 4995–4997 (2004).

183. Mizukami, S., Ando, Y. & Miyazaki, T. Ferromagnetic resonance linewidth for NM/80NiFe/NM films (NM= Cu, Ta, Pd and Pt). *J. Magn. Magn. Mater.* **226,** 1640 (2001).

184. Ruiz-Calaforra, A. *et al.* The role of the non-magnetic material in spin pumping and magnetization dynamics in NiFe and CoFeB multilayer systems. *J. Appl. Phys.* **117,** 163901 (2015).

185. Natarajarathinam, A. *et al.* Influence of capping layers on CoFeB anisotropy and damping. *J. Appl. Phys.* **112,** 053909 (2012).

186. Mizukami, S., Ando, Y. & Miyazaki, T. The study on ferromagnetic resonance linewidth for NM/80NiFe/NM (NM= Cu, Ta, Pd and Pt) films. *Jap. J. Appl. Phys.* **40,** 580 (2001).

187. Iihama, S. *et al.* Gilbert damping constants of Ta/CoFeB/MgO (Ta) thin films measured by optical detection of precessional magnetization dynamics. *Phys. Rev. B* **89,** 174416 (2014).

188. Shaw, J. M., Nembach, H. T. & Silva, T. J. Determination of spin pumping as a source of linewidth in sputtered $Co_{90}Fe_{10}$/Pd multilayers by use of broadband ferromagnetic resonance spectroscopy. *Phys. Rev. B* **85,** 054412 (2012).

189. Liu, X., Zhang, W., Carter, M. J. & Xiao, G. Ferromagnetic resonance and damping properties of CoFeB thin films as free layers in MgO-based magnetic tunnel junctions. *J. Appl. Phys.* **110,** 033910 (2011).

190. Shaw, J. M., Silva, T. J., Schneider, M. L. & McMichael, R. D. Spin dynamics and mode structure in nanomagnet arrays: Effects of size and thickness on linewidth and damping. *Phys. Rev. B* **79,** 184404 (2009).

191. Heinrich, B., Woltersdorf, G., Urban, R. & Simanek, E. Role of spin current in magnetic relaxations of metallic multilayer films. *J. Magn. Magn. Mater.* **258,** 376 (2003).

192. Yan, W., Wang, H., Du, W., Zhao, J. & Zhang, X. Magnetocrystalline anisotropy and Gilbert damping of Co_2MnAl films epitaxially grown on GaAs. *J. Phys. D: Applied Physics* **49,** 065005 (2016).

193. Thonig, D. & Henk, J. Gilbert damping tensor within the breathing Fermi surface model: anisotropy and non-locality. *New J. Phys.* **16,** 013032 (2014).

194. Mizukami, S., Ando, Y. & Miyazaki, T. Effect of spin diffusion on Gilbert damping for a very thin permalloy layer in Cu/permalloy/Cu/Pt films. *Phys. Rev. B* **66,** 104413 (10 Sept. 2002).

195. Sun, Y. *et al.* Damping in Yttrium Iron Garnet Nanoscale Films Capped by Platinum. *Phys. Rev. Lett.* **111,** 106601 (10 Sept. 2013).

196. Boone, C. T., Nembach, H. T., Shaw, J. M. & Silva, T. J. Spin transport parameters in metallic multilayers determined by ferromagnetic resonance measurements of spin-pumping. *J. Appl. Phys.* **113,** 153906 (2013).

197. Baker, A. A., Figueroa, A. I., van der Laan, G. & Hesjedal, T. Tailoring of magnetic properties of ultrathin epitaxial Fe films by Dy doping. *AIP Advances* **5,** 077117 (2015).

198. Rowan-Robinson, R. M. *Spin-orbit phenomena and interfacial proximity effects in magnetic multilayers* http://etheses.dur.ac.uk/11692/. PhD thesis (Durham University, 2016).

199. Głowiński, H. *et al. Damping in Finemet films capped by platinum* in *Microwave, Radar and Wireless Communications (MIKON), 2016 21st International Conference on* (2016), 1–4.

200. Zhang, W. *et al.* Determination of the Pt spin diffusion length by spin-pumping and spin Hall effect. *Appl. Phys. Lett.* **103,** 242414 (2013).

201. Tao, X. D. *et al.* The spin Hall angle and spin diffusion length of Pd measured by spin pumping and microwave photoresistance. *J. Appl. Phys.* **115,** 17C504 (2014).

202. Emori, S. *et al.* Spin transport and dynamics in all-oxide perovskite $\mathrm{La_{2/3}Sr_{1/3}MnO_3/SrRuO_3}$ bilayers probed by ferromagnetic resonance. *Phys. Rev. B* **94,** 224423 (2016).

203. Tang, M., Li, W., Ren, Y., Zhang, Z. & Jin, Q. Y. Lack of dependence between intrinsic magnetic damping and perpendicular magnetic anisotropy in Cu $(\mathrm{t_{Cu}})/[\mathrm{Ni/Co}]_N$ multilayers. *J. Magn. Magn. Mater.* **428,** 269 (2017).

204. Tang, M. *et al.* Magnetic damping and perpendicular magnetic anisotropy in Pd-buffered [Co/Ni] 5 and [Ni/Co] 5 multilayers. *RSC Advances* **7,** 5315 (2017).

205. Lubitz, P., Krebs, J. J., Miller, M. M. & Cheng, S. Temperature dependence of ferromagnetic resonance as induced by NiO pinning layers. *J. Appl. Phys.* **83,** 6819 (1998).

206. Lubitz, P., Rubinstein, M., Krebs, J. J. & Cheng, S.-F. Frequency and temperature dependence of ferromagnetic linewidth in exchange biased Permalloy. *J. Appl. Phys.* **89,** 6901 (2001).

207. Dubowik, J. *et al.* Temperature dependence of ferromagnetic resonance in permalloy/NiO exchange-biased films. *Euro. Phys. J. B* **45,** 283 (2005).

208. Counil, G. *et al.* Temperature dependences of the resistivity and the ferromagnetic resonance linewidth in permalloy thin films. *IEEE Trans. Magn.* **42,** 3323 (2006).

209. Joyeux, X. *et al.* Configuration and temperature dependence of magnetic damping in spin valves. *J. Appl. Phys.* **110,** 063915 (2011).

210. Zhao, Y. *et al.* Experimental investigation of temperature-dependent Gilbert damping in permalloy thin films. *Sci. Rep.* **6,** 22890 (2016).

211. He, S. & Panagopoulos, C. A broadband ferromagnetic resonance dipper probe for magnetic damping measurements from 4.2 K to 300 K. *Rev. Sci. Instrum.* **87,** 043110 (2016).

212. Okada, A. *et al.* Magnetization dynamics and its scattering mechanism in thin CoFeB films with interfacial anisotropy. *Proc. Natil. Acad. U.S.A.* **114,** 3815 (2017).

213. Verhagen, T. G. A. *et al.* Temperature dependence of spin pumping and Gilbert damping in thin Co/Pt bilayers. *J. Phys. Condens. Matter* **28,** 056004 (2016).

214. Moradi, H. & Gehring, G. A. The temperature dependence of the spin-wave damping in Co/CoO bilayers. *J. Magn. Magn. Mater.* **256,** 3 (2003).

215. Kalarickal, S. S., Krivosik, P., Das, J., Kim, K. S. & Patton, C. E. Microwave damping in polycrystalline Fe-Ti-N films: Physical mechanisms and correlations with composition and structure. *Phys. Rev. B* **77,** 054427 (2008).

216. Shaw, J. M., Nembach, H. T. & Silva, T. J. Damping phenomena in $Co_{90}Fe_{10}$/Ni multilayers and alloys. *Appl. Phys. Lett.* **99,** 012503 (2011).

217. Rantschler, J. O. *et al.* Effect of 3d, 4d, and 5d transition metal doping on damping in permalloy thin films. *J. Appl. Phys.* **101,** 3911 (2007).

218. Bailey, W., Kabos, P., Mancoff, F. & Russek, S. Control of magnetization dynamics in $Ni_{81}Fe_{19}$ thin films through the use of rare-earth dopants. *IEEE Trans. Magn.* **37,** 1749 (2001).

219. Woltersdorf, G., Kiessling, M., Meyer, G., Thiele, J.-U. & Back, C. H. Damping by slow relaxing rare earth impurities in $Ni_{80}Fe_{20}$. *Phys. Rev. Lett.* **102,** 257602 (2009).

220. Reidy, S. G., Cheng, L. & Bailey, W. E. Dopants for independent control of precessional frequency and damping in $Ni_{81}Fe_{19}$ (50 nm) thin films. *Appl. Phys. Lett.* **82,** 1254 (2003).

221. McCord, J., Strache, T., Mönch, I., Mattheis, R. & Fassbender, J. Spatial manipulation of magnetic damping in ferromagnetic-antiferromagnetic films by ion irradiation. *Phys. Rev. B* **83,** 224407 (2011).

222. King, J. A. *et al.* Local control of magnetic damping in ferromagnetic/nonmagnetic bilayers by interfacial intermixing induced by focused ion-beam irradiation. *Appl. Phys. Lett.* **104,** 242410 (2014).

223. Kubota, T. *et al.* Half-metallicity and Gilbert damping constant in CoFeMnSi Heusler alloys depending on the film composition. *Appl. Phys. Lett.* **94,** 122504 (2009).

224. Oogane, M. *et al.* Gilbert magnetic damping constant of epitaxially grown Co-based Heusler alloy thin films. *Appl. Phys. Lett.* **96,** 252501 (2010).

225. Beaujour, J.-M. L., Kent, A. D., Ravelosona, D., Tudosa, I. & Fullerton, E. E. Ferromagnetic resonance study of Co/Pd/Co/Ni multilayers with perpendicular anisotropy irradiated with helium ions. *J. Appl. Phys.* **109,** 033917 (2011).

226. Gilmore, K., Idzerda, Y. U. & Stiles, M. D. Identification of the Dominant Precession-Damping Mechanism in Fe, Co, and Ni by First-Principles Calculations. *Phys. Rev. Lett.* **99,** 027204 (2 July 2007).

227. Schreiber, F., Pflaum, J., Frait, Z., Mühge, T. & Pelzl, J. Gilbert damping and g-factor in Fe_xCo_{1-x} alloy films. *Solid State Commun.* **93,** 965 (1995).

228. Oogane, M. & Mizukami, S. Tunnel magnetoresistance effect and magnetic damping in half-metallic Heusler alloys. *Philos. Trans. Royal Soc. A* **369,** 3037 (2011).

229. Malinowski, G. *et al.* Control of speed and efficiency of ultrafast demagnetization by direct transfer of spin angular momentum. *Nat. Phys.* **4,** 855 (2008).

230. Zhang, G., Hübner, W., Lefkidis, G., Bai, Y. & George, T. F. Paradigm of the time-resolved magneto-optical Kerr effect for femtosecond magnetism. *Nat. phys.* **5,** 499 (2009).

231. Kyuno, K., Ha, J.-G., Yamamoto, R. & Asano, S. Magnetoelastic contribution to the interface anisotropy of Pd/Co metallic multilayers. *Phys. Rev. B* **54,** 1092–1099 (2 July 1996).

232. Nakajima, N. *et al.* Perpendicular Magnetic Anisotropy Caused by Interfacial Hybridization via Enhanced Orbital Moment in Co/Pt Multilayers: Magnetic Circular X-Ray Dichroism Study. *Phys. Rev. Lett.* **81,** 5229–5232 (23 Dec. 1998).

233. Lee, H. *et al.* Spin pumping in $Co_{56}Fe_{24}B_{20}$ multilayer systems. *J. Phys. D: Applied Physics* **41,** 215001 (2008).

234. Hickey, M. C. & Moodera, J. S. Origin of Intrinsic Gilbert Damping. *Phys. Rev. Lett.* **102,** 137601 (13 Mar. 2009).

235. Blon, T. *et al.* Magnetic easy-axis switching in Co/Pt and Co/Au superlattices induced by nitrogen ion beam irradiation. *Nucl. Instr. Meth. Phys. Res. B* **257.** Ion Beam Modification of Materials, 374–378. ISSN: 0168-583X (2007).

236. Bowen, D. K. & Tanner, B. K. *High resolution X-ray diffractometry and topography* (CRC press, 2005).

237. Ding, L. *et al.* Effects of different Pt intercalation locations on the transport properties of spin-polarized electrons in NiFe films. *J. Magn. Magn. Mater.* **354,** 81–84. ISSN: 0304-8853 (2014).

238. Avedesian, M. M., Baker, H., *et al. ASM specialty handbook: magnesium and magnesium alloys* (ASM international, 1999).

239. Conger, R. & Moore, G. Direct Observation of High-Speed Magnetization Reversal in Films. *J. Appl. Phys.* **34,** 1213–1214 (1963).

240. Keatley, P. S., Kruglyak, V., Gangmei, P. & Hicken, R. Ultrafast magnetization dynamics of spintronic nanostructures. *Philos. Trans. Royal Soc. A* **369,** 3115–3135 (2011).

241. Barman, A. & Haldar, A. in (eds Camley, R. E. & Stamps, R. L.) 1–108 (Academic Press, 2014).

242. Ounadjela, K. & Hillebrands, B. *Spin Dynamics in Confined Magnetic Structures II* 2003.

243. Brataas, A., Tserkovnyak, Y. & Bauer, G. E. W. Scattering Theory of Gilbert Damping. *Phys. Rev. Lett.* **101,** 037207 (3 July 2008).

244. A.Umerski (Personal Communication).

245. Huda, M. N., Niranjan, M. K., Sahu, B. R. & Kleinman, L. Effect of spin-orbit coupling on small platinum nanoclusters. *Phys. Rev. A* **73,** 053201 (5 May 2006).

246. Fadley, C. & Shirley, D. ELECTRONIC DENSITIES OP STATES FROM X-RAY PHOTOELECTRON SPECTROSCOPY (1970).

247. Huang, J. *et al.* Epitaxial growth and characterization of (100) and (110) permalloy films. *J. Cryst. Growth* **171,** 442–446. ISSN: 0022-0248 (1997).

248. Bader, S. & Parkin, S. Spintronics. *Annu. Rev. Condens. Matter Phys.* **1,** 71–88 (2010).

249. Kruglyak, V. V., Demokritov, S. O. & Grundler, D. Magnonics. *J. Phys. D: Applied Physics* **43,** 264001 (2010).

250. Kruglyak, V. & Hicken, R. Magnonics: Experiment to prove the concept. *J. Magn. Magn. Mater.* **306,** 191–194. ISSN: 0304-8853 (2006).

251. Wang, Q. *et al.* Magnonic band gaps in two-dimension magnonic crystals with diffuse interfaces. *J. Appl. Phys.* **115,** 113904 (2014).

252. Saha, S., Barman, S., Ding, J., Adeyeye, A. O. & Barman, A. Tunable magnetic anisotropy in two-dimensional arrays of Ni80Fe20 elements. *Appl. Phys. Lett.* **103,** 242416 (2013).

253. Mandal, R. *et al.* Effects of antidot shape on the spin wave spectra of two-dimensional Ni80Fe20 antidot lattices. *Appl. Phys. Lett.* **103,** 262410 (2013).

254. Kumar, D., Kłos, J. W., Krawczyk, M. & Barman, A. Magnonic band structure, complete bandgap, and collective spin wave excitation in nanoscale two-dimensional magnonic crystals. *J. Appl. Phys.* **115,** 043917 (2014).
255. Jaafar, M. *et al.* Pattern-induced magnetic anisotropy in FePt thin films by ion irradiation. *Phys. Rev. B* **83,** 094422 (9 Mar. 2011).
256. Baibich, M. N. *et al.* Giant Magnetoresistance of (001)Fe/(001)Cr Magnetic Superlattices. *Phys. Rev. Lett.* **61,** 2472–2475 (21 Nov. 1988).
257. Takahashi, S. & Maekawa, S. Spin current, spin accumulation and spin Hall effect. *Sci. Technol. Adv. Mater.* **9,** 014105 (2008).
258. Ganguly, A. *et al.* Thickness dependence of spin torque ferromagnetic resonance in Co75Fe25/Pt bilayer films. *Appl. Phys. Lett.* **104,** 072405 (2014).
259. Kajiwara, Y., Ando, K., Nakayama, H., Takahashi, R. & Saitoh, E. Spin pumping in polycrystalline magnetic insulator/metal Pt films. *IEEE Trans. Magn.* **47,** 2739–2742 (2011).
260. He, P. *et al.* Quadratic Scaling of Intrinsic Gilbert Damping with Spin-Orbital Coupling in $L1_0$ FePdPt Films: Experiments and Ab Initio Calculations. *Phys. Rev. Lett.* **110,** 077203 (7 Feb. 2013).
261. Parra, R. E. & Cable, J. W. Neutron study of magnetic-moment distribution in Ni-Pt alloys. *Phys. Rev. B* **21,** 5494–5504 (12 June 1980).
262. Laraoui, A. *et al.* Study of individual ferromagnetic disks with femtosecond optical pulses. *J. Appl. Phys.* **101,** 09C105 (2007).
263. Barman, A. *et al.* Imaging the dephasing of spin wave modes in a square thin film magnetic element. *Phys. Rev. B* **69,** 174426 (17 May 2004).
264. Rezende, S. *et al.* Enhanced spin pumping damping in yttrium iron garnet/Pt bilayers. *Appl. Phys. Lett.* **102,** 012402 (2013).
265. Najafabadi, R. & Srolovitz, D. Order-disorder transitions at and segregation to (001) Ni-Pt surfaces. *Surface Science* **286,** 104–115. ISSN: 0039-6028 (1993).
266. Fassbender, J., Ravelosona, D. & Samson, Y. Tailoring magnetism by light-ion irradiation. *J. Phys. D: Applied Physics* **37,** R179 (2004).

267. Bonder, M. *et al.* Ion irradiation of Co/Pt multilayer films. *J. Appl. Phys.* **93,** 7226–7228 (2003).

268. Burn, D. & Atkinson, D. Control of domain wall pinning by localised focused Ga+ ion irradiation on Au capped NiFe nanowires. *J. Appl. Phys.* **116,** 163901 (2014).

269. Allwood, D. A. *et al.* Magnetic Domain-Wall Logic. *Science* **309,** 1688–1692. ISSN: 0036-8075 (2005).

270. Diegel, M., Mattheis, R. & Halder, E. 360/spl deg/domain wall investigation for sensor applications. *IEEE trans. magn.* **40,** 2655–2657 (2004).

271. Atkinson, D., Eastwood, D. & Bogart, L. Controlling domain wall pinning in planar nanowires by selecting domain wall type and its application in a memory concept. *Appl. Phys. Lett.* **92,** 022510 (2008).

272. Parkin, S. S. P., Hayashi, M. & Thomas, L. Magnetic Domain-Wall Racetrack Memory. *Science* **320,** 190–194. ISSN: 0036-8075 (2008).

273. Kravchuk, V. P. Influence of Dzialoshinskii–Moriya interaction on static and dynamic properties of a transverse domain wall. *J. Magn. Magn. Mater.* **367,** 9–14. ISSN: 0304-8853 (2014).

274. Emori, S. *et al.* Interfacial spin-orbit torque without bulk spin-orbit coupling. *Phys. Rev. B* **93,** 180402 (18 May 2016).

275. Dzialoshinskii, I. Thermodynamic theory of weak ferromagnetism in antiferromagnetic substances. *J. Exp. Theor. Phys.* **5,** 1259–1272 (1957).

276. Jué, E. *et al.* Chiral damping of magnetic domain walls. *Nat. Mate.* **15,** 272 (2016).

277. Stashkevich, A. A. *et al.* Experimental study of spin-wave dispersion in Py/Pt film structures in the presence of an interface Dzyaloshinskii-Moriya interaction. *Phys. Rev. B* **91,** 214409 (21 June 2015).

278. Yang, H., Thiaville, A., Rohart, S., Fert, A. & Chshiev, M. Anatomy of Dzyaloshinskii-Moriya Interaction at Co/Pt Interfaces. *Phys. Rev. Lett.* **115,** 267210 (26 Dec. 2015).

279. Yoshimura, Y. *et al.* Soliton-like magnetic domain wall motion induced by the interfacial Dzyaloshinskii-Moriya interaction. *Nat. Phys.* **12,** 157–161 (2016).

280. Gladii, O., Haidar, M., Henry, Y., Kostylev, M. & Bailleul, M. Frequency nonreciprocity of surface spin wave in permalloy thin films. *Phys. Rev. B* **93,** 054430 (5 Feb. 2016).

281. Cho, J. *et al.* Thickness dependence of the interfacial Dzyaloshinskii–Moriya interaction in inversion symmetry broken systems. *Nat. commun.* **6,** 7635 (2015).

282. Ley Domínguez, D. *et al.* High-resolution electron microscopy in spin pumping NiFe/Pt interfaces. *J. Appl. Phys.* **117,** 17D910 (2015).

283. Ganguly, A. *et al.* Time-domain detection of current controlled magnetization damping in Pt/Ni81Fe19 bilayer and determination of Pt spin Hall angle. *Appl. Phys. Lett.* **105,** 112409 (2014).

284. Haazen, P. *et al.* Domain wall depinning governed by the spin Hall effect. *Nat. Mate.* **12,** 299 (2013).

285. Weindler, T. *et al.* Magnetic Damping: Domain Wall Dynamics versus Local Ferromagnetic Resonance. *Phys. Rev. Lett.* **113,** 237204 (23 Dec. 2014).

286. Wang, W. *et al.* Phenomenological description of the nonlocal magnetization relaxation in magnonics, spintronics, and domain-wall dynamics. *Phys. Rev. B* **92,** 054430 (5 Aug. 2015).

287. Atkinson, D. *et al.* Magnetic domain wall dynamics in a permalloy nanowire. *IEEE Trans. Magn.* **39,** 2663–2665 (2003).

288. Burn, D. M. & Atkinson, D. Suppression of Walker breakdown in magnetic domain wall propagation through structural control of spin wave emission. *Appl. Phys. Lett.* **102,** 242414 (2013).

289. Brandão, J. & Atkinson, D. Controlling the stability of both the structure and velocity of domain walls in magnetic nanowires. *Appl. Phys. Lett.* **109,** 062405 (2016).

290. Allwood, D., Xiong, G., Cooke, M. & Cowburn, R. Magneto-optical Kerr effect analysis of magnetic nanostructures. *J. Phys. D: Applied Physics* **36,** 2175 (2003).

291. Vansteenkiste, A. & de Wiele, B. V. MuMax: A new high-performance micromagnetic simulation tool. *J. Magn. Magn. Mater.* **323,** 2585–2591. ISSN: 0304-8853 (2011).

292. Rave, W., Ramstöck, K. & Hubert, A. Corners and nucleation in micromagnetics1Presented at the ICM'97 in Cairns, Australia.1. *J. Magn. Magn. Mater.* **183,** 329–333. ISSN: 0304-8853 (1998).

293. Bogart, L. K., Atkinson, D., O'Shea, K., McGrouther, D. & McVitie, S. Dependence of domain wall pinning potential landscapes on domain wall chirality and pinning site geometry in planar nanowires. *Phys. Rev. B* **79,** 054414 (5 Feb. 2009).

294. Uhlig, W. C., Donahue, M. J., Pierce, D. T. & Unguris, J. Direct imaging of current-driven domain walls in ferromagnetic nanostripes. *J. Appl. Phys.* **105,** 103902 (2009).

295. Bogart, L., Eastwood, D. & Atkinson, D. The effect of geometrical confinement and chirality on domain wall pinning behavior in planar nanowires. *J. Appl. Phys.* **104,** 033904 (2008).

296. Hrabec, A. *et al.* Spin-orbit interaction enhancement in permalloy thin films by Pt doping. *Phys. Rev. B* **93,** 014432 (1 Jan. 2016).

297. Suhl, H. Theory of the magnetic damping constant. *IEEE Trans. Magn.* **34,** 1834 (1998).

298. Nembach, H. T., Shaw, J. M., Weiler, M., Jué, E. & Silva, T. J. Linear relation between Heisenberg exchange and interfacial Dzyaloshinskii–Moriya interaction in metal films. *Nat. Phys.* **11,** 825 (2015).

299. Tacchi, S. *et al.* Interfacial Dzyaloshinskii-Moriya Interaction in $\mathrm{Pt}/\mathrm{CoFeB}$ Films: Effect of the Heavy-Metal Thickness. *Phys. Rev. Lett.* **118,** 147201 (14 Apr. 2017).

300. Stein, F.-U., Bocklage, L., Weigand, M. & Meier, G. Time-resolved imaging of nonlinear magnetic domain-wall dynamics in ferromagnetic nanowires. *Sci. Rep.* **3,** 1737 (2013).

301. Tretiakov, O. A. & Abanov, A. Current Driven Magnetization Dynamics in Ferromagnetic Nanowires with a Dzyaloshinskii-Moriya Interaction. *Phys. Rev. Lett.* **105,** 157201 (15 Oct. 2010).

302. Thiaville, A. & Nakatani, Y. in *Spin dynamics in confined magnetic structures III* 161–205 (Springer, 2006).

303. Mougin, A., Cormier, M., Adam, J. P., Metaxas, P. J. & Ferré, J. Domain wall mobility, stability and Walker breakdown in magnetic nanowires. *E. P. L.* **78,** 57007 (2007).

304. Hayward, T. Intrinsic nature of stochastic domain wall pinning phenomena in magnetic nanowire devices. *Sci. Rep.* **5,** 13279 (2015).

305. Chen, G. *et al.* Tailoring the chirality of magnetic domain walls by interface engineering. *Nat. commun.* **4,** 2671 (2013).

306. Pham, T. H. *et al.* Very large domain wall velocities in Pt/Co/GdOx and Pt/Co/Gd trilayers with Dzyaloshinskii-Moriya interaction. *E. P. L.* **113,** 67001 (2016).

307. Barati, E. & Cinal, M. Gilbert damping in binary magnetic multilayers. *Phys. Rev. B* **95,** 134440 (2017).

308. D'Allivy Kelly, O. *et al.* Inverse spin Hall effect in nanometer-thick yttrium iron garnet/Pt system. *Appl. Phys. Lett.* **103,** 082408 (2013).

309. Onbasli, M. *et al.* Pulsed laser deposition of epitaxial yttrium iron garnet films with low Gilbert damping and bulk-like magnetization. *APL Materials* **2,** 106102 (2014).

310. Chang, H. *et al.* Nanometer-thick yttrium iron garnet films with extremely low damping. *IEEE Magnetics Letters* **5,** 1–4 (2014).

311. Liu, C., Mewes, C. K., Chshiev, M., Mewes, T. & Butler, W. H. Origin of low Gilbert damping in half metals. *Appl. Phys. Lett.* **95,** 022509 (2009).

312. Edwards, D. M. & Wessely, O. The quantum-mechanical basis of an extended Landau–Lifshitz–Gilbert equation for a current-carrying ferromagnetic wire. *J. Phys. Condens. Matter* **21,** 146002 (2009).

313. Fallarino, L. *et al.* Magnetic properties of epitaxial CoCr films with depth-dependent exchange-coupling profiles. *Phys. Rev. B* **95,** 134445 (13 Apr. 2017).

314. Honda, S., Takahashi, K. & Kusuda, T. Wall Energy and Exchange Stiffness in CoCr Films Sputtered on Low Temperature Substrates. *Jap. J. Appl. Phys.* **26,** L593 (1987).

315. Inaba, N., Futamoto, M. & Nakamura, A. Temperature dependence of magnetocrystalline anisotropy energy determined using Co-Cr-Ta single crystal thin films. *IEEE trans. magn.* **34,** 1558–1560 (1998).

316. Kirby, B. J. *et al.* Spatial Evolution of the Ferromagnetic Phase Transition in an Exchange Graded Film. *Phys. Rev. Lett.* **116,** 047203 (4 Jan. 2016).